



THE HONG KONG
POLYTECHNIC UNIVERSITY

香港理工大學

Pao Yue-kong Library

包玉剛圖書館

Copyright Undertaking

This thesis is protected by copyright, with all rights reserved.

By reading and using the thesis, the reader understands and agrees to the following terms:

1. The reader will abide by the rules and legal ordinances governing copyright regarding the use of the thesis.
2. The reader will use the thesis for the purpose of research or private study only and not for distribution or further reproduction or any other purpose.
3. The reader agrees to indemnify and hold the University harmless from and against any loss, damage, cost, liability or expenses arising from copyright infringement or unauthorized usage.

IMPORTANT

If you have reasons to believe that any materials in this thesis are deemed not suitable to be distributed in this form, or a copyright owner having difficulty with the material being included in our database, please contact lbsys@polyu.edu.hk providing details. The Library will look into your claim and consider taking remedial action upon receipt of the written requests.

**RAYS-CONCENTRATING MECHANISM AND
THERMAL PERFORMANCE OF PARABOLIC
TROUGH SOLAR COLLECTORS**

ZOU BIN

PhD

The Hong Kong Polytechnic University

**This programme is jointly offered by The Hong Kong
Polytechnic University and Harbin Institute of Technology**

2020

The Hong Kong Polytechnic University
Department of Building Services Engineering
Harbin Institute of Technology
Department of Building Thermal Engineering

**Rays-Concentrating Mechanism and Thermal
Performance of Parabolic Trough Solar Collectors**

ZOU Bin

**A thesis submitted in partial fulfilment of the requirements for the
Degree of Doctor of Philosophy**

August 2019

CERTIFICATE OF ORIGINALITY

I hereby declare that this thesis is my own work and that, to the best of my knowledge and belief, it reproduces no material previously published or written, nor material that has been accepted for the award of any other degree or diploma, except where due acknowledgement has been made in the text.

_____ (Signed)

ZOU Bin (Name of student)

ABSTRACT

The parabolic trough concentrator (PTC) is currently the most cost-effective and widely used solar collector in concentrating solar power (CSP) area, showing great development prospect. The performance of the PTC is the determinant of the whole PTC-based thermal system, which depends on the rays-concentrating of the reflector and the heat transfer in the receiver tube. In previous studies, attentions were mainly focused on simulating the overall optical performance, while the theoretically quantitative analyses of the rays-concentrating of the reflector were seldom discussed. The optical performance of the PTC under non-ideal conditions were never examined based on the individual characterization of non-ideal optical factors, and related theoretical analyses were also scarcely performed. Furthermore, thermal improvement of the receiver tube based on the idea of enhancing the heat transfer between the fluid and the high heat flux area of the absorber wall was seldom explored as well in the past. Therefore, this thesis is committed to investigating comprehensively the optical and thermal performance of the PTC, aiming to reveal its mechanism of photo-thermal conversion and to propose an effective thermal improvement method. The Monte Carlo Rays Tracing (MCRT) coupled with theoretical analysis is used for investigating the rays-concentrating process, and a computational fluid dynamics (CFD) tool is adopted for simulation of the thermal and hydraulic performance of the parabolic trough receiver (PTR).

Firstly, the optical performance of the PTC under ideal optical conditions was explored. The MCRT models were established and validated by other proven methods presented in literatures. Detailed geometrical analyses of the ideal rays-concentrating process were conducted. Several important parameters reflecting the rays-spillage, the variation of heat flux distribution range and the shadowing effect of the absorber tube were derived theoretically. Based on the MCRT and geometrical analyses, the effects of structural parameters on the PTC's optical performance were investigated. It was revealed that there was a critical diameter, within which the absorber could only receive partially reflected rays, resulting in rays-spillage and consequently causing huge optical loss. Both the aperture width and the focal length should be kept in a certain range to avoid rays-spillage. The distribution range of high local concentration ratio (*LCR*) on the absorber outer surface increased with increasing aperture width, while decreased with increasing focal length. The peak *LCR* increased constantly with increasing aperture width, while dropped firstly and then increased with increasing focal length. Larger absorber diameter reduced both the peak *LCR* and the high *LCR* distribution range, and improved the optical efficiency. As the focal length was small or the absorber diameter was larger enough, the apex area of parabolic reflector and the bottom part of the absorber tube could not receive any solar rays due to the shadowing effect of the absorber itself. All the critical parameters corresponding to above optical phenomena were deduced through geometrical analyses and could be used to explain the changing optical properties of the PTC under the ideal condition.

Then, an investigation on the optical performance of the PTC under non-ideal optical conditions was implemented. All the non-ideal optical factors including the sunshape, all the optical errors and non-zero incident angle were characterized separately based on their generation principles. Coordinate transformation was performed and the effective sunshape model was established for optical modeling under non-ideal optical conditions. Results showed that larger circumsolar ratio (CSR) and specular error produced more uniform heat flux distribution. The advantage of the high optical quality reflector in improving optical efficiency was obvious only in clear days. When tracking error and slope error were maintained within a certain range (less than 4 mrad and 2 mrad respectively), the drop of optical efficiency was limited. The downtrend of the optical efficiency caused by tracking error became gentler under larger slope errors, and the optical loss was more sensitive to slope error than to tracking error. The offset direction along X-axis caused the greatest optical loss, and that along positive Y-axis posed threat of overheat to the absorber. When absorber alignment error and tracking error were in the opposite direction, the optical loss could be compensated, defined as compensation effect, whereas that in the same direction enlarged the optical loss, defined as weakening effect. The slope error weakened the compensation effect and aggravated the weakening effect.

Succeeding to the above MCRT simulations, detailed theoretical analyses on the rays-concentrating process of the PTC under non-ideal optical conditions were conducted. Based on the theory of spatial analytic geometry, the critical absorber diameter under

any optical error conditions was derived theoretically. And then, a new simple algorithm based on the idea of viewing the sun as consisting of countless line light sources was developed for quick calculation of optical efficiency. The proposed algorithm, compared with the MCRT, had a great advantage of time saving, which was suitable for engineering calculation. Finally, based on the derived formulas and the proposed algorithm, the effective sunshape size was further discussed for the sake of engineering application. In addition, the changing properties of optical efficiency achieved by the MCRT in the preceding chapter were also expounded using the theoretical results.

Finally, the thermal performance improvement of the parabolic trough receiver (PTR) was explored. The basic thermal performance of the conventional straight-smooth PTR (CSS-PTR) was analyzed, and a unilateral spiral ribbed PTR (USR-PTR) was proposed based on the idea of enhancing the heat transfer between the fluid and the high heat flux area (i.e. bottom part) of the absorber to improve its thermal performance. In order to realize the simulation of the heat transfer under actual heat flux conditions, the heat flux distribution obtained by MCRT in preceding chapters was loaded as the boundary condition on the absorber outer surface by User Defined Functions (UDF). It was revealed that the temperature distribution of the absorber is completely dependent on the heat flux distribution, and the circumferential temperature difference remained constant in the longitudinal direction. As the flow rate grew, the distribution of fluid temperature on the cross section changed from annular stratification to vertical stratification. When the annulus space of the receiver was filled with air or the glass

envelope was broken, the collector efficiency was reduced by 4.31% and 26.1% respectively, indicating that ensuring high vacuum degree in the annulus is critical to achieving high performance. Comparisons of the USR-PTR and the CSS-PTR showed that, in most cases of the discussed flow rates (0.5~3.5 kg/s), the overall performance of the USR-PTR was better than that of the CSS-PTR. The circumferential temperature difference of the USR-PTR could be reduced by 8.5%~27.4% to the CSS-PTR. The thermal improvement mechanism of the USR-PTR was also analyzed according to field synergy theory, which indicates that the synergy between the velocity field and the temperature gradient field of the fluid in the USR-PTR was much better than that in the CSS-PTR. Finally, based on the performance evaluation criteria (PEC), the influences of the rib's structural parameters, including pitch interval, rib height, corner radius, crest radius and spiral angle, on the overall performance of the USR-PTR were investigated comprehensively. The PEC of the USR-PTR by adjusting individually the above five rib structural parameters was 1.125, 1.098, 1.108, 1.096 and 1.301, respectively.

In summary, this thesis conducted a detailed study on the optical and thermal performance of the PTC, aiming to reveal its rays-concentrating mechanism and to seek effective thermal improvement measures. The findings in this study enrich the basic research theory in the field of PTC, and provide important theoretical guidance for the application and promotion of PTCs. The developed algorithm for optical efficiency is suitable for engineering application, and the proposed thermal improvement method provides a new idea for engineers and designers to optimize the structure of the PTR.

PUBLICATIONS DURING PHD STUDY

Journal papers:

- [1] **Bin Zou**, Jiankai Dong, Yang Yao, Yiqiang Jiang. An experimental investigation on a small-sized parabolic trough solar collector for water heating in cold areas. *Applied Energy* 2016; 163: 396-407.
- [2] **Bin Zou**, Jiankai Dong, Yang Yao, Yiqiang Jiang. A detailed study on the optical performance of parabolic trough solar collectors with Monte Carlo Ray Tracing method based on theoretical analysis. *Solar Energy* 2017; 147: 189-201.
- [3] **Bin Zou**, Hongxing Yang, Yang Yao, Yiqiang Jiang. A detailed study on the effects of sunshape and incident angle on the optical performance of parabolic trough solar collectors. *Applied Thermal Engineering* 2017; 126: 81-91.
- [4] **Bin Zou**, Yang Yao, Yiqiang Jiang, Hongxing Yang. A new algorithm for obtaining the critical tube diameter and intercept factor of parabolic trough solar collectors. *Energy* 2018; 150: 451-467.
- [5] **Bin Zou**, Yiqiang Jiang, Yang Yao, Hongxing Yang. Impacts of non-ideal optical factors on the performance of parabolic trough solar collectors. *Energy* 2019; 183:

1150-1165.

[6] **Bin Zou**, Yiqiang Jiang, Yang Yao, Hongxing Yang. Optical performance of parabolic trough solar collectors under condition of multiple optical factors. *Applied Thermal Engineering* 2019; 160: 114070.

[7] **Bin Zou**, Yiqiang Jiang, Yang Yao, Hongxing Yang. Thermal performance improvement using unilateral spiral ribbed absorber tube for parabolic trough solar collector. *Solar Energy* 2019; 183: 371-385.

Other Publications:

[1] Jiwei Guo, **Bin Zou**, Chao Shen, Yiqiang Jiang. Performance analysis of heat pump waste heat recovery system in public bathroom. *Building Science* 2019; 35(2): 68-73. (In Chinese)

ACKNOWLEDGEMENTS

During my PhD study period, there were many people who have given me so much support and help. It is my pleasure to take this opportunity to express my grateful acknowledgements to all of them for their great help.

First and foremost, I would like to express my most sincere gratitude to my chief supervisor, Prof. Yang Hongxing, for his expert guidance, continuous encouragement and constant support during my pursuing the doctoral degree. Moreover, his profound academic strength, positive life attitude and friendly personality set an example for my life-long learning.

My deep thanks are also devoted to my co-supervisors, Prof. Yao Yang and Prof. Jiang Yiqiang from Harbin Institute of Technology (HIT). During my PhD study, both Prof. Yao and Prof. Jiang have been carefully guided me. At regular meetings, they gave me valuable suggestions and comments which broadened my thoughts, so that my thesis could be completed successfully.

I also wish to express my warm thanks to Prof. Lu Lin, for her insightful views and great help on my research.

Furthermore, I would like to express my deep thanks to all the members in the

Renewable Energy Research Group for their help and support during my study at PolyU.

I also thank the members in the Institute of Heat Pump and Air Conditioning Technology very much for their help and company during my study at HIT.

I also appreciate very much The Hong Kong Polytechnic University and Harbin Institute of Technology for providing me with the opportunity to participate in the Joint PhD Programme Leading to Dual Awards. It is my great honor to study in these two excellent universities.

My heartfelt gratitude goes to my beloved parents, Mr. Zou Zhongping and Ms. Huang Wenhua, for their love, support and paying without expecting any return.

Finally, I sincerely thank all the experts and professors who took time out from their busy schedule to review this thesis.

TABLE OF CONTENTS

CERTIFICATE OF ORIGINALITY	I
ABSTRACT.....	II
PUBLICATIONS DURING PHD STUDY	VII
ACKNOWLEDGEMENTS.....	IX
TABLE OF CONTENTS.....	XI
LIST OF FIGURES	XVII
LIST OF TABLES	XXVII
NOMENCLATURE.....	XXIX
CHAPTER 1	1
INTRODUCTION	1
1.1 Background of concentrating solar power	1
1.2 Introduction to parabolic trough solar collector.....	3
1.3 Objectives of the thesis	7
1.4 Organization of the thesis	8
CHAPTER 2	12
LITERATURE REVIEW AND RESEARCH METHODOLOGY	12
2.1 Introduction.....	12
2.2 Optical performance of the PTC	12
2.2.1 Optical analysis of the PTC	12
2.2.2 Optical performance improvement of the PTC.....	15

2.3 Effects of non-ideal optical factors on the performance of PTC	19
2.3.1 Characterization of non-ideal optical factors	19
2.3.2 Research on the effects of non-ideal optical factors on the performance of the PTC	23
2.4 Thermal performance of the PTC	25
2.4.1 Experimental study of the thermal performance.....	26
2.4.2 Numerical study of the thermal performance	29
2.4.3 Thermal performance improvement of the PTC	33
2.5 Research gaps and methodology.....	43
2.5.1 Research gaps.....	44
2.5.2 Methodology	45
CHAPTER 3	49
OPTICAL PERFORMANCE OF PARABOLIC TROUGH SOLAR COLLECTOR UNDER IDEAL OPTICAL CONDITIONS.....	49
3.1 Introduction.....	49
3.2 MCRT modeling and validation.....	50
3.2.1 MCRT modeling	51
3.2.3 Model validation	57
3.3 Geometrical analysis of the ideal rays-concentrating process	61
3.4 Effects of structural parameters on the optical performance	67
3.4.1 Effects of aperture width.....	68
3.4.2 Effects of focal length.....	74

3.4.3 Effects of absorber outer diameter	81
3.5 Summary	85
CHAPTER 4	88
OPTICAL PERFORMANCE OF PARABOLIC TROUGH SOLAR COLLECTOR UNDER NON-IDEAL OPTICAL CONDITIONS.....	88
4.1 Introduction.....	88
4.2 Description of non-ideal optical factors.....	89
4.2.1 Sunshape	89
4.2.2 Optical errors	92
4.2.3 Incident angle.....	96
4.3 Coordinate transformation and effective sunshape modeling.....	97
4.3.1 Coordinate transformation	97
4.3.2 Effective sunshape modeling	100
4.4 Effects of non-ideal optical factors on the optical performance	103
4.4.1 Effects of effective sunshape	104
4.4.2 Effects of tracking error and slope error	109
4.4.3 Effects of absorber alignment error	114
4.4.4 Effects of incident angle	120
4.5 Summary	129
CHAPTER 5	133
THEORETICAL ANALYSIS OF THE OPTICAL PERFORMANCE UNDER NON- IDEAL OPTICAL CONDITIONS	133

5.1 Introduction.....	133
5.2 Derivation of critical absorber diameter	134
5.3 Algorithm development for optical efficiency	147
5.4 Results and discussion	153
5.4.1 Algorithm validation and analysis	153
5.4.2 Effective solar radial size.....	157
5.4.3 Theoretical analysis of optical efficiency	162
5.4.4 Coupling effects of optical errors.....	167
5.5 Summary.....	170
CHAPTER 6	173
THERMAL PERFORMANCE IMPROVEMENT USING UNILATERAL SPIRAL RIBBED ABSORBER TUBE FOR PARABOLIC TROUGH SOLAR COLLECTOR	173
6.1 Introduction.....	173
6.2 Introduction to the USR-PTR	174
6.2.1 Description of the USR-PTR	174
6.2.2 Material properties	175
6.3 Parameters for assessing the thermal performance of the PTR	178
6.3.1 Performance evaluation criteria (PEC).....	178
6.3.2 Field synergy theory	179
6.4 Numerical model and validation.....	181
6.4.1 Analysis of the heat transfer in the receiver tube.....	181

6.4.2 Numerical model.....	184
6.4.3 Boundary conditions and solution method	185
6.4.4 Grid independence checking.....	188
6.4.5 Model validation	190
6.5 Thermal performance of the CSS-PTR.....	193
6.5.1 Distribution of fluid temperature and velocity.....	193
6.5.2 Distribution of absorber tube temperature	197
6.5.3 Distribution of glass envelope temperature	201
6.5.4 Analysis of heat loss and collector efficiency	204
6.6 Comparison of USR-PTR and CSS-PTR.....	205
6.6.1 Comparison of thermal performance	206
6.6.2 Comparison of hydraulic performance	210
6.6.3 Comparison of field synergy.....	215
6.7 Influences of structural parameters of the rib	218
6.7.1 Influences of the pitch interval of the rib.....	218
6.7.2 Influences of the height of the rib	221
6.7.3 Influences of the corner radius of the rib	225
6.7.4 Influences of the crest radius of the rib.....	228
6.7.5 Influences of the spiral angle of the rib	231
6.8 Summary	234
CHAPTER 7	238
CONCLUSIONS AND RECOMMENDATIONS FOR FUTURE WORK	238

7.1 Conclusions.....	238
7.2 Recommendations for future work.....	244
REFERENCES	246

LIST OF FIGURES

Chapter 1

Fig. 1.1 Four typical types of concentrating solar collectors (CSC): (a) parabolic trough collector (PTC), (b) heliostat field collector (HFC), (c) linear Fresnel collector (LFC), (d) parabolic dish collector (PDC)	2
Fig. 1.2 Schematic of a PTC module: (a) PTC module, (b) receiver tube	4
Fig. 1.3 Rays-concentrating of the PTC	5
Fig. 1.4 Schematic for sun-tracking of the PTC	6
Fig. 1.5 Deformation of the receiver tube and breakage of the glass envelope caused by the uneven heat flux distribution	6

Chapter 2

Fig. 2.1 Four types of secondary reflective mirrors: (a) reflective glass surface, (b) reflective annulus insulation, (c) aplanatic secondary mirror, (d) tailored seagull secondary mirror	17
Fig. 2.2 The schematic of the test system built in Sandia National Laboratories.....	26
Fig. 2.3 The rotating testing platform built in Sandia National Laboratories	27
Fig. 2.4 Receiver tubes with different metal radiation shields: with solar selective coating (left) and without solar selective coating (right)	35
Fig. 2.5 Flow chart of methodology	47

Chapter 3

Fig. 3.1 The rays-concentrating process of the PTC under ideal conditions	51
---------------------------------------------------------------------------------	----

Fig. 3.2 The flowchart of MCRT	56
Fig. 3.3 Variation of the LCR_{max} with the total number of rays	59
Fig. 3.4 Effect of the total number of rays on the distribution of the LCR	59
Fig. 3.5 Comparison of distribution of LCR obtained by different methods	61
Fig. 3.6 The rays-concentrating process for any point on the reflector	63
Fig. 3.7 The case leading to rays-spillage	64
Fig. 3.8 The case that the bottom of the absorber cannot receive concentrated beam ...	66
Fig. 3.9 The distribution of LCR under different aperture widths: (a) $3\text{ m} \leq W_c \leq 15\text{ m}$, (b) $0.5\text{ m} \leq W_c \leq \text{m}$, (c) partially enlarged detail	69
Fig. 3.10 Variation of theoretical calculated angles with aperture width	70
Fig. 3.11 Variation of Θ with the absolute value of point A	71
Fig. 3.12 Variation of optical efficiency with aperture width	72
Fig. 3.13 Variation of rim angle and critical diameter with aperture width	72
Fig. 3.14 Variation of the maximum and the average LCR and the ζ with aperture width	73
Fig. 3.15 The distribution of LCR under different focal lengths: (a) $0.1\text{ m} \leq f_c \leq 2.25\text{ m}$, (b) partial enlarged detail, (c) $2\text{ m} \leq f_c \leq 5.75\text{ m}$, (d) partially enlarged detail	76
Fig. 3.16 Variation of Θ with the absolute value of point A under different focal lengths	77
Fig. 3.17 Variation of Θ and the minimum absolute value of point A with focal length	78
Fig. 3.18 Variation of theoretical calculated angle with aperture width	78

Fig. 3.19 Variation of optical efficiency with focal length	79
Fig. 3.20 Variation of rim angle and critical diameter with focal length	79
Fig. 3.21 Variation of the maximum and the average <i>LCR</i> and the ζ with focal length ..	80
Fig. 3.22 The distribution of <i>LCR</i> under different absorber outer diameters: (a) $30 \text{ mm} \leq d_{a,o} \leq 100 \text{ mm}$, (b) $20 \text{ mm} \leq d_{a,o} \leq 35 \text{ mm}$, (c) partially enlarged detail	82
Fig. 3.23 Variation of Θ with the absolute value of point A	83
Fig. 3.24 Variation of optical efficiency with absorber outer diameter	84
Fig. 3.25 Variation of the maximum and the average <i>LCR</i> and the ζ with absorber outer diameter	84
Fig. 3.26 Variation of the effective angle span receiving concentrated beam with absorber outer diameter	85

Chapter 4

Fig. 4.1 Schematic of the sunshape	89
Fig. 4.2 Buie's sunshape plotted in log-log space	91
Fig. 4.3 Effect of specular error on the reflected sunshape	92
Fig. 4.4 Schematic of tracking error	94
Fig. 4.5 Schematic of slope error	95
Fig. 4.6 Schematic of absorber alignment error	95
Fig. 4.7 Schematic of incident angle and end loss	97
Fig. 4.8 Incidence of sunrays under non-ideal conditions	98
Fig. 4.9 Coupling effect of tracking error and slope error	98

Fig. 4.10 Schematic of coordinate transformation	99
Fig. 4.11 Schematic of optical cone	101
Fig. 4.12 Flow chart of the sampling of the radial angle of incident sunlight	103
Fig. 4.13 Effects of CSR on the distribution of <i>LCR</i> in the case of $\sigma_{sp}=3$ mrad	105
Fig. 4.14 Effects of specular error on the distribution of <i>LCR</i> in the case of CSR=0.1	106
Fig. 4.15 Variation of the optical efficiency with CSR under different specular errors	108
Fig. 4.16 Variation of the optical efficiency with specular error under different CSRs	109
Fig. 4.17 Effects of tracking error on the distribution of local <i>LCR</i>	111
Fig. 4.18 Effects of slope error on the distribution of <i>LCR</i>	111
Fig. 4.19 Variation of the optical efficiency with tracking error under different slope errors	112
Fig. 4.20 Variation of the optical efficiency with slope error under different tracking errors	113
Fig. 4.21 Effects of the absorber alignment error on the distribution of <i>LCR</i> : (a) $a=0^\circ$, (b) $a=90^\circ$	115
Fig. 4.22 Effects of absorber alignment error on the optical efficiency: (a) variation with offset distance under different offset angles, (b) variation with offset angle under different offset distances	117
Fig. 4.23 Variation of the optical efficiency with offset angle for $l_a=0.03$ m under	

different tracking errors in the case of $\sigma_{sl}=3$ mrad	119
Fig. 4.24 Variation of the optical efficiency with offset angle for $l_a=0.03$ m under different slope errors in the case of $b_{tr}=5$ mrad	120
Fig. 4.25 Circumferential distribution of LCR at two sections under different incident angles: (a) $z=2$ m, (b) $z=7.5$ m	121
Fig. 4.26 Variation of $L_{end\ loss}$ with the absolute value of abscissa of any point A on the reflector under different incident angles	123
Fig. 4.27 Longitudinal distribution of LCR at different circumferential angles in the case of $\theta_{in}=30^\circ$	124
Fig. 4.28 Color map of heat flux distribution on the absorber outer surface under different incident angles: (a) $\theta_{in}=15^\circ$, (b) $\theta_{in}=30^\circ$, (c) $\theta_{in}=45^\circ$, (d) $\theta_{in}=60^\circ$	125
Fig. 4.29 Variation of optical efficiency with incident angle under ideal condition ...	126
Fig. 4.30 Variation of optical efficiency with incident angle under different effective sunshape: (a) different CSRs, (b) different specular errors	127
Fig. 4.31 Variation of optical efficiency with incident angle under different tracking errors	128
Fig. 4.32 Variation of optical efficiency with incident angle under different slope errors	129
Fig. 4.33 Variation of optical efficiency with incident angle under different absorber alignment errors	129

Chapter 5

Fig. 5.1 Offset direction is on the right side of the centerline (AO') of the reflected optical cone: (a) $0 < a \leq 90^\circ - \psi_A$, (b) $-90^\circ < a \leq 0$, (c) $-90^\circ - \psi_A < a \leq -90^\circ$	136
Fig. 5.2 Offset direction is on the left side of the centerline (AO') of the reflected optical cone: (a) $90^\circ - \psi_A < a \leq 90^\circ$, (b) $90^\circ < a \leq 180^\circ$, (c) $180^\circ < a \leq 270^\circ - \psi_A$	139
Fig. 5.3 The situation that point A is on the right half of the reflector ($x_A > 0$)	140
Fig. 5.4 Three cases for calculating the critical radius for any point on the reflector ...	143
Fig. 5.5 The reflection process of sunrays	147
Fig. 5.6 Schematic for calculating the intensity of line light source	148
Fig. 5.7 Schematic for calculating the energy intercepted by the absorber tube	150
Fig. 5.8 Variation of energy ratio bounded by radial angle of line light source under different specularity errors	159
Fig. 5.9 Variation of energy ratio bounded by radial angle of line light source under different CSRs	160
Fig. 5.10 Variation of energy ratio contained in the solar disk with specularity error under different CSRs	161
Fig. 5.11 Variation of optical efficiency with CSR under different specularity errors .	162
Fig. 5.12 Variation of the acceptance angle with the abscissa of point A	163
Fig. 5.13 Variation of energy ratio bounded by radial angle for $\sigma_{sp}=1$ mrad and $\sigma_{sp}=7$ mrad in the cases of CSR=0.3 and CSR=0.7	164
Fig. 5.14 Variation of optical efficiency with specularity error under different CSRs	166
Fig. 5.15 Variation of optical efficiency under different combinations of absorber alignment error and equivalent deflecting error: (a) $l_a=0.04$ m, (b) $l_a=0.07$ m	168

Fig. 5.16 Variation of critical diameter with offset angle under different equivalent deflecting errors ($l_a=0.04$ m)	170
-------------------------------------------------------------------------------------------------------------------------------	-----

Chapter 6

Fig. 6.1 Schematic of the USR-PTR: (a) 3D model, (b) longitudinal section	175
Fig. 6.2 Variation of thermophysical parameters of the HTF with temperature: (a) density, (b) specific heat, (c) conductivity, (d) dynamic viscosity	177
Fig. 6.3 Heat transfer analysis in the receiver tube: (a) heat transfer process, (b) thermal resistance network	182
Fig. 6.4 Heat flux distribution on the absorber outer surface; (a) produced by MCRT, (b) loaded by UDF	186
Fig. 6.5 Schematic of domain discretization (meshing): (a) transverse section, (b) longitudinal section	192
Fig. 6.6 Comparison of the results between simulation and empirical formulas: (a) results of Nu , (b) results of f	194
Fig. 6.7 Fluid temperature distribution at each section	194
Fig. 6.8 Fluid temperature distribution at $z=7.5$ m	194
Fig. 6.9 Distribution of fluid velocity along Y-axis at $z=7.5$ m	194
Fig. 6.10 Vector diagram of fluid velocity at $z=7.5$ m	194
Fig. 6.11 The distribution of fluid temperature at $z=7.5$ m under different mass flow rates: (a) $m=1$ kg/s, (b) $m=3$ kg/s, (c) $m=5$ kg/s, (d) $m=7$ kg/s	196
Fig. 6.12 The distribution of fluid velocity along Y axis at $z=7.5$ m under different mass	

flow rates: (a) $m=1$ kg/s, (b) $m=7$ kg/s	197
Fig. 6.13 Distribution of the absorber temperature at each section	198
Fig. 6.14 Circumferential distribution of the absorber outer surface temperature at different sections	199
Fig. 6.15 Longitudinal distribution of the absorber outer surface temperature at different circumferential angles	199
Fig. 6.16 Distribution of the temperature of inner and outer surfaces of the absorber at $z=7.5$ m	200
Fig. 6.17 Distribution of the glass envelope temperature at each section	201
Fig. 6.18 Circumferential distribution of the glass envelope inner surface temperature at different sections	202
Fig. 6.19 Distribution of the temperature of the inner and outer surfaces of the glass envelope at $z=7.5$ m	203
Fig. 6.20 Heat loss and collector efficiency under different receiver tube conditions .	205
Fig. 6.21 Variation of the Nusselt number (Nu) with mass flow rate (m)	207
Fig. 6.22 Distribution of the fluid temperature in the longitudinal section under condition of $m=2$ kg/s ($z=0.6\sim 0.7$ m): (a) CSS-PTR, (b) USR-PTR	208
Fig. 6.23 Distribution of the absorber temperature under condition of $m=2$ kg/s ($z=0.6\sim 0.7$ m): (a) inner surface of the CSS-PTR, (b) inner surface of the USR-PTR, (c) outer surface of the CSS-PTR, (d) outer surface of the USR-PTR	209
Fig. 6.24 Variation of the maximum ($T_{a,max}$) and minimum ($T_{a,min}$) temperature of the absorber at $z=0.6$ m with mass flow rate (m)	210

Fig. 6.25 Variation of the pressure drop (ΔP) with mass flow rate (m)	211
Fig. 6.26 Variation of the friction factor (f) with mass flow rate (m)	212
Fig. 6.27 Diagram of the fluid velocity vector in the longitudinal section under condition of $m=2$ kg/s ($z=0.6\sim 0.7$ m): (a) CSS-PTR, (b) USR-PTR	213
Fig. 6.28 Diagram of fluid velocity vector in different cross sections of the USR-PTR under condition of $m=2$ kg/s: (a) $z=0.6$ m, (b) $z=0.63$ m, (c) $z=0.65$ m, (d) $z=0.67$ m ..	213
Fig. 6.29 Distribution of the turbulent kinetic energy (TKE) in the longitudinal section under condition of $m=2$ kg/s ($z=0.6\sim 0.7$ m): (a) CSS-PTR, (b) USR-PTR	215
Fig. 6.30 Distribution of synergy angle in the longitudinal section under condition of $m=2$ kg/s ($z=0.6\sim 0.7$ m)	217
Fig. 6.31 Variation of the average synergy angle	218
Fig. 6.32 Variation of the dot product of the velocity vector and the temperature gradient	218
Fig. 6.33 Variation of Nu/Nu_0 with mass flow rate under different pitch intervals	219
Fig. 6.34 Variation of ff/f_0 with mass flow rate under different pitch intervals	220
Fig. 6.35 Variation of PEC with mass flow rate under different pitch intervals	221
Fig. 6.36 Variation of Nu/Nu_0 with mass flow rate under different rib heights	222
Fig. 6.37 Variation of ff/f_0 with mass flow rate under different rib heights	223
Fig. 6.38 Variation of PEC with mass flow rate under different rib heights	224
Fig. 6.39 Variation of Nu/Nu_0 with mass flow rate under different corner radiuses	226
Fig. 6.40 Variation of ff/f_0 with mass flow rate under different corner radiuses	227
Fig. 6.41 Variation of PEC with mass flow rate under different corner radiuses	228

Fig. 6.42 Variation of Nu/Nu_0 with mass flow rate under different crest radiuses	229
Fig. 6.43 Variation of ff_0 with mass flow rate under different crest radiuses	230
Fig. 6.44 Variation of PEC with mass flow rate under different crest radiuses	231
Fig. 6.45 Variation of Nu/Nu_0 with mass flow rate under different spiral angles	232
Fig. 6.46 Variation of ff_0 with mass flow rate under different spiral angles	233
Fig. 6.47 Variation of PEC with mass flow rate under different spiral angles	234

LIST OF TABLES

Chapter 2

Table 2.1 Summary of studies on heat transfer enhancement in the absorber tube of the PTC	39
-------------------------------------------------------------------------------------------------	----

Chapter 3

Table 3.1 Parameters of the SEGS LS-2 PTC module	52
--------------------------------------------------------	----

Chapter 5

Table 5.1 Cases for algorithm comparison and validation	154
---------------------------------------------------------------	-----

Table 5.2 Comparison of optical efficiencies obtained by the MCRT and the proposed algorithm	156
----------------------------------------------------------------------------------------------------	-----

Table 5.3 Comparison of the computing time for MCRT and the proposed algorithm	157
--------------------------------------------------------------------------------------	-----

Chapter 6

Table 6.1 Property parameters of various materials	176
----------------------------------------------------------	-----

Table 6.2 Thermophysical parameters of the HTF (Syltherm 800)	176
---------------------------------------------------------------------	-----

Table 6.3 Constants in the turbulence model	185
---------------------------------------------------	-----

Table 6.4 Parameters of the USR-PTR used for grid independence checking	189
-------------------------------------------------------------------------------	-----

Table 6.5 Results for grid independence checking	189
--------------------------------------------------------	-----

Table 6.6 Typical test data selected from Ref. [77] for model validation	190
Table 6.7 Comparison of results between simulation and test	191
Table 6.8 Mass flow rate and the corresponding inlet Reynolds number	206

NOMENCLATURE

$A_{a,i}$	area of the absorber inner surface	m^2
A_i	area of the i th grid	m^2
a	offset angle of the absorber	$^\circ$
b	equivalent deflecting error	mrad
b_{sl}	deflecting angle caused by slope error	mrad
b_{tr}	deflecting angle caused by tracking error	mrad
c_1, c_2, c_μ	constants in turbulence model	—
c_p	specific heat at constant pressure	J/kg·K
d	diameter	m
d_A	critical diameter for point A on the reflector	m
$d_{a,c}$	critical diameter of the absorber	m
e	auxiliary calculating angle / relative deviation	$^\circ / \%$
F_i	mass force components	m/s^2
f	friction factor	—
f_c	focal length the PTC module	m
h_{g-amb}	heat transfer coefficient between glass and ambient air	$W/m^2 \cdot K$
Δh	height of the rib	mm
I_D	direct normal solar irradiance	W/m^2
I_{eff}	effective solar irradiance incident on the aperture	W/m^2
I_i	local heat flux density on the i th grid	W/m^2

k	pulsation kinetic energy	—
L_a	the length of the absorber tube	m
L_c	the length of the used PTC module	m
$L_{end,loss}$	the length of the absorber that cannot receive reflected rays caused by end loss	m
l_a	offset distance of the absorber	m
m	mass flow rate	kg/s
$N_{a,c}$	the grid number around the absorber	—
N_n	the total number of grids divided on the absorber	—
Nu	Nusselt number	—
P	pressure	Pa
Pr	Prandtl number	—
p	Pressure / pitch interval of the rib	Pa / mm
q	heat transfer per unit time	W
q_{loss}	heat loss per unit time	W
q_{solar}	solar energy absorbed by the absorber	W
q_u	useful energy obtained by the fluid	W
R	thermal resistance	$m^2 \cdot K/W$
R_{co}	corner radius of the rib	mm
R_{cr}	crest radius of the rib	mm
Re	Reynolds number	—
r	radius of any point on the sun	m

r_A	critical radius for point A on the reflector	m
$r_{a,c}$	critical radius of the absorber	m
T	temperature	K
ΔT	circumferential temperature difference	K
u_i, u_j	velocity components	m/s
V	average fluid velocity	m/s
V_{amb}	ambient wind velocity	m/s
W_c	aperture width of the PTC module	m
x_A	abscissa of any point A on the reflector	---
x, y, z	Cartesian coordinates	---

Greek symbols

α_a	absorptance of the selective coating	---
α_s	spiral angle of the rib	°
β	angle in the optical cone corresponding to the actual absorber radius	mrad
β'	angle in the optical cone corresponding to the dotted circle radius	mrad
β_s	field synergy angle	°
γ	intercept factor	---
δ	radial angle of the solar disk ($\delta=4.65$ mrad)	mrad
δ_a	radial acceptance angle of the absorber	mrad

δ_{eff}	effective solar radial angle	mrاد
δ_{ij}	Kronecker delta	---
δ_t	thickness of the thermal boundary layer	mm
δ_{Δ}	maximum radial angle of the Buie's model ($\delta_{\Delta}=43.6$ mrاد)	mrاد
ε	turbulent dissipation rate	---
ε_{coa}	emittance of the selective coating	---
ζ	non-uniformity of the circumferential heat flux distribution	---
η	efficiency	%
η_c	collector efficiency	%
η_o	optical efficiency	%
η_t	thermal efficiency of the receiver tube	%
$\Delta\eta_o$	optical efficiency difference between the new algorithm and MCRT	%
Θ	angle span at the bottom of the absorber without receiving any reflected rays	°
θ_c	critical radial angle for any two specularly errors	mrاد
θ_{in}	incident angle	°
θ_l	radial angle of line light source	mrاد
θ_s	radial angle of the point on the sun	mrاد
θ_{sp}	the deflecting angle caused by specularly error	mrاد

l_a	absorber wall thickness	mm
l_g	glass envelope wall thickness	mm
$\kappa_1 \sim \kappa_5$	random number	---
λ	thermal conductivity	W/m·K
μ	dynamic viscosity	Pa·s
μ_t	turbulence viscosity	Pa·s
ξ	end loss factor	---
ρ	density	kg/m ³
ρ_r	reflectance of the reflector	---
σ_ε	Prandtl number for turbulent dissipation rate	---
σ_k	Prandtl number for turbulent kinetic energy	---
σ_{sl}	standard deviation of slope error based on Gaussian distribution	mrad
σ_{sp}	standard deviation of specular error based on Gaussian distribution	mrad
σ_{sun}	standard deviation of Gaussian sunshape model	
σ_t	turbulence Prandtl number	---
ζ	time average strain rate	%
τ_g	transmittance of the glass envelope	---
ϕ	auxiliary calculating angle	°
φ_a	circle angle of the absorber	°
φ_s	circumferential angle of the point on the sun	mrad

χ	Circumsolar ratio	
ψ_A	position angle of point A on the reflector	°
ψ_{rim}	rim angle	°
Ω	effective angle span receiving concentrated rays	°
ω	solid angle	sr

Subscript

<i>a</i>	absorber tube
<i>amb</i>	ambient
<i>c</i>	collector
<i>cond</i>	conduction
<i>conv</i>	convection
<i>f</i>	fluid
<i>g</i>	glass envelope
<i>i</i>	inner surface
<i>in</i>	inlet
<i>max</i>	maximum
<i>min</i>	minimum
<i>o</i>	outer surface
<i>out</i>	outlet
<i>rad</i>	radiation
<i>s</i>	solar / simulation

t test

Abbreviations

CFD	computational fluid dynamics
CSC	concentrating solar collector
CSP	concentrating solar power
CSR	circumsolar ratio
CSS-PTR	conventional straight and smooth parabolic trough receiver
EES	Engineering Equation Solver
FEM	Finite Element Method
FVM	Finite Volume Method
HFC	heliostat field concentrator
HTF	heat transfer fluid
<i>LCR</i>	local concentration ratio
LFC	linear Fresnel collector
MCM	Monte Carlo Method
MCRT	Monte Carlo Ray Tracing
NREL	National Renewable Energy Laboratory
PDC	parabolic dish collector
PEC	performance evaluation criterion
PTC	parabolic trough collector

PTR	parabolic trough receiver
RTM	Ray Tracing Method
SEGS	Solar Electric Generating System
UDF	User Defined Functions
USR-PTR	unilateral spiral ribbed parabolic trough receiver

CHAPTER 1

INTRODUCTION

1.1 Background of concentrating solar power

With the economic development and the constant advance of industrialization and urbanization, the global energy consumption has been growing rapidly [1]. Due to the relatively low cost and mature technologies, fossil fuels are the most commonly used energy resource worldwide, which account for more than 80 percent of the total energy consumption [2]. It is expected that the global total primary energy consumption will be more than 14 billion tons of oil equivalent by 2020 [3]. Moreover, environmental issues caused by combustion of fossil fuel, such as air pollution, global warming, have already become serious problems facing human beings. Overall, energy shortage and environmental degradation caused by the overuse of fossil fuels have to some extent been the ‘Achilles’ Heel’ limiting sustainable development of human society.

As the most widely distributed renewable energy, solar energy is a promising alternative energy resource to fossil fuels [5, 6], which has attracted extensive attention worldwide [7]. Concentrating solar power (CSP) is a very important technology of solar thermal utilization, which has been developed and applied in many countries [8-10]. In 2014, the global total installed capacity of CSP was 4.5 GW, among which Spain and the United States were the top two, with 2.3 GW and 1.7 GW respectively [11]. In recent

years, some other countries, such as Morocco, China, South Africa, provided strong support and funding for the development and application of CSP technologies. According to the statistical data from the CSPPLAZA [12], those three countries accounted for more than 80 percent of the new installed CSPs in 2018. Concentrating solar collectors (CSC), which concentrate the incident sunrays onto a relatively small receiver to produce high temperature media, are the most important component of CSP system. There are mainly four typical types of concentrating solar collectors (CSC), which are parabolic trough collector (PTC), heliostat field collector (HFC), linear Fresnel collector (LFC) and parabolic dish collector (PDC), as presented in Fig. 1.1 [8].

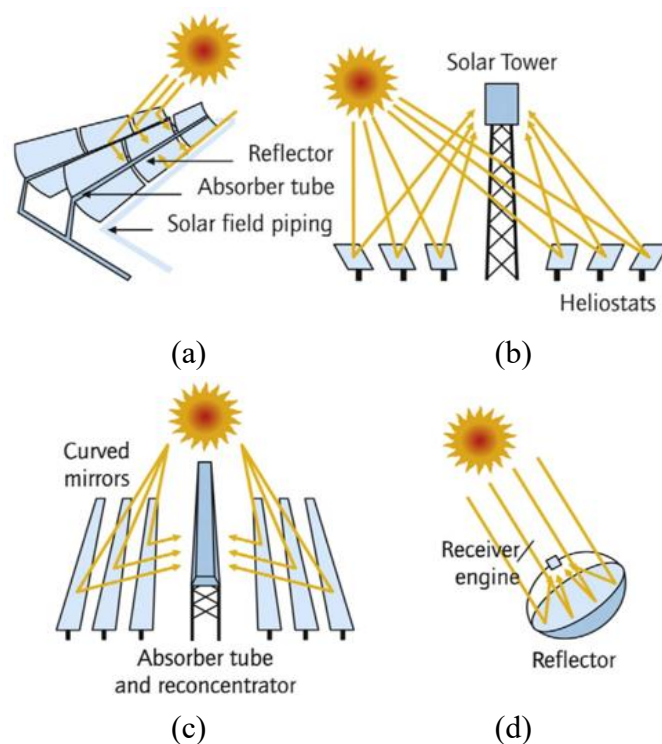
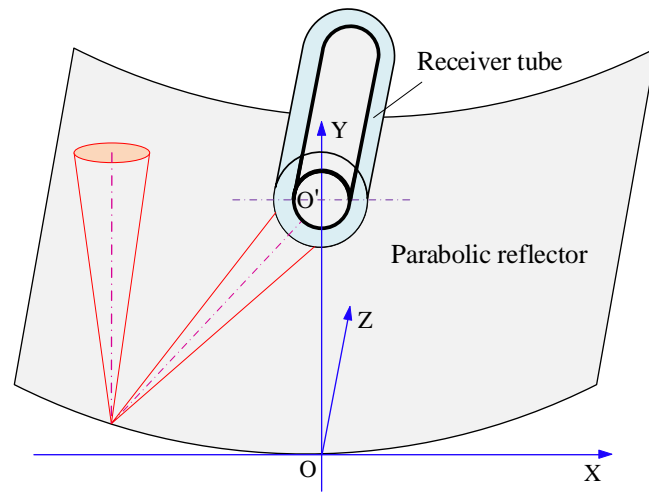


Fig. 1.1 Four typical types of concentrating solar collectors (CSC) [8]: (a) parabolic trough collector (PTC), (b) heliostat field collector (HFC), (c) linear Fresnel collector (LFC), (d) parabolic dish collector (PDC)

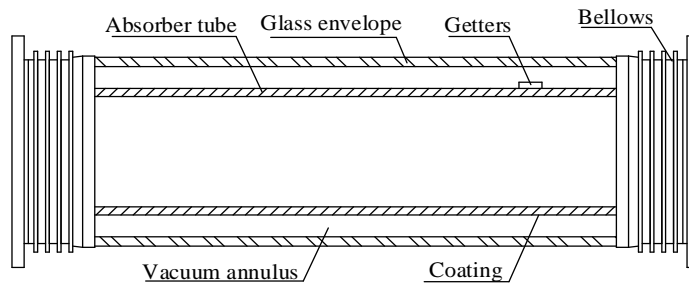
Currently, the parabolic trough collector (PTC) technology is the most cost-effective and mature technology in CSP area, which occupies almost 80 percent of the global CSP installations [10, 13, 14]. Apart from power generation, PTCs have also been applied in many other fields, such as industrial process heat production, desalination, domestic water heating, refrigeration and air-conditioning [15-20], showing promising development prospects.

1.2 Introduction to parabolic trough solar collector

The parabolic trough solar collector (PTC) is a typical kind of linear solar concentrator which is mainly composed of a parabolic reflector and a receiver tube, as shown in Fig. 1.2(a). As Fig. 1.2(b) shows, the receiver tube consists of a metal absorber tube with selective absorbing coating on its outer surface and a glass envelope. The annulus between the metal absorber tube and glass envelope is kept vacuum to reduce heat loss and protect the coating from oxidation. Metal bellows are used as the metal-glass joints to compensate the expansion difference between the metal and glass. Some other parts, such as getters and evacuation nozzle are also used to maintain the vacuum state in the annulus.



(a)



(b)

Fig. 1.2 Schematic of a PTC module: (a) PTC module, (b) receiver tube

The rays-concentrating process of the PTC is shown in Fig. 1.3. The incident solar rays are reflected and concentrated by the parabolic reflector onto the receiver tube that is installed at the focal line of the parabolic reflector. The solar selective absorbing coating on the outer surface of the absorber tube absorbs and converts the reflected rays to thermal energy which is then transferred to the heat transfer fluid (HTF) flowing inside the absorber tube.

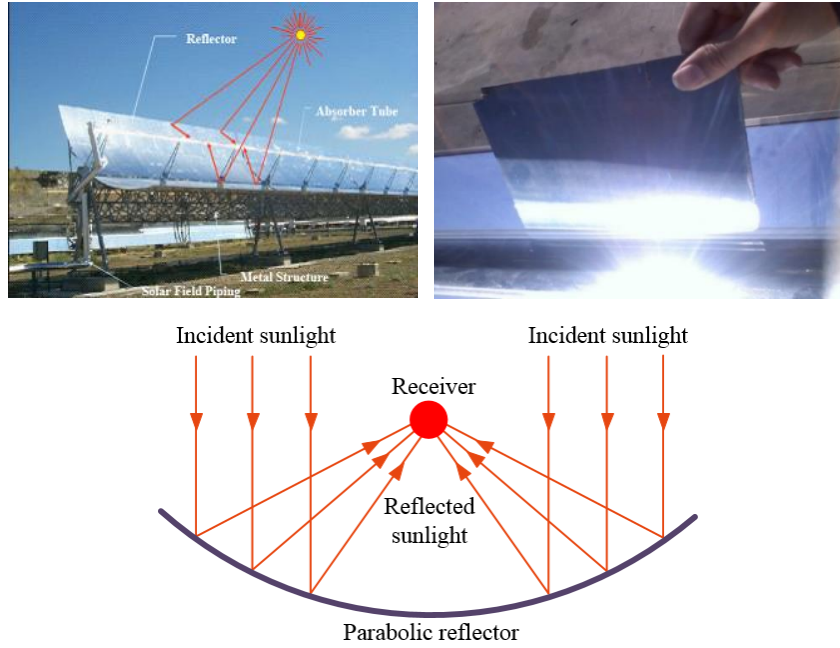


Fig. 1.3 Rays-concentrating of the PTC

In order to ensure that the reflected sunrays reach the absorber at all time, a tracking system is installed for adjusting the reflector to keep the aperture plane perpendicular to the incoming sunrays, as shown in Fig. 1.4. There are two types of sun-tracking systems: double-axis tracking and single-axis tracking. Due to its better stability and lower technical complexity, the single-axis tracking is the commonly used sun-tracking mode. The south-north oriented or east-west oriented installation mode can be determined, depending on the geographical location, solar irradiance and operating time. For most regions of China, the east-west oriented installation is preferable for achieving better annual operating performance.

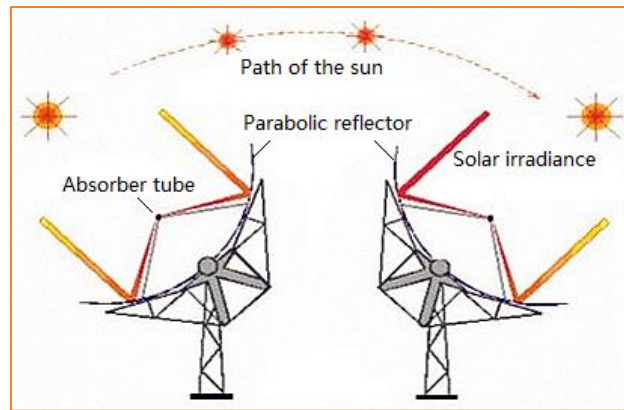


Fig. 1.4 Schematic for sun-tracking of the PTC

Due to the distinctive rays-concentrating process, the heat flux distribution on the absorber tube outer surface is extremely uneven, complicating the optical-thermal performance of the PTC. Moreover, the uneven heat flux distribution is likely to cause thermal deformation of the receiver tube, which leads to breakage of the glass envelop, consequently weakening severely the PTC's performance, as shown in Fig. 1.5 [21]. Therefore, the photo-thermal conversion process, including rays concentrating of the reflector and heat transfer in the receiver tube, is of great significance to the PTC's performance, which deserves close attention.

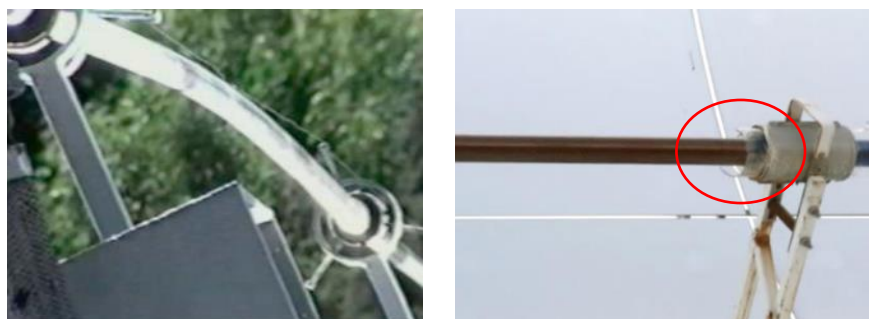


Fig. 1.5 Deformation of the receiver tube and breakage of the glass envelope caused by the uneven heat flux distribution [21]

1.3 Objectives of the thesis

The most important component of the PTC-based solar thermal system is the parabolic trough concentrator (PTC), of which the performance depends on the rays-concentrating of the reflector and the heat transfer in the receiver tube. Therefore, investigation and optimization of the optical and thermal performance of the PTC is of great significance to promoting its development and application.

A detailed literature review on previous researches of the PTC is conducted in Chapter 2. Although lots of studies were performed previously, there are still some research gaps. As for the optical performance, the non-ideal optical factors were rarely characterized individually based on their generation principles, and their coupling effects were seldom investigated. Besides, detailed theoretical analysis and parametrical derivation for the rays-concentrating of the PTC were also scarcely discussed. As for the thermal performance, previous researches seldom investigated the effects of uneven heat flux on the distribution and variation of fluid velocity and temperature. Furthermore, thermal improvement techniques based on enhancing the heat transfer between the fluid and the absorber wall with high heat flux were also rarely discussed.

Therefore, this study is committed to investigating the optical and thermal performance of the PTC and proposing effective thermal improvement method accordingly. The main objectives of the thesis are summarized as follows:

- (1) To reveal the rays-concentrating mechanism of the PTC under ideal optical conditions using MCRT coupled with theoretically quantitative analysis.
- (2) To investigate the effects of non-ideal optical factors on the PTC's optical performance based on individual characterization of each optical factor.
- (3) To develop a theoretical algorithm for the critical absorber diameter and optical efficiency under non-ideal optical conditions.
- (4) To investigate the thermal improvement performance of the novel unilateral spiral ribbed receiver tube which is proposed based on enhancing the heat transfer between the fluid and the high heat flux area of the absorber tube.

1.4 Organization of the thesis

In the first chapter, the background of global energy consumption and the concentrating solar power (CSP) technology, are introduced. As the mostly widely used concentrating solar collector (CSC), the parabolic trough collector (PTC) is further introduced, and its main structure and working principle are also described in detail. To understand and reveal clearly the photo-thermal conversion of the PTC, the main tasks of this project are to explore the optical and thermal performance of the PTC and to search for

corresponding thermal improvement method.

Chapter 2 provides a comprehensive literature review on the studies on the optical and thermal performance of the PTC. As for the optical performance, studies on optical simulation, optical improvement and effects of non-ideal optical factors are summarized. As for the thermal performance, review is conducted in terms of experimental and numerical studies, and thermal improvement techniques. Based on the literature review, the limitations of previous studies are summarized and the research gaps are identified. Finally, the methodology of this study is presented.

Chapter 3 conducts a study on the optical performance of the PTC under ideal optical conditions. The Monte Carlo Ray Tracing (MCRT) method is introduced and the optical models are established. In addition, theoretical analyses of the ideal rays-concentrating process are conducted. The geometrical parameters reflecting some important optical properties including the rays-spillage, the distribution range variation of local concentration ratio (*LCR*) and the shadowing effect of the absorber tube are deduced theoretically. Based on the MCRT and theoretical analyses, the effects of structural parameters, including aperture width, focal length and absorber diameter, on the PTC's optical performance are investigated in detail.

In Chapter 4, the optical performance of the PTC under non-ideal optical conditions are investigated comprehensively. All the non-ideal optical factors, including sunshape,

optical errors, and non-zero incident angle are theoretically defined based on their generation principles. Coordinate transformation is performed for optical modeling, and the effective sunshape model is established to realize random sampling for non-ideal incident sunlight. The optical performance under various non-ideal optical factors are explored and the coupling effects of different optical factors on the optical efficiency are further discussed.

Chapter 5 focuses on theoretical study on the optical performance of the PTC under non-ideal optical conditions. Firstly, the critical absorber diameter under any optical error conditions is theoretically derived. And then, a new simple and efficient algorithm for the optical efficiency is developed based on the idea of viewing the sun as consisting of countless line light sources. Finally, based on the derived formulas and the proposed algorithm, the effective sunshape size is discussed, and the changing properties of optical efficiency obtained by the MCRT are also expounded theoretically.

Chapter 6 investigates the thermal performance improvement of the PTC using the novel unilateral spiral ribbed receiver tube. Numerical models are established, and validated by test results and classical empirical formulas. The heat flux distributions obtained by the MCRT in Chapter 3 and 4 are added as the boundary condition on the absorber outer surface by User Defined Functions (UDF). Based on the detailed analyses of the thermal performance of the conventional receiver tube, a novel unilateral spiral ribbed receiver tube is proposed to improve its thermal performance.

Detailed comparisons are conducted between the proposed receiver tube and conventional straight-smooth receiver tube, revealing the advantage and potential of the new receiver tube in thermal improvement for the PTC. The mechanism of heat transfer enhancement of the proposed receiver is further analyzed according to the field synergy theory. Based on the performance evaluation criteria (PEC), the influences of the rib's structural parameters on the overall performance of the new receiver tube are also examined comprehensively.

Chapter 7 summarizes the main conclusions and achievements of this thesis and proposes several recommendations for future work.

CHAPTER 2

LITERATURE REVIEW AND RESEARCH METHODOLOGY

2.1 Introduction

As mentioned previously, the photo-thermal conversion of the PTC involves two processes: rays-concentrating of the reflector and heat transfer in the receiver tube. Therefore, this chapter will conduct a detailed literature review in terms of optical and thermal performance of the PTC. Based on the literature review, the research gaps will be identified and the research flow chart of this thesis will be presented.

2.2 Optical performance of the PTC

The features of the rays-concentrating of the PTC are academically defined as the optical performance, having great effects on the overall performance of a PTC system. There were lots of researches conducted previously on the optical performance of the PTC, which mainly focused on two aspects: optical analysis and optical improvement.

2.2.1 Optical analysis of the PTC

During 1970s and 1980s, researchers investigated the PTC's optical performance using

mathematical analysis based on the idea of optical cone [22-28], among which the semi-finite integral model for calculating the energy flux developed by Jeter [26-28] is the most influential. Jeter's results were usually adopted as references for optical model validation by other researchers [30, 34-36, 67, 68, 72]. In recent years, the Monte Carlo Ray Tracing (MCRT) method has been the major method to study the optical performance of CSCs due to its high adaptability and flexibility. Cheng et al. [29] proposed a general modeling method and developed a unified code with MCRT for optical analysis of the CSC. Based on the developed MCRT code, Cheng et al. [30, 31] conducted detailed parametrical study and discussed the effects of rays-spillage on the performance of the PTC, and performed comparative and sensitive analysis for different types of PTCs as well. In their later study, Cheng et al. [32] proposed an optical optimization method based on the particle swarm optimization algorithm (PSOA) and the MCRT. In order to reduce the computing time of the MCRT, a trade-off between the computational accuracy and the computing complexity was made properly. In their latest study [33], a new algorithm for the optical efficiency fitting formulas was developed based on the proposed PSOA-MCRT optimization model. The algorithm had great potential in application for optical efficiency related analyses. Zhao et al. [34] carried out an optical simulation of the PTC using MCRT to calculate the flux density distribution. In the study, the non-parallelism of the incident sunlight, the geometric concentration ratio, the rim angle, the reflectance of the reflector, the transmittance of the glass envelope and the absorptance of the coating were considered.

Since large number of rays are required for MCRT simulation, the required computing time is usually very long, which causes inconvenience for engineering application. Some researchers were committed to optimizing the MCRT to reduce the computing cost. Liang et al [35] compared three optical models which were Monte Carlo Method (MCM), initializing rays' position using Finite Volume Method (FVM) and determining optical actions using MCM, and initializing rays' position using FVM and changing optical rays' energy by multiplying the reflectance, transmittance and absorptance. It was revealed that the last model was the most time-efficient, while its flexibility and adaptability were not as good as the MCM. In their later study [36], a MCRT and FVM coupled optical simulation method was proposed, combing the advantages the two methods. The proposed method used results from MCRT to determine the suitable grid configuration of FVM and then performed optical simulation using FVM. Fan et al [37] found that running the MCRT for several more times with less number of rays could achieve the results with the same accuracy as that with large number of rays, while reduced the running time significantly. Thus, they proposed an optimized method combing the MCRT and the iteration method to reduce the computing cost.

Some other studies were also conducted relating to approaches for optical analysis. Song et al. [38] proposed a simple algorithm for calculating the heat flux distribution on the flat absorber surface of the PTC. Their algorithm was developed based on two facts that the flux density is independent of the axial direction and the rays coming from a slice on the solar disk will form a slice on the absorber as well. The proposed

algorithm was a 2D model, having less computing complexity compared with the MCRT which was a 3D model. In their later studies, Song et al. [39] applied the algorithm to circular absorber and, meanwhile, developed a corresponding software tool for facilitating the calculating process. Serrano-Aguilera et al. [40, 41] proposed an Inverse Monte Carlo Ray Tracing (IMCRT) method to define the reflector geometry of a PTC. This method could redefine the reflector shape in order to produce more homogeneously distributed heat flux on the absorber tube. The methods discussed above are usually limited in special application for some specific problems.

The optical performance of the PTC has been studied by many researchers, and some useful results and conclusions were also presented in their work. Due to the obvious advantages of high accuracy and flexibility, MCRT has been the most widely used method for investigating the optical performance of the PTC. However, the MCRT also has a drawback of time consuming, which limits its application in engineering practice. Although some simple methods were proposed by scholars to perform optical analysis, those methods usually have limitations on computing accuracy and application conditions.

2.2.2 Optical performance improvement of the PTC

The aims of improving the optical performance of the PTC are to increase the optical efficiency or improve the uniformity of the heat flux distribution on the absorber outer

surface. The most direct way to increase the optical efficiency is to improve the optical property of each component, such as the reflectance of the reflector, the transmittance of the glass envelope and the absorptance of the coatings. Numerous studies have been implemented to develop materials with excellent optical properties, and many advanced materials have been applied in various PTCs [42-44]. Nowadays, the optical properties of the materials used in commercial PTCs are all at high level. Some other measures were also taken for improving the optical performance of the PTC, mainly including modifying the reflector and receiver tube. Tsai et al. [45] adopted a free-form trough reflector to improve the uniformity of the heat flux distribution. It was stated that the proposed configuration increased the heat flux uniformity, and also enhanced the thermal performance of the PTC for a small concentration ratio (about 2). Zhu et al. [46] designed a stretched and discrete parabolic reflector which was based on the linear Fresnel ideal. Additionally, they used a secondary reflector and a movable absorber tube to increase the optical efficiency. Results showed that the proposed structure had comparative efficiency and less investment cost, compared with conventional PTCs. Ma et al. [47] proposed a compound cylindrical solar concentrator which was composed of a centrally placed receiver and lens located above. It was presented that the maximum optical efficiency was about 84%. Wang et al. [48] assembled several reflectors with different aperture widths in the longitudinal direction of the PTC to change the concentration ratio along the receiver tube. By using this newly designed structure, a more proper temperature distribution on the absorber was achieved.

Using secondary reflector was an effective to compensate the rays-spillage and enhance the uniformity of the heat flux distribution on the absorber tube, which has also been studied in the past. Canavarro et al. [49] designed the second stage concentrator using the Simultaneous Multiple Surface (SMS) method. It was demonstrated that the new PTC collected remarkable more energy than the conventional one. Wang et al. [50] used a secondary reflector and moved the absorber a short distance to the primary reflector. They stated that the heat flux was distributed more uniformly and the peak temperature of the absorber was 6 K smaller than the conventional one. In order to increase the concentration ratio and avoid rays-spillage at the same time, Rodriguez-Sanchez et al. [51] reduced the absorber diameter and added a flat reflective mirror above the absorber. It was presented that the concentration ratio increase could be up to 80%.

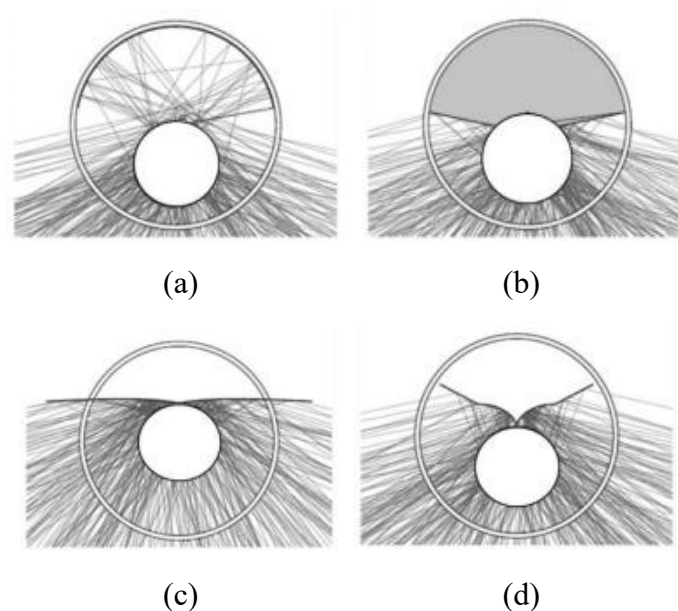


Fig. 2.1 Four types of secondary reflective mirrors [52]: (a) reflective glass surface, (b) reflective annulus insulation, (c) aplanatic secondary mirror, (d) tailored seagull

secondary mirror

Wirz et al. [52] examined and optimized four different types of secondary mirror designs, which were reflective glass surface, reflective annulus insulation, aplanatic secondary mirror and tailored seagull secondary mirror, to increase the thermal efficiency, as displayed in Fig. 2.1. The results showed that the four secondary optical designs increased the thermal efficiency between 0.8% and 1.6% compared with the benchmark one.

Some other measures were also taken to enhance the optical performance of the PTC. Wang et al. [53] investigated the impacts of the glass envelope on the heat flux distribution on the absorber outer surface, and proposed that the glass envelope with elliptic cross section could improve the flux distribution uniformity. It was proved that using the glass envelope with elliptic cross section reduced the maximum heat flux by 32.3%. Xu et al [54] performed a detailed study on the effect of the end loss on the optical efficiency, and proposed that setting a plane reflective mirror at one end of the PTC to compensate the end loss. In their later study [55], another two measures, which were extending heat absorber tube and inclining the PTC, were also discussed for compensating the end loss. Both the experimental and theoretical results proved that those proposed compensation measures were feasible and effective. Bellos et al. [56] investigated quantitatively the optical increase of setting the secondary reflector at one end of the PTC. They found that, for the PTC with focal length to length ratio of 0.236, the yearly optical enhancement was 21.7%.

Developing and using materials with high optical properties (reflectance, transmittance and absorptance) have been a widely used way to enhance the optical efficiency of the PTC. Adding secondary reflector and modifying the receiver tube can also improve the optical performance of the PTC. However, these measures increase significantly the structural complexity of PTC components, which is difficult to implement. As a matter of fact, the optical improvement techniques that change the collector structure have scarcely been applied in engineering practice. Therefore, much more attention is currently paid to thermal improvement of the receiver tube in the field of the PTC.

2.3 Effects of non-ideal optical factors on the performance of PTC

In practical engineering, there are various non-ideal optical factors, such as non-zero incident angle, uneven incident solar radiation distribution (i.e. sunshape) and optical errors including specular error, slope error, tracking error and absorber alignment error, which influence greatly the performance of the PTC. Plenty of researches have been conducted to investigate the effects of different non-ideal optical factors on the performance of the PTC.

2.3.1 Characterization of non-ideal optical factors

Proper description of each non-ideal optical factor is the prerequisite for research on the PTC's optical performance under practical conditions. Many researchers have put

great effort into characterizing various non-ideal optical factors. As for the incident angle, the most commonly used method was using an incident angle modifier ($K(\theta_{in})$) to represent the weakening effect on the optical efficiency. The formula of the incident angle modifier is given by Eq. (2.1) [57]. The incident angle modifier can be conveniently used to quickly estimate the overall optical efficiency of the PTC.

$$K(\theta_{in}) = \cos \theta_{in} - \frac{W_c}{L_c} \left(1 + \frac{W_c^2}{48f_c^2} \right) \sin \theta_{in} \quad (2.1)$$

As was known, the non-zero incident angle resulted in both cosine loss and end loss, which were both dependent on the position of the point on the reflector. Thus, the generic incident angle modifier is just an approximation method for quick calculating optical efficiency, which cannot reflect the mathematical relations between cosine loss and end loss with the coordinate of each point on the reflector.

As for description of the sunshape, a widely used sunshape model was the uniform distribution model which views the sun as a uniform radiant disk with the radial angle of 4.65 mrad [30, 31, 35, 36, 38]. However, because of the limb darkening and atmospheric attenuation scattering, the radiant intensity distribution on the solar image obtained on earth is uneven [58-60]. Thus the uniform distribution model is not applicable for actual situation. Some researchers [61-64] proposed a Gaussian distribution model to describe the sunshape. In their models, the coupling effects of the sunshape and all the optical errors were defined by convolving all the Gaussian models together. However, the Gaussian mode is just an approximation to the real sunshape. In order to describe the real sunshape, Buie et al. [60] developed a generic sunshape model

based on the vast data collected by the Lawrence Berkeley Laboratories (LBL) and the German Aerospace Center (DLR). In their sunshape model, the solar profile was divided into two parts: the solar disk with a radial angle of 4.65 mrad and the aureole (circumsolar region) which was produced by the scattering caused by solar beam interacting with atmospheric particles [58, 59]. The most important parameter in their model is the circumsolar ratio (CSR) which is defined as the ratio of the energy contained within the circumsolar region (aureole) to the total energy contained in both the solar disk and aureole. The CSR varies with geographic locations and atmospheric conditions, and can be practically measured by a pyrheliometer or active cavity radiometer (ACR). Buie's model was validated and applied in 11 sites in the US [65], having great reliability. Therefore, this study will also adopt the Buie's sunshape model to define the practical solar image, which will be discussed in detail in Chapter 4.

As for the optical errors, the most widely used treatment is the Gaussian approximation model proposed by Bendt [66]. In their model, all the optical errors were characterized by Gaussian distribution, and the total optical error was expressed by the square root of the sum of the square of each optical error. The coupling effects of the sunshape and the optical errors were defined by convolving all the Gaussian models together, which was given by Eq. (2.2).

$$B(\theta) = \frac{1}{\sqrt{2\pi}\sigma_{opt}} \int_{-\infty}^{\infty} \exp\left(-\frac{\theta'^2}{2\sigma_{opt}^2}\right) B_{sun}(\theta - \theta') d\theta' \quad (2.2)$$

where $\sigma_{opt} = \sqrt{\sigma_{specular}^2 + 4\sigma_{slope}^2 + \sigma_{tracking}^2 + \sigma_{displacement}^2}$

Thomas et al. [61] further added the standard deviation of the Gaussian sunshape model to the total standard deviation to form a new sunshape model, as shown by Eq. (2.3)

$$B_{eff}(\theta) = \frac{1}{\sqrt{2\pi}\sigma_{opt}} \exp\left(-\frac{\theta^2}{2\sigma_{opt}^2}\right) \quad (2.3)$$

where $\sigma_{opt} = \sqrt{\sigma_{sun}^2 + \sigma_{specular}^2 + 4\sigma_{slope}^2 + \sigma_{tracking}^2 + \sigma_{displacement}^2}$

Theadwell et al. [62] separated the absorber displacement error (i.e. the absorber alignment error) from the others, as given in Eq. (2.4).

$$\sigma_{opt} = \sqrt{\sigma_{sun}^2 + \sigma_{specular}^2 + 4\sigma_{slope}^2 + \sigma_{tracking}^2} \quad (2.4)$$

Guyen and Bannerot [63] clarified optical performance influencing factors including solar width, optical errors, material properties, structural imperfection and operating conditions. In their later study [64], optical errors were further divided into two types: random and non-random. The coupling effects of the random errors were expressed by Gaussian model, as given by Eq. (2.5).

$$\sigma_{opt} = \sqrt{\sigma_{sun}^2 + \sigma_{specular}^2 + 4\sigma_{slope}^2} \quad (2.5)$$

Currently, the Gaussian approximation model is the most widely used model to define the sunshape and optical errors, which, however, cannot reflect the essence of each optical error and lose the geometrical and spatial dependence of optical errors. In order to describe the optical factors more accurately, optical factors should be defined separately based on their generation principles.

2.3.2 Research on the effects of non-ideal optical factors on the performance of the PTC

In engineering practice, due to the deflecting and scattering effects of various non-ideal optical factors, the heat flux distribution on the absorber is strikingly different from that obtained in ideal case (i.e. without optical factors), which leads to different optical and thermal performance of the PTC. Thus, the effects of non-ideal optical factors on the performance of the PTC deserve extensive exploration. Grena [67] investigated the effects of several non-ideal factors, such as incident angle, tracking error and defects of the collector, on the optical performance of the PTC based on a 3D recursive ray tracing algorithm. In the study, the collector defects, including mirror imperfection and deformation and receiver delocalization, were treated by Gaussian model. In his later study [68], Grena further discussed the efficiency gain with an infrared-reflective film on the non-radiation part of the receiver. Huang et al. [69] calculated the optical efficiency using an analytical model coupled with an integration algorithm, and developed a program accordingly. In their study, the coupling effects of all the optical errors were treated by the Gaussian model. Zhu et al. [70, 71] proposed a new approach based on the First-Principle theory for calculating the intercept factor. Their method defined the slope error and the absorber alignment error individually, and convolved other optical factors based on Gaussian model. It was indicated that the method was much more time saving than the MCRT.

In recent years, some studies were conducted to investigate the effects of several typical optical errors on the performance of the PTC. Zhao et al. [72] combined MCRT and coordinate transformation to investigate the influences of absorber installation error and tracking error on the heat flux distribution. They stated that the allowable margins for installation error and tracking error under condition of geometrical concentration ratio of 20 and rim angle of 90° were $\pm 0.2\%$ (X-axis direction) and $-1.0\% \sim 0.5\%$ (Y-axis direction), and ± 4 mrad, respectively. Mwesigye et al. [73] conducted a detailed numerical simulation on the effects of slope error and specular error on the optical and thermal performance of the PTC using MCRT coupled with CFD method. The two optical errors discussed in the study were both in the range between 0 mrad and 5 mrad. The results showed that the intercept factor and the thermal efficiency were reduced by 21% and 17% respectively as the optical errors increased from 0 mrad to 5 mrad. Zhang et al. [74] investigated the effects of three types of geometrical deformations which were global deformation, local rotation deformation and local linear deformation on the optical performance of the PTC. It was found that the elliptic profile of the concentrator led to a hot spot on the absorber, which would threaten the absorber's safety. As the rotation angle was in the range of -0.3° to 0.3° and the linear deformation was less than 6% of half the aperture width, the optical efficiency was not reduced obviously. Song et al. [75] investigated numerically the individual influences of several non-ideal optical factors including incident angle, tracking error and absorber alignment error on the stability and safety of the PTC. It was revealed that peak circumferential temperature difference under the worst condition was two times that under the ideal condition.

Aichouba et al. [76] explored the variation of displacement of the receiver tube under different fluid temperatures and its influences on the solar energy intercepted by the absorber tube. It was presented in their study that when the fluid temperature ranged from 293 °C to 393 °C, the intercepted solar energy decreased from 2.8% to 38%.

There were lots of studies carried out in the past to investigate the effects of non-ideal optical factors on the PTC's performance. However, most of them were performed based on the Gaussian approximation of the all the optical factors. Although some researches have indeed examined the influences of several typical optical errors. Those work usually partially discussed the individual effects of single optical error without proper coupling with other optical factors. Since various non-ideal optical factors coexist in practice, each of them should be defined theoretically to characterize non-ideal optical condition. The coupling effects of multiple non-ideal optical factors are also worth deep exploration.

2.4 Thermal performance of the PTC

The PTC is a kind of device converting the solar energy into thermal energy, of which the thermal performance is another important aspect deserving in-depth exploration. The following sections will make a review on the studies on the thermal performance of the PTC from the aspects of experimental and simulation study respectively. The thermal improvement techniques proposed previously will also be summarized.

2.4.1 Experimental study of the thermal performance

In order to provide data reference source for engineers and maintainers at Solar Electric Generating System (SEGS) plants to optimize the operation of the plants, Sandia National Laboratories carried out a detailed test on the operating performance of the SEGS LS-2 PTC in their built rotating platform [77]. The schematic diagram of the test system is shown in Fig. 2.2 [77].

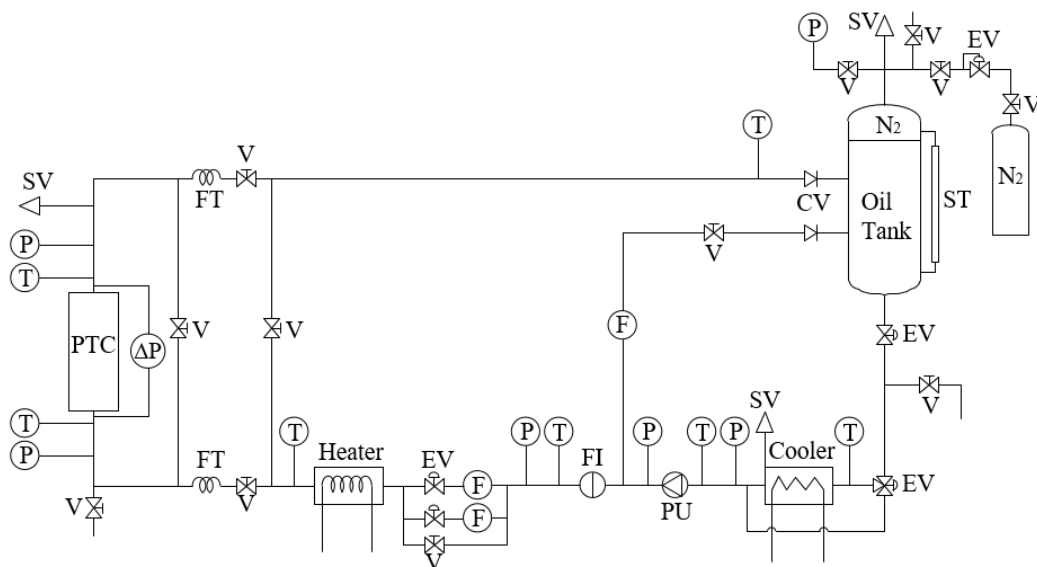


Fig. 2.2 The schematic of the test system built in Sandia National Laboratories [77]

In Sandia test, two types of selective coatings were used: black chrome and cermet, and three receiver configurations were tested: vacuum annulus, air-filled annulus and without glass envelope. The Sandia test results were very comprehensive and accurate, having been widely used as reference by many researchers for model validation [93, 94,

98, 99, 101, 108, 110]. In later years, Sandia National Laboratories tested several types of PTCs which used different receiver tubes manufactured by different companies [78, 79]. The rotating test platform built in Sandia National Laboratories is shown by Fig. 2.3 [79]. The National Renewable Energy Laboratory (NREL) implemented heat loss testing on two types of parabolic trough receivers (PTR) which were the Solel's UVAC3 PTR and the Schott 2008 PTR70 [80, 81]. The test was conducted in the temperature range from 100 °C to 500 °C with the increment of 50 °C. Based on the testing data, the correlations of the heat loss with the temperature for the two tested PTRs were also summarized.



Fig. 2.3 The rotating test platform built in Sandia National Laboratories [79]

In addition to the typical tests introduced above, some small experiments were also conducted for specific PTCs or PTRs. Gong et al. [82] tested the heat loss of their own developed PTR, Sanle-3, for high temperature application. In their study, a 1D model and a 3D end model were established to estimate the heat loss of the PTR, and further optimized based on the test data. Kumaresan et al. [83] carried out an experimental study of the operating performance of the PTC integrated with a thermal storage tank.

It was found that the peak instantaneous efficiency was 62.5%, and the overall efficiency decreased after 12:00 due to the decreasing insolation and the increasing heat loss. Chafie et al. [84] established an experimental platform, the Research and Technology Center of Energy (CRTEn) in Tunisia, for testing the PTC's performance. The test was conducted according to the ASHRAE 93-1986 standard. The results showed that the average thermal efficiency for sunny and cloudy days was 41.09% and 28.91% respectively. Zhang et al. [85] conducted a field experiment which had two processes of heating and cooling to test the thermal performance of a PTC with a double glazing U-type solar receiver. In their test, the thermal efficiency was kept in a range between 47.2% and 79.1%. Lei et al. [86] tested the overall heat loss of the newly designed PTR utilized in China's first 50 MW PTC-based power project. Three methods including steady state equilibrium method, quasi-steady-state equilibrium method and surface temperature measurement method were adopted. They stated that the proposed PTR had less heat loss than existing ones. Xu et al. [87, 88] compared the characteristics of three different test methods which were the steady-state method in the ASHRAE 93 standard, the quasi-dynamic method in the EN 12975-2 standard and their own developed dynamic method, and established an outdoor platform to test the impacts of several key parameters including solar irradiance, ambient temperature, fluid temperature and mass flow rate on the PTC's performance. Coccia et al. [89] built a test bench which consisted of the hydraulic circuit and the calculation system to determine the thermal efficiency of the PTC. Lu et al. [90] studied experimentally the thermal performance and the deformation property of the PTR. The temperature distribution of

the glass cover was tested directly. Results showed that the thermal efficiency was 57.8-65.6% in the case of solar irradiance of 183-842 W/m² and fluid temperature of 473 K. Wu et al. [91] conducted an experimental study on a PTC system which used a low melting point salt as the HTF. It was found that the heat loss of the tested PTR was larger than that of the PTR70 tested in previous literature [81], and the heat loss caused by the joints accounted for 5% of the total heat loss of the receiver tube.

Field test and experiment are effective ways to investigate directly the thermal performance of the PTC. However, it costs much generally. The typical large scale test systems in the world are all sponsored by large commercial corporations or the government. Most research groups can only build small and simplified testbeds for specific collectors or receiver tubes, and the findings are usually limitedly in both accuracy and applicability. Therefore, numerical simulation, compared with experimental study, is a more practical, flexible and adaptable method for studying the thermal performance of the PTC.

2.4.2 Numerical study of the thermal performance

Due to its advantages of low cost and high adaptability, numerical simulation is the most commonly used method to study the thermal performance of the PTC [92]. Forristall [93] compared one-dimensional and two-dimensional heat transfer models implemented by Engineering Equation Solver (EES). All the parameters relating to

optical and thermal properties were discussed, and recommendations for model improvement were also proposed. It was found that the accuracy of the two-dimensional model was higher than that of the one dimensional model as the length of the receiver was more than 100 m. Padilla et al. [94] conducted a 1D heat transfer analysis for the PTR. In their model, the absorber and the glass envelope were divided into several small segments and the energy equation was applied in each segment. Their models were verified by test results [77]. They stated that the models could be used for calculating the heat loss and efficiency of the PTC under various operating conditions. Daniel et al. [95] carried out a numerical study to compare the thermal performance of the evacuated receiver, non-evacuated receiver and vacuum shell receiver. It was found that although the vacuum shell receiver performed less than the evacuated one, it reduced the construction complexity and improved the stability of the receiver. Kalogirou [96] established detailed 1D heat transfer models considering all the heat transfer forms in the receiver tube, and solved the models using Engineering Equation Solver (EES). The simulation results were compared with the experimental results, and good agreement was obtained. Patil et al. [97] performed a numerical simulation on the heat loss of a non-evacuated receiver tube. It was revealed that there existed a critical receiver radius (or diameter) to obtain the minimum heat loss. Yilmaz et al. [98] carried out a similar simulation which combined the optical models and thermal models. Their models were solved by EES and validated by test results [77]. Behar et al. [99] proposed an analytical model which was also validated by test results [77]. It was revealed in the study that the thermal efficiency obtained by the analytical model was more accurate than that

obtained by the EES. Liang et al. [100] summarized different 1D mathematical models under different assumptions and proposed a simple algorithm to make the control equations linear and more solvable. They stated that the 1D model was accurate enough and simpler to calculate the thermal efficiency and heat loss, compared with the 3D model. Huang et al. [101] coupled the 2D thermal model with 3D optical model to predict the PTC's overall performance. In order to simplify the calculation process, the authors ignored the convection in the axial direction. Their method reduced the computing time without weakening much the accuracy. Guo et al. [102] discussed the influences of various operational conditions on both heat loss and exergy loss. They argued that optical heat loss far outweighed the heat loss of receiver. In their later study [103], a multi-parameter optimization was conducted based on genetic algorithm (GA), using thermal efficiency and exergy efficiency as objective functions respectively. Although 1D and 2D thermal models can be used to calculate the heat loss and the thermal efficiency conveniently, it cannot be used to analyze the uneven heat flux distribution on the absorber tube wall. This is because those kinds of models treat the absorber as a whole with uniform temperature.

In order to simulate the thermal performance under actual conditions of uneven heat flux distribution, combining the optical model and the 3D heat transfer model has been developed. He and Cheng et al. [104-106] proposed a method coupling MCRT and the FVM to study the heat transfer performance of the PTR. In their studies, a 3D thermal model was developed in terms of non-uniform solar flux. The heat flux distribution was

calculated by MCRT, and added to simulation program as the boundary condition. Lu et al. [107] developed a non-uniform heat transfer model to describe the uneven heat flux distribution on the absorber. They divided the absorber and the glass cover into two regions with uneven temperature distributions. It was found that, compared with the uniform model, the results achieved by the non-uniform model were more accurate, especially in sunny conditions. Cheng et al. [108] also developed a non-uniform thermal model which divided the receiver into two halves and two inactive ends. The model could be used with intelligent algorithm for optimizing the performance of the PTC. Wang et al. [109] studied numerically the performance of the PTC under non-uniform heat flux conditions using the rays trace method (RTM) coupled with Finite Element Method (FEM). In particular, the circumferential temperature difference (CTD) and the deformation of the absorber were examined. Hachicha et al. [110] used a geometrical-numerical method to determine the heat flux distribution on the absorber outer surface. Their model discretized the receiver tube into many small segments in both axial and azimuthal directions using the FVM method, and then calculated the heat flux and temperature in each segment. A simulation on the transient performance of the PTC using molten salt as the HTF was conducted by Zaversky et al. [111] who used the FVM and analyzed the effect of the number of control volumes on the calculation accuracy. Silva et al. [112] developed a new 3D dynamic non-linear model which combined optical model, thermal model and hydraulic model together. Their model, compared with experimental results, had an error of only 1.2%. Wu et al. [113, 114] combined Monte-Carlo Method (MCM) and Finite Element Method (FEM) to analyze

the heat flux distribution around the absorber tube and the heat transfer in the PTC system. The biggest deviation between numerical results and experimental results was just 5%. Okafor et al. [115] performed a numerical study on the effects of non-uniform heat flux distribution on the buoyancy-driven secondary flow, the heat transfer coefficient and the friction factor under the condition of laminar flow. It was found that the secondary flow and heat transfer coefficient were increased with increasing the non-uniformity of the heat flux. Yang et al. [116] developed a 3D volume element model for simulating the heat transfer of the PTC and stated that the first and second law efficiencies usually had opposite trend, and the heat gain was more obvious than the exergy gain in transient cases.

Numerical simulation is a very flexible and powerful method for investigating the thermal performance of the PTC. In past numerical studies, most researchers focused on developing different models, including 1D, 2D, 3D and some simplified models. Some researchers have done certain explorations on the thermal performance of the PTC using their own models. However, the effects of uneven heat flux on the distributions of the fluid temperature and velocity and their causes have not been analyzed deeply.

2.4.3 Thermal performance improvement of the PTC

There were two major aspects for improving the thermal performance of the PTC:

reducing the heat loss of the receiver tube and enhancing the heat transfer between the heat transfer fluid (HTF) and the absorber tube. As for reducing the heat loss, researchers usually modified the receiver structure. Some researchers added insulation materials in the upper part of the annulus between the absorber and the glass envelope to reduce heat loss. Al-Ansary et al. [117] explored the heat loss reduction of placing insulation in the non-vacuum receiver. It was found that the thermal performance was enhanced for medium temperature. Chandra et al. [118] conducted a numerical optimization to abridge the economy and efficiency between the insulation-added receiver and the vacuum receiver. Osorio et al. [119] filled the annulus with a transparent insulation material. It was revealed that the thermal efficiency of the new PTC was improved, compared with conventional PTC, as the fluid temperature was more than 300 °C. In order to reduce the heat radiation loss, Yang et al. [120] proposed a receiver with two selective coatings on the absorber outer surface. The coating with high absorptance was deposited on the bottom part of the absorber and the coating with low emissivity was deposited on the upper part. Results showed that the heat loss was reduced by 30%. Wang et al. [121] added a metal shield in the upper part of the annulus to reduce the heat radiation loss. There were two types of radiation shields: one with solar selective coating on the outer surface and the other without, as shown in Fig. 2.4. It was proved that the heat loss of the receiver tube was reduced by 23.4% and 24.2% respectively by using those two new configurations under the condition of absorber temperature of 600 °C. When using the shield with coating in real conditions, the heat-collection efficiency and exergetic efficiency were improved by 7.1% and 4.7%

respectively in the case of inlet fluid temperature of 580 °C [122].



Fig. 2.4 Receiver tubes with different metal radiation shields [121]: with solar selective coating (left) and without solar selective coating (right)

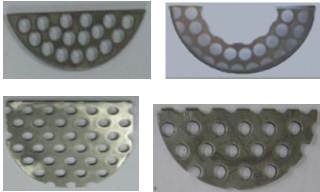
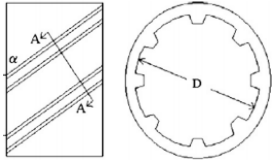

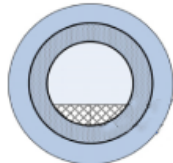
Enhancing the heat transfer between the working fluid and the absorber tube can not only increase the thermal efficiency but also reduce the circumferential temperature difference, thereby improving the safety and stability of the receiver [123, 124]. Therefore, much more research has focused on the heat transfer enhancement in the receiver in recent years. In the studies of Kumar et al. [125, 126] and Reddy et al. [127], a PTR with insertion of porous disc was investigated numerically and experimentally, and the conclusion was drawn that both the circumferential temperature difference and the heat loss were effectively reduced. Munoz et al. [128] adopted the internal helically finned tube as the absorber of the PTR, and achieved 3% increase of the collector efficiency compared with conventional smooth PTR. Cheng et al. [129] introduced longitudinal vortex generators to improve the heat transfer in the absorber tube without much pressure drop. It was found that both the absorber wall temperature and the heat loss of the new PTR was decreased obviously. Wang et al. [130] investigated the

thermal performance improvement of a PTR for direct steam generation by inserting metal foams. It was indicated that the Nusselt number was increased by 10-12 times and the peak circumferential temperature difference of the absorber was reduced by 45%. Song et al. [131] presented that the heat transfer could be obviously improved by inserting helical screw-tape in the absorber tube. Ghadirijafarbeigloo et al. [132] inserted a louvered twisted-tape into the absorber to enhance the heat transfer, and found that the new configuration increased significantly both the heat transfer coefficient and the friction factor compared with the plain twisted-tape inserted tube. Mwesigye et al. [133, 134] proposed a new type of PTR with centrally inserted perforated plate. It was found that the peak circumferential temperature gradient of the absorber was reduced by up to 67% and the thermal efficiency was increased by 1.2% ~ 8%. Chang et al. [135] conducted a parametric analysis on the thermal performance of the PTR with twisted tape inserts. They stated that the Nusselt number could be increased by 2.5 times by setting proper tape parameters. Wang et al. [136, 137] used the symmetric and asymmetric outward convex corrugated tubes as the absorbers of the PTR to increase the heat transfer performance. Compared with the conventional straight PTR, the maximum increase of the overall performance factor for those two PTRs was 1.35 and 1.48 respectively. Mwesigye et al. [138] adopted the wall-detached twisted tape inserts to enhance the heat transfer. Results showed that the thermal efficiency was increased by 10% and circumferential temperature difference was reduced by 68%. Kalidasan et al. [139] utilized the absorber with internal hinged blades for heat transfer enhancement, and the average efficiency was improved by about 8.5%. Jaramillo et al.


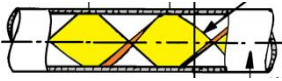
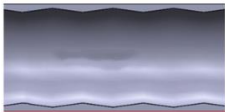
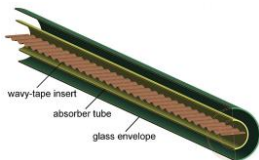
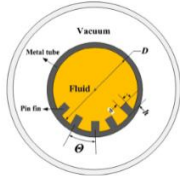
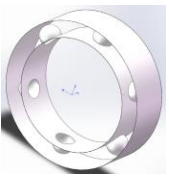
[140] explored the conditions under which the twisted tape inserted tube was suitable to be used. They stated that the twisted tape insert should be used in the case that the entropy generation was less than 1. Bellos et al. [141] explored the thermal efficiency enhancement by using converging-diverging absorber tube. The results showed that the thermal efficiency was increased by 4.55%. Zhu et al. [142, 143] inserted a wavy-tape in the absorber tube to enhance the heat transfer, and stated that the wavy-tape insert reduced both the heat loss and thermal stress greatly. Gong et al. [144] added pin fin arrays on the bottom side of the absorber tube and achieved respectively 9% and 12% improvement in the Nusselt number and the overall performance factor. Huang et al. [145] investigated numerically the heat transfer performance of the dimpled PTRs, and revealed that both the Nusselt number and the friction factor were increased obviously. Bellos et al. [146-149] investigated the thermal performance of internally finned absorber. It was presented in their study that the geometric configuration with 20 mm length and 4 mm thickness was the optimum to achieve the highest thermal enhancement index. In another work of Bellos et al. [150], the performance enhancement of a novel PTR with star shape insert was investigated. It was revealed that the drop of the heat loss was up to 14% and the pumping work was still very low (16 W) although the pressure drop was increased. Bellos et al. [151] also investigated the thermal enhancement of the PTR with cylindrical inserts, and stated that the heat loss was reduced about 5.63%. Ghasemi et al. [152] examined that thermal performance of the PTR with porous rings inserting, and found that the Nusselt number was increased remarkably. Chang et al. [153] inserted the concentric and eccentric rods as

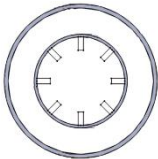
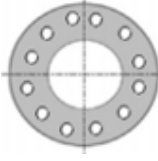
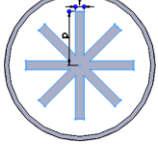

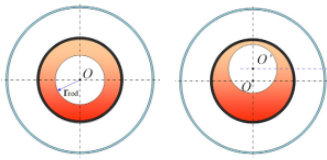
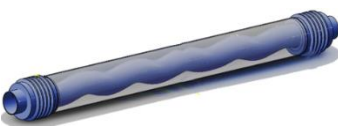
turbulators to enhance the overall thermal performance of the PTR. It was revealed that the Nusselt number was 1.1 ~ 7.42 times to the conventional PTR by changing the rod diameter and the performance evaluation criterion (PEC) was in the range of 1.68 ~ 1.84 by changing the eccentricity. Bitam et al. [154] proposed a novel PTR with an S-curved/sinusoidal absorber tube. It was indicated that the average Nusselt number was increased by 45% ~ 63%, while the friction factor was increased by less than 40.8%, which led to a maximum PEC of 1.35. Studies on heat transfer enhancement in the absorber tube were summarized chronologically in Table 2.1.

Table 2.1 Summary of studies on heat transfer enhancement in the absorber tube of the PTC

Literatures	Heat transfer enhancement techniques		Thermal performance improvement
	Description	Geometrical model	
Kumar and Reddy et al. [125-127]	Porous disc insert		<p>64.3% increase of Nu</p> <p>Pressure drop is increased by 457 Pa</p>
Munoz et al. [128]	Internal helically finned tube		<p>3% increase of the collector efficiency</p> <p>40% increase of parasitic loss</p>
Cheng et al. [129]	Longitudinal vortex generators		<p>0.11%~13.62% decrease of heat loss</p> <p>18%~67% increase of Nu</p> <p>0.25~2.1 times increase of f</p>
Wang et al. [130]	Metal foams insert		<p>10~12 times increase of Nu</p> <p>400~700 times increase of f</p> <p>PEC ranged in 1.1~1.5</p>

Song et al. [131]	Helical screw-tape insert		3~6 times decrease of heat loss 23 times increase of pressure loss
Ghadirijafarbeigloo et al. [132]	Louvered twisted-tape insert		150% increase of Nu 210% increase of f
Mwesigye et al [133, 134]	Perforated plate insert		1.2%~8% increase of thermal efficiency 8%~133.5% increase of Nu 1.4~95 times increase of f
Chang et al. [135]	Twisted tape insert		2.9 times increase of Nu 2.5 times increase of f
Wang et al. [136, 137]	Symmetric and asymmetric outward convex corrugated tubes		1.35 and 1.48 times increase of PEC 15% and 80% increase of Nu 1.03~1.3 times increase of f
Mwesigye et al [138]	Wall-detached twisted tape insert		5%~10% increase of thermal efficiency 1.05~2.69 time increase of Nu 1.6~14.5 times increase of f

Kalidasan et al. [139]	Internal hinged blades		8.5% increase of average efficiency
Jaramillo et al. [140]	Twisted tape insert		Used for entropy generation less than 1.
Bellos et al. [141]	Converging-diverging tube		4.55% increase of thermal efficiency 36%~72% increase of pressure drop
Zhu et al. [142, 143]	Wavy-tape insert		260%~310% increase of Nu 17.5%~33.1% decrease of heat loss 382%~405% increase of f
Gong et al. [144]	Pin fin arrays		9% increase of Nu 12% increase of PEC 15.8% increase of pressure drop
Huang et al. [145]	Dimpled absorber tube		1%~21% increase of Nu 1%~34% increase of f

Bellos et al. [146-149]	Internally finned absorber		0.82% increase of thermal efficiency 65.8% increase of Nu About 4 times increase of f
Ghasemi et al. [152]	Porous ring inserts		The Nu was increased obviously The PEC was less than 1
Bellos et al. [150]	Star flow insert		14% decrease of heat loss 60% increase of Nu 900% increase of pressure drop
Bellos et al. [151]	Multiple cylindrical inserts		5.63% decrease of heat loss 26.88% increase of heat transfer coefficient
Chang et al. [153]	Rod insert		1.1~7.42 times increase of Nu PEC ranged in 1.68~1.84
Bitam et al. [154]	Sinusoidal absorber tube		45%~63% increase of Nu 40.8% increase of f The maximum PEC was 1.35

Note: ' Nu ' represents Nusselt number; ' f ' represents friction factor; 'PEC' represents performance evaluation criteria.

Reducing heat loss by adding extra components, such as insulation materials and radiation shields, increases remarkably the structural complexity of the PTR and cannot improve the temperature distribution uniformity of the absorber, which, in fact, have not been applied in engineering practice. Much more research was focused on enhancing the internal heat transfer of the absorber tube, since it has outstanding advantage of increasing the thermal efficiency and reducing the circumferential temperature difference. Inserting turbulators and modifying the absorber wall shape are the two main ways used to enhance the heat transfer between the fluid and the absorber tube. Those measures increase the heat transfer at the cost of increasing significantly the pressure loss. In particular, inserts cause easily blockage and deposition, especially for some special heat transfer fluid such as molten salt and nanofluids. Considering the fact that the heat flux is mainly distributed on the part of the absorber facing to the reflector (i.e. the bottom part), enhancing the heat transfer between the bottom inner surface (i.e. high heat flux area) of the absorber tube and the fluid will improve significantly the thermal performance of the PTR, which is worth exploration.

2.5 Research gaps and methodology

A comprehensive literature review on the optical and thermal performance of the PTR was conducted in this chapter. Based on the literature review, the research gaps of previous studies are identified in this section. And then, the methodology of this study will be presented.

2.5.1 Research gaps

Although numerous studies were carried out in the field of PTC, there are still several research gaps, which are summarized as follows:

- (1) Although the optical performance of the PTC under ideal optical conditions has been studied previously, theoretically quantitative analyses of the changing optical properties were still scarce. In particular, some special optical performance, such as the distribution range of the heat flux and its variation and uniformity, the rays-spillage and the shadowing effect of the absorber tube were scarcely analyzed theoretically.
- (2) Although some research examined the influences of typical optical errors on the performance of the PTC, most of them were performed based on the Gaussian approximation of the all the optical factors or just discussed the individual effects of single optical error without proper coupling with other optical errors. Since various non-ideal optical factors coexist in practice, each of them should be defined separately in a theoretically correct way. The coupling effects of multiple non-optical factors on the PTC's performance also deserve exploration.
- (3) The critical absorber diameter under non-ideal conditions has never been derived

previously. Since the widely used MCRT method has drawbacks of time-consuming and high complexity, it is necessary to develop a simple algorithm for quick calculation of optical efficiency in engineering practice.

- (4) Thermal improvement based on the idea of enhancing the heat transfer between the fluid and the high heat flux area (i.e. bottom area) of the absorber wall was rarely explored in the past. This study will propose a novel unilateral spiral ribbed absorber tube for improving the thermal performance of the receiver tube, and conduct detailed numerical simulation to discuss its thermal improvement potential.

2.5.2 Methodology

Firstly, the optical performance of the PTC under ideal optical conditions is investigated using MCRT method. A detailed geometrical analysis of the rays-concentrating process of the PTC is conducted, taking into account the variation of the heat flux distribution range and its uniformity, the rays-spillage and the shadowing effect of the absorber tube. The effects of the structural parameters, including aperture width, focal length and absorber tube diameter, on the optical performance of the PTC are explored comprehensively, and the changing properties under different critical conditions are discussed based on geometrical analysis.

Then, an investigation on the optical performance of the PTC under non-ideal optical

conditions is implemented. All the non-ideal optical factors, such as sunshape, optical errors which include specular error, slope error, tracking error and absorber alignment error, and non-zero incident angle, are characterized separately according to their generation principles. Coordinate transformation is used for MCRT modeling under non-ideal optical conditions and the effective sunshape model is established for rays sampling. The influences of multiple non-ideal optical factors on the optical performance of the PTC are investigated comprehensively.

Succeeding to the MCRT simulations, detailed theoretical analyses on the optical performance of the PTC under non-ideal optical conditions are conducted. The formulas of the critical absorber diameter under any optical error conditions are theoretically derived. Furthermore, a new simple and efficient algorithm which was based on the idea of line light source is developed for quick calculation of the optical efficiency. Based on the derived formulas and the proposed algorithm, the effective solar radial size is discussed, and the variation of optical efficiency achieved by the MCRT in the previous chapter is further expounded theoretically.

After above optical studies of the PTC, a study on the thermal performance improvement of the receiver tube are performed. Based on the idea of enhancing the heat transfer between the high heat flux area (i.e. bottom part) of the absorber and the fluid, a novel unilateral spiral ribbed absorber tube is proposed for improving the thermal performance of the receiver tube. Numerical models are established, and

validated by test results and classical empirical formulas. The heat flux distributions obtained by the MCRT in preceding chapters are loaded as the boundary condition on the absorber outer surface by User Defined Functions (UDF). Detailed comparisons are conducted between the proposed receiver tube and conventional straight-smooth receiver tube, revealing the advantage and potential of the new receiver in thermal improvement for the PTC. The mechanism of heat transfer enhancement of the proposed receiver is further analyzed according to the field synergy theory. Finally, based on the performance evaluation criteria (PEC), the influences of the rib's structural parameters on the overall performance of the new receiver tube are explored comprehensively.

The flow chart of the methodology is presented in Fig. 2.5.

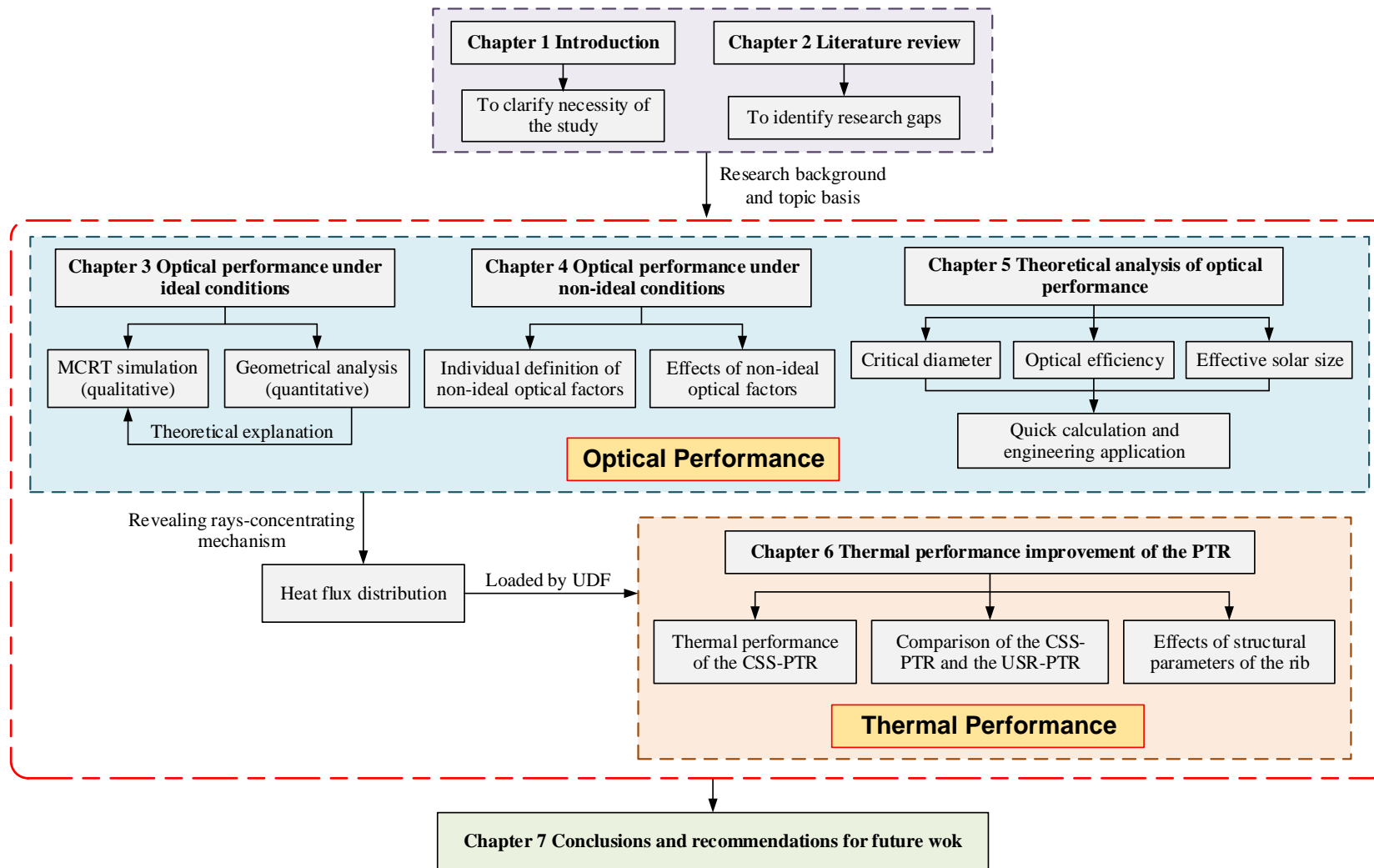


Fig. 2.5 Flow chart of methodology

CHAPTER 3

IDEAL OPTICAL PERFORMANCE OF THE PARABOLIC TROUGH SOLAR COLLECTOR AND ITS GEOMETRICAL ANALYSIS

3.1 Introduction

The parabolic trough solar collector (PTC) is a typical linear solar concentrator. The solar rays reflected by the parabolic mirror converge on the absorber outer surface, forming uneven heat flux distribution, which is the critical factor determining the overall performance of the PTC. The Monte Carlo Ray Tracing (MCRT) method, which has advantage of high accuracy and great flexibility, is a powerful tool to study the PTC's performance. However, MCRT is just a simulation method based on random experiment which cannot give quantitative analysis of the PTC's rays-concentrating process. Therefore, this chapter investigates the optical performance of the PTC under ideal optical conditions based on the MCRT coupled with geometrical analyses. Optical modes are established, and validated by comparing with other proven methods. Detailed geometrical analyses of the ideal rays-concentrating process are conducted, taking into account the rays-spillage, the variation of heat flux distribution range and the shadowing effect of the absorber tube. Based on the established optical models and geometrical analyses, the effects of three main structural parameters, including aperture width, focal length and absorber diameter, on the optical performance of the PTC are

discussed comprehensively.

3.2 MCRT modeling and validation

Monte Carlo Ray Tracing (MCRT) method combines the Monte Carlo Method (MCM), based on statistics and randomized trials, with the Ray Tracing Method (RTM), based on geometrical optics. Its basic principles are as follows: Firstly, it initializes the position, direction, energy of each ray incident on the aperture plane of the PTC by probability distribution functions. And then the optical behaviors, such as reflection, transmission, absorption, on each interface are determined by comparing a series of uniformly generated random numbers with the optical property parameters (reflectance, transmittance and absorptance), and the propagating path of each ray in the PTC system is traced accordingly. Finally, the intersection point position of each ray on the absorber surface is calculated and recorded. According to the recorded data, the heat flux distribution on the absorber outer surface is determined, and some other optical characteristics can also be further analyzed. Under ideal optical conditions, the sunshape is viewed as a disk of uniform brightness with radial angle of 4.65 mrad, and all the optical errors are zero. The following assumptions are used: 1) The reflectance, transmittance and absorptance are viewed as constants. 2) The effects of the refraction of glass envelope and the reflection of absorber tube are ignored.

3.2.1 MCRT modeling

The schematic of the rays-concentrating process of the PTC under ideal conditions is shown in Fig. 3.1. Two Cartesian coordinate systems (OXYZ and O'X'Y'Z') are established. The origin of coordinates are respectively the apex (O) of parabola and any point (O') on the reflector. X-Y plane contains the cross section of the parabolic trough with Y axis passing through the vertex and the focus, and Z axis is through the vertex and parallel to the focal line. Several important parameters, such as the aperture width (W_c), the focal length (f_c), the absorber tube outer diameter ($d_{a,o}$), the glass envelope diameter ($d_{g,o}$), the rim angle (ψ_{rim}) and the radial angle of the solar disk ($\delta=4.65$ mrad) are also displayed in the figure. In the figure, φ_a represents the circumferential angle of the absorber tube, which is used to characterize the circumferential distribution of the local concentration ratio (and heat flux distribution) in later sections (and chapters).

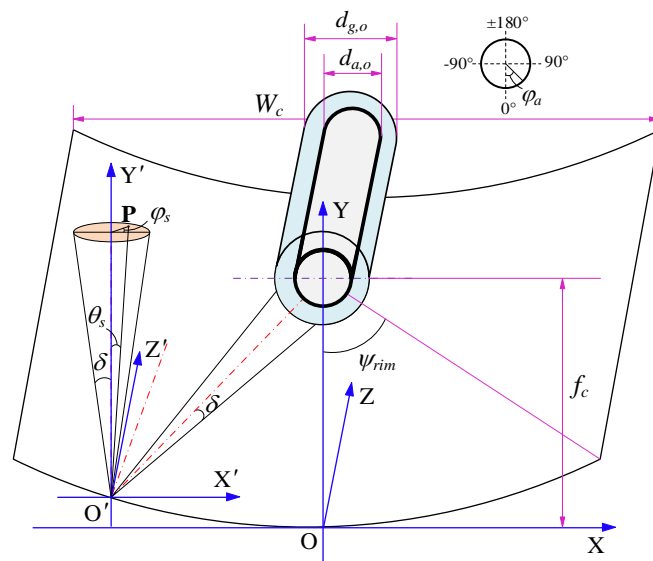


Fig. 3.1 The rays-concentrating process of the PTC under ideal conditions

The SEGS LS-2 PTC module has been tested on the AZTRAK rotating test platform at Sandia National Laboratory (SNL) [77], and detailed testing data, which were widely used as the reference for other studies, were obtained. In this thesis, the SEGS LS-2 PTC module was also adopted as the original physical model, whose specifications are given in Table 3.1 [77]. In the figure, α_a , ρ_r , τ_g are respectively the absorptance, reflectance and transmittance. l_a and l_g are respectively the thickness of the absorber tube wall and the glass envelope wall. L_c is the length of the PTC module.

Table 3.1 Parameters of the SEGS LS-2 PTC module [77]

Parameter	Value	Unit
W_c	5	m
f_c	1.84	m
L_c	7.8	m
$d_{a,o}$	0.07	m
$d_{g,o}$	0.115	m
l_a	2	mm
l_g	3	mm
α_a	0.96	---
ρ_r	0.93	---
τ_g	0.95	---

As Fig. 3.1 depicts, since solar rays incident on the aperture of the PTC are uniform, the coordinate of their hitting point on the reflector in the coordinate system OXYZ can be expressed by Eq. (3.1).

$$\begin{cases} x = W_c \cdot \kappa_1 - W_c / 2 \\ y = \frac{x^2}{4f_c} \\ z = L_c \cdot \kappa_2 \end{cases} \quad (3.1)$$

where κ_1 and κ_2 are random numbers.

The starting point (P) of any solar ray on the solar disk in coordinate system O'X'Y'Z' is given by Eq. (3.2).

$$\begin{cases} x' = PO' \sin \theta_s \cos \varphi_s \\ y' = PO' \cos \theta_s \\ z' = PO' \sin \theta_s \sin \varphi_s \end{cases} \quad (3.2)$$

where θ_s and φ_s are respectively the radial angle and circumferential angle of any point on the solar disk.

Thus, considering the symmetry of the solar disk, the unit direction vector of the incident ray in coordinate system O'X'Y'Z' can be expressed by Eq. (3.3).

$$\mathbf{s}' = (\sin \theta_s \cos \varphi_s, -\cos \theta_s, \sin \theta_s \sin \varphi_s) \quad (3.3)$$

Under ideal conditions which view the sunshape as a disk of uniform brightness, the radial angle (θ_s) and the circumferential angle (φ_s) of the starting point (P) on the solar disk are given by Eq. (3.4).

$$\begin{cases} \theta_s = \arctan(\sqrt{\kappa_3} \tan \delta) \\ \varphi_s = 2 \cdot \pi \cdot \kappa_4 \end{cases} \quad (3.4)$$

where κ_3 and κ_4 are random numbers.

Since the calculations of ray tracing have to be implemented in the same coordinate system, the vectors in coordinate system O'X'Y'Z' should be transformed to the vectors in coordinate system OXYZ. From Fig. 3.1, it can be clearly seen that the coordinate system O'X'Y'Z' can be realized simply through the translation of the coordinate system OXYZ. As is well known, the translation will not change a vector. Therefore, the unit direction vector (s) in coordinate system OXYZ is the same as that (s') in coordinate system O'X'Y'Z', which is given by Eq. (3.5).

$$s = s' \quad (3.5)$$

The equations of the parabolic reflector and the inner surface of the glass envelope in the coordinate system OXYZ are expressed by Eq. (3.6) and Eq. (3.7), respectively.

$$x^2 = 4f_c y \quad (3.6)$$

$$x^2 + (y - f_c)^2 = d_{g,i}^2 / 4 \quad (3.7)$$

where $d_{g,i}$ is the inner diameter of the glass envelope.

According to theory of space analytic geometry, the inner normal unit vectors of these two surfaces are given by Eq. (3.8) and Eq. (3.9), respectively.

$$\mathbf{n}_0 = \left(-\frac{x}{\sqrt{x^2 + 4f_c^2}}, \frac{2f_c}{\sqrt{x^2 + 4f_c^2}}, 0 \right) \quad (3.8)$$

$$\mathbf{n}_1 = \left(-\frac{2x}{d_{g,i}}, -\frac{2(y-f_c)}{d_{g,i}}, 0 \right) \quad (3.9)$$

If $\boldsymbol{\lambda}$, \mathbf{n} and \mathbf{r} represent respectively the unit incident ray vector, the normal unit vector, and the unit reflected ray vector of a surface (parabolic reflector or glass envelope), the following equation can be obtained according to Fresnel law.

$$\mathbf{r} = \boldsymbol{\lambda} - 2 \cdot (\boldsymbol{\lambda} \cdot \mathbf{n}) \cdot \mathbf{n} \quad (3.10)$$

When a ray reaches a surface, the optical behavior (reflection, absorption or transmission) happens. The judgment of the optical behavior is made by comparing a random number with the optical property parameter. For example, when a ray reaches the surface of the reflector, a random number (κ_5) will be generated, and used for comparing with the reflectance (ρ_r) of the reflector. If $\kappa_5 \leq \rho_r$, the ray is reflected, or it will be abandoned. Other optical behaviors, such as transmission and absorption, are determined by the same way. Corresponding random numbers will also be generated and used. For more clarity, the flowchart of the MCRT is shown in Fig. 3.2.

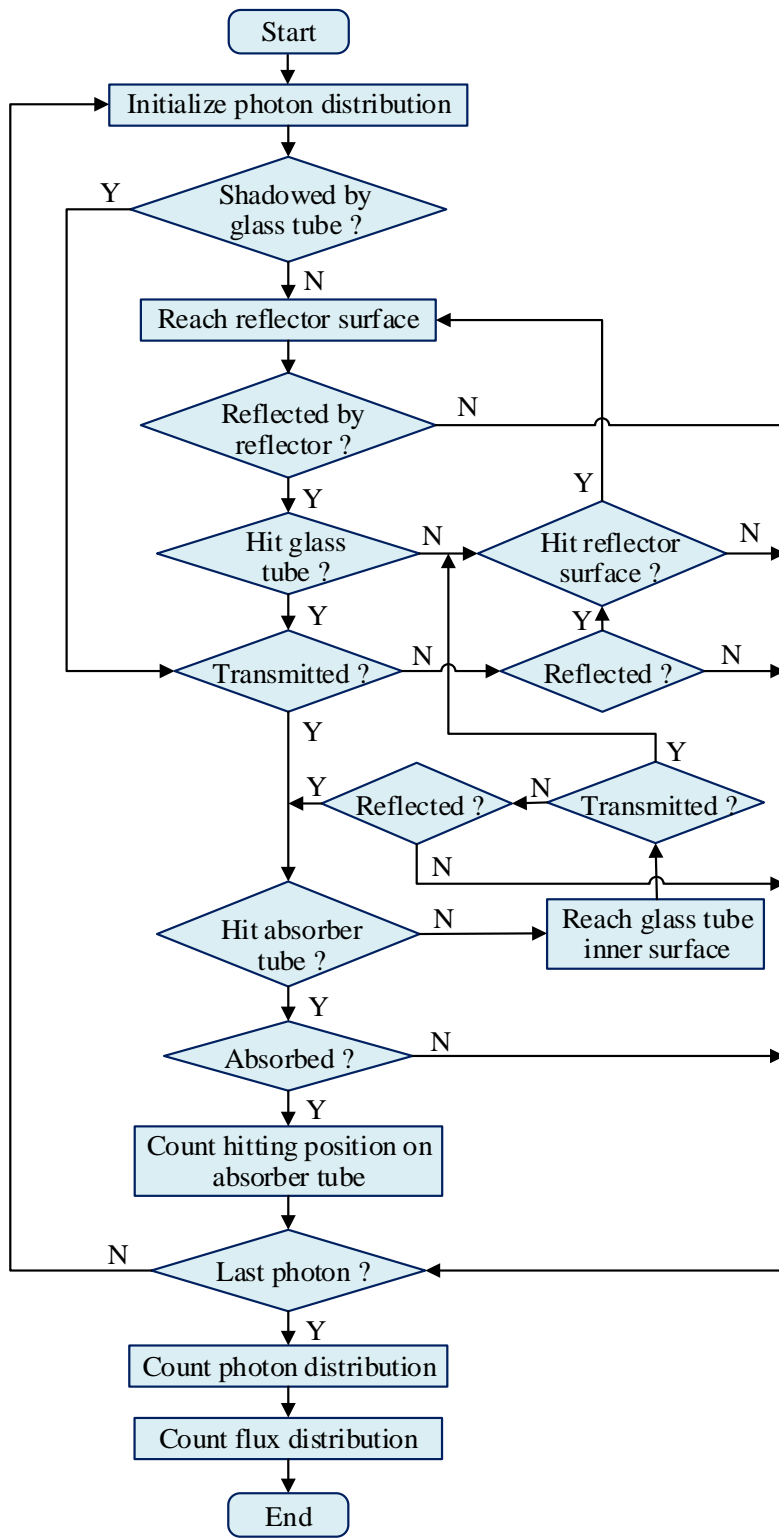


Fig. 3.2 The flowchart of the MCRT

3.2.3 Model validation

3.2.3.1 Parameter definition

The local concentration ratio (LCR_i) is defined as the ratio of local energy flux density on the absorber wall (I_i) to the normal solar radiation intensity (I_D) incident on the aperture, which reflects directly the distribution of the heat flux density, and is expressed by Eq. (3.11).

$$LCR_i = \frac{I_i}{I_D} \quad (3.11)$$

where LCR_i is the local concentration ratio of the i th grid, I_i is the local energy flux density on the i th grid, I_D is the direct normal solar radiation intensity.

In order to analyze the characteristics of the heat flux density distribution in more detail, the average local concentration ratio (LCR_{ave}) and the non-uniformity (ζ) of the circumferential heat flux distribution [30] are further presented, the expressions of which are given by Eq. (3.12) and Eq. (3.13) respectively.

$$LCR_{ave} = \frac{\sum_{i=1}^{N_{a,c}} LCR_i}{N_{a,c}} \quad (3.12)$$

$$\zeta = \frac{\sum_{i=1}^{N_{a,c}} |LCR_i - LCR_{ave}|}{N_{a,c} \cdot LCR_{ave}} \quad (3.13)$$

where LCR_{ave} is the average local concentration ratio, ζ is the non-uniformity of the circumferential heat flux distribution. $N_{a,c}$ is the grid number around the absorber

tube. According to [72], the results of 180 grid divisions around the absorber tube were the best when the number of rays was less than 10^8 . The total number of rays in this study is less than 10^8 , which will be discussed in the following section. Thus, 180 small grids ($N_{a,c}=180$) are divided around the absorber in this work. When the incident angle is zero, the heat flux distribution along the longitudinal (axial) direction of the absorber is uniform. Thus, the absorber is viewed as a whole in the longitudinal direction in this chapter.

The optical efficiency is defined as the ratio of absorbed energy to the total energy incident on the aperture, which can be calculated by Eq. (3.14).

$$\eta_o = \frac{\sum_{i=1}^{N_n} I_i \cdot A_i}{I_D \cdot W_c \cdot L_c} \quad (3.14)$$

Where η_o is the optical efficiency, N_n is the total number of grid, A_i is the area of the i th grid.

3.2.3.2 Suitable number of solar rays

In general, the more the solar rays are adopted, the more accurate the results will be. However, more solar rays require longer computing time. Thus, suitable number of solar rays should be determined considering both the results' accuracy and the computing time. Fig. 3.3 and Fig. 3.4 show respectively the variation of the maximum local concentration ratio (LCR_{max}) and the distribution of LCR in the cases of different

number of solar rays.

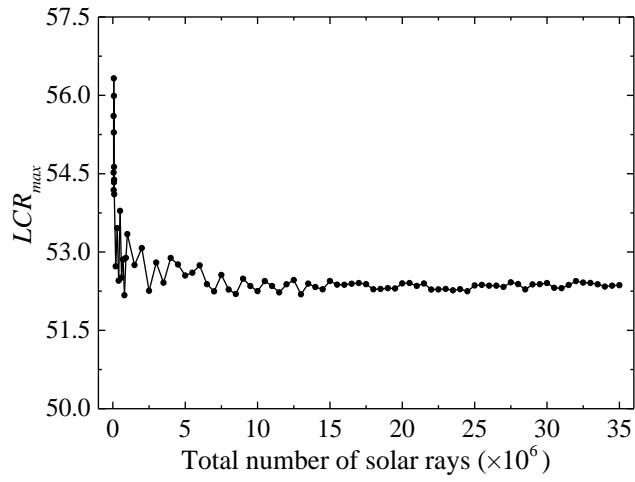


Fig. 3.3 Variation of the LCR_{max} with the total number of rays

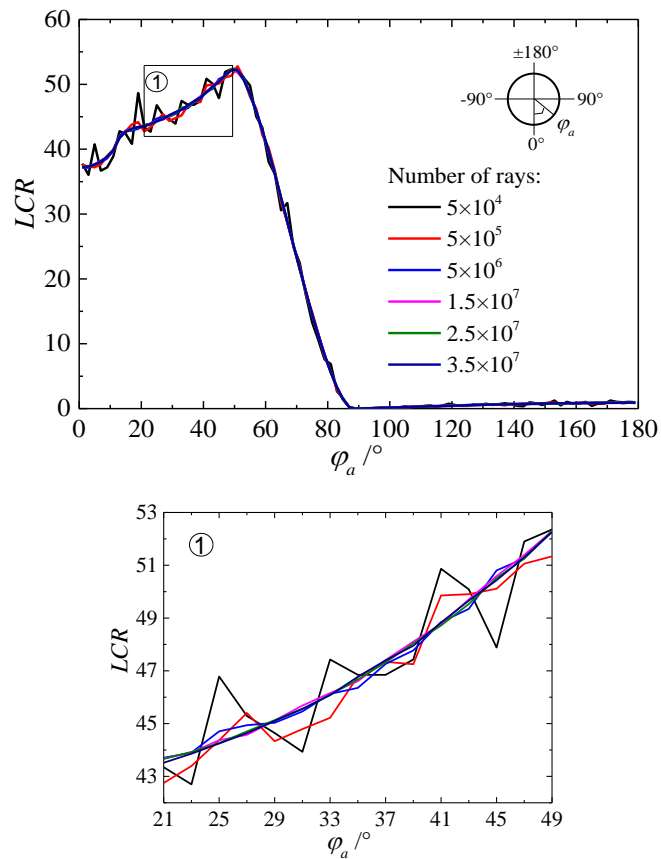


Fig. 3.4 Effect of the total number of rays on the distribution of the LCR

It is clearly seen from Fig. 3.3 that the LCR_{\max} was maintained almost constant as the total number of solar rays was more than 1.5×10^7 . Fig. 3.4 also shows that when the total number of solar rays was more than 1.5×10^7 , the LCR distribution curves became smooth. This indicates that the total number of solar rays should be more than 1.5×10^7 to obtain accurate results. On the basis of comprehensive consideration of results' accuracy and computing time, 5×10^7 rays are finally adopted for rays sampling in this study.

3.2.3.3 Model validation

The developed MCRT models were validated against the results presented in literatures [27, 39, 110] which adopted respectively analytical method, geometrical-numerical method and descending dimension integral algorithm for the same PTC module. The radial angle of the incident solar disk used was 7.5 mrad [27]. The major parameters of the PTC module used for model validation were as follows [27]: the aperture width was 4.4 m, the focal length was 1.1 m, the absorber diameter was 0.07 mm, the reflectance, transmittance and absorptance were all viewed as 1. The results of the distribution of LCR are shown in Fig. 3.5. It can be clearly seen from the figure that the results obtained by the developed MCRT models agreed very well with that presented in the literatures, which indicates that the four methods can be mutually validated.

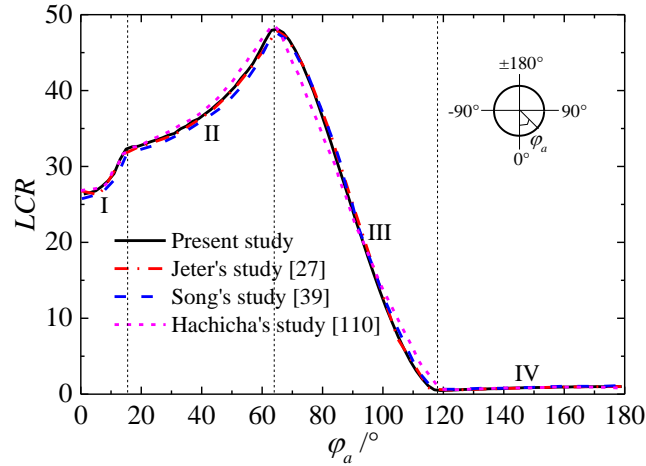


Fig. 3.5 Comparison of distribution of LCR obtained by different methods

As Fig. 3.5 displays, the distribution of LCR could be divided into four parts, which have been defined in previous study [30]. The four parts are: (I) the shelter region, (II) the heat flux increasing region, (III) the heat flux decreasing region and (IV) the direct insolation region. These four parts will change obviously with variation of the geometrical parameters of the PTC, which will be discussed in later sections.

3.3 Geometrical analysis of the ideal rays-concentrating process

Previous studies have only qualitatively discussed the basic distribution law of LCR without exploration of the underlying geometric principles and theoretical basis. This section will carry out detailed geometrical analyses of the ideal rays-concentrating process of the PTC, taking into account the rays-spillage, the variation of heat flux distribution range and the shadowing effect of the absorber tube. Several critical parameters will be deduced theoretically, which can be used to explain the changing

optical performance of the PTC under critical conditions.

In engineering practice, when the outer diameter of the absorber tube is smaller than the size of the spot formed by the reflected optical cone, some reflected sunlight will escape from around the absorber tube, resulting in great optical loss, which is defined as the rays-spillage effect. The required minimum diameter of the absorber to avoid rays-spillage is defined as the critical absorber diameter. The critical absorber diameter under ideal optical condition can be calculated by Eq. (3.15) [30].

$$d_{a,c} = 2 \cdot \left(\frac{W_c^2}{16f_c} + f_c \right) \cdot \sin \delta \quad (3.15)$$

where $d_{a,c}$ is the critical diameter under ideal condition, and δ is the maximum radial angle of the solar disk.

The rim angle (ψ_{rim}) is the angle between the reflected rays from the reflector edge and Y axis, as shown in Fig. 3.1, which is theoretically given by Eq. (3.16).

$$\psi_{rim} = \begin{cases} \arcsin\left(\frac{8(W_c/f_c)}{(W_c/f_c)^2 + 16}\right) & 0^\circ < \psi_{rim} \leq 90^\circ \\ 180 - \arcsin\left(\frac{8(W_c/f_c)}{(W_c/f_c)^2 + 16}\right) & 90^\circ < \psi_{rim} < 180^\circ \end{cases} \quad (3.16)$$

Generally, the upper side of the absorber tube absorbs directly the incident solar radiation, and the bottom side receives the concentrated solar beam from the reflector.

Obviously, both the areas that receive concentrated beam and that receive directly incident solar rays change with different geometrical configurations of the PTC. The

general rays-concentrating process of the PTC is depicted in Fig. 3.6. It can be seen from the figure that the reflected beam from point A forms a focal shape \widehat{BG} on the absorber tube.

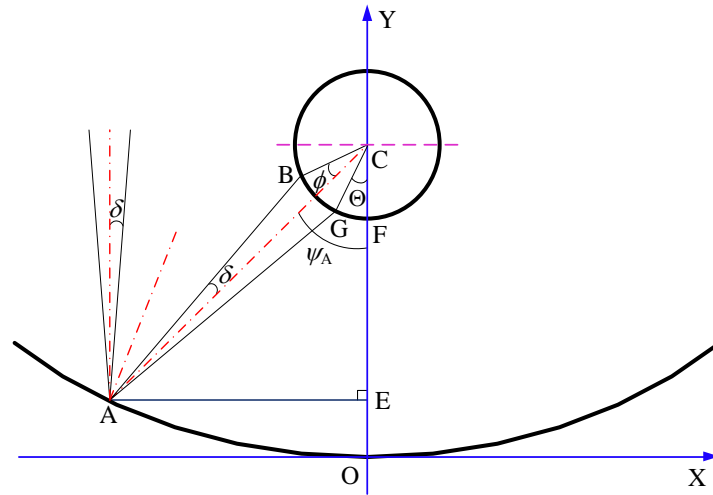


Fig. 3.6 The rays-concentrating process for any point on the reflector

According to the geometric characteristics of the parabola, the distance from any point of the parabola to the focal point is equal to the distance from the point to the directrix.

Therefore, AC can be expressed by Eq. (3.17).

$$AC = \frac{x_A^2}{4f_c} + f_c \quad (3.17)$$

where x_A is the abscissa of point A.

In $\triangle ABC$, $\angle BCA$ can be calculated by the law of sine, and given by Eq. (3.18).

$$\phi = \angle BCA = \arcsin \left[\left(\frac{x_A^2}{2f_c d_{a,o}} + \frac{2f_c}{d_{a,o}} \right) \cdot \sin \delta \right] - \delta \quad (3.18)$$

It can be easily seen that the arc \widehat{BF} will receives concentrated beam when the starting

position of the reflected rays varies in the arc $\widehat{A\hat{O}}$. Thus, the maximum angle span that receives concentrated beam can be obtained in the case that the point A is the edge of the parabola. Under this condition, the abscissa of point A is $\pm W/2$, and the position angle (ψ_A) is equal to the rim angle (ψ_{rim}). Considering the symmetry of the parabola, the angle span that receives concentrated beam can be calculated by Eq. (3.19).

$$\Omega = 2 \cdot \left(\psi_{rim} + \arcsin \left[\left(\frac{W_c^2}{8f_c d_{a,o}} + \frac{2f_c}{d_{a,o}} \right) \cdot \sin \delta \right] - \delta \right) \quad (3.19)$$

where Ω is the angle span receiving concentrated beam.

When the outer diameter of the absorber is smaller than the required diameter, partial reflected beam will escape from around the absorber. As Fig. 3.7 shows, AB' is the outermost ray of the reflected optical cone ($\angle B'AC = \delta$), and AB is the reflected ray within the reflected optical cone and it is tangent to the absorber. From the figure, we can easily find that the reflected rays in $\angle B'AB$ will escape from the absorber.

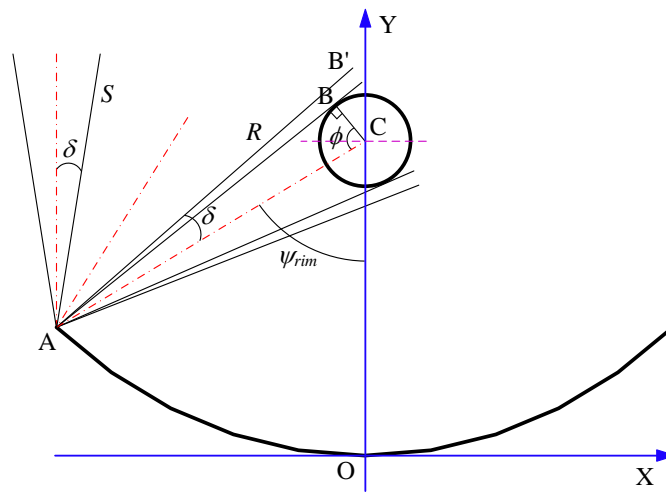


Fig. 3.7 The case leading to rays-spillage

In $\triangle ABC$, $\angle BCA$ can be given by Eq. (3.20).

$$\phi = \angle BCA = 90 - (\angle B'AC - \angle B'AB) = 90 - (\delta - \angle B'AB) \quad (3.20)$$

$\angle B'AB$ is smaller than δ ($\delta = 4.65 \text{ mrad} = 0.27^\circ$) and thus, compared with 90° , has little effect on the whole receiving angle. Eq. (3.20) can be concisely expressed as Eq. (3.21).

$$\phi = \angle BCA = 90 - \delta \quad (3.21)$$

As a result, the comprehensive expression of the angle span (Ω) receiving concentrated beam is presented as Eq. (3.22)

$$\Omega = \begin{cases} 2 \cdot \left(\psi_{rim} + \arcsin \left[\left(\frac{W_c^2}{8f_c d_{a,o}} + \frac{2f_c}{d_{a,o}} \right) \cdot \sin \delta \right] - \delta \right) & d_a \geq d_{a,c} \\ 2 \cdot (\psi_{rim} + 90 - \delta) & d_a < d_{a,c} \end{cases} \quad (3.22)$$

If the focal length of the PTC is small enough or the diameter of the absorber tube is large enough, the bottom area of the absorber cannot receive any concentrated rays due to the shadowing effect of the absorber itself. As shown in Fig. 3.6, the arc \widehat{BG} is the focal shape formed by the reflected beam from point A, and Θ is the angle span that cannot receive reflected rays from point A.

In $\triangle ACG$ and $\triangle ACE$, $\angle ACG$ and $\angle ACE$ can be calculated by Eq. (3.23) and Eq. (3.24), respectively.

$$\angle ACG = \phi \quad (3.23)$$

$$\angle ACE = \psi_A = \arcsin \frac{AE}{AC} = \arcsin \left(\frac{|x_A|}{x_A^2 / 4f_c + f_c} \right) \quad (3.24)$$

Thus, Θ can be easily calculated by Eq. (3.25).

$$\Theta = \angle ACE - \angle ACG = \psi_A - \phi \quad (3.25)$$

By Eq. (3.18), Eq. (3.21) and Eq. (3.23) ~ Eq. (3.25), we can easily get the relationship between the angle span (Θ) that cannot receive concentrated beam and the abscissa of point A (x_A). If Θ stays greater than zero whichever point the reflected beam are from, an area at the bottom of the absorber that cannot receive any concentrated beam exists. Therefore, the calculation equation (Eq. (3.22)) of the effective angle span (Ω) that receives concentrated beam should be modified as Eq. (3.26).

$$\Omega = \begin{cases} 2 \cdot \left(\psi_{rim} + \arcsin \left[\left(\frac{W_c^2}{8f_c d_{a,o}} + \frac{2f_c}{d_{a,o}} \right) \cdot \sin \delta \right] - \delta \right) - 2 \cdot \Theta & d_{a,o} \geq d_{a,c}, \Theta > 0 \\ 2 \cdot (\psi_{rim} + 90 - \delta) - 2 \cdot \Theta & d_{a,o} < d_{a,c}, \Theta > 0 \end{cases} \quad (3.26)$$

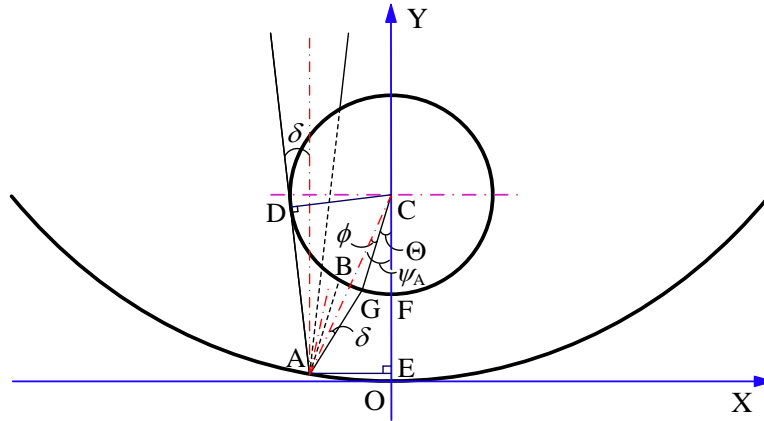


Fig. 3.8 The case that the bottom of the absorber cannot receive concentrated beam

A critical situation is shown in Fig. 3.8. The outermost ray (DA) of the incident optical cone is tangent to the absorber. The arc \widehat{AO} cannot receive any directly incident rays because of the shadowing effect of the absorber, and thus the arc \widehat{GF} cannot receive

any reflected rays. It can be easily found from Fig. 3.8 that the coordinate of point D is

$(-\frac{d_{a,o}}{2} \cos \delta, -\frac{d_{a,o}}{2} \sin \delta + f_c)$, and the direction vector of DA is $(1, -\cot \delta)$. Thus,

the equation of line DA can be given by Eq. (3.27).

$$y = -\cot \delta \cdot \left(x + \frac{d_{a,o}}{2} \cos \delta \right) - \frac{d_{a,o}}{2} \sin \delta + f_c \quad (3.27)$$

By solving the parabola equation (Eq. (3.6)) and Eq. (3.27), the abscissa of point A is obtained, and expressed by Eq. (3.28). According to this formula, the width of the apex area of the reflector that cannot receive any incident solar rays can be easily calculated. The above parameters derived theoretically will be applied to the analysis of subsequent simulation results.

$$x_A = \sqrt{4f_c^2 \cot^2 \delta - 2f_c(d_{a,o} \cos \delta \cot \delta + d_{a,o} \sin \delta - 2f_c)} - 2f_c \cot \delta \quad (3.28)$$

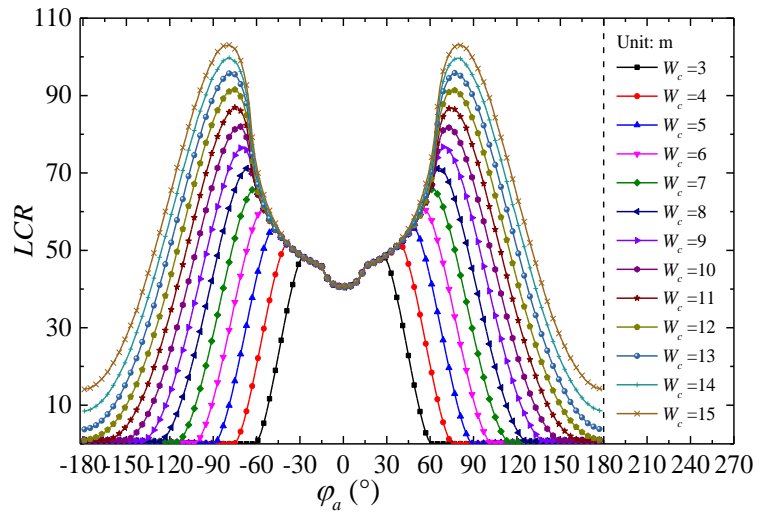
3.4 Effects of structural parameters on the optical performance

This part will investigate in detail the effects of structural parameters, including aperture width, focal length and absorber diameter, on the optical performance of the PTC based on the MCRT method coupled with theoretical analysis. The SEGS LS-2 PTC module is used as the prototype, some important parameters of which are listed in Table 3.1.

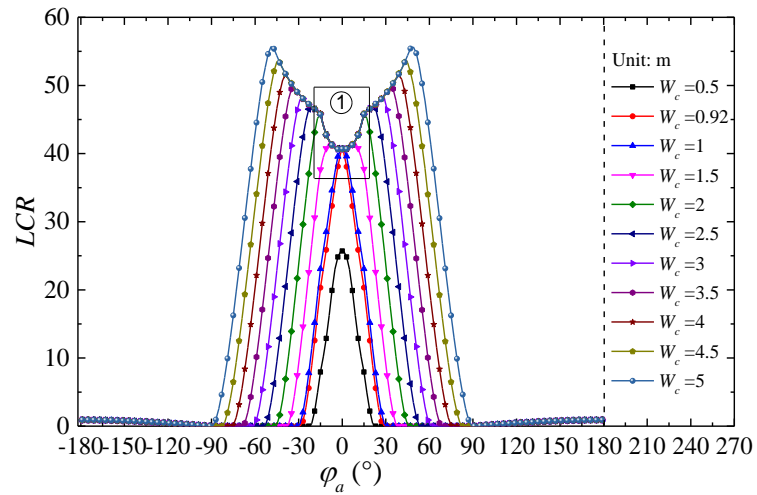
3.4.1 Effects of aperture width

Fig. 3.9 displays the effects of aperture width (W_c) on the distribution of local concentration ratio (LCR). Fig. 3.9(a) shows the results of the distribution of LCR for W_c varying from 3 to 15m. It can be seen from the figure that most distribution curves had the aforementioned four parts. The maximum of LCR increased continuously with the increase of W_c , and the value of LCR at $\phi_a = 0^\circ$ remained constantly at about 41. The angle span of the shelter region (part I) remained unchanged at about 15° . Nevertheless, both the energy flux increasing region (part II) and the energy flux decreasing region (part III) increased with increasing W_c , reducing the direct insolation region (part IV). The angle, which can be calculated by $\phi + \psi_{rim}$, corresponding to the minimum of CL in part III increased with the increase of W_c . When W_c increased to a certain degree (about 12 m), part III disappeared, which means the entire circumference of the absorber tube can receive concentrated rays.

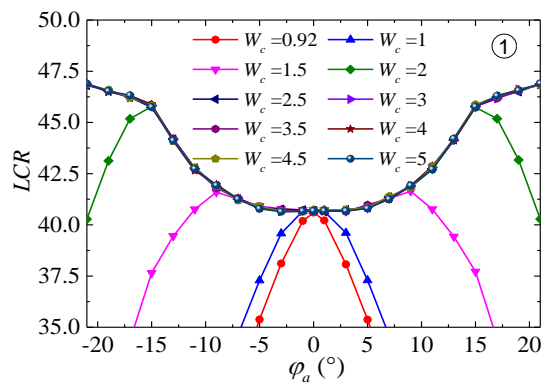
Fig. 3.10 shows the theoretical results of different calculated angles under different aperture width (W_c). From Fig. 3.10, it can be seen that the effective angle receiving concentrated beam (Ω) increased constantly with the increase of W_c , and completely coincided with $2 \times (\phi + \psi_{rim})$ when W_c was less than 12 m, and reached the maximum value of 360° afterwards. When $2 \times (\phi + \psi_{rim})$ was 180° or 360° , the corresponding W_c was 5 m and 12 m, respectively. That means when W_c is less than 5 m, the angle span from $\phi + \psi_{rim}$ to 90° (also from -90° to $-(\phi + \psi_{rim})$) cannot



(a)



(b)



(c)

Fig. 3.9 The distribution of LCR under different aperture widths: (a) $3 \text{ m} \leq W_c \leq 15 \text{ m}$,

(b) $0.5 \text{ m} \leq W_c \leq 5 \text{ m}$, (c) partially enlarged detail

receive any rays, and the entire absorber tube circumference can receive concentrated beam with W_c larger than 12 m. The same characteristics are also shown in Fig. 3.9(a). The value of φ_a corresponding to the minimum LCR was 90° (and -90°) with $W_c=5$ m and decreased with W_c less than 5 m. When W_c was larger than 12 m, the angle spans of part I, part II and part III covered the whole circumference of the absorber tube, and part III disappeared.

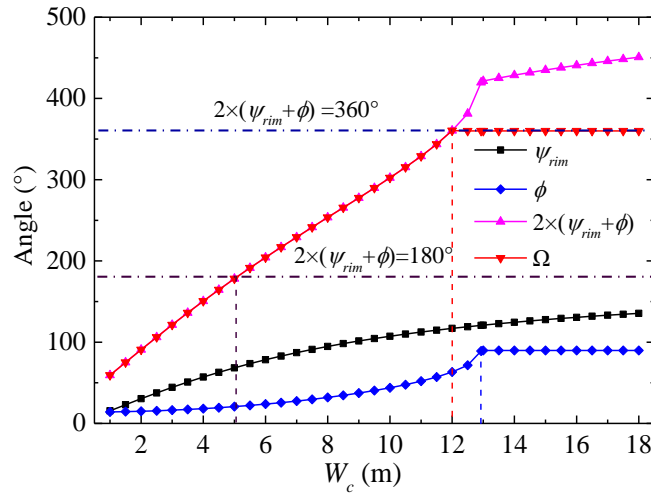


Fig. 3.10 Variation of theoretical calculated angles with aperture width

The results for some small values of W_c are further studied and depicted in Fig. 3.9(b). It can be clearly observed that part I became smaller and smaller when W_c was less than 2 m, and disappeared with W_c less than 0.92 m. When W_c was smaller than 0.92 m, the value of LCR for $\varphi_a = 0^\circ$ was smaller than 41. For more clarity, a partially enlarged view is shown in Fig. 3.9(c). It can be seen that when $W_c=0.92$ m, the only peak value of the LCR was 41 corresponding to $\varphi_a = 0^\circ$. All these phenomena can be

explained by the theoretical results given in Fig. 3.11. It can be easily found from Fig. 3.11 that Θ increased with the increase of the absolute value of the abscissa of point A (using absolute value because of the symmetry of the parabola). When $|x_A|$ was less than 0.46, Θ was negative, which indicates that the reflected optical cone from any point that is in the range between 0 and 0.46 covers the bottom of the absorber ($\varphi_a = 0^\circ$). Besides, only was $|x_A|$ less than 0.46, the reflected rays reached the bottom of absorber tube. Consequently, the value of LCR at $\varphi_a = 0^\circ$ remains constant with W_c larger than 0.92 m ($W_c = 2|x_A|$). When W_c is smaller than 0.92 m, the value of LCR for $\varphi_a = 0^\circ$ will be smaller than 41 due to smaller reflection area of the parabolic reflector.

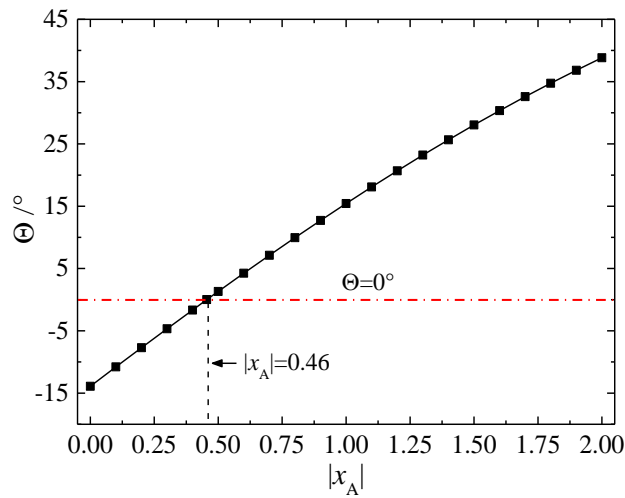


Fig. 3.11 Variation of Θ with the absolute value of point A

The variation of the optical efficiency (η_o) under different aperture widths are shown in Fig. 3.12. From the figure, it can be found that η_o almost maintained constant at a high value of 83.85% when W_c was less than 12.93 m, and then dropped significantly

as W_c was more than 12.93 m.

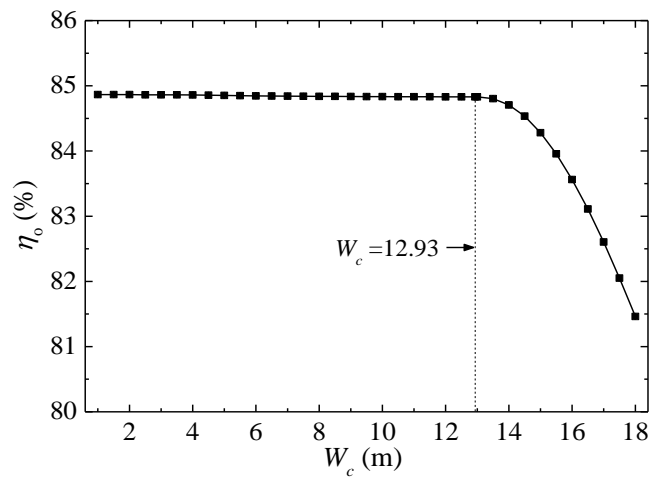


Fig. 3.12 Variation of optical efficiency with aperture width

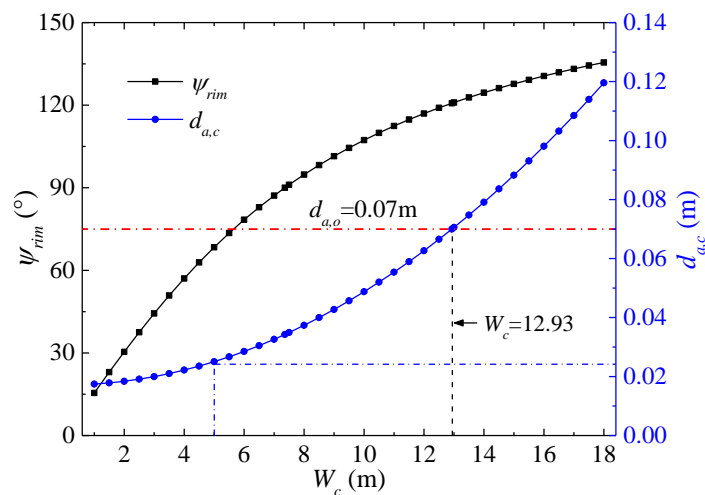


Fig. 3.13 Variation of rim angle and critical diameter with aperture width

From the theoretical results presented in Fig. 3.13, we can easily find the reason for the above variation trend of the optical efficiency. As Fig. 3.13 shows, both the rim angle (ψ_{rim}) and the critical absorber diameter ($d_{a,c}$) increased with increasing aperture width (W_c). When W_c was larger than 12.93 m, $d_{a,c}$ was larger than the actual absorber outer diameter ($d_{a,o}=0.07$ m), causing partial reflected rays escaping from around the

absorber (i.e. rays-spillage). In this case, the absorber is just an interception of the reflected optical cone, and the rays-spillage effect has the dominating effect on the optical performance.

Fig. 3.14 shows the variations of the maximum and the average local concentration ratio (LCR_{max} and LCR_{ave}) and the non-uniformity of the heat flux distribution (ζ) with aperture width (W_c). From the figure, we can see that both the LCR_{max} and LCR_{ave} increased with the increase of W_c , whereas the variation trend of ζ was inverse. The possible reason can also be found in Fig. 3.10. It can be found from Fig. 3.10 that the effective angle span receiving concentrated beam (Ω) increased with the increase of W_c , which means the concentrated rays are distributed in a larger angle span, causing smaller non-uniformity (ζ). Form the above analyses, it can be found that the simulation results are well explained by theoretical results, proving again that the established MCRT models in this work are accurate and reliable.

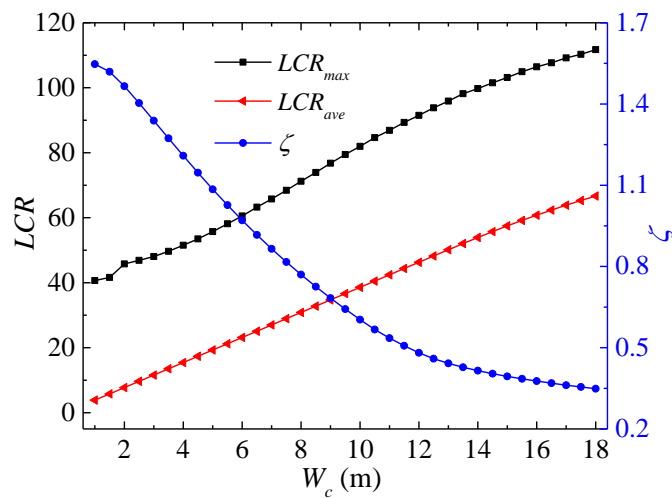
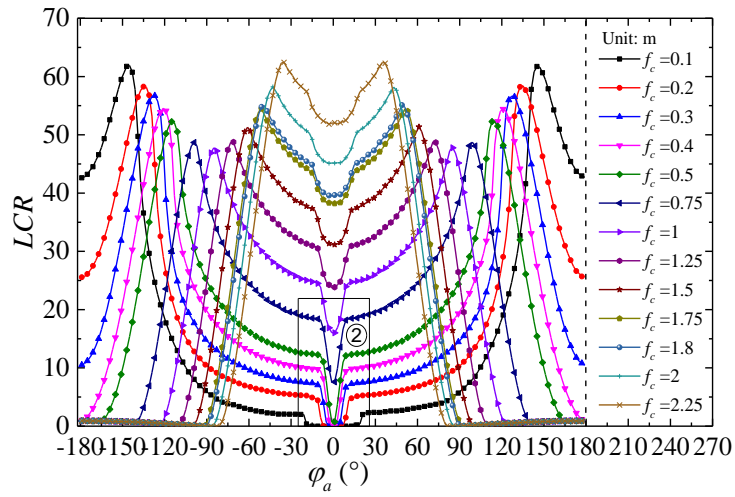


Fig. 3.14 Variation of the maximum and the average LCR and the ζ with aperture width

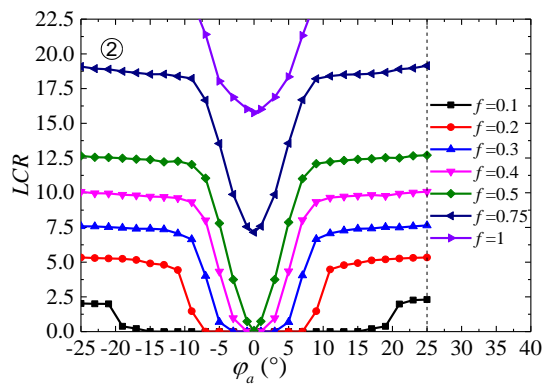
3.4.2 Effects of focal length

Fig. 3.15 shows the effects of the focal length (f_c) on the distribution of LCR . From Fig. 3.15(a), it can be seen that part II shrank obviously with increasing f_c , while part IV expanded. It can also be found that when f_c was smaller than a certain degree (about 0.5 m), an area with extremely small (almost zero) LCR appeared before part I, and part IV disappeared with further decrease of f_c (smaller than 0.4 m). For more clarity, a partially enlarged view is shown in Fig. 3.15(b). It is obviously seen that the area with near-zero LCR existed when f_c was less than 0.5 m, and the smaller f_c was, the larger this area was. The results for a series of larger values of f_c are depicted in Fig. 3.15(c). It can be seen that both part I and part II disappeared when f_c was larger than a certain value, and the only peak value of LCR was obtained at $\varphi_a = 0^\circ$. For more clarity, another partially enlarged view is shown in Fig. 3.15(d). From the figure, it is easily found that when f_c was larger than 4 m, only one peak value of LCR exists at the position of $\varphi_a = 0^\circ$.

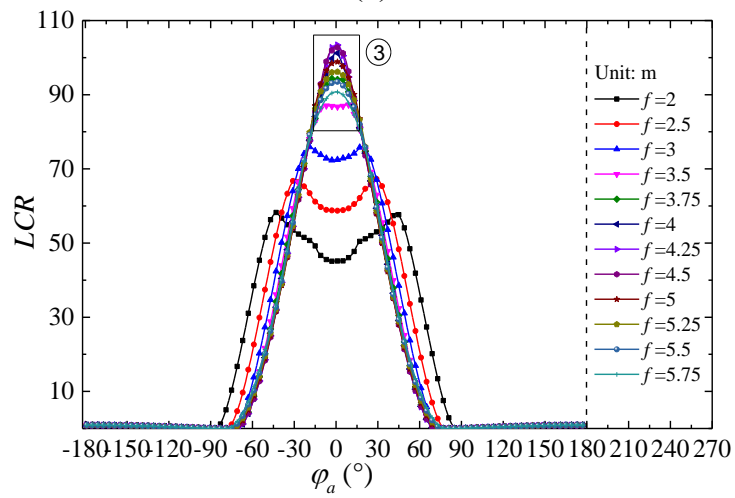
All the simulation results presented above can be accounted for by the theoretical results shown in Figs. 3.16 ~ 3.18. Given that the aperture width of the adopted PTC module is 5 m (given in Table 3.1), the maximum of the absolute value of the abscissa of point A ($|x_A|$) is 2.5 m. It can be seen from Fig. 3.16 that Θ increased with the increase of $|x_A|$. When f_c was larger than 4 m, Θ was smaller than zero for any $|x_A|$, which



(a)



(b)



(c)

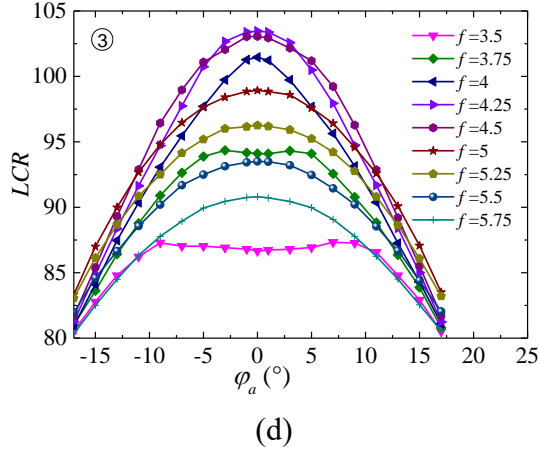


Fig. 3.15 The distribution of LCR under different focal lengths: (a) $0.1 \text{ m} \leq f_c \leq 2.25 \text{ m}$, (b) partial enlarged detail, (c) $2 \text{ m} \leq f_c \leq 5.75 \text{ m}$, (d) partially enlarged detail

indicates that the bottom of the absorber ($\varphi_a = 0^\circ$) can receive reflected rays from any point of the reflector in this case. Thus, the only peak value of LCR will always appear at the bottom of the absorber when f_c is more than 4 m, as shown in Fig. 3.15(c). From Fig. 3.16, we can also find that Θ increased with the increase of $|x_A|$, and the minimum of Θ increased with the decrease of f_c . More detailed information are displayed in Fig. 3.17, which shows the variation of Θ and the minimum absolute value of point A ($|x_{A|\min}$) with focal length. $|x_{A|\min}$ represents the minimum value of the point that can receive directly solar rays incident on the reflector (shown in Fig. 3.8). It can be observed that when f_c was less than 7.5 m, both Θ and $|x_{A|\min}$ decreased with the increase of f_c . Afterwards, Θ almost maintained constantly at -90° , and $|x_{A|\min}$ increased with further increasing f_c . When f_c was smaller than 0.5 m, Θ was larger than zero, which means that there is an area (the area with near-zero LCR in Fig. 3.15(a)) at the absorber bottom that cannot receive any reflected rays from the reflector. We can also find that when f_c was smaller than 7.5, $|x_{A|\min}$ remained

positive and decreasing, indicating that there is an area on the parabolic reflector that cannot receive any directly incident solar rays due to the shadowing effect of the absorber tube. In practice, there is a small gap at the vertex of the parabolic reflector to install the bracket. Therefore, if half of the width of the gap is smaller than $|x_A|_{\min}$, all the incident rays can be reflected by the reflector, otherwise some rays will escape from the gap, causing optical loss. Fig. 3.18 depicts the theoretical results of different calculated angles for different focal length (f_c). As the figure shows, when f_c was smaller than 0.4 m, $2 \times (\phi + \psi_{rim})$ was larger than 360° , which indicates that the entire circumference of the absorber tube can receive concentrated rays, causing disappearance of part IV, as shown in Fig. 3.15(a).

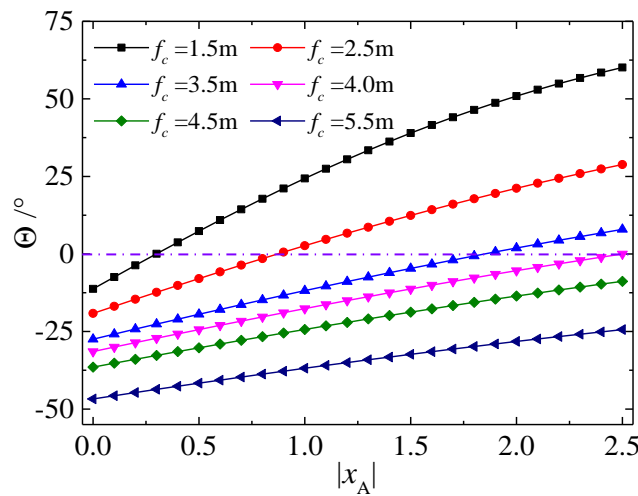


Fig. 3.16 Variation of Θ with the absolute value of point A under different focal lengths

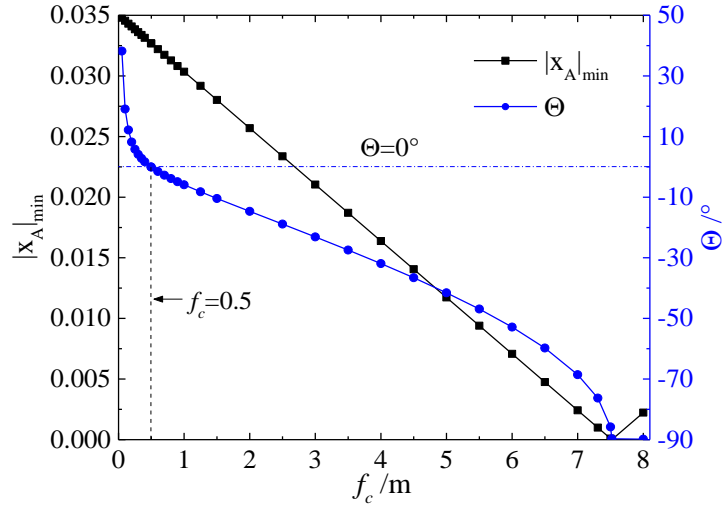


Fig. 3.17 Variation of Θ and the minimum absolute value of point A with focal length

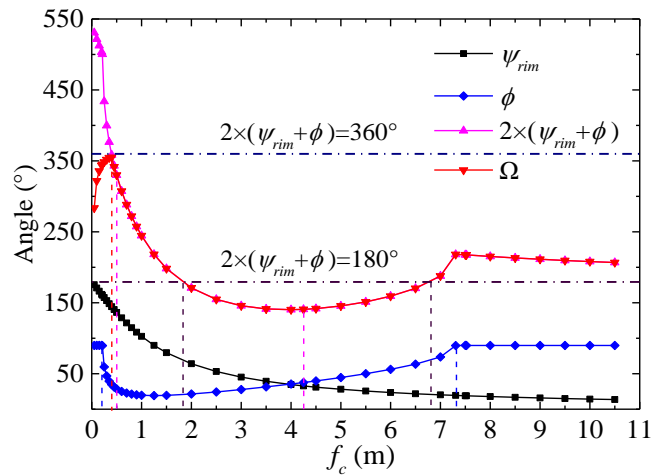


Fig. 3.18 Variation of theoretical calculated angle with focal length

Fig. 3.19 shows the variation of optical efficiency (η_o) with focal length (f_c). It can be clearly seen that η_o was kept constantly at about 84.85% when f_c varied from 0.21 m to 7.31 m. Whereas, a rapid drop appeared when f_c was smaller than 0.21 m or larger than 7.31 m. The main reason can be found in Fig. 3.20, which presents the variations of the rim angle (ψ_{rim}) and the critical diameter ($d_{a.c}$) with f_c . From the

figure, it can be seen that ψ_{rim} decreased continuously, and $d_{a,c}$ decreased sharply and then increased gradually with the increase of f_c . when f_c was smaller than 0.21 m or larger than 7.31 m, $d_{a,c}$ was larger than $d_{a,o}$ ($d_{a,o}=0.07\text{m}$), causing rays-spillage. Consequently, η_o was weakened greatly because of the rays-spillage effect.

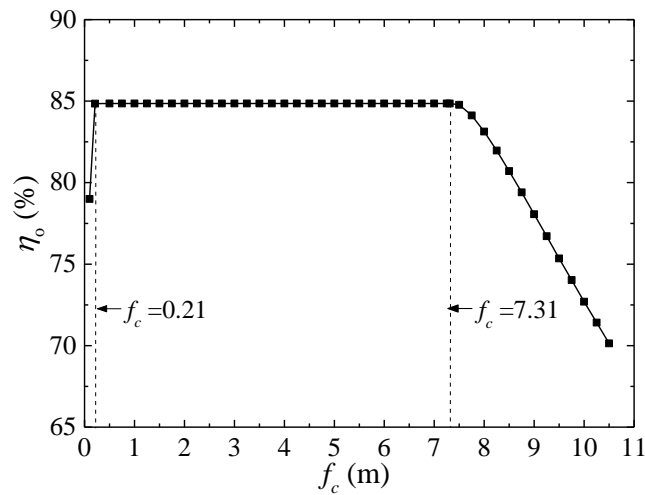


Fig. 3.19 Variation of optical efficiency with focal length

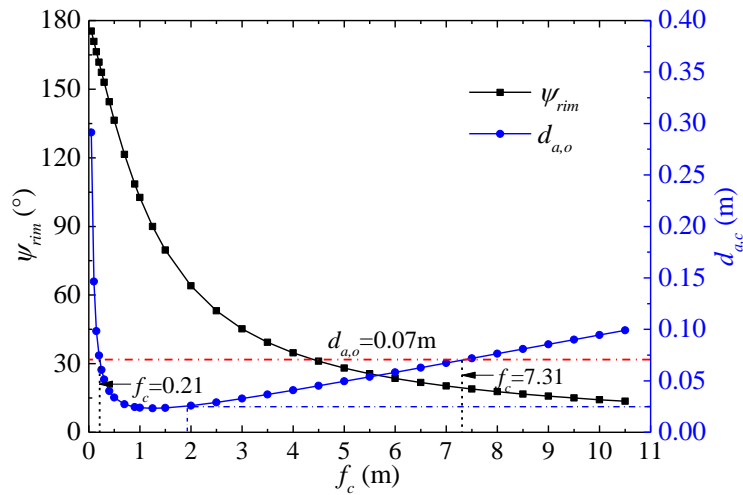


Fig. 3.20 Variation of rim angle and critical diameter with focal length

Fig. 3.21 shows the variations of the maximum and the average local concentration ratio (LCR_{max} and LCR_{ave}) and the non-uniformity of the heat flux distribution (ζ)

with focal length (f_c). When f_c was less than 0.21 m or larger than 7.31 m, LCR_{ave} decreased because of rays-spillage. LCR_{max} decreased first and then increased to the peak value at $f_c=4.25$ m, and dropped with increasing f_c . The variation trend of ζ was similar to that of LCR_{max} . The minimum of ζ appeared at $f_c=0.5$ m, whereas the minimum of LCR_{max} appeared at $f_c=1$ m. The possible reason may be found in Fig. 3.18. When f_c was about 0.5 m, the effective angle span receiving concentrated rays (Ω) was almost at the maximum value, which indicates that the concentrated rays are distributed at a large angle span, causing small non-uniformity (ζ). It can also be found in Fig. 3.21 that when $f_c=4.25$ m, ζ reached the maximum value and then decreased constantly. From Fig. 3.18, it is clearly seen that when $f_c=4.25$ m, the effective angle span receiving concentrated rays (Ω) was at the minimum value, which means the concentrated rays are distributed at the smallest angle span, leading to the largest non-uniformity (ζ).

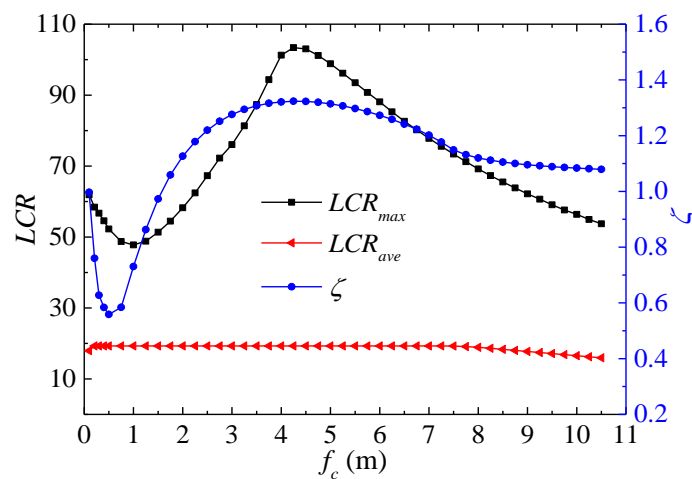
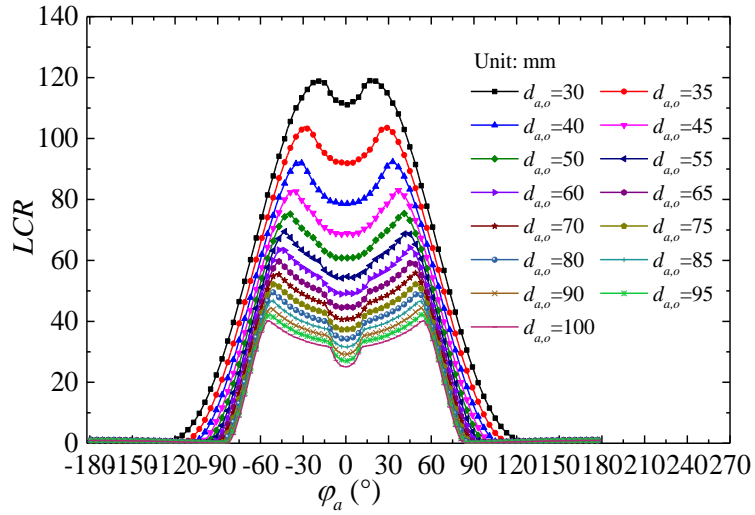


Fig. 3.21 Variation of the maximum and the average LCR and the ζ with focal length

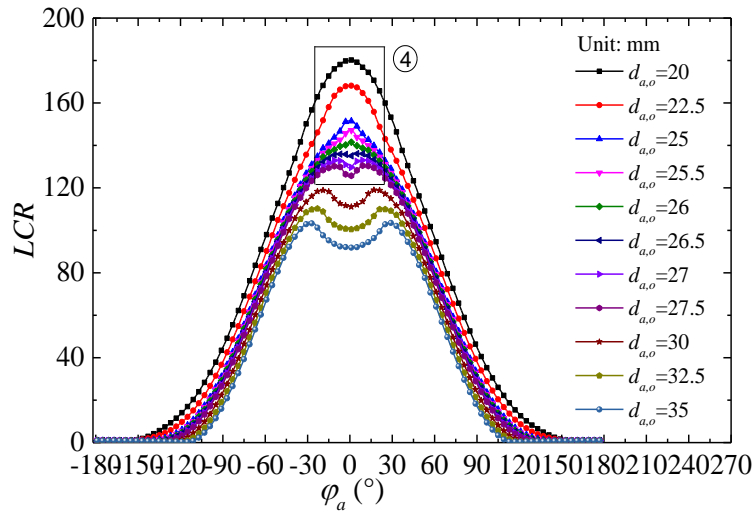
3.4.3 Effects of absorber outer diameter

Fig. 3.22 shows the effects of the absorber outer diameter ($d_{a,o}$) on the distribution of LCR . From Fig. 3.22(a), It can be found that the angular range of both part II and part IV increased with the increase of $d_{a,o}$, while part III decreased. When $d_{a,o}$ was small to a certain value (about 50 mm), part I disappeared. The results for a series of smaller values of $d_{a,o}$ are depicted in Fig. 3.22(b). It can be seen that both part I and part II disappeared when $d_{a,o}$ was smaller than a certain value (about 26 mm), and the only peak value of LCR was obtained at $\varphi_a = 0^\circ$. For greater clarity, a partially enlarged view is shown in Fig. 3.22(c). From the figure, we can easily find that when $d_{a,o}$ was smaller than 26 mm, only one peak value of LCR existed at the position of $\varphi_a = 0^\circ$.

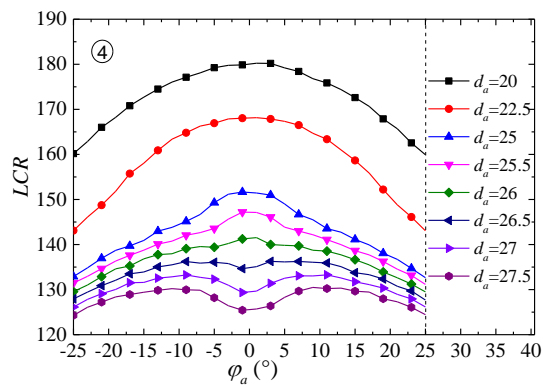
The possible reason can be found from theoretical results shown in Fig. 3.23. It can be clearly observed that when $d_{a,o}$ was smaller than 26 mm, the maximum of Θ was smaller than zero for any $|x_A|$, which indicates that the bottom of the absorber ($\varphi_a = 0^\circ$) can receive all the reflected rays from any point of the reflector. Therefore, the only peak value of LCR will always appear at the bottom of the absorber ($\varphi_a = 0^\circ$) in this case. The figure also shows that when $d_{a,o}$ was larger than 26 mm, Θ was greater than zero for $|x_A|$ larger than a certain value. Assuming that the value of $|x_A|$ corresponding to $\chi = 0^\circ$ is expressed by $|x_A|_{\chi=0}$. It is clearly seen that $|x_A|_{\chi=0}$ decreased with the increase of $d_{a,o}$. This demonstrates that the larger the absorber



(a)



(b)



(c)

Fig. 3.22 The distribution of LCR under different absorber outer diameters: (a) $30 \text{ mm} \leq d_{a,o} \leq 100 \text{ mm}$, (b) $20 \text{ mm} \leq d_{a,o} \leq 35 \text{ mm}$, (c) partially enlarged detail

diameter ($d_{a,o}$) is, the less the bottom ($\varphi_a = 0^\circ$) of the absorber receive reflected rays, leading to smaller LCR at $\varphi_a = 0^\circ$. Obviously, Fig. 3.22 shows that the LCR at $\varphi_a = 0^\circ$ decreased continuously with the increase of $d_{a,o}$, which is in conformity with the above theoretical analysis results.

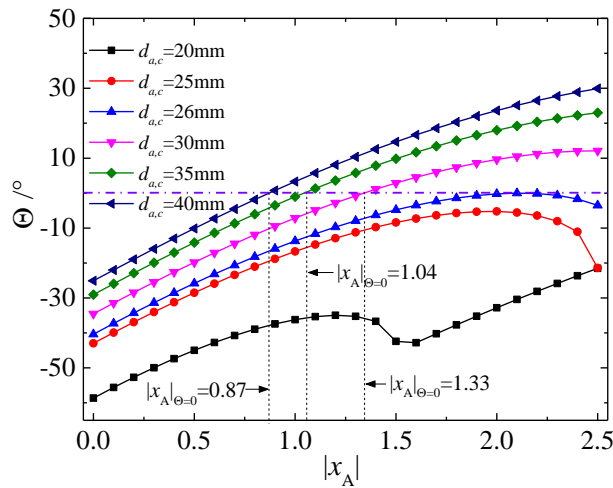


Fig. 3.23 Variation of Θ with the absolute value of point A

Fig. 3.24 shows the variation of optical efficiency (η_o) with absorber outer diameter ($d_{a,o}$). It can be clearly seen that η_o increased gradually when $d_{a,o}$ was more than 25 mm. This is because larger the absorber diameters have larger absorbing area, thus receiving more solar rays. However, η_o decreased sharply as $d_{a,o}$ was less than 25 mm. This can also be explained by the rays-spillage effect. As Fig. 3.13 and Fig. 3.20 show (the blue dash dot line), the critical diameter ($d_{a,c}$) for the adopted PTC module ($W_c = 5$ m and $f_c = 1.84$ m) was 25 mm. Thus, when $d_{a,c}$ is less than 25 mm, rays-spillage is the dominating factor weakening the optical efficiency.

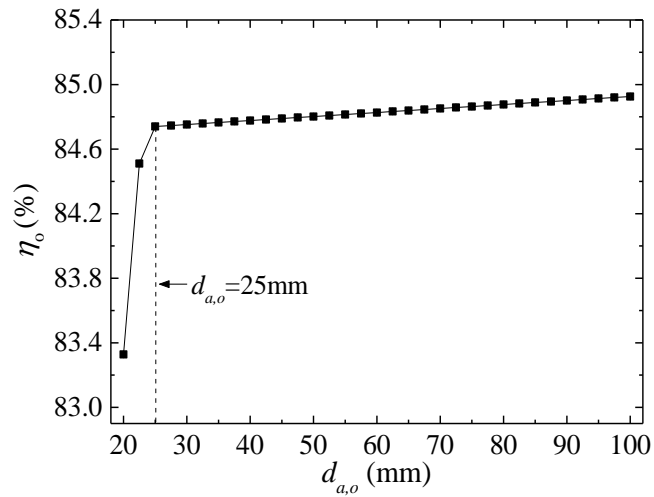


Fig. 3.24 Variation of optical efficiency with absorber outer diameter

Fig. 3.25 shows the variations of the maximum and the average local concentration ratio (LCR_{max} and LCR_{ave}) and the non-uniformity of the heat flux distribution (ζ) with absorber outer diameter ($d_{a,o}$). From the figure, it can be seen that both the LCR_{max} and LCR_{ave} decreased with the increase of $d_{a,o}$, whereas the variation trend of ζ was inverse.

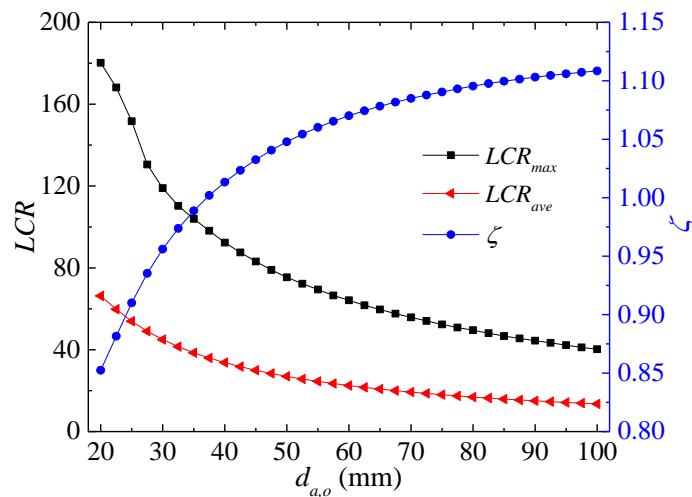


Fig. 3.25 Variation of the maximum and the average LCR and the ζ with absorber outer diameter

The possible reason can be found in Fig. 3.26. From the figure, it can be observed that the effective angle span receiving concentrated rays (Ω) decreased with the increase of $d_{a,o}$, which demonstrates that the concentrated rays are distributed at a smaller angle span, consequently causing larger non-uniformity (ζ).

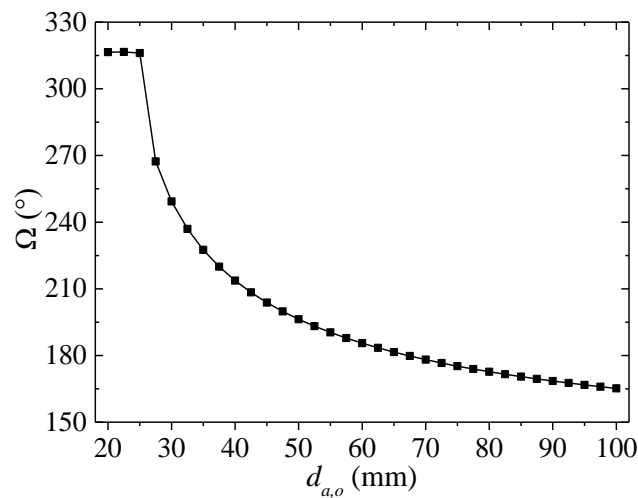


Fig. 3.26 Variation of the effective angle span receiving concentrated beam with absorber outer diameter

3.5 Summary

In this chapter, the optical performance of the PTC under ideal optical conditions was explored in detail based on the MCRT method. The optical models were established and validated by comparing the results with that obtained by other proven methods presented in literatures. Detailed geometrical analyses of the ideal rays-concentrating process of the PTC were also conducted, taking into account the rays-spillage, the

variation of heat flux distribution range and the shadowing effect of the absorber tube. Based on the established optical models and geometrical analyses, the effects of structural parameters, including aperture width, focal length and absorber diameter, on the optical performance of the PTC were investigated comprehensively. The major conclusions are summarized as follows:

- (1) The optical performance of the PTC is closely dependent on the geometrical configuration. There is a critical absorber diameter, smaller than which the absorber can only receive partially reflected rays, resulting in rays-spillage and hence causing huge optical loss. Both the aperture width and the focal length should be kept in a certain range ($W_c \leq 12.93$ m and 0.21 m $\leq f_c \leq 7.31$ m) to avoid rays-spillage. The distribution range of high local concentration ratio (*LCR*) on the absorber outer surface increases with increasing aperture width, while decreases with increasing focal length. The peak *LCR* increases constantly with increasing aperture width, while drops firstly and then increases with increasing focal length. As the aperture width is smaller or the focal length is larger than a certain value ($W_c \leq 0.92$ m or $f_c \geq 4$ m), the only peak *LCR* occurs at the bottom of the absorber (i.e. $\varphi_a = 0^\circ$), Larger absorber diameter reduces both the peak *LCR* and the high *LCR* distribution range, and improves the optical efficiency. As the focal length is small or the absorber diameter is large enough, the apex area of parabolic reflector and the bottom area of the absorber cannot receive any solar rays due to the shadowing effect of the absorber itself.

(2) Some important parameters, including the critical absorber diameter, the rim angle, the effective angle span receiving concentrated rays, the angle span at the bottom of the absorber that cannot receive concentrated rays and the width at the apex area of the reflector that cannot receive incident solar rays, are derived theoretically. The variation of these parameters with different geometrical configurations are also discussed. The simulation results obtained by the MCRT, especially some special properties such as the rays-spillage effect, the shadowing effect of the absorber, the variation of the angle span of each heat flux distribution region and its non-uniformity, can be well predicted and explained by theoretical results for any geometrical configurations.

CHAPTER 4

OPTICAL PERFORMANCE OF PARABOLIC TROUGH SOLAR COLLECTOR UNDER NON-IDEAL OPTICAL CONDITIONS

4.1 Introduction

In engineering practice, there are various optical factors, such as uneven sunshape, optical errors including specular error, tracking error, slope error and absorber alignment error, and non-zero incident angle, which have remarkable influences on the rays-concentrating of the PTC. In previous studies, efforts were mainly focused on individual effects of several typical optical errors or simple description of the combined effects of optical errors using a unified Gaussian model. Therefore, this chapter is committed to investigating the optical performance of the PTC under non-ideal optical conditions based on the theoretically individual characterization of each optical factor. All the optical factors are characterized separately according to their generation principles. The effective sunshape model is established for sampling of incident rays by convolving the incident sunshape model with the specular error model. The effects of various optical factors on the PTC's optical performance are examined comprehensively.

4.2 Description of non-ideal optical factors

In the past, the widely used way to describe the combined effects of optical factors were the Gaussian model. The Gaussian model adopted a total optical error expressed by the square root of the sum of the square of each optical factor to represent the combined effect of all the optical factors, which is just an approximation model. The Gaussian model, in fact, cannot reflect the essence of each optical error and lose the geometrical and spatial dependence of some optical errors, such as slope error and absorber alignment error. Thus, it is theoretically necessary and more reasonable to characterize each optical factor separately according to their generation principles.

4.2.1 Sunshape

Due to the limb darkening and atmospheric attenuation scattering, the radial size of the solar image obtained on earth is widened and the radiation intensity in the solar image is redistributed, which is defined as sunshape, as shown in Fig. 4.1.

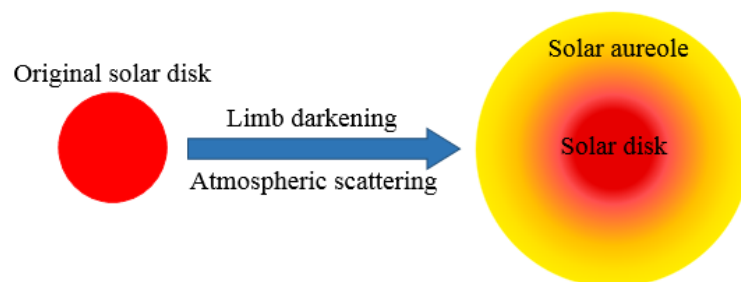


Fig. 4.1 Schematic of the sunshape

In order to describe the practical sunshape, Buie et al. [60] developed a generic sunshape model based on the vast data collected by the Lawrence Berkeley Laboratories (LBL) and the German Aerospace Center (DLR). In their sunshape model, the solar profile was divided into two parts: the solar disk with a radial angle of 4.65 mrad and the aureole (circumsolar region) which was produced by the small angle forward scattering caused by the solar beam interacting with atmospheric particles. Buie's model was validated and applied in 11 sites in the US [62], having great accuracy. In Buie's model, the brightness at any point is normalized against the central intensity and given by Eq. (4.1)

$$\phi(\theta_s) = \begin{cases} \frac{\cos(0.326\theta_s)}{\cos(0.308\theta_s)} & \theta_s \leq 4.65 \text{ mrad} \\ e^{\kappa\theta_s^\gamma} & \theta_s > 4.65 \text{ mrad} \end{cases} \quad (4.1)$$

Where θ_s is the radial angle of any point on the solar image, parameters κ and γ are given by Eq. (4.2) and Eq. (4.3) respectively.

$$\kappa = 0.9 \log(13.5\chi) \chi^{-0.3} \quad (4.2)$$

$$\gamma = 2.2 \log(0.52\chi) \chi^{0.43} - 0.1 \quad (4.3)$$

where χ is the circumsolar ratio (usually expressed by CSR), which is defined as the ratio of the energy contained within the circumsolar region (aureole) to the total energy contained in both the solar disk and aureole, and given by Eq. (4.4).

$$\chi = \frac{2\pi \int_{\delta}^{\delta_\Delta} \phi(\theta_s) \sin(\theta_s) d\theta_s}{2\pi \int_0^{\delta_\Delta} \phi(\theta_s) \sin(\theta_s) d\theta_s} \quad (4.4)$$

where δ and δ_Δ are the radial angular size of the solar disk ($\delta=4.65$ mrad) and the upper limit of the circumsolar region respectively.

From Eq. (4.1) ~ Eq. (4.4), it can be seen that the circumsolar ratio (CSR) is the most important parameter determining the sunshape, which is associated with geographic locations and atmospheric conditions. The CSR can be practically measured by a pyrheliometer or an active cavity radiometer (ACR) [58]. Different pyrheliometers or ACRs have different acceptance angles (usually ranging between 5° and 7°). In Buie's study, the acceptance angle was determined as 5° in order to keep consistent with the database of LBL. Therefore, in this study, 5° or alternatively expressed as the radial angle of 2.5° (43.6 mrad) is also used as the upper limit of the circumsolar region (i.e. $\delta_\Delta = 43.6$ mrad). As a matter of fact, by summarizing the meteorological parameters, the dominant CSR can be easily obtained and used as the representative CSR for a specific site. It was proved from Buie's sunshape model that it is the linear relationship between the solar irradiance profile and the radial angle in the circumsolar region in log-log space, as plotted in Fig. 4.2.

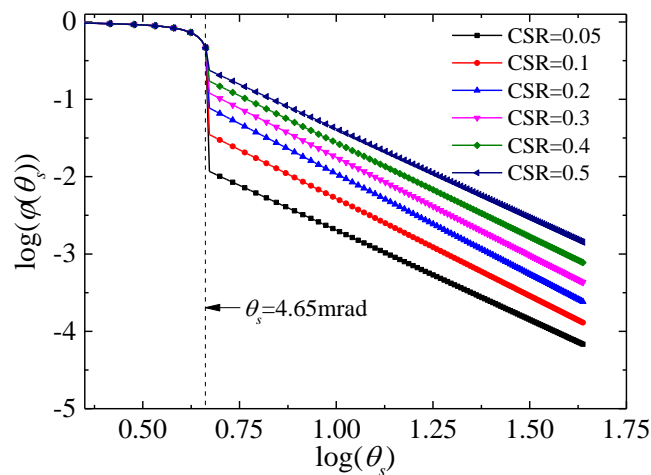


Fig. 4.2 Buie's sunshape plotted in log-log space

4.2.2 Optical errors

There are mainly four types of optical errors in practice, which include specular error, slope error, tracking error and absorber alignment error. All the four optical errors will be defined theoretically in this section.

4.2.2.1 Specularity error

In actual system, due to the non-specular reflective property of the reflector, the original incident sunshape will be distorted after reflection, which is defined as specularity error. The specularity error accounts for the imperfect microscopic texture of the reflector material. With the specularity error, the solar rays in the reflected optical cone will be redistributed, forming a reflected sunshape that is different from the incident sunshape, as shown in Fig. 4.3.

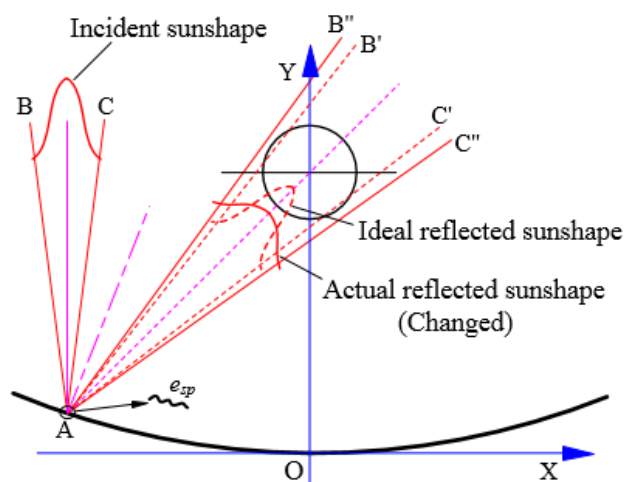


Fig. 4.3 Effect of specularity error on the reflected sunshape

In Fig. 4.3, $\angle B'AC'$ is the ideal reflected optical cone unaffected by specular error, and $\angle B''AC''$ is the actual reflected optical cone reformed by specular error. Obviously, the actual reflected sunshape (solid red line) is absolutely different from the ideal reflected sunshape (dashed red line). Pettit [155] investigated the specular reflectance properties of three mirror materials including silvered glass, metallized film and polished aluminum. It was proved in the work that the mirror scatters the solar beam approximately according to a Gaussian distribution. In fact, the Gaussian distribution has been proved to be appropriate to characterize the specular error [61, 155, 156]. Thus the probability distribution function of the specular error is given by Eq. (4.5).

$$R(\theta_{sp}) = \frac{1}{\sqrt{2\pi}\sigma_{sp}} \exp\left(-\frac{\theta_{sp}^2}{2\sigma_{sp}^2}\right) \quad (4.5)$$

where σ_{sp} is the standard deviation of the distribution function, which is used to represent the specular error in later sections.

4.2.2.2 Tracking error

Tracking error (b_r) is the angle between the plane containing the vertex and focal line of the collector, and the plane containing the focal line and the sun, as shown in Fig. 4.4. It is determined by the accuracy of the tracking system and does not change with the points on the reflector. The same tracking error can be applied for all points on the reflector at each moment.

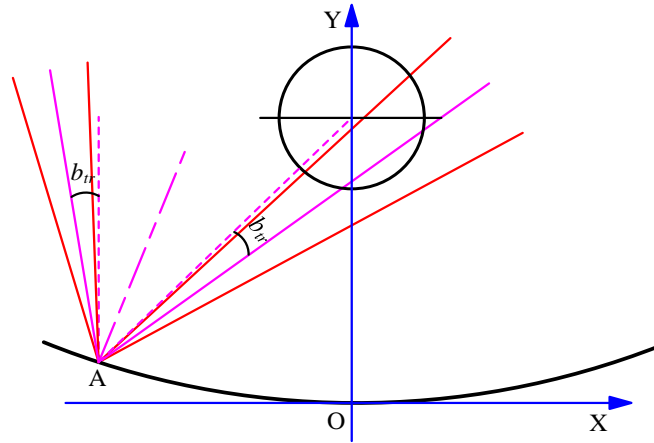


Fig. 4.4 Schematic of tracking error

4.2.2.3 Slope error

Slope error (b_{sl}) is defined as the angular deviation of the actual surface normal direction from the ideal normal direction, as shown in Fig. 4.5. Generally, the slope error is not constant over the reflector surface. In practice, the slope error of any point on the reflector can be measured by photogrammetry [157, 158]. What should be noted is that an angular deviation of the surface normal vector causes twice the angular deviation of the reflected rays, as shown in Fig. 4.5. If no measured data are available, Gaussian model is usually used to define the distribution of slope error, which is given by Eq. (4.6).

$$R(b_{sl}) = \frac{1}{\sqrt{2\pi}\sigma_{sl}} \exp\left(-\frac{b_{sl}^2}{2\sigma_{sl}^2}\right) \quad (4.6)$$

where σ_{sl} is the standard deviation of the distribution function, which is used to represent the slope error in later sections.

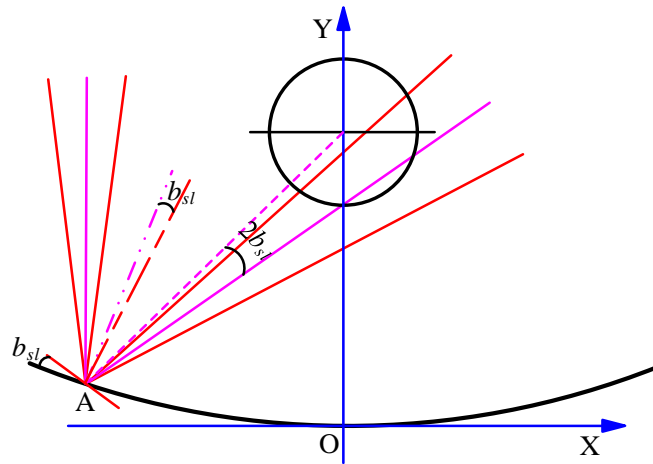


Fig. 4.5 Schematic of slope error

4.2.2.4 Absorber alignment error

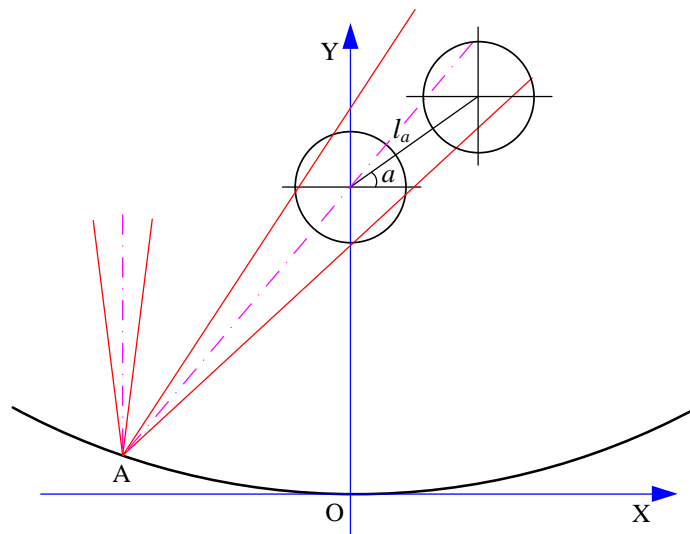


Fig. 4.6 Schematic of absorber alignment error

Absorber alignment error defines the installation deviation of the absorber tube from the focal line of the parabolic reflector, as shown in Fig. 4.6. Absorber alignment error is usually specified by two parameters: the offset distance (l_a) and the offset angle (a).

Obviously, the effects of the absorber alignment error depend on both the offset distance (l_a) and the offset angle (a).

4.2.3 Incident angle

In practice, due to the limitation of single-axis tracking mode, the non-zero incident angle is inevitably produced. As Fig. 4.7 shows, the incident angle (θ_{in}) is defined as the angle between the incident rays and the transverse section that is perpendicular to the focal line. Due to the non-zero incident angle, the effective solar radiation intensity (I_{eff}) incident on the collector aperture, compared with the direct normal solar radiation intensity (I_D), is reduced, which is defined as the cosine loss. In addition, one end of the absorber tube cannot receive any reflected sunrays, and some reflected solar rays escape from the other side of the PTC, as shown in Fig. 4.7, which is defined as end loss.

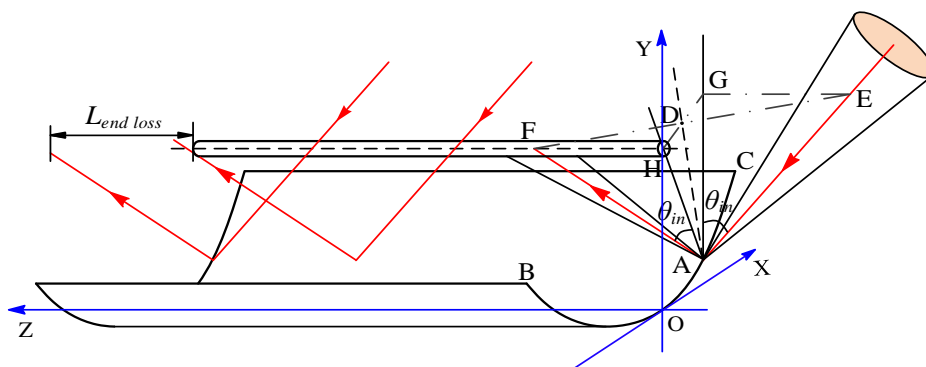


Fig. 4.7 Schematic of incident angle and end loss

The effective solar radiation intensity caused by the cosine loss is calculated by Eq.

(4.7).

$$I_{eff} = I_D \cdot \cos \theta_{in} \quad (4.7)$$

where θ_{in} is the incident angle.

The length of the absorber that cannot receive reflected sunrays from point A on the reflector, caused by the end loss, can be calculated by Eq. (4.8).

$$L_{end\ loss} = HF = AH \cdot \tan \theta_{in} = \left(x_A^2 / 4f_c + f_c \right) \cdot \tan \theta_{in} \quad (4.8)$$

4.3 Coordinate transformation and effective sunshape modeling

4.3.1 Coordinate transformation

Fig. 4.8 shows the incidence of sunrays under non-ideal optical conditions. In the figure, θ_s and φ_s are respectively the radial angle and circumferential angle of any point on the solar disk; θ_{in} is the incident angle; b is the coupling effect of tracking error and slope error. From Fig. 4.4 and Fig. 4.5, it can be easily found that when the tracking error (anticlockwise direction) and the slope error (clockwise direction) are in the opposite direction, the deviation directions of the reflected optical cone in these two cases are the same (clockwise direction). Therefore, if the direction of the tracking error is viewed as positive, the coupling effect of tracking error and slope error for any point on the reflector can be represented by an equivalent deflecting error (b) which is equal to the tracking error minus double the slope error (i.e. $b = b_{tr} - 2b_{sl}$), as shown in Fig. 4.9.

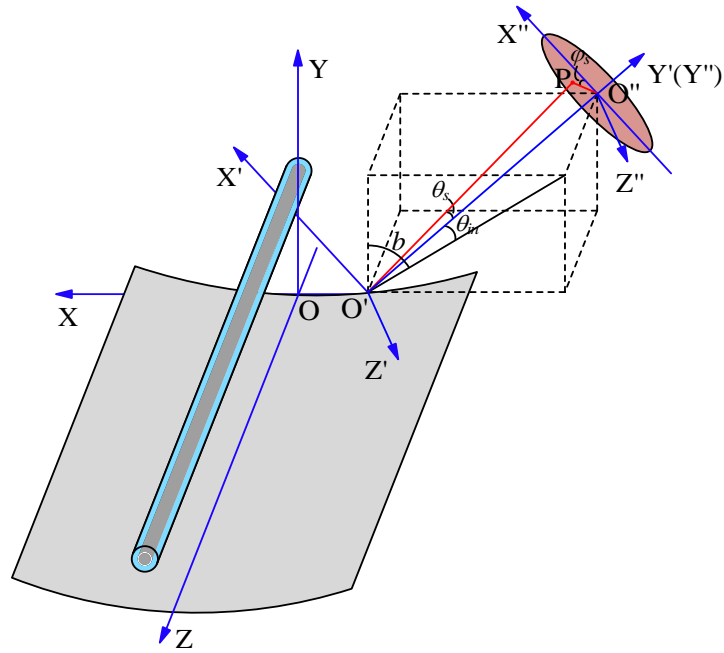


Fig. 4.8 Incidence of sunrays under non-ideal conditions

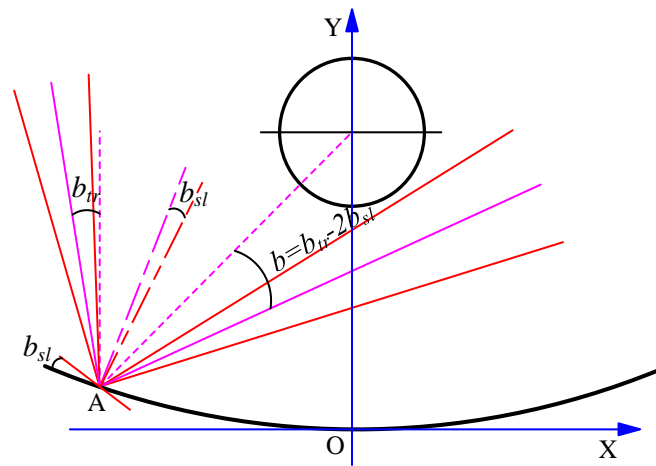


Fig. 4.9 Coupling effect of tracking error and slope error

According to Section 3.2.1, the unit direction vector of the incident ray in coordinate system $O'X''Y''Z''$ is given by Eq. (4.9).

$$s' = (\sin \theta_s \cos \varphi_s, -\cos \theta_s, \sin \theta_s \sin \varphi_s) \quad (4.9)$$

Since the calculations of ray tracing have to be run in the same coordinate system, the

vectors in coordinate system $O'X'Y'Z'$ should be transformed to the vectors in coordinate system $OXYZ$. As Fig. 4.8 shows, the coordinate system $O'X'Y'Z'$ can be transformed to coordinate system $OXYZ$ through translation and rotation. Given the fact that the translation does not change a vector, only the effect of rotation needs to be considered. From Fig. 4.8, it can be found that the coordinate system $OXYZ$ can be achieved by first rotating the coordinate system $O'X'Y'Z'$ around the X' axis by the angle of θ_{in} and then around the Z' axis by the angle of b . Taking the first rotation as example (i.e. the rotation around X' axis), we give the calculation process of coordinate transformation as follows.

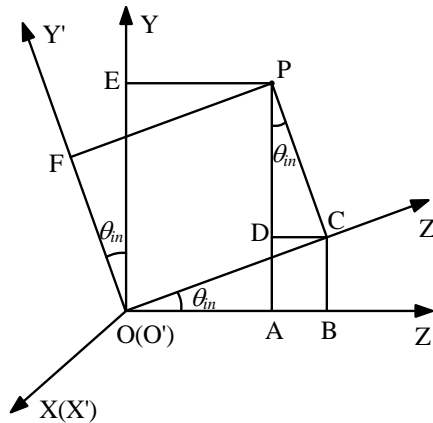


Fig. 4.10 Schematic of coordinate transformation

Fig. 4.10 shows the schematic for calculation of coordinate transformation. According to the figure, for any point P, the following geometrical relations can be easily obtained.

$$\begin{cases} x_p = x_p' \\ y_p = OE = AP = AD + DP = BC + DP = OC \cdot \sin \theta_{in} + PC \cdot \cos \theta_{in} = z_p' \cdot \sin \theta_{in} + y_p' \cdot \cos \theta_{in} \\ z_p = OA = OB - AB = OB - CD = OC \cdot \cos \theta_{in} - PC \cdot \sin \theta_{in} = z_p' \cdot \cos \theta_{in} - y_p' \cdot \sin \theta_{in} \end{cases} \quad (4.10)$$

where the symbols with and without superscript “'” are respectively the coordinates in

coordinate system $O'X'Y'Z'$ and $OXYZ$. Based on Eq. (4.10), the coordinate transformation matrix for the first rotation can be expressed as Eq. (4.11).

$$M_1 = \begin{bmatrix} 1 & 0 & 0 \\ 0 & \cos \theta_{in} & \sin \theta_{in} \\ 0 & -\sin \theta_{in} & \cos \theta_{in} \end{bmatrix} \quad (4.11)$$

Similarly, the coordinate transformation matrix for the second rotation (i.e. the rotation around Z' axis) can be obtained, and given as Eq. (4.12).

$$M_2 = \begin{bmatrix} \cos b & -\sin b & 0 \\ \sin b & \cos b & 0 \\ 0 & 0 & 0 \end{bmatrix} \quad (4.12)$$

Therefore, the unit direction vector (s') in coordinate system $O'X'Y'Z'$ can be transformed to the unite direct vector (s) in coordinate system $OXYZ$ by Eq. (4.13)

$$s = M_2 \cdot M_1 \cdot s' \quad (4.13)$$

4.3.2 Effective sunshape modeling

As mentioned in Section 4.2.2.1, due to the diffusing effect of the specular error, the sunrays in the reflected optical cone will be redistributed. Therefore, the reflected sunshape need to be remodeled, defined as the effective sunshape in this study. According to mathematical theory, the effective sunshape model after reflection can be established by convolving the original sunshape model (i.e. Eq. (4.1)) with the specular error model (i.e. Eq. (4.5)), and given by Eq. (4.14).

$$\phi_{eff}(\theta_s) = \int_{-\delta_\lambda}^{\delta_\lambda} \phi(\theta') R(\theta_s - \theta') d\theta' \quad (4.14)$$

When running the MCRT, the start position of any incident sunray on the sun should be determined based on Eq. (4.14), and its probability density function can be derived as follows.

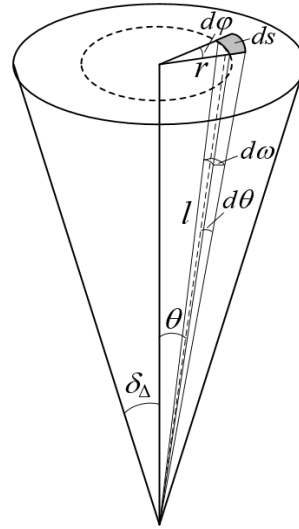


Fig. 4.11 Schematic of optical cone

Fig. 4.11 shows the schematic of optical cone. In the figure, l is the distance between any start point on the sun and the hitting point on the reflector, r is the radius of any start point on the sun, $d\omega$ is the solid angle of the micro-element, $d\theta$ and $d\phi$ are respectively the radial angular increment and the circumferential angular increment, ds is the area of the micro-element. If the solid angle determined by the radial angle of θ_s is expressed by ω , the energy contained in that solid angle can be calculated by the following equation.

$$E(\theta_s) = \int_{\omega} \phi_{\text{eff}}(\theta) d\omega \quad (4.15)$$

where the solid angle of the micro-element ($d\omega$) is given by Eq. (4.16).

$$d\omega = \frac{ds}{l^2} \quad (4.16)$$

From Fig. 4.11, the area of the micro-element (ds) is calculated by Eq. (4.17)

$$ds = rd\varphi \cdot ld\theta = l^2 \sin\theta d\theta d\varphi \quad (4.17)$$

Considering that the maximum radial angle of the sunshape is very small (≤ 0.0436 rad), the following relation can be obtained:

$$\sin\theta = \theta \quad (4.18)$$

Combining Eq. (4.15) ~ Eq. (4.18), the energy bounded by any radial angle of θ_s can be finally expressed by Eq. (4.19).

$$E(\theta_s) = \int_0^{2\pi} \int_0^{\theta_s} \phi_{eff}(\theta) \theta d\theta d\varphi \quad (4.19)$$

Therefore, the probability distribution model of the radial angle of the start point of any solar ray on the sun can be expressed by Eq. (4.20)

$$F(\theta_s) = \frac{E(\theta_s)}{E(\delta_\Delta)} \quad (4.20)$$

Combining Eq. (4.19) and Eq. (4.20), the final expression of the probability distribution model is given as Eq. (4.21).

$$F(\theta_s) = \frac{\int_0^{\theta_s} \phi_{eff}(\theta) \theta d\theta}{\int_0^{\delta_\Delta} \phi_{eff}(\theta) \theta d\theta} \quad (4.21)$$

The derivative of the above equation generates the probability density function:

$$f(\theta_s) = \frac{\phi_{eff}(\theta_s) \theta_s}{\int_0^{\delta_\Delta} \phi_{eff}(\theta) \theta d\theta} \quad (4.22)$$

Eq. (4.22) is exactly the sampling function for incident sunrays. It can be found from Eq. (4.1), Eq. (4.5) and Eq. (4.14) that the expression of the Eq. (4.22) is very complex,

and it is almost impossible to get its inverse function directly. Consequently, the commonly used direct sampling method is not applicable in this study. Instead, we use the acceptance-rejection sampling method (i.e. hit-and-miss method) for random variable sampling, the principle of which is expounded as follows: The probability density function $f(x)$ is defined between a and b ($a \leq x \leq b$), and M is the upper limit of $f(x)$ (i.e. $0 < f(x) \leq M$). Two uniformly distributed random numbers κ_1 and κ_2 are generated. If $M\kappa_2 \leq f(a + (b-a)\kappa_1)$, accept κ_1 , otherwise abandon κ_1 . The flowchart of the acceptance-rejection sampling for the radial angle of the start position of incident sunlight is shown in Fig. 4.12.

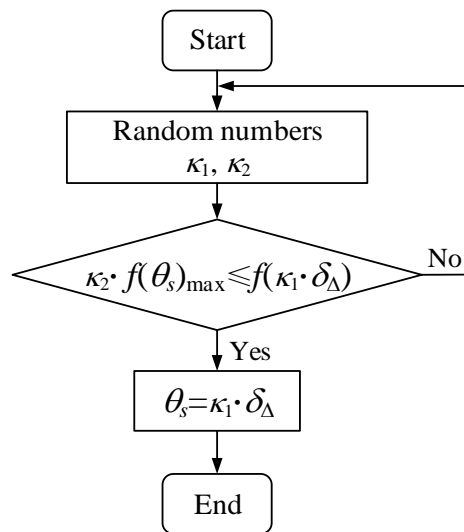


Fig. 4.12 Flow chart of the sampling of the radial angle of incident sunlight

4.4 Effects of non-ideal optical factors on the optical performance

This section examines comprehensively the effects of non-ideal optical factors on the PTC's optical performance based on the above established models. The SEGS LS-2

PTC module is also adopted as the prototype for the study.

4.4.1 Effects of effective sunshape

According to the effective sunshape model (i.e. Eq. (4.14)), it can be found that the effects of the effective sunshape on the PTC's optical performance depend on both the original incident solar profile (CSR) and the specular error (σ_{sp}), which are discussed in detail in this section.

4.4.1.1 Effects on the distribution of local concentration ratio

Fig. 4.13 shows the effects of circumsolar ratio (CSR) on the distribution of local concentration ratio (LCR) in the case of $\sigma_{sp}=3$ mrad. It can be seen from the figure that the angle span that receives the reflected rays (i.e. high flux area) increased and the maximum LCR decreased with the increase of CSR, indicating that more uniform heat flux distribution was produced by larger CSR. This is because more solar energy will be distributed in the circumsolar area and the radiation intensity at the central region of the solar disk is reduced as the CSR increases, producing more uniform incident solar radiation distribution. From the figure, it can also be found that all the curves were symmetrical about $\varphi_a=0^\circ$, and the double peaks of the curves were gradually transformed to the single peak with further increase of CSR.

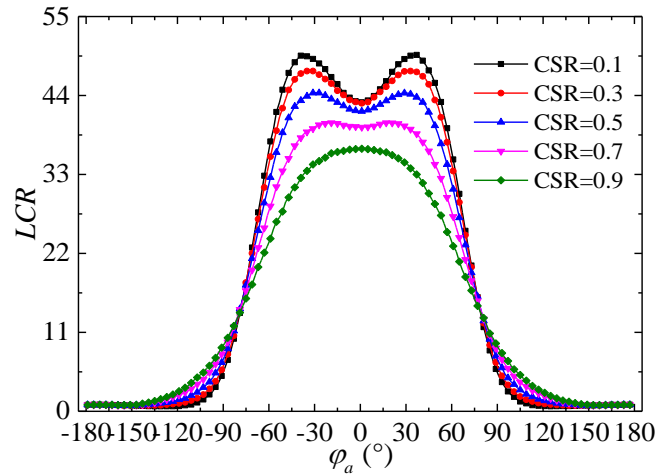


Fig. 4.13 Effects of CSR on the distribution of LCR in the case of $\sigma_{sp}=3$ mrad

Fig. 4.14 depicts the effects of specular error (σ_{sp}) on the distribution of local concentration ratio (LCR) in the case of $CSR=0.1$. It can be seen from the figure that with the increase of σ_{sp} , the distribution curve of LCR became more homogenous, showing more uniform flux distribution on the absorber surface. The reason is that larger specular errors scatter more reflected rays to a larger angle span in the reflected optical cone, producing a more uniform reflected sunshape. It can also be seen from Fig. 4.14 that in the high heat flux area of the absorber tube, a part of the heat flux was reduced and the other was increased with the increase of σ_{sp} . For example, when σ_{sp} was 5 mrad, the heat flux in the circumferential angle range between -75° and -25° (also between 25° and 75°) was smaller than that obtained for $\sigma_{sp}=1$ mrad, whereas the heat flux in the range between -25° and 25° was larger than that for $\sigma_{sp}=1$ mrad. This indicates that the specular error plays a role of cutting peaks and filling valleys in the high heat flux area.

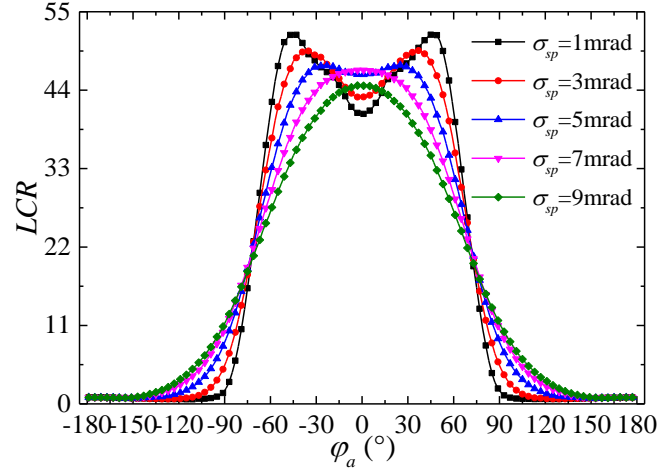


Fig. 4.14 Effects of specularity error on the distribution of LCR in the case of
 $CSR=0.1$

4.4.1.2 Coupling effects on the optical efficiency

Fig. 4.15 shows the variation of the optical efficiency (η_o) with circumsolar ratio (CSR) under different specularity errors (σ_{sp}). It can be observed from the figure that η_o declined consistently with the increase of CSR for all the specularity errors discussed. This is because with the increase of CSR, more solar radiation energy is distributed in the circumsolar area, causing more sunrays escaping from the PTC system (i.e. intercept factor reduced) and hence leading to larger optical loss. Taking $\sigma_{sp}=1$ mrad as an example, as the CSR rose from 0 to 0.5, the η_o decreased from 84.81% to 77.51%, dropping by 7.3%. It can also be found from Fig. 4.15 that the optical efficiency curves for two different specularity errors usually intersected at a certain CSR. When the CSR varied within a range less than the intersection point, the η_o for smaller σ_{sp} was larger than the η_o for larger σ_{sp} . Whereas, if the CSR increased beyond the

intersection point, the η_o for smaller σ_{sp} would be smaller than the η_o for larger σ_{sp} . For example, the optical efficiency curves for $\sigma_{sp}=1$ mrad and $\sigma_{sp}=7$ mrad intersected at CSR=0.47. When the CSR was less than 0.47, the optical efficiency for $\sigma_{sp}=1$ mrad was larger than that for $\sigma_{sp}=7$ mrad, whereas it was smaller as the CSR was larger than 0.47. This indicates that when the weather is not good enough (i.e. CSR is large), reflectors with poorer specular quality (i.e. σ_{sp} is large) may produce larger efficiency. The reason is that when CSR is large enough, more energy is distributed in the peripheral area of the solar disk, and larger specular errors scatter more peripheral radiation to the center area than smaller ones. Meanwhile, although part of the original central energy of the solar disk is dispersed to a larger radial angle range, the relatively large acceptance angle of the absorber tube can still receive most of those dispersed sunrays. This is exactly the effect of cutting peaks and filling valleys of the specular error in the high flux area, which was presented in Fig. 4.14. Therefore, with larger CSRs, larger specular errors distribute more energy in an angle range that can be intercepted by the absorber under, producing higher efficiency. It can also be found from Fig. 4.15 that the intersection point between the efficiency curve for $\sigma_{sp}=1$ mrad and other curves increased with the increase of σ_{sp} . The intersection point between the curve for $\sigma_{sp}=1$ mrad with $\sigma_{sp}=3$ mrad, $\sigma_{sp}=5$ mrad, $\sigma_{sp}=7$ mrad and $\sigma_{sp}=9$ mrad was CSR=0.02, CSR=0.08, CSR=0.47, and more than 0.9, respectively. This demonstrates that the reflectors with high optical quality have less or even no advantage in improving the optical efficiency in bad weather.

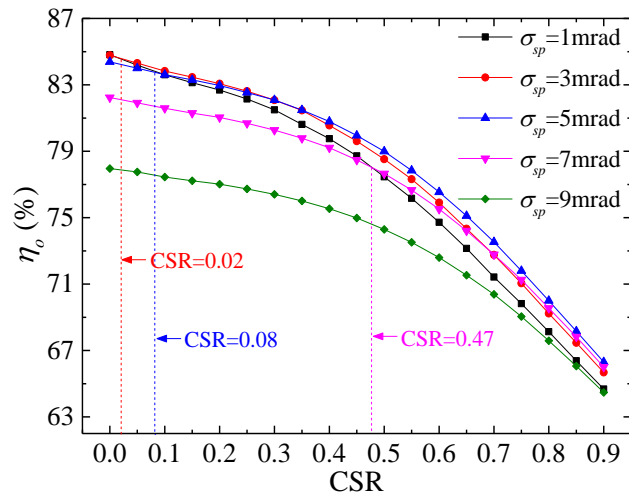


Fig. 4.15 Variation of the optical efficiency with CSR under different specularity

errors

Fig. 4.16 shows the variation of the optical efficiency (η_o) with specularity error (σ_{sp}) under different circumsolar ratios (CSR). It is easily seen from the figure that η_o increased slowly firstly when σ_{sp} was small and then dropped quickly with further increasing σ_{sp} for all the discussed CSRs. When σ_{sp} was small (less than 6 mrad), the optical efficiency differences between different CSRs were obvious, and became smaller and smaller with increasing σ_{sp} continuously. This demonstrates that the effects of CSR dominate when σ_{sp} is small and become less obvious as σ_{sp} increases to a large value range. From the figure, it can be found that the specularity error producing the highest efficiency for CSR=0.1, CSR=0.2, CSR=0.3, CSR=0.4 and CSR=0.35 was 3 mrad, 3.5mrad, 4 mrad, 4.5mrad and 5 mrad respectively. This demonstrates again that the advantage of the reflector with high optical quality is more obvious in better weather. Therefore, the optical quality of the reflector used in sites with excellent solar resource should be as good as possible. Whereas, for the places

with relatively high atmospheric turbidity (CSR is usually more than 0.2), it is not necessary to improve the specular quality of the reflector to a very high degree ($\sigma_{sp} < 3$ mrad). Because almost no improvement or even small reduction of optical efficiency will be caused by reflectors with specular error less 3 mrad in that cases, whereas the costs of those high quality mirrors are remarkable.

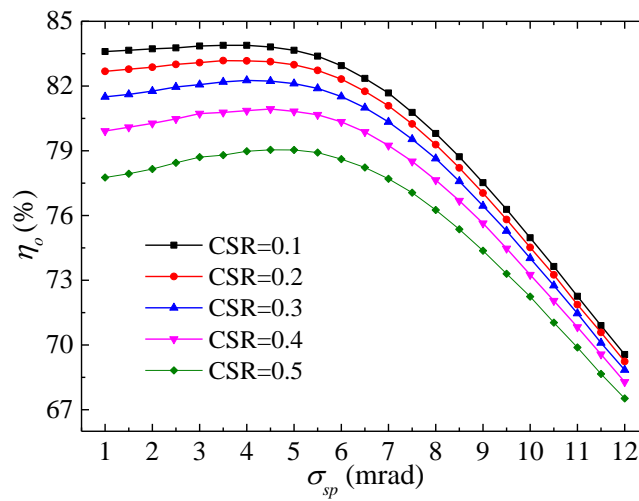


Fig. 4.16 Variation of the optical efficiency with specular error under different CSRs

4.4.2 Effects of tracking error and slope error

This section discusses the effects of tracking error and slope error on the optical performance of the PTC. The study was conducted with the effective sunshape of CSR=0.1 and $\sigma_{sp} = 5$ mrad.

4.4.2.1 Effects on the distribution of local concentration ratio

Fig. 4.17 shows the effects of tracking error (b_{tr}) on the distribution of local concentration ratio (LCR). It is clearly seen from the figure that the LCR curves moved toward the right side of $\varphi_a=0^\circ$ which is the opposite side of the tracking error (left side shown in Fig. 4.4). This indicates that the tracking error (b_{tr}) destroys the symmetry of the LCR distribution and more energy will be reflected to the opposite direction of the tracking error. It can also be found from the figure that the peak LCR increased slightly firstly with b_{tr} increasing from 0 mrad to 5 mrad and then decreased obviously with b_{tr} further rising to 15 mrad. The left peak was always larger than the right one. This indicates that as the tracking error vary in a range of small values (< 5 mrad), the peak heat flux on the same side of the tracking error will be enhanced, while that on the opposite side will be weakened. When b_{tr} was larger than 7 mrad, the double peaks of LCR curves were transformed to the single peak, and the circumferential angle (φ_a) corresponding to the peak LCR moved gradually to the right (i.e. the opposite side of the tracking error).

Fig. 4.18 displays the effects of slope error (σ_{sl}) on the distribution of local concentration ratio (LCR). Because of the symmetry of Gaussian distribution, the LCR curves maintained symmetrical about $\varphi_a=0^\circ$ for any slope errors. The double peaks of the LCR curves were transformed to the single peak when σ_{sl} was more than 2.5 mrad. The peak LCR decreased and the angle span of the high heat flux increased with the

increase of σ_{sl} . This means that the slope error (σ_{sl}) flattens the LCR curves and produces more uniform energy distribution on the absorber surface.

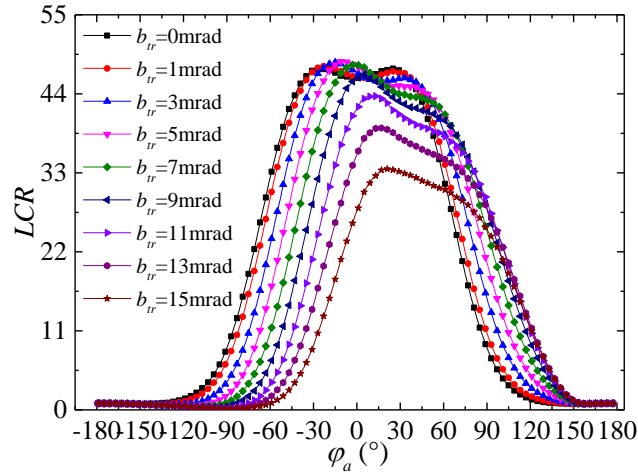


Fig. 4.17 Effects of tracking error on the distribution of local LCR

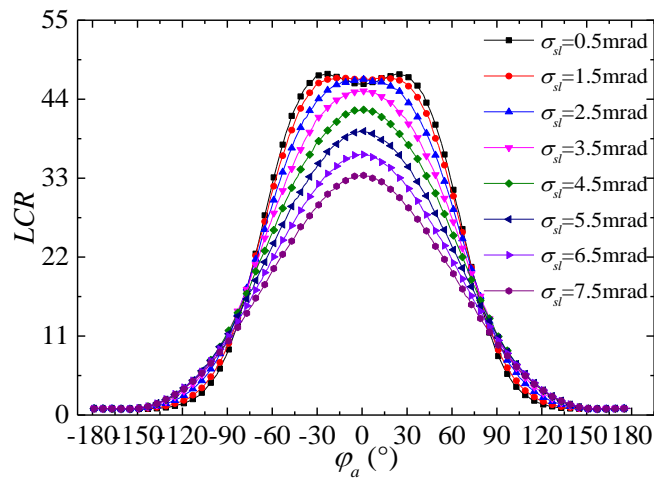


Fig. 4.18 Effects of slope error on the distribution of LCR

4.4.2.2 Coupling effects on the optical efficiency

The coupling effects of tracking error (b_{tr}) and slope error (σ_{sl}) on the optical efficiency (η_o) are displayed in Fig. 4.19 and Fig. 4.20. Fig. 4.19 shows the variation

of the optical efficiency (η_o) with tracking error (b_{tr}) under different slope errors (σ_{sl}). It shows clearly that η_o dropped constantly with the increase of b_{tr} under all the discussed σ_{sl} . The downtrend of the optical efficiency curves became gentler with increasing σ_{sl} . Generally, when b_{tr} varied in a range of small values, the η_o dropped slightly, indicating that there is a small tracking error threshold within which the PTC maintains a relatively high efficiency. For example, when b_{tr} increased from 0 mrad to 4 mrad, the η_o under the condition of $\sigma_{sl}=0$ mrad decreased from 83.6% to 82.6%, dropping just by 1%. Therefore, in practice, the accuracy of the tracking system should be less than the threshold of the tracking error to achieve high performance for the PTC. From Fig. 4.19, it can also be observed that when σ_{sl} was less than 6 mrad, all of the optical efficiency curves intersected at $b_{tr}=17$ mrad after which the optical efficiencies for larger σ_{sl} were larger than the optical efficiencies for smaller σ_{sl} . This indicates that larger slope errors can to some extent compensate the optical loss caused by larger tracking errors.

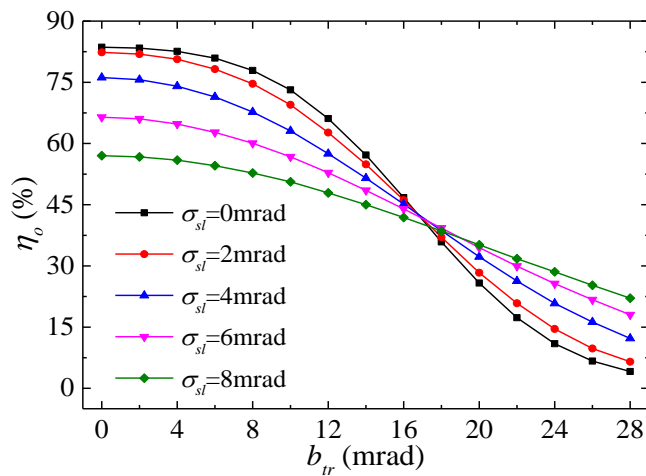


Fig. 4.19 Variation of the optical efficiency with tracking error under different slope errors

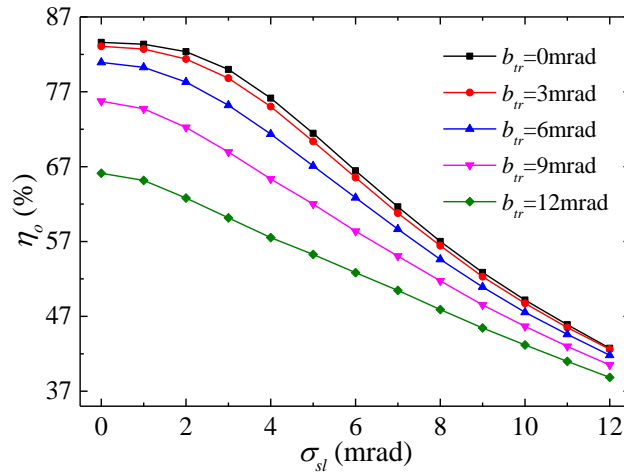


Fig. 4.20 Variation of the optical efficiency with slope error under different tracking errors

Fig. 4.20 shows the variation of the optical efficiency (η_o) with slope error (σ_{sl}) under different tracking errors (b_{tr}). Obviously, η_o decreased consistently with the increase of σ_{sl} . There is also a small range of σ_{sl} during which the η_o maintains at a relatively high level. For example, when σ_{sl} was less than 2 mrad, the η_o under the condition of $b_{tr}=0$ mrad was kept more than 82.36%. It can also be found from Fig. 4.20 that the optical efficiency difference between any two b_{tr} became smaller with the increase of σ_{sl} . This demonstrates that large slope errors, compared with the tracking error, have dominant influences on the optical efficiency. Comparing Fig. 4.19 and Fig. 4.20, it can be found that the optical efficiency (η_o) was more sensitive to the slope error (σ_{sl}) than to the tracking error (b_{tr}). For example, when b_{tr} increased from 0 mrad to 8 mrad, the η_o for $\sigma_{sl}=0$ mrad decreased from 83.6% to 77.9%, dropping only by 5.7%. Whereas, when σ_{sl} increased from 0 mrad to 8 mrad, the η_o for $b_{tr}=0$ mrad declined remarkably from 83.6% to 57%, dropping by 26.6% which was much

larger than the former (5.7%). The reason is that an angular deviation of the surface normal vector causes twice the angular deviation of the reflected rays (as shown in Fig. 4.5), which leads to greater sensitivity of the optical efficiency to the slope error. Therefore, improving the local topography of the reflector surface is an effective way to improve the PTC's performance.

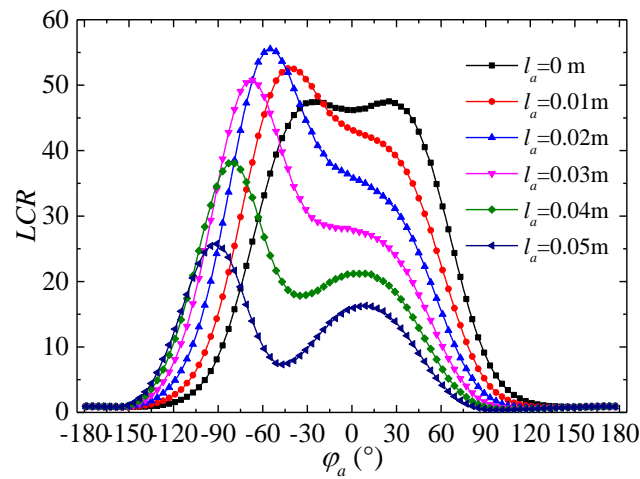
4.4.3 Effects of absorber alignment error

This section first investigates the effects of the offset distance (l_a) on the distribution of LCR under condition of two typical offset angles (a). And then the coupling effects of the absorber alignment error with other two typical optical errors (tracking error and slope error) on the optical efficiency are further discussed. The study was also conducted with the effective sunshape of $CSR=0.1$ and $\sigma_{sp}=5$ mrad.

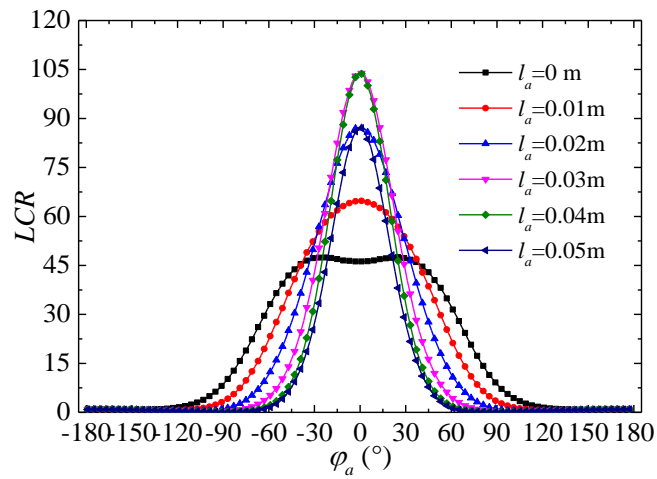
4.4.3.1 Effects on the distribution of local concentration ratio

Fig. 4.21 shows the effects of the absorber alignment error on the distribution of local concentration ratio (LCR). Fig. 4.21(a) shows the results under different offset distances (l_a) in the case of $a=0^\circ$ (i.e. the positive direction of X-axis). It can be seen from the figure that when l_a was more than zero, the LCR curves moved toward the left side of $\varphi_a=0^\circ$ which is the opposite side of the offset direction ($a=0^\circ$). This indicates that more energy is distributed on the opposite side of the offset direction. Fig. 4.21(a) also shows

that when the l_a was within the range between 0.01 m and 0.03 m, there was only one peak for the LCR curves. When the l_a increased more than 0.04 m, two peaks with different concentration ratios occurred. It can be expected that when l_a increased to a certain degree, the minimum LCR between those two peaks will be zero.



(a)



(b)

Fig. 4.21 Effects of the absorber alignment error on the distribution of LCR : (a) $a=0^\circ$,

(b) $a=90^\circ$

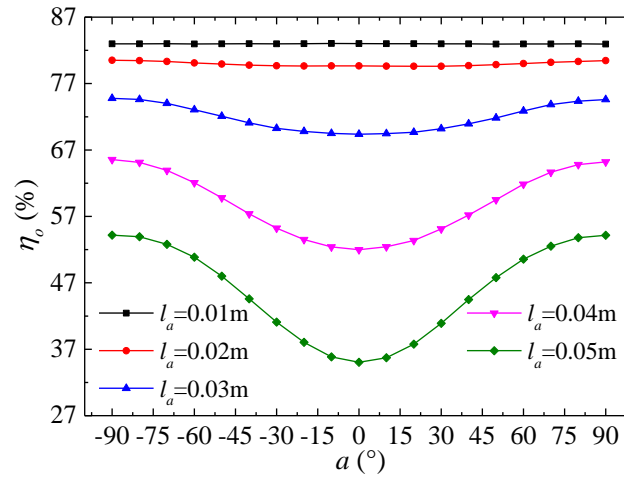
Fig. 4.21 (b) shows the results under different offset distances (l_a) in the case of $a=90^\circ$

(i.e. the positive direction of Y-axis). It can be obviously seen from the figure that the offset direction along the Y-axis did not change the symmetry of the circumferential heat flux distribution on the absorber surface. It can also be clearly found that the high heat flux area shrank consistently and the LCR curves became steeper with the increase of l_a . The two peaks of the LCR curves were changed to one peak when l_a was more than 0.01 m. The peak LCR increased sharply firstly and then declined quickly with the increase of l_a . The maximum LCR in ideal case ($l_a=0$ m) was only 47.5, whereas the maximum LCR obtained in the case of $l_a=0.03$ m was 104 which is almost 2.19 times that obtained in ideal case. This demonstrates that the offset direction along positive Y-axis may result in overheating on the absorber tube surface, which threatens the safety of the PTC system significantly and hence should be avoided in engineering practice.

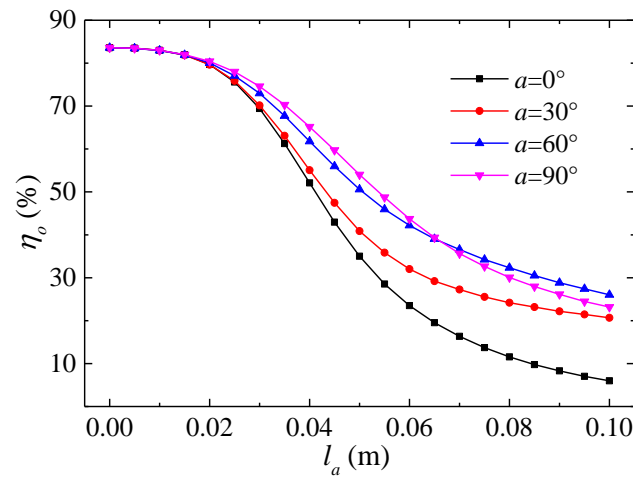
4.4.3.2 Coupling effects on the optical efficiency

The effects of the absorber alignment error, including offset distance (l_a) and offset angle (a), on the optical efficiency are shown in Fig. 4.22. Fig. 4.22(a) shows the variation of the optical efficiency (η_o) with offset angle (a) for different offset distances (l_a). Given the symmetry of the parabola, only the optical efficiency curves in the offset angle range between -90° and 90° were plotted in Fig. 4.22(a). It can be seen from the figure that all the optical efficiency curves were almost symmetrical about $a=0^\circ$ (the difference is less than 0.1%), which means that when only the absorber alignment error exists, it just need to investigate the optical efficiency in the offset angle range between

0° and 90°. The minimum of the η_o was always obtained at $a=0^\circ$, indicating that the offset direction along X-axis causes the largest optical loss.



(a)



(b)

Fig. 4.22 Effects of absorber alignment error on the optical efficiency: (a) variation with offset distance under different offset angles, (b) variation with offset angle under different offset distances

Fig. 4.22(b) displays the variation of the optical efficiency (η_o) with offset distance (l_a)

for different offset angles (a). It shows that η_o decreased with the increase of l_a for all the discussed a . If l_a was less than 0.02 m, the drop rate of η_o was small, which means that the installation deviation of the absorber tube in engineering practice should be smaller than a limit of 0.02 m to ensure a high performance. When l_a was more than 0.02 m, all the optical efficiency curves dropped quickly, among which the curve for $a=0^\circ$ fell fastest, which demonstrates again that the offset direction along X-axis causes the greatest optical loss under the same offset distance.

Fig. 4.23 shows the coupling effects of absorber alignment error and tracking error (b_{tr}) on the optical efficiency (η_o) under the condition of $\sigma_{st}=3$ mrad. It is easily seen from the figure that when b_{tr} is zero, the optical efficiency curve was symmetrical about $a=90^\circ$. An important fact found in Fig. 4.23 was that the optical efficiencies (η_o) at $a=0^\circ$ under the condition of non-zero tracking error ($b_{tr} \neq 0$) were always larger than that under the condition of no tracking error ($b_{tr}=0$). Whereas the optical efficiencies (η_o) at $a=180^\circ$ under the condition of non-zero tracking error ($b_{tr} \neq 0$) were smaller than that under the condition of no tracking error ($b_{tr}=0$). For example, the η_o at $a=0^\circ$ for $l_a=0.03$ m in the case of $b_{tr}=10$ mrad was about 77.96%, larger than the η_o which was about 62.83% in the case of $b_{tr}=0$ mrad. Whereas, the η_o at $a=180^\circ$ for $l_a=0.03$ m in the case of $b_{tr}=10$ mrad was just 26.67% which was much smaller than the η_o (62.83%) obtained without tracking error. From Fig. 4.4, it is easily found that $a=0^\circ$ is in the opposite direction of the tracking error (b_{tr}) and $a=180^\circ$ is in the same direction. Therefore, it can be concluded from the above findings that when the absorber

alignment error and the tracking error are in the opposite direction, the optical loss can to some extent be compensated by themselves, defined as compensation effect, whereas if the two errors are in the same direction, the optical loss will be enlarged, defined as weakening effect.

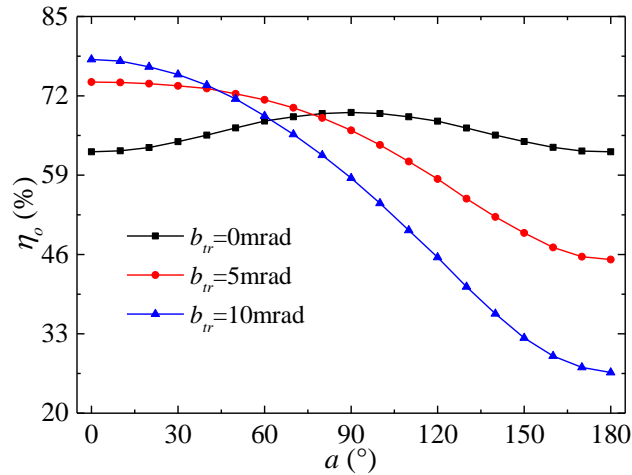


Fig. 4.23 Variation of the optical efficiency with offset angle for $l_a=0.03$ m under different tracking errors in the case of $\sigma_{sl}=3$ mrad

Fig. 4.24 shows the coupling effects of absorber alignment error and slope error (σ_{sl}) on the optical efficiency (η_o) under the condition of $b_{tr}=5$ mrad. Obviously, due to the coupling effects (i.e. compensation effect or weakening effect) of absorber alignment error and tracking error, the η_o for $a=0^\circ$ were larger than the η_o for $a=180^\circ$. It can also be found from the figure that σ_{sl} weakened the compensation effect and aggravated the weakening effect. Moreover, the extent to which the slope error (σ_{sl}) reduced the compensation effect was greater than that it aggravated the weakening effect. For example, when σ_{sl} increased from 1 mrad to 9 mrad, the η_o for $a=0^\circ$ was reduced from 79.84% to 50.06%, dropping by 29.78%. Whereas, the η_o for $a=180^\circ$

was reduced from 45.96% to 39.78%, dropping only by 6.18% with σ_{sl} increasing from 1 mrad to 9 mrad as well.

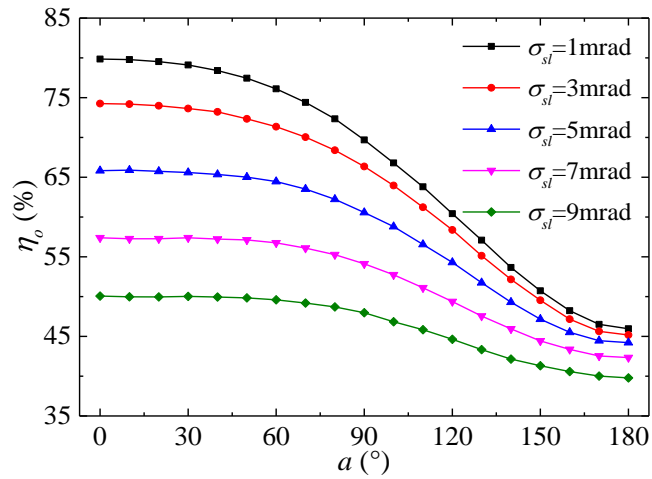
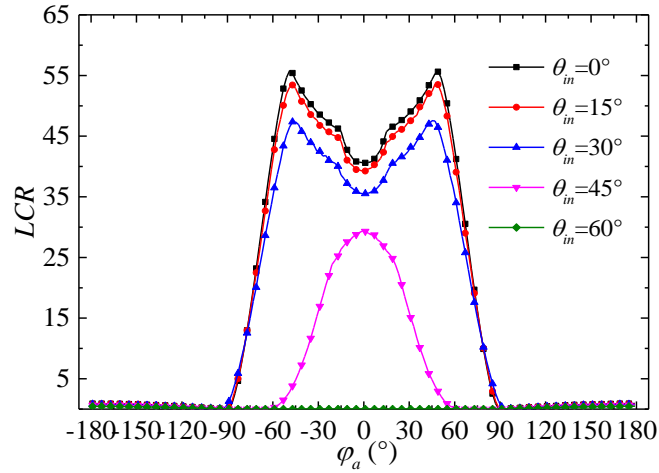


Fig. 4.24 Variation of the optical efficiency with offset angle for $l_a = 0.03$ m under different slope errors in the case of $b_{lr} = 5$ mrad

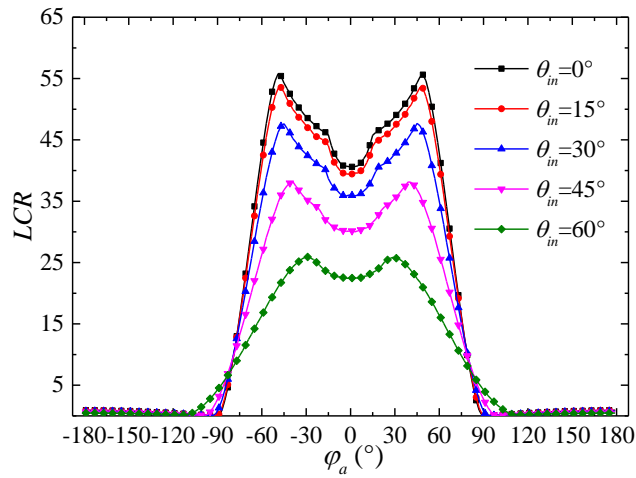
4.4.4 Effects of incident angle

This section first investigates the effects of incident angle on the distribution of local concentration ratio on the absorber outer surface under ideal conditions (without other optical factors). And then the coupling effects of incident angle with other optical factors, including effective sunshape and optical errors, on the optical efficiency are discussed comprehensively.

4.4.4.1 Effects on the distribution of local concentration ratio



(a)



(b)

Fig. 4.25 Circumferential distribution of LCR at two sections under different incident angles: (a) $z=2$ m, (b) $z=7.5$ m

When the incident angle is not zero, the heat flux distribution in the longitudinal direction (Z -axis) is also uneven. Therefore, two cross sections with different longitudinal distances (i.e. $z=2$ m and $z=7.5$ m) are adopted as representatives for analysis. Fig. 4.25 shows the circumferential distribution of LCR at $z=2$ m and $z=7.5$ m under different incident angles (θ_{in}). It can be seen from the figure that when θ_{in} was less than 30° , the distribution of LCR at the two sections (i.e. $z=2$ m and $z=7.5$ m) were

the same, and the value of LCR decreased with increasing θ_{in} . The reason is that when θ_{in} is less than 30° , both the two sections can receive all the reflected rays from the entire aperture width (i.e. the end loss does not affect the flux distribution at those two sections), and larger θ_{in} causes larger cosine loss, hence decreasing the LCR . Whereas, when θ_{in} was equal to 45° , the LCR at $z=2$ m dropped significantly and the high LCR area shrank obviously, compared with that at $z=7.5$ m. In particular, when θ_{in} increased to 60° , except the small heat flux absorbed directly by the upper side of the absorber (i.e. $|\varphi_a| > 90^\circ$), the LCR at the bottom part of the absorber was zero. The reason is shown in Fig. 4.26 which displays the variation of the end loss ($L_{end\ loss}$) with the absolute value of abscissa of point A ($|x_A|$) under different incident angles (θ_{in}) based on Eq. (4.8). Note that since the aperture width of the LS-2 PTC is 5 m (given in Table 3.1), the maximum of $|x_A|$ was set as 2.5. It can be easily found from Fig. 4.26 that when θ_{in} was less than 30° , $L_{end\ loss}$ was always smaller than 2 m for any $|x_A|$, indicating that the section at $z=2$ m can receive all the reflected rays from the entire aperture width in this case (i.e. without effect from the end loss). When θ_{in} was 45° , only the reflected rays from the points with $|x_A|$ less than 1.2 m can be received by the section of $z=2$ m, which reduces remarkably the LCR on the absorber tube. As θ_{in} was 60° , $L_{end\ loss}$ for all the points on the reflector width was larger than 2 m (the minimum was 3.19 m), which means that all the sunrays reflected by the reflector cannot be received by the section of $z=2$ m in this case. Therefore, the LCR at the bottom of the absorber at $z=2$ m was zero for $\theta_{in}=60^\circ$, as shown in Fig. 4.25(a). From Fig. 4.26, it can also be found that when the incident angle was less than 60° , $L_{end\ loss}$ for

the whole reflector was smaller than 7.5 m (the maximum was only 4.5 m), which means that the section with $z=7.5$ m can receive all the reflected rays from the entire aperture under condition of $0^\circ \leq \theta_{in} \leq 60^\circ$. Thus, the LCR distribution at $z=7.5$ m is only affected by the cosine loss, producing larger LCR than the section of $z=2$ m in the case of $\theta_{in} \geq 45^\circ$. As Fig. 4.25(b) shows, due to the increase of cosine loss, the high heat flux decreased consistently with the increase of incident angle. It can also be found from Fig. 4.25(b) that the angle span of the high flux area increased with the increase of θ_{in} . This is because the distance of the reflected rays from the reflector to the absorber (i.e. AF in Fig. 4.7) becomes larger as θ_{in} increases, producing a larger spot on the outer surface of the absorber.

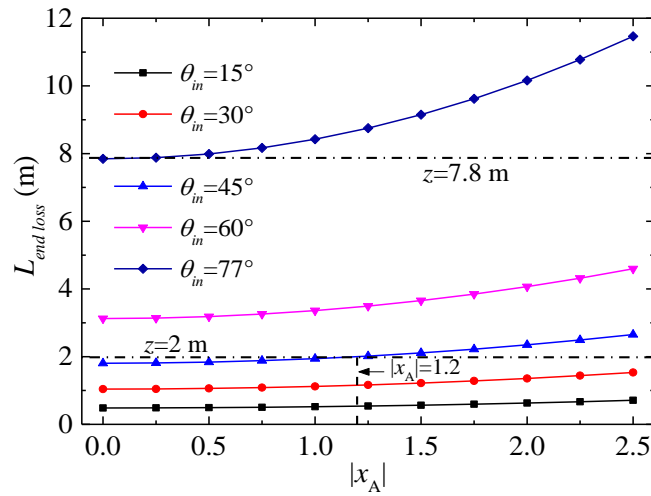


Fig. 4.26 Variation of $L_{end\ loss}$ with the absolute value of abscissa of any point A on the reflector under different incident angles

Fig. 4.27 shows the longitudinal distribution of local concentration ratio (LCR) at different circumferential angles on the absorber in the case of $\theta_{in} = 30^\circ$. It can be found

from the figure that when $|\varphi_a|$ was larger than 90° , the LCR along the absorber was kept nearly zero. This is because the upper side of the absorber (i.e. $|\varphi_a| > 90^\circ$) cannot receive reflected sunrays. When $|\varphi_a|$ was smaller than 90° , there was a section at one end of the absorber tube having extremely small LCR (almost zero), and afterwards, LCR increased sharply to a relatively constant value. It can also be found that when two circumferential angles were symmetrical to each other ($\pm 45^\circ$ and $\pm 75^\circ$ shown in Fig. 4.27), the distributions of LCR for them were coincident. From the figure, we can also find that the length of the section with near-zero LCR at $\varphi_a = \pm 75^\circ$ was larger than that at $\varphi_a = 0^\circ$ and $\varphi_a = \pm 45^\circ$. This can also be explained by the theoretical results shown in Fig. 4.26, from which, it can be seen that $L_{end\ loss}$ increased with the increase of $|x_A|$, indicating that wider aperture widths cause larger end loss. The position with larger $|\varphi_a|$ mainly receives the reflected rays from larger $|x_A|$ which cause larger $L_{end\ loss}$. Therefore, the length of the section with near-zero LCR for larger $|\varphi_a|$ is larger than that for smaller $|\varphi_a|$.

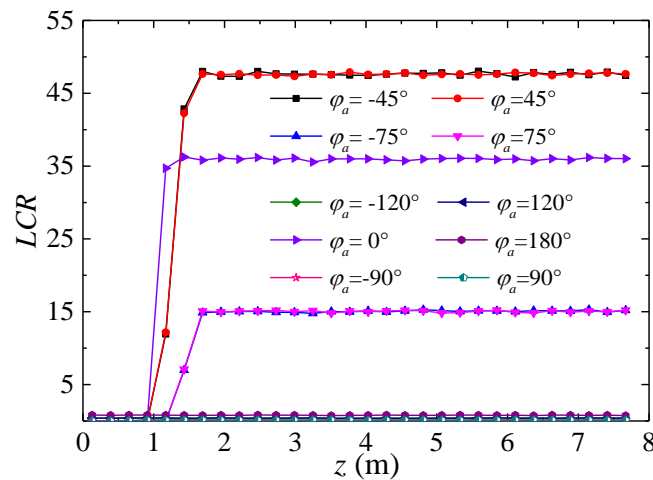


Fig. 4.27 Longitudinal distribution of LCR at different circumferential angles in the case of $\theta_{in} = 30^\circ$

bottom part of the absorber) faded with the increase of θ_{in} , demonstrating that the high heat flux decreases with increasing θ_{in} , which is the same as what is presented in Fig. 4.25. This is because the larger incident angle increases the cosine loss, which reduces the effective incident solar radiation intensity, hence decreasing the heat flux.

4.4.4.2 Coupling effects on the optical efficiency

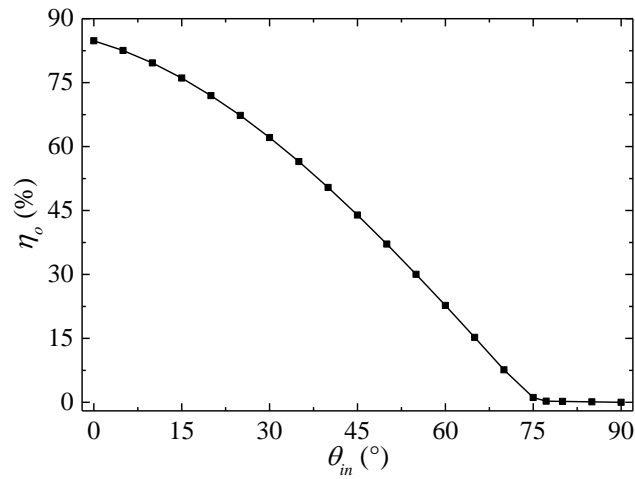
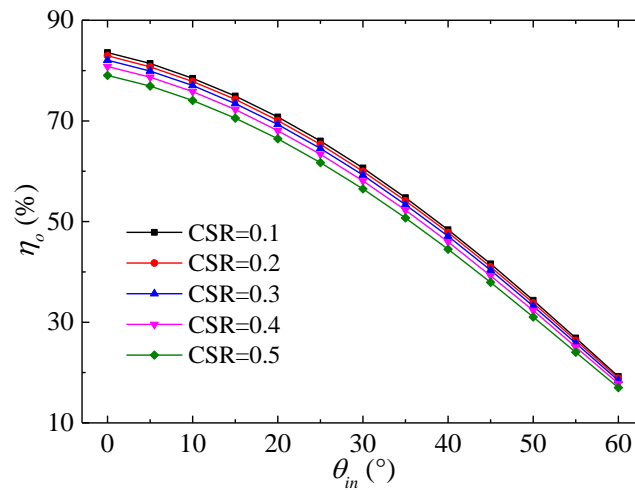


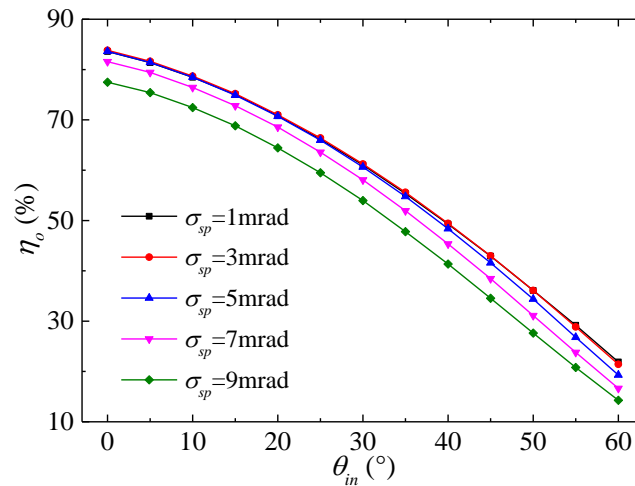
Fig. 4.29 Variation of optical efficiency with incident angle under ideal condition

Fig. 4.29 shows the variation of optical efficiency (η_o) with the incident angle (θ_{in}) under ideal condition. Obviously, due to the cosine loss and end loss, η_o decreased consistently with the increase of θ_{in} . When θ_{in} was larger than 77° , η_o maintained constantly at an extremely small value (almost zero). The reason can also be found in Fig. 4.26. It can be seen from Fig. 4.26 that when θ_{in} was 77° , the minimum of $L_{end\ loss}$ was larger than 7.8 m which is exactly the length of the SGES LS-2 PTC ($L_c=7.8$ m). This indicates that when the incident angle is more than 77° , all the reflected rays escape

from one side of the PTC, hence leading to bear-zero optical efficiency. This nice agreement between simulation results and theoretical results proves further the accuracy and reliability of established optical models.



(a)



(b)

Fig. 4.30 Variation of optical efficiency with incident angle under different effective sunshape: (a) different CSRs, (b) different specularity errors

The coupling effects of the incident angle (θ_{in}) with other optical factors on the optical efficiency (η_o) are shown in Fig. 4.30 ~ Fig. 4.33. It is clearly seen from those five

figures that η_o decreased consistently with the increase of θ_{in} under any optical factors. From Fig. 4.30(b), it can be found that when θ_{in} was less than 30° , changing the specularly error in the small range of less than 5 mrad had little influences on the optical efficiency. From other four figures, it can be found that the effects of optical factors (CSR, tracking error, slope error and absorber alignment error) became less obvious as θ_{in} increased. This is because the effects of the incident angle become gradually dominant as it increases continuously. From Fig. 4.33, it can be found that the offset direction along X-axis ($a=0^\circ$) caused the greatest optical loss (the smallest optical efficiency) for the same offset distance. As l_a increased, the optical efficiency difference between any two a increased. This demonstrates that the optical efficiency is more sensitive to the offset angle under larger offset distances. However, the sensitivity of the optical efficiency to the absorber alignment error decreases with the increase of incident angle.

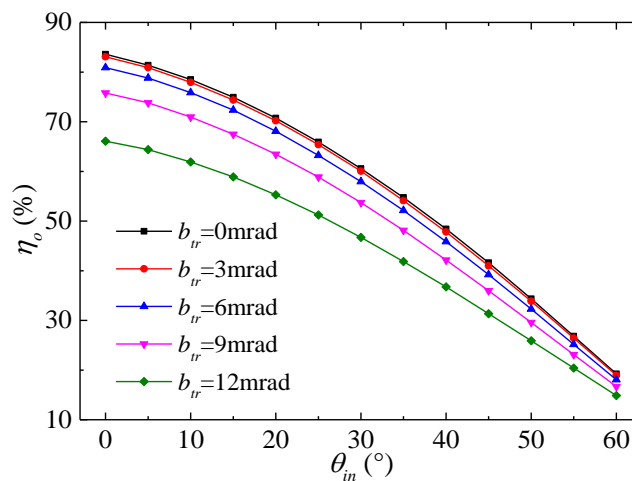


Fig. 4.31 Variation of optical efficiency with incident angle under different tracking

errors

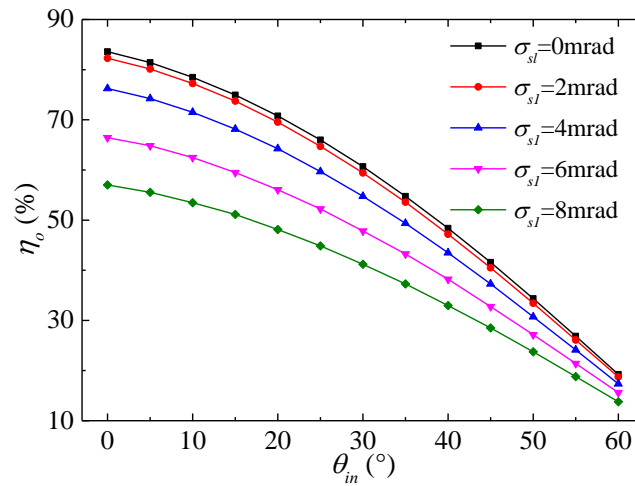


Fig. 4.32 Variation of optical efficiency with incident angle under different slope

errors

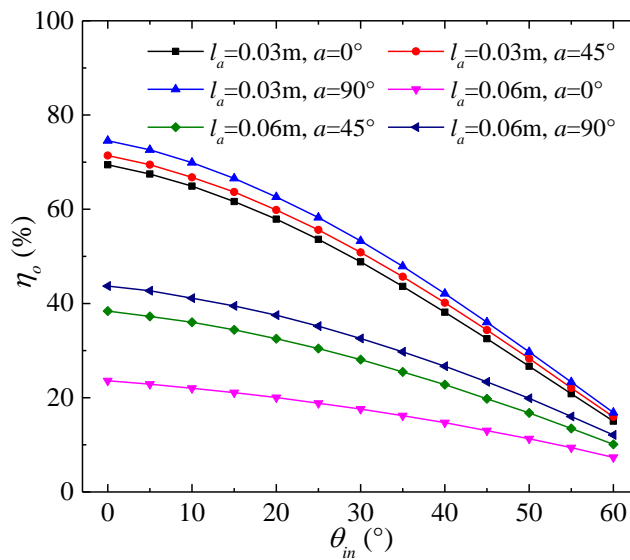


Fig. 4.33 Variation of optical efficiency with incident angle under different absorber

alignment errors

4.5 Summary

This chapter carried out a detailed investigation on the optical performance of the PTC under the non-ideal optical conditions. All the non-ideal optical factors, such as uneven

sunshape and various optical errors including specular error, tracking error, slope error and absorber alignment error were characterized individually according to their generation principles. An effective sunshape model was established for sampling of incident sunrays by convolving the original sunshape model with the specular error model. The coupling effects of the sunshape and optical errors on the optical performance of the PTC were studied comprehensively and some important findings are summarized as follows:

- (1) Both larger CSRs and larger specular errors produce more uniform heat flux distribution around the absorber surface. Small specular errors (< 5 mrad) play the role of cutting peaks and filling valleys in the high heat flux area. The weakening effect of CSR on the optical efficiency becomes less obvious with increasing specular error. The advantage of the high optical quality reflector in improving the optical efficiency is more outstanding in clearer weather. For the sites with relatively high atmospheric turbidity ($CSR > 0.2$), high quality reflector ($\sigma_{sp} < 3$ mrad) achieves little improvement or even cause small reduction of optical efficiency.
- (2) More energy is distributed on the absorber part that is on the opposite side of the tracking error. The slope error flattens the curves of local concentration ratio and produces more uniform heat flux distribution. When the offset direction is in the positive Y-axis direction (i.e. $\alpha = 90^\circ$), the peak local concentration ratio is 2.19 times that obtained without any optical errors, posing threat of overheating on the

absorber surface, which should be avoided in engineering practice.

- (3) The downtrend of the optical efficiency with tracking error becomes gentler with increasing slope error. Both the tracking error and the slope error should be less than a threshold (4 mrad and 2 mrad respectively) to achieve high optical efficiency. When the tracking error is larger than a certain value (>17 mrad), the larger slope errors can to some extent compensate the optical loss caused by the tracking error. The optical efficiency is more sensitive to the slope error than to the tracking error. Therefore, improving the local topography of the reflector surface is an effective way to enhance the PTC's performance.
- (4) When there only exists the absorber alignment error, the optical efficiency curves are almost symmetrical about $\alpha=0^\circ$. The offset direction along X-axis causes the greatest optical loss for the same offset distance. When the absorber alignment error and the tracking error are in the opposite direction, the optical loss can to some extent be compensated by themselves, defined as compensation effect, whereas that in the same direction will aggravate the optical loss, defined as weakening effect. The slope error weakens the compensation effect and aggravates the weakening effect. Moreover, the extent to which the slope error reduces the compensation effect is greater than the extent to which the slope error aggravates the weakening effect.

(5) The non-zero incident angle results in cosine loss and end loss, which, respectively, reduces effective incident solar irradiance and causes rays-spillage at one end of the collector, weakening significantly the optical efficiency of the PTC. Due to the end loss, a near-zero heat flux section is formed at one end of the absorber, the length of which increases with increasing incidence angle. The weakening effects of optical factors (CSR, tracking error, slope error and absorber alignment error) become less obvious as incident angle increases. The optical efficiency is more sensitive to the offset angle under larger offset distances, and this sensitivity decreases with the increase of incident angle.

CHAPTER 5

THEORETICAL ANALYSIS OF THE OPTICAL PERFORMANCE UNDER NON-IDEAL OPTICAL CONDITIONS

5.1 Introduction

As mentioned in Section 3.3, the absorber diameter should be larger than the critical diameter to avoid rays-spillage. However, the critical absorber diameter under non-ideal optical conditions has previously never been discussed. Although the MCRT is an effective method for simulating the rays-concentrating of the PTC, it has complicated theoretical basis and requires long computing time, which limits its application in engineering practice. Thus, it is necessary to develop a simple and efficient method for engineering calculation and analysis. This chapter first derive the formula of critical absorber diameter under any optical error conditions based on the theory of spatial analytic geometry. And then, a new simple algorithm is developed theoretically for quick calculation of optical efficiency. Moreover, based on the derived formulas and the proposed algorithm, the effective sunshape size is further discussed. Finally, the changing properties of optical efficiency obtained by the MCRT in the preceding chapter are also expounded using the theoretical results.

5.2 Derivation of critical absorber diameter

As mentioned in Section 4.2.2, the solar profile will be reshaped because of the dispersion effect of the specular error. A new effective radial angular size (δ_{eff}) of the reflected optical cone should be determined before any calculation and analysis in engineering practice. Details about the effective size of the reflected sunshape will be discussed in Section 5.4. This section uses directly the effective radial size (δ_{eff}) for derivation of the critical absorber diameter ($d_{a,c}$). For ideal conditions (without any optical errors), the critical diameter based on the solar disk (δ) has been given by Eq. (3.15). Therefore, using δ_{eff} replacing δ in Eq. (3.15), the formula of the critical diameter for any point A based on the effective radial angle (δ_{eff}) without optical errors can be expressed by Eq. (5.1).

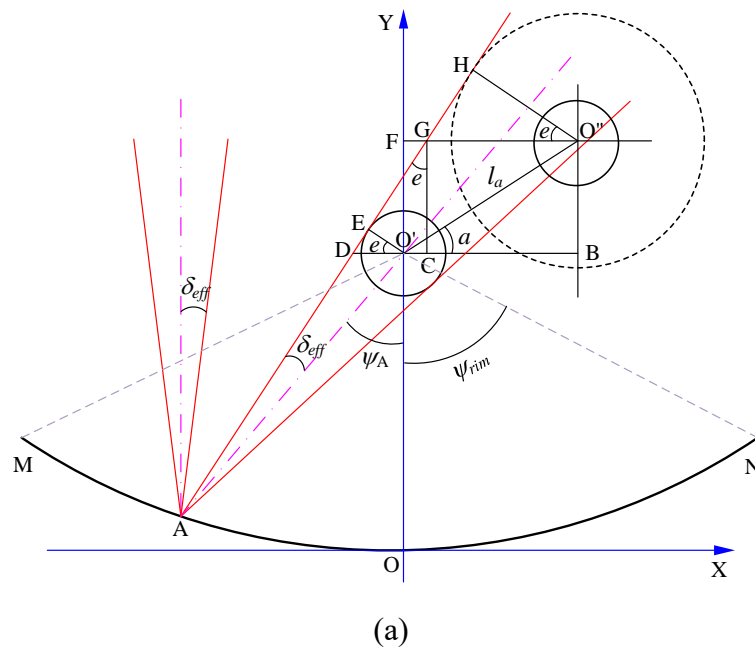
$$d_{A,ideal} = 2 \cdot r_{A,ideal} = 2 \cdot \left(\frac{x_A^2}{4f_c} + f_c \right) \cdot \sin \delta_{eff} \quad (5.1)$$

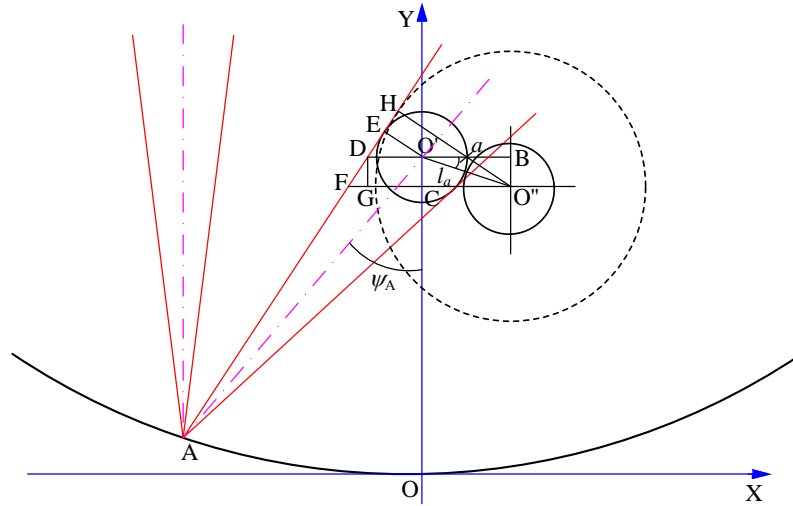
where $d_{A,ideal}$ and $r_{A,ideal}$ are the critical diameter and critical radius respectively for any point A on the reflector under ideal conditions (without optical errors). Please note that the critical radius ($r_{A,ideal}$) will be used in the following derivation process.

According to the formula of rim angle (Eq. (3.16)), the position angle (ψ_A) of point A can be calculated by Eq. (5.2).

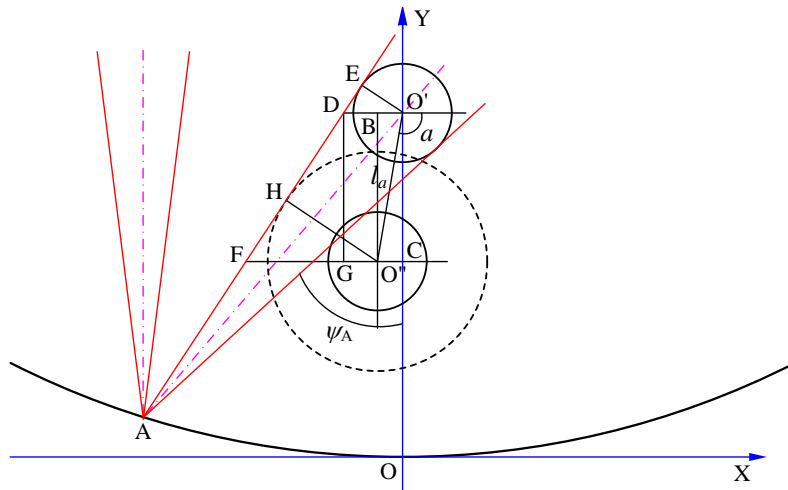
$$\psi_A = \begin{cases} \arcsin\left(\frac{|x_A|}{x_A^2/4f_c + f_c}\right) & 0^\circ < \psi_A \leq 90^\circ \\ 180^\circ - \arcsin\left(\frac{|x_A|}{x_A^2/4f_c + f_c}\right) & 90^\circ < \psi_A < 180^\circ \end{cases} \quad (5.2)$$

The idea of deriving the critical diameter under non-ideal conditions is as follows: firstly, derive the critical diameter under condition of only absorber alignment error; then, based on the derived critical diameter, further derive the critical diameter under any optical errors. As Fig. 5.1 shows, point A is any point on the left half of the parabolic reflector (i.e. $x_A \leq 0$) and line AO' is the centerline of the reflected optical cone. In this study, we define the clockwise direction as the right side of AO' . In Fig. 5.1, point O' is the focus of the parabola, and the absorber tube is installed away from the focus with an offset distance (l_a) and an offset angle (a). The outermost rays of the reflected optical cone are tangent to the dotted circle. Obviously, the radius of the dotted circle ($O'H$) is exactly the critical radius (half the critical diameter).





(b)



(c)

Fig. 5.1 Offset direction is on the right side of the centerline (AO') of the reflected optical cone: (a) $0 < a \leq 90^\circ - \psi_A$, (b) $-90^\circ < a \leq 0$, (c) $-90^\circ - \psi_A < a \leq -90^\circ$

When the offset direction is on the right side of line AO' (i.e. $-90^\circ - \psi_A < a \leq 90^\circ - \psi_A$), it can be divided into three cases, which are $0 < a \leq 90^\circ - \psi_A$, $-90^\circ < a \leq 0$ and $-90^\circ - \psi_A < a \leq -90^\circ$, as shown in Fig. 5.1(a), Fig. 5.1(b) and Fig. 5.1(c) respectively. Taking the first case (as shown in Fig. 5.1(a)) as an example, we present the detailed derivation process of the critical tube diameter,

which is given as follows.

In Fig. 5.1(a), the auxiliary calculation angle (e) can be easily calculated by Eq. (5.3).

$$e = \psi_A - \delta_{eff} \quad (5.3)$$

For point A, the critical radius is derived as follows:

$$\begin{aligned} r_A &= O''H = O''G \times \cos e = (O''F - GF) \times \cos e \\ &= (BO' - CO') \times \cos e = [BO' - (CD - O'D)] \times \cos e \\ &= \left[|O'O'' \times \cos a| - GC \times \tan e + \frac{EO'}{\cos e} \right] \times \cos e \\ &= \left[|O'O'' \times \cos a| - O''B \times \tan e + \frac{EO'}{\cos e} \right] \times \cos e \\ &= \left[l_a \times \cos a - l_a \times \sin a \times \tan e + \frac{r_{A,ideal}}{\cos e} \right] \times \cos e \\ &= \left[l_a \times \cos a \times \cos e - l_a \times \sin a \times \sin e + r_{A,ideal} \right] \\ &= l_a \times \cos(a + e) + r_{A,ideal} \end{aligned}$$

Combined with Eq. (5.3), the critical radius can be expressed by Eq. (5.4).

$$r_A = l_a \times \cos(a + \psi_A - \delta_{eff}) + r_{A,ideal} \quad (5.4)$$

Similarly, the expressions of critical radius for the other two cases, as shown in Fig.

5.1(b) and Fig. 5.1(c) respectively, which actually are the same as Eq. (5.4). Therefore,

when the offset direction is on the right side of line AO' (i.e.

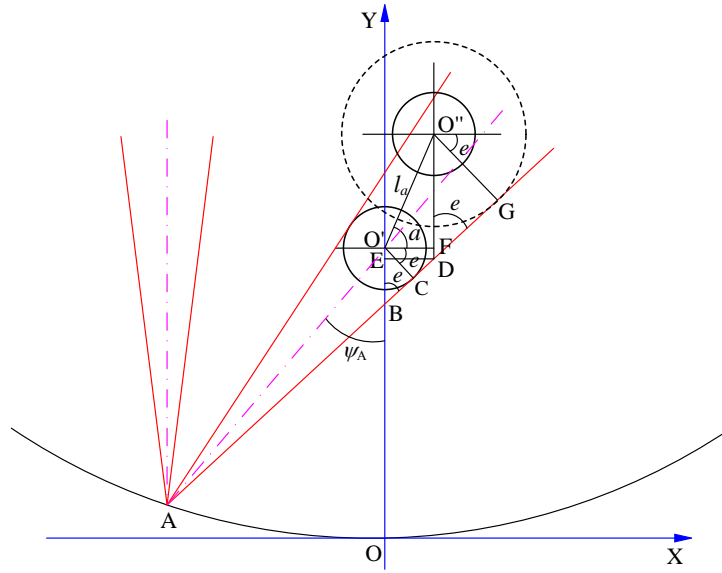
$-90^\circ - \psi_A < a \leq 90^\circ - \psi_A$), the expression of critical radius is finally given by Eq. (5.5).

$$r_A = l_a \times \cos(a + \psi_A - \delta_{eff}) + r_{A,ideal} \quad -90^\circ - \psi_A < a \leq 90^\circ - \psi_A \quad (5.5)$$

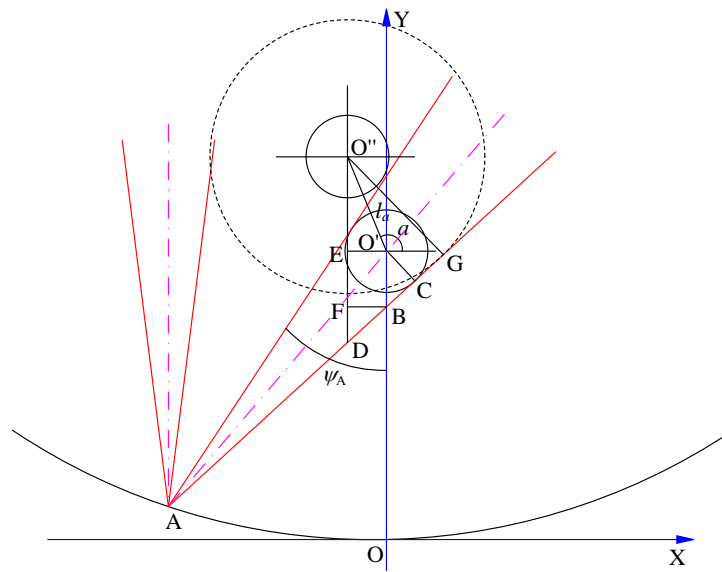
When the offset direction is on the left side of line AO' ($90^\circ - \psi_A < a \leq 270^\circ - \psi_A$),

it can also be divided into three cases, which are $90^\circ - \psi_A < a \leq 90^\circ$, $90^\circ < a \leq 180^\circ$

and $180^\circ < a \leq 270^\circ - \psi_A$, as shown in Fig. 5.2(a), Fig. 5.2(b) and Fig. 5.2(c) respectively.



(a)



(b)

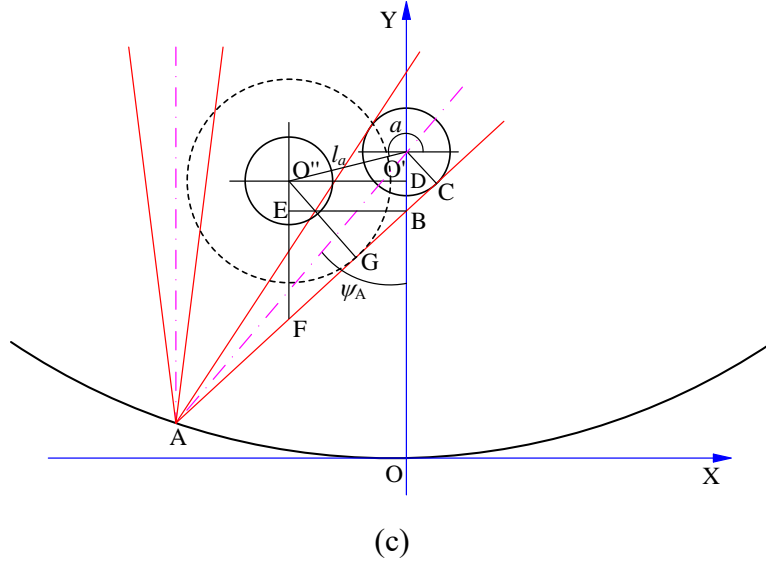


Fig. 5.2 Offset direction is on the left side of the centerline (AO') of the reflected optical cone: (a) $90^\circ - \psi_A < a \leq 90^\circ$, (b) $90^\circ < a \leq 180^\circ$, (c) $180^\circ < a \leq 270^\circ - \psi_A$

We also give the detailed derivation of the critical radius for the first case (shown in Fig. 5.2(a)) as follows:

The auxiliary calculation angle (e) in Fig. 5.2(a) can be given by Eq. (5.6).

$$e = \psi_A + \delta_{eff} \quad (5.6)$$

For point A, the critical radius is derived as follows:

$$\begin{aligned} r_A &= O''G = O''D \times \sin e = (O''F + FD) \times \sin e \\ &= (O''F + OE) \times \sin e = [O''F + O'B - EB] \times \sin e \\ &= \left[|O'O'' \times \sin a| + \frac{O'C}{\sin e} - ED \times \cot e \right] \times \sin e \\ &= \left[O'O'' \times \sin a + \frac{O'C}{\sin e} - O'F \times \cot e \right] \times \sin e \\ &= [l_a \times \sin a + r_{A,ideal} - |l_a \times \cos a| \times \cot e] \times \sin e \\ &= l_a \times \sin a \times \sin e - l_a \times \cos a \times \cos e + r_{A,ideal} \end{aligned}$$

$$= -l_a \times \cos(a + e) + r_{A,ideal}$$

Combined with Eq. (5.6), the critical radius can be expressed by Eq. (5.7).

$$r_A = -l_a \times \cos(a + \psi_A + \delta_{eff}) + r_{A,ideal} \quad (5.7)$$

Similarly, the expressions of critical radius for the other two cases, as shown in Fig. 5.2(b) and Fig. 5.2(c) respectively, which actually are the same as Eq. (5.7). Therefore, when the offset direction is on the left side of line AO' (i.e. $90^\circ - \psi_A < a \leq 270^\circ - \psi_A$), the expression of critical radius is finally given by Eq. (5.8).

$$r_A = -l_a \times \cos(a + \psi_A + \delta_{eff}) + r_{A,ideal} \quad 90^\circ - \psi_A < a \leq 270^\circ - \psi_A \quad (5.8)$$

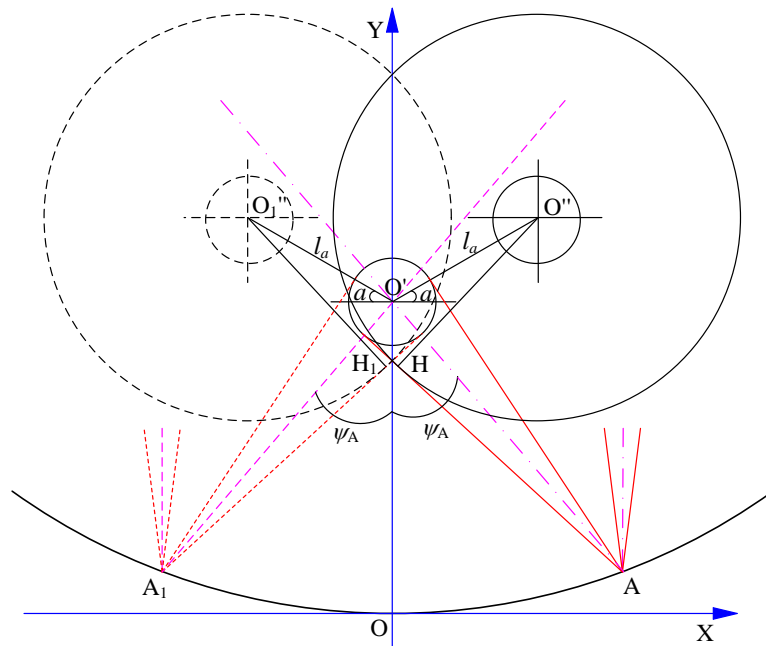


Fig. 5.3 The situation that point A is on the right half of the reflector ($x_A > 0$)

When point A is on the right half of the parabolic reflector (i.e. $x_A > 0$), the critical tube radius can be obtained similarly due to the symmetry of parabola. Fig. 5.3 shows the situation that point A is on the right half the parabolic reflector (i.e. $x_A > 0$).

Obviously, the critical radius is equal to $O''H$. Point A_1 and point A are symmetrical about Y -axis. From the figure, it can be clearly seen that $O''H$ is equal to $O_1''H_1$ ($O''H = O_1''H_1$). Therefore, the critical radius corresponding to a for $x_A > 0$ is equal to the critical radius corresponding to $180^\circ - a$ for $x_A < 0$. Therefore, using $180^\circ - a$ replacing a in Eq. (5.5) and Eq. (5.8), we can obtain the critical radius for $x_A > 0$, which is presented as follows:

When the offset direction is on the right side of line AO' (i.e. $\psi_A - 90^\circ < a \leq 90^\circ + \psi_A$), the range of $180^\circ - a$ is $90^\circ - \psi_A \leq 180^\circ - a < 270^\circ - \psi_A$, satisfying the condition of Eq. (5.8). Thus, the critical radius can be calculated by Eq. (5.9).

$$r_A = l_a \times \cos(a - \psi_A - \delta_{eff}) + r_{A,ideal} \quad \psi_A - 90^\circ < a \leq 90^\circ + \psi_A \quad (5.9)$$

Similarly, when the offset direction is on the left side of line AO' (i.e. $90^\circ + \psi_A < a \leq 270^\circ + \psi_A$), we can calculate the critical radius using Eq. (5.5), as expressed by Eq. (5.10).

$$r_A = -l_a \times \cos(a - \psi_A + \delta_{eff}) + r_{A,ideal} \quad 90^\circ + \psi_A < a \leq 270^\circ + \psi_A \quad (5.10)$$

Therefore, according to Eq. (5.5), Eq. (5.6), Eq. (5.9) and Eq. (5.10), for any point A on the reflector, the critical radius can be summarized as follows:

When point A is on the left half of the parabolic reflector (i.e. $x_A < 0$), the critical radius is given by Eq. (5.11).

$$r_{A,left} = \begin{cases} l_a \times \cos(a + \psi_A - \delta_{eff}) + r_{A,ideal} & -90^\circ - \psi_A < a \leq 90^\circ - \psi_A \\ -l_a \times \cos(a + \psi_A + \delta_{eff}) + r_{A,ideal} & 90^\circ - \psi_A < a \leq 270^\circ - \psi_A \end{cases} \quad (5.11)$$

When point A is on the right half of the parabolic reflector (i.e. $x_A > 0$), the critical radius is given by Eq. (5.12).

$$r_{A,right} = \begin{cases} l_a \times \cos(a - \psi_A - \delta_{eff}) + r_{A,ideal} & \psi_A - 90^\circ < a \leq 90^\circ + \psi_A \\ -l_a \times \cos(a - \psi_A + \delta_{eff}) + r_{A,ideal} & 90^\circ + \psi_A < a \leq 270^\circ + \psi_A \end{cases} \quad (5.12)$$

Eq. (5.11) and Eq. (5.12) are the formulas of critical radius for any point on the reflector under the condition of only absorber alignment error. In practice, there are other two optical errors deflecting the reflected optical cone: tracking error and slope error. Therefore, based on Eq. (5.11) and Eq. (5.12), the critical radius under the condition that tracking error, slope error and absorber alignment error exist simultaneously is further derived as follows.

As presented in Section 4.3.1, the coupling effect of tracking error and slope error for any point on the reflector can be represented by an equivalent deflecting error (b) which is equal to the tracking error minus double the slope error (i.e. $b = b_{tr} - 2b_{sl}$) (as shown in Fig. 4.9). All the three cases for calculating the critical radius for any point on the reflector under the condition of coexistence of all the optical errors are displayed Fig.

5.4. The three cases are detailed as follows:

Case 1: The offset direction ($O'O''$) is between AC and AC' , as shown in Fig. 5.4(a).

Case 2: The offset direction ($O'O''$) is on the right side of AC' , as shown in Fig. 5.4(b).

Case 3: The offset direction ($O'O''$) is on the left side of AC , as shown in Fig. 5.4(c).

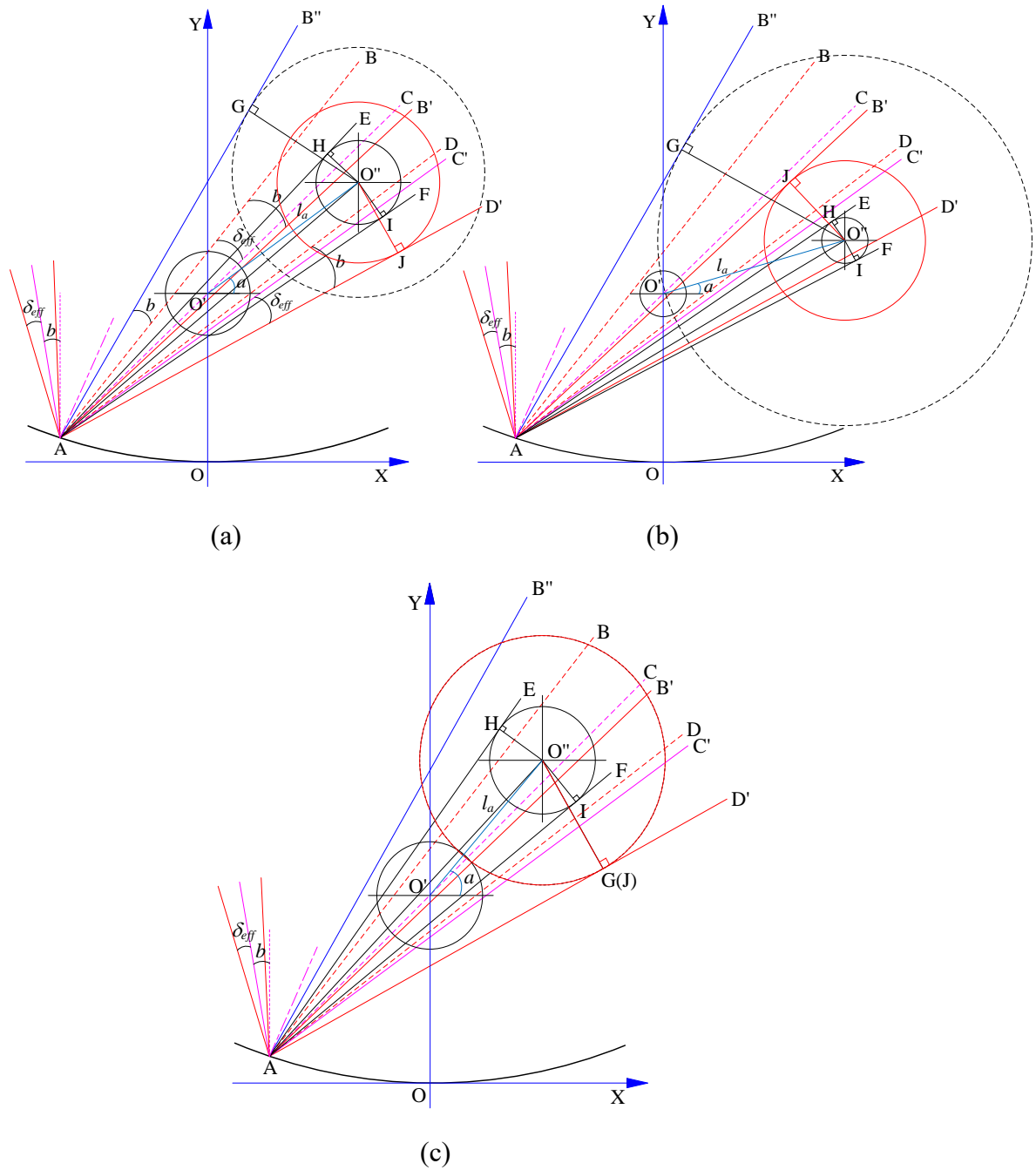


Fig. 5.4 Three cases for calculating the critical radius for any point on the reflector

As Fig. 5.4 shows, point A is any point on the left half of the parabolic reflector (i.e. $x_A \leq 0$). Given the symmetry of parabola, only the derivation process under the condition that the equivalent deflecting error (b) is on the left side of the vertical direction is conducted here. In Fig. 5.4, point O' is the focus of the parabola, and the

absorber tube is installed away from the focal line with an offset distance (l_a) and an offset angle (a). $\angle B'AD'$ is the actual reflected optical cone under the condition of equivalent deflecting error and $\angle BAD$ is the reflected optical cone formed without equivalent tracking error. AC' and AC are the centerlines of $\angle B'AD'$ and $\angle BAD$ respectively.

From Fig. 5.4, the following relations can be easily obtained:

$$\angle BAC = \angle CAD = \angle B'AC' = \angle C'AD' = \delta_{eff} \quad (5.13)$$

$$\angle BAB' = \angle CAC' = \angle DAD' = b \quad (5.14)$$

On the opposite side (i.e. left side) of the reflected cone, an auxiliary line (AB'') which makes $\angle B''AB$ equal to the equivalent deflecting error (i.e. $\angle B''AB = b$) is drawn to facilitate the derivation. Thus the following relation can be obtained:

$$\angle B''AC = \angle CAD' = \delta_{eff} + b \quad (5.15)$$

Therefore, $\angle B''AD'$ can be viewed as the reflected optical cone formed by a solar disk with a radial size angle of $\delta_{eff} + b$ under the condition of no deflecting error. In this case, the radius ($O''G$) of the black dotted circle in the figure is exactly the critical radius under the condition of only absorber alignment error for the solar disk size of $\delta_{eff} + b$. Mathematical formulas of the critical radius for any point under the condition of absorber alignment error have been obtained above by Eq. (5.11) and Eq. (5.12).

Therefore, using $\delta_{eff} + b$ replacing δ_{eff} in Eq. (5.11) and Eq. (5.12), the radius ($O''G$) of the black dotted circle can be expressed by Eq. (5.16) and Eq. (5.17).

When point A is on the left half of the parabolic reflector (i.e. $x_A < 0$):

$$r_{dot,A,left} = \begin{cases} l_a \times \cos(a + \psi_A - \delta_{eff} - b) + r'_{A,ideal} & -90^\circ - \psi_A < a \leq 90^\circ - \psi_A \\ -l_a \times \cos(a + \psi_A + \delta_{eff} + b) + r'_{A,ideal} & 90^\circ - \psi_A < a \leq 270^\circ - \psi_A \end{cases} \quad (5.16)$$

When point A is on the right half of the parabolic reflector (i.e. $x_A > 0$):

$$r_{dot,A,right} = \begin{cases} l_a \times \cos(a - \psi_A - \delta_{eff} - b) + r'_{A,ideal} & \psi_A - 90^\circ < a \leq 90^\circ + \psi_A \\ -l_a \times \cos(a - \psi_A + \delta_{eff} + b) + r'_{A,ideal} & 90^\circ + \psi_A < a \leq 270^\circ + \psi_A \end{cases} \quad (5.17)$$

where $r'_{A,ideal}$ is calculated by substituting $\delta_{eff} + b$ for δ_{eff} in Eq. (5.1), and is given by Eq. (5.18).

$$r'_{A,ideal} = \left(\frac{x_A^2}{4f_c} + f_c \right) \cdot \sin(\delta_{eff} + b) \quad (5.18)$$

In Fig.5.4, the coordinates of point A and point O" are $(x_A, x_A^2/4f_c)$ and $(l_a \cos a, l_a \sin a + f_c)$ respectively. Thus the length of AO" is given by Eq. (5.19).

$$AO'' = \sqrt{(x_A - l_a \cos(a))^2 + (x_A^2/4f_c - l_a \sin(a) - f_c)^2} \quad (5.19)$$

Taking Case 1 (as shown in Fig. 5.4(a)) as an example, the calculation process of the real critical radius, which is exactly the radius (O"J) of the red circle in the figure, is given as follows:

$$\begin{aligned} r_A &= O''J = AO'' \cdot \sin \angle O''AD' \\ &= AO'' \cdot \sin(\angle B''AD' - \angle B''AO'') \\ &= AO'' \cdot \sin\left(2b + 2\delta_{eff} - \arcsin\left(\frac{r_{dot,A}}{AO''}\right)\right) \\ &= AO'' \cdot \left[\sin(2b + 2\delta_{eff}) \cos\left(\arcsin\left(\frac{r_{dot,A}}{AO''}\right)\right) - \cos(2b + 2\delta_{eff}) \sin\left(\arcsin\left(\frac{r_{dot,A}}{AO''}\right)\right) \right] \\ &= AO'' \cdot \left[\sqrt{1 - \left(\frac{r_{dot,A}}{AO''}\right)^2} \cdot \sin(2b + 2\delta_{eff}) - \frac{r_{dot,A}}{AO''} \cdot \cos(2b + 2\delta_{eff}) \right] \end{aligned}$$

$$= \sqrt{AO^2 - r_{dot,A}^2} \cdot \sin(2b + 2\delta_{eff}) - r_{dot,A} \cdot \cos(2b + 2\delta_{eff})$$

Combined with Eq. (5.16), Eq. (5.17) and Eq. (5.19), the critical radius for point A in

Case 1 can be calculated and expressed by Eq. (5.20).

$$\begin{cases} r_{A,left} = \sqrt{AO^2 - r_{dot,A,left}^2} \cdot \sin(2b + 2\delta_{eff}) - r_{dot,A,left} \cdot \cos(2b + 2\delta_{eff}) & x_A \leq 0 \\ r_{A,right} = \sqrt{AO^2 - r_{dot,A,right}^2} \cdot \sin(2b + 2\delta_{eff}) - r_{dot,A,right} \cdot \cos(2b + 2\delta_{eff}) & x_A > 0 \end{cases} \quad (5.20)$$

Similarly, the critical radius for point A in Case 2 and Case 3 can be deduced, and given

by Eq. (5.21) and Eq. (5.22) respectively.

Case 2:

$$\begin{cases} r_{A,left} = r_{dot,A,left} \cdot \cos(2b) - \sqrt{AO^2 - r_{dot,A,left}^2} \cdot \sin(2b) & x_A \leq 0 \\ r_{A,right} = r_{dot,A,right} \cdot \cos(2b) - \sqrt{AO^2 - r_{dot,A,right}^2} \cdot \sin(2b) & x_A > 0 \end{cases} \quad (5.21)$$

Case 3:

$$\begin{cases} r_{A,left} = r_{dot,A,left} & x_A \leq 0 \\ r_{A,right} = r_{dot,A,right} & x_A > 0 \end{cases} \quad (5.22)$$

Since the critical radius is the required radius to receive all the reflected rays from the entire reflector, the maximum of the calculated critical radiuses for all point A on the reflector should be finally selected as the critical radius of the PTC, which is given by Eq. (5.23).

$$r_{a,c} = \max \left[\max \left(r_{A,left}, r_{A,right} \right) \right] \quad -0.5W_c \leq x_A \leq 0.5W_c \quad (5.23)$$

Therefore, the critical absorber diameter is expressed by twice the critical absorber radius, as given by Eq. (5.24).

$$d_{a,c} = 2 \times r_{a,c} \quad (5.24)$$

5.3 Algorithm development for optical efficiency

Fig. 5.5 shows the reflection process of sunrays, from which it can be seen that the sun can be viewed as consisting of countless line light sources that are parallel to the longitudinal direction (Z-axis direction) of the absorber. It can be easily understood that a line light source on the sun will also form a line light on the absorber tube after reflection. Therefore, if we can obtain the intensity of the line light source, the sunshape (brightness of the solar disk) can be expressed just by the radial angle of line light source (θ_l), which will reduce the computational complexity significantly.

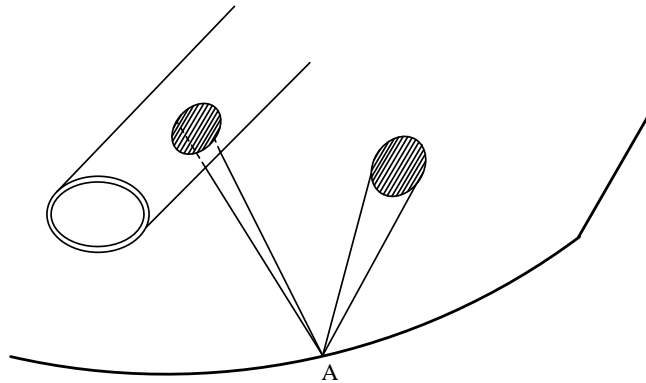


Fig. 5.5 The reflection process of sunrays

The derivation of the intensity of the line light source is given as follows:

Fig. 5.6 shows the schematic of the optical cone. In the figure, θ' is the radial angle of any point C on the line light source, $AO=l$, $AC=l'$, $\angle BAO=\theta_l$, $BC=\tau$, $d\tau$ is the length of the micro-element, $d\omega$ is solid angle of the micro-element.

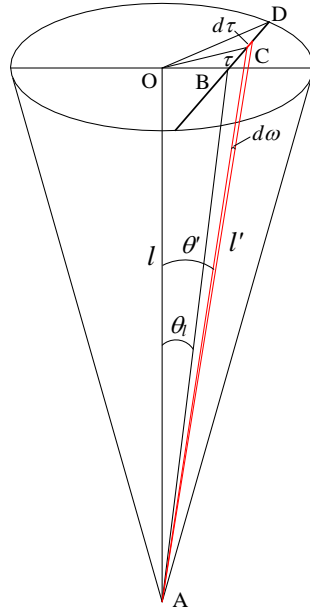


Fig. 5.6 Schematic for calculating the intensity of line light source

The intensity of the line light source can be calculated by Eq. (5.25).

$$\psi_{eff}(\theta_i) = 2 \times \int_{BD} \phi_{eff}(\theta') d\omega \quad (5.25)$$

where $\phi_{eff}(\theta')$ is the solar radiation intensity at any point on the line light source, calculated by Eq. (3.14).

In the figure, the following geometrical relationships can be obtained:

$$OB = AO \times \tan \theta_i = l \times \tan \theta_i \quad (5.26)$$

$$OC = \sqrt{OB^2 + BC^2} = \sqrt{(l \tan \theta_i)^2 + \tau^2} \quad (5.27)$$

In $\triangle AOC$, $\angle OAC$ can be calculated by Eq. (5.28).

$$\angle OAC = \arctan \frac{OC}{OA} = \arctan \frac{\sqrt{(l \tan \theta_i)^2 + \tau^2}}{l} \quad (5.28)$$

Considering that the radial angle of the optical cone is very small, the following relation is obtained:

$$l' = l \quad (5.29)$$

Thus,

$$d\omega = \frac{d\tau}{l} \quad (5.30)$$

Combining Eq. (5.25), Eq. (5.28) and Eq. (5.30), the intensity of line light source can be calculated by the following formula:

$$\psi_{eff}(\theta_l) = 2 \times \int_0^{\sqrt{(l \tan \delta_\Delta)^2 - (l \tan \theta_l)^2}} \phi_{eff} \left[\arctan \left(\frac{\sqrt{(l \tan \theta_l)^2 + \tau^2}}{l} \right) \right] \frac{d\tau}{l} \quad (5.31)$$

Make $\tau' = \frac{\tau}{l}$, Eq. (5.31) will be transformed to Eq. (5.32).

$$\psi_{eff}(\theta_l) = 2 \times \int_0^{\sqrt{(\tan \delta_\Delta)^2 - (\tan \theta_l)^2}} \phi_{eff} \left[\arctan \left(\sqrt{(\tan \theta_l)^2 + \tau'^2} \right) \right] d\tau' \quad (5.32)$$

Due to the small radial angle of the optical cone, the following relations are obtained:

$$\tan \theta_l = \theta_l, \quad \tan \delta_\Delta = \delta_\Delta$$

Consequently, Eq. (5.32) can be further simplified to Eq. (5.33).

$$\psi_{eff}(\theta_l) = 2 \times \int_0^{\sqrt{\delta_\Delta^2 - \theta_l^2}} \phi_{eff} \left(\sqrt{\theta_l^2 + \tau'^2} \right) d\tau' \quad (5.33)$$

Therefore, if the angle span between any two line light sources is expressed by $\Delta\theta_l$,

the energy bounded can be calculated by Eq. (5.34).

$$\Phi(\Delta\theta_l) = \int_{\Delta\theta_l} \psi_{eff}(\theta_l) d\theta_l \quad (5.34)$$

There are totally two situations, as shown in Fig. 5.7, for calculating the energy intercepted by the absorber tube under coexistence of all the optical errors:

Case 1: The offset direction (O'O") is on the right side of AC, as shown in Fig. 5.7(a).

Case 2: The offset direction (O'O") is on the left side of AC, as shown in Fig. 5.7(b).

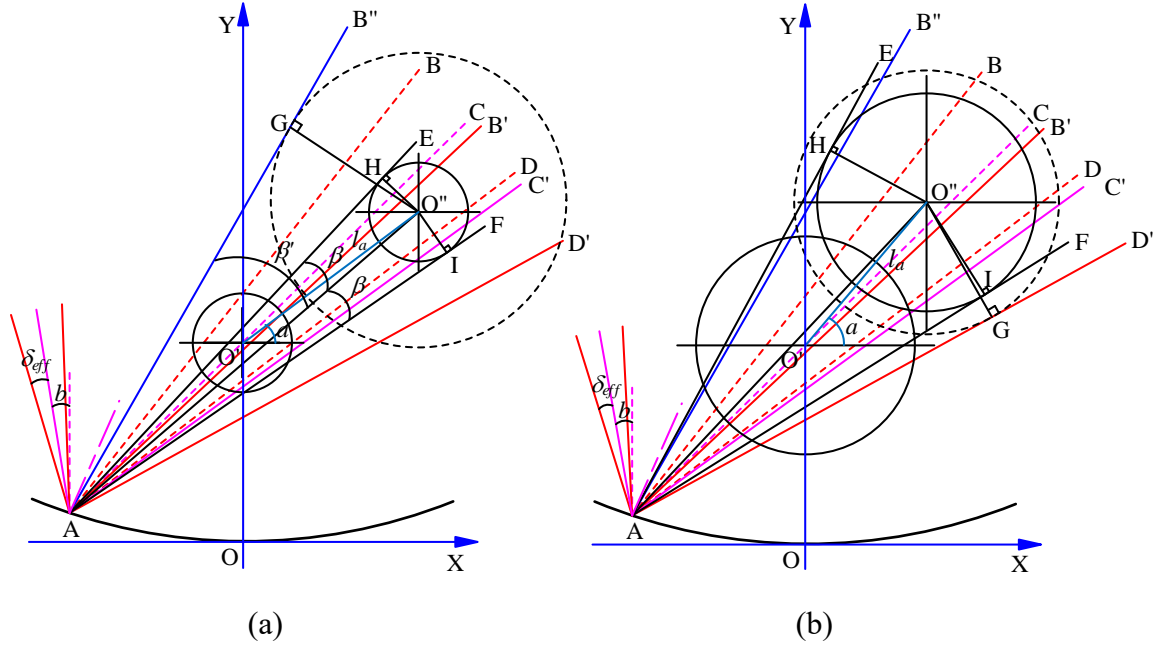


Fig. 5.7 Schematic for calculating the energy intercepted by the absorber tube

Taking Case 1 as an example (shown in Fig. 5.7(a)), we present the detailed procedures for calculating the energy intercepted by the absorber tube as follows:

In Fig. 5.7(a), $\angle EAO''$ (β) and $\angle B''AO''$ (β') are the angles in the reflected optical cone corresponding to the actual absorber tube radius and the black dotted circle radius respectively. Obviously, β and β' can be calculated by Eq. (5.35) and Eq. (5.36) respectively.

$$\beta = \arcsin\left(\frac{r_{a,o}}{AO''}\right) \quad (5.35)$$

$$\beta' = \arcsin\left(\frac{r_{dot}}{AO''}\right) \quad (5.36)$$

where $r_{a,o}$ is the outer radius of the absorber tube, r_{dot} and AO'' are calculated by Eq. (5.16) ~ Eq. (5.19).

It is clearly seen from Fig. 5.7(a) that the energy intercepted by the absorber tube can

be calculated by Eq. (5.37) based on Eq. (5.34).

$$\Phi = \int_{-\angle C'AF}^{\angle C'AE} \psi_{eff}(\theta_l) d\theta_l \quad (5.37)$$

The angle span intercepted by the absorber tube in this case is calculated as follows:

$$\angle C'AF = \angle B'AF - \angle B'AC' = (\angle B'AO' + \angle O'AF) - (\angle B'AB' + \angle B'AC') \quad (5.38)$$

Combined with Eq. (5.13) ~ Eq. (5.15), the following formulas are obtained:

$$\angle C'AF = (\beta' + \beta) - (2b + \delta_{eff}) \quad (5.39)$$

$$\angle C'AE = \angle EAF - \angle C'AF = 2\beta - [(\beta' + \beta) - (2b + \delta_{eff})] = 2b + \delta_{eff} + \beta - \beta' \quad (5.40)$$

Therefore, combining Eq. (5.37), Eq. (5.39) and Eq. (5.40), the energy intercepted by the absorber tube in Case 1 is calculated by Eq. (5.41).

$$\Phi = \int_{2b + \delta_{eff} - \beta - \beta'}^{2b + \delta_{eff} + \beta - \beta'} \psi_{eff}(\theta_l) d\theta_l \quad (5.41)$$

Similarly, the formula for calculating the energy intercepted by the absorber tube in Case 2 can be derived and given by Eq. (5.42).

$$\Phi = \int_{\beta' - \beta - \delta_{eff}}^{\beta' + \beta - \delta_{eff}} \psi_{eff}(\theta_l) d\theta_l \quad (5.42)$$

Eq. (5.41) and Eq. (5.42) are the formulas for calculating the energy intercepted by the absorber tube under the condition that the incident angle is zero. Therefore, further derivation is needed for incident angle larger than zero. The end loss caused by non-zero incident angle without optical errors is calculated by Eq. (4.8). Since the absorber alignment error in practice is usually very small, $\angle HAF$ can be viewed as equal to the incident angle under optical error conditions. Therefore, the ratio of the absorber length that receives the reflected rays to the total length of the absorber, defined as end loss factor, can be expressed by Eq. (5.43).

$$\xi = 1 - \frac{AH \cdot \tan \theta_{in}}{L_c} \quad (5.43)$$

where AH is equal to AO", calculated by Eq. (5.19).

Combined with the cosine loss (Eq. (4.7)), Eq. (5.41) and Eq. (5.42), for any point on the reflector, the energy intercepted by the absorber tube can be finally expressed by Eq. (5.44) and Eq. (5.45).

Case 1:

$$\Phi = \xi \cdot \cos \theta_{in} \cdot \int_{2b+\delta_{eff}-\beta-\beta'}^{2b+\delta_{eff}+\beta-\beta'} \psi_{eff}(\theta_l) d\theta_l \quad (5.44)$$

Case 2:

$$\Phi = \xi \cdot \cos \theta_{in} \cdot \int_{\beta'-\beta-\delta_{eff}}^{\beta'+\beta-\delta_{eff}} \psi_{eff}(\theta_l) d\theta_l \quad (5.45)$$

Consequently, for the whole reflector, the total energy intercepted by the absorber tube can be calculated by Eq. (5.46).

$$E = \int_{-W_c/2}^{W_c/2} \Phi dx_A \quad (5.46)$$

Therefore, the intercept factor (γ) and the optical efficiency (η_o) of the PTC can be calculated by Eq. (5.47) and Eq. (5.48) respectively.

$$\gamma = \frac{E}{2 \times \int_{-W_c/2}^{W_c/2} \int_0^{\delta_{eff}} \psi_{eff}(\theta_l) d\theta_l dx_A} \quad (5.47)$$

$$\eta_o = \gamma \times \rho_r \times \tau_g \times \alpha_a \times 100\% \quad (5.48)$$

From Eq. (5.48), it can be found that when the intercept factor is 1 (i.e. $\gamma=1$), the maximum optical efficiency ($\eta_{o,max}$) will be obtained as follows:

$$\eta_{o,max} = 1 \times 0.93 \times 0.95 \times 0.96 \times 100\% = 84.816\%$$

5.4 Results and discussion

This section first compares the proposed algorithm with the MCRT in terms of both results' accuracy and computing time to reveal the advantage of the proposed algorithm. And then, based on the developed algorithm, the effective solar radial size is discussed for purpose of engineering application. Finally, the changing properties of optical efficiency obtained by MCRT in the preceding chapter are expounded using the theoretical results.

5.4.1 Algorithm validation and analysis

To validate the proposed algorithm, the results obtained by the algorithm and the MCRT method were compared. Eight cases in Table 5.1 were used for comparison and validation. The incident angles of the first six cases were zero, while those of the last two cases were 45° and 30° respectively. Case I and Case II used the uniform sunshape model, and Case III and Case IV adopted the Gaussian sunshape model with a standard deviation of 3mrad ($\sigma_{sun}=3\text{mrad}$). Case V, Case VI, Case VII and Case VIII were conducted based on Buie's sunshape model with CSR of 0.1 (CSR=0.1). Case I, Case III, Case V and Case VII used the same set of optical errors, and Case II, Case IV and Case VI and Case VIII adopted another same set of optical errors. The slope error in Table 5.1 was determined in two methods: kept constant at 1.5mrad (Case I, Case III, Case V and Case VII) and generated by Gaussian model with a standard deviation of

3mrad (Case II, Case IV, Case VI and Case VIII).

Table 5.1 Cases for algorithm comparison and validation

Cases	Sunshape	Specularity error	Slope error	Tracking error	Absorber alignment error	Incident angle
I	Uniform $\delta=4.65$ mrad	$\sigma_{sp}=5$ mrad	$b_{sl}=1.5$ mrad	$b_{tr}=8$ mrad	$l_a=0.04$ m $a=\pi/4$	0
II		$\sigma_{sp}=3$ mrad	$\sigma_{sl}=3$ mrad	$b_{tr}=5$ mrad	$l_a=0.07$ m $a=\pi/2$	
III	Gaussian $\sigma_{sun}=3$ mrad	$\sigma_{sp}=5$ mrad	$b_{sl}=1.5$ mrad	$b_{tr}=8$ mrad	$l_a=0.04$ m $a=\pi/4$	0
IV		$\sigma_{sp}=3$ mrad	$\sigma_{sl}=3$ mrad	$b_{tr}=5$ mrad	$l_a=0.07$ m $a=\pi/2$	
V	Buie's model CSR=0.1	$\sigma_{sp}=5$ mrad	$b_{sl}=1.5$ mrad	$b_{tr}=8$ mrad	$l_a=0.04$ m $a=\pi/4$	0
VI		$\sigma_{sp}=3$ mrad	$\sigma_{sl}=3$ mrad	$b_{tr}=5$ mrad	$l_a=0.07$ m $a=\pi/2$	
VII	CSR=0.1	$\sigma_{sp}=5$ mrad	$b_{sl}=1.5$ mrad	$b_{tr}=8$ mrad	$l_a=0.04$ m $a=\pi/4$	45°
VIII		$\sigma_{sp}=3$ mrad	$\sigma_{sl}=3$ mrad	$b_{tr}=5$ mrad	$l_a=0.07$ m $a=\pi/2$	30°

The optical efficiencies obtained by the proposed algorithm and the MCRT for those eight cases were summarized in Table 5.2. It is clearly seen from Table 5.2 that the results obtained by the proposed algorithm agreed very well with the results obtained by MCRT. The maximum optical efficiency difference was 1.11% and the average was about 0.55%. This indicates that the algorithm and the MCRT can be mutually validated.

From the table, it can be found that the optical efficiency obtained by the proposed

algorithm was always smaller than that obtained by MCRT. This is because the proposed algorithm only calculates the reflected rays, while the MCRT takes into account the sunrays incident directly onto the absorber tube outer surface. Comparing the results for Case I, Case III and Case V, it can be seen that the effect of the sunshape model was obvious. The optical efficiency achieved by the proposed algorithm in Case I was 79.86%, which was much larger than that obtained in Case III and Case V, which were 70.88% and 70.38% respectively. This demonstrates that the uniform sunshape model results in overestimation of the PTC's performance, which will be discussed in the following section. The results of Case III and Case V were almost the same, indicating that the effects of the Gaussian model with a standard deviation of 3 mrad are similar to the effects of Buie's model with CSR of 0.1 under the condition of optical errors given in the Table 5.1. It is easily understood that changing the standard deviation (σ_{sun}) of the Gaussian model or changing the CSR of Buie's model will result in different efficiencies. It can also be found from Table 5.2 that the optical efficiencies produced in Case II, Case IV and Case VI were pretty close. This indicates that the effects of sunshape models are much slighter than the optical errors in those cases. Comparing Case V and Case VII, and Case VI and Case VIII, it can be easily found that the weakening effect of non-zero incident angle was remarkable.

Table 5.2 Comparison of optical efficiencies obtained by the MCRT and the proposed algorithm

Cases Method	I	II	III	IV	V	VI	VII	VIII
	MCRT	81.04%	38.02%	70.97%	38.43%	70.72%	37.89%	34.49%
Algorithm	79.93%	37.62%	70.88%	38.05%	70.38%	37.41%	33.78%	27.21%
$\Delta\eta_o$	1.11%	0.4%	0.09%	0.38%	0.34%	0.48%	0.71%	0.87%

It is proved from above comparison that the proposed algorithm has the same accuracy as the MCRT for calculating the optical efficiency. However, the required computing time of these two methods is completely different. The major factor influencing the computing time of MCRT is the number of used rays. As mentioned in Section 3.2.3, 5×10^7 rays were adopted for rays sampling in this study. The two main influencing factors for the proposed algorithm are the step size of the abscissa of point A (dx_A) and the step size of the radial angle of the line light source ($d\theta_l$). Considering that different sunshape models have different radial angular sizes and energy distributions, the step sizes for each sunshape model were also determined differently, as given in Table 5.3. In this study, a computer with the CPU of Intel Core i7-3770 (3.4 GHz) and the RAM of 8.0 GB was used. Taking Case I, Case III and Case V as examples, the required computing time for MCRT and the proposed method were presented in Table 5.3. It can be clearly seen from Table 5.3 that the computing time of the proposed algorithm was much smaller than the computing time of MCRT, indicating that the proposed algorithm

has a great advantage of saving time, and is very suitable for engineering application.

Table 5.3 Comparison of the computing time for MCRT and the proposed algorithm

Cases	I	II	III
	$dx_A=0.005$	$dx_A=0.005$	$dx_A=0.005$
Method	$d\theta_I=\delta/50$	$d\theta_I=4\sqrt{\sigma_{sun}^2 + \sigma_{sp}^2}/100$	$d\theta_I=\delta_\Delta/200$
MCRT	0.68 h	2.38 h	4.47 h
This algorithm	8.2 s	198.6 s	453.5 s

Note: ‘h’ represents ‘hours’, ‘s’ represents ‘seconds’.

5.4.2 Effective solar radial size

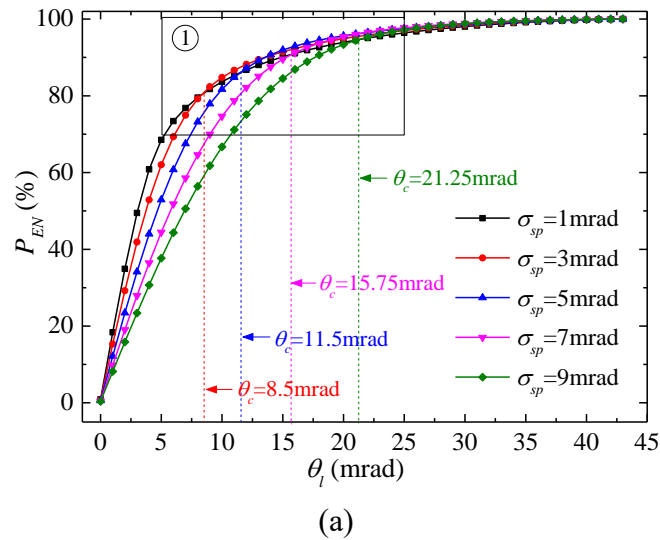
According to the sunshape model, it is easily found that the radiation intensity at any point on the sun decreases with the radial angle. As the radial angle is large enough, the radiation intensity will be negligible. Thus determining an appropriate radial angle, defined as effective solar radial size (δ_{eff}) in this paper, to represent the whole reflected solar profile is very important for engineering design and calculation. The total energy bounded by any angle span ($\Delta\theta_l$) in the reflected optical cone has been given by Eq. (5.34). Consequently, the ratio of the energy bounded by radial angle (θ_l) of any line light source to the total energy in the optical cone can be calculated by Eq. (5.49).

$$P_{EN}(\theta_l) = \frac{2 \times \int_0^{\theta_l} \psi_{eff}(\theta) d\theta}{2 \times \int_0^{\delta_\Delta} \psi_{eff}(\theta) d\theta} \quad (5.49)$$

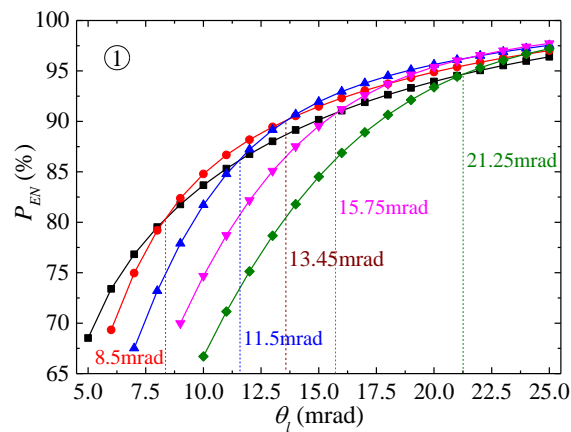
Fig. 5.8 depicts the variation of energy ratio (P_{EN}) bounded by any radial angle (θ_l) of line light source for different specular errors (σ_{sp}) in the case of CSR=0.5. Obviously, P_{EN} increased for all cases with the increase of θ_l and finally rose to near 100% as θ_l was large enough. It can be seen from the figure that when θ_l was small, the growth of P_{EN} for small σ_{sp} was faster than that for large σ_{sp} . For example, the energy ratio of 70% was achieved at the radial angle of 5.2 mrad for $\sigma_{sp}=1$ mrad, whereas a radial angle of 10.75 mrad was required to obtain the same energy ratio in the case of $\sigma_{sp}=9$ mrad. This indicates that more energy will be scattered into the circumsolar region under condition of larger specular errors. The figure also shows that when θ_l was larger than a certain value, defined as critical radial angle (θ_c) in this paper, P_{EN} for larger σ_{sp} was larger than P_{EN} for smaller σ_{sp} . For example, when θ_l was larger than 8.5 mrad, 11.5 mrad, 15.75 mrad and 21.25 mrad, P_{EN} for $\sigma_{sp}=3$ mrad, $\sigma_{sp}=5$ mrad, $\sigma_{sp}=7$ mrad and $\sigma_{sp}=9$ mrad were larger than P_{EN} for $\sigma_{sp}=1$ mrad. For more clarity, a partially enlarged view is shown in Fig. 5.8(b), which depicts clearly the critical radial angle (θ_c) for any couple of specular errors (σ_{sp}).

From the above analyses, it can be found that the radiant energy was distributed more uniformly in the case of larger specular errors. In practice, if the radial acceptance angle of the absorber tube is smaller than the critical radial angle of a certain couple of specular errors, the optical efficiency for the smaller specular error will be larger than the optical efficiency for the larger specular error. Otherwise, the optical efficiency for the smaller specular error will be smaller. From Fig. 5.8, it can also be found that if it is acceptable to use the radial angle that contains the energy ratio of 95%

to represent the whole solar profile, the effective radial sizes (δ_{eff}) of the reflected sunshape for $\sigma_{sp}=1$ mrad, $\sigma_{sp}=3$ mrad, $\sigma_{sp}=5$ mrad, $\sigma_{sp}=7$ mrad and $\sigma_{sp}=9$ mrad in the condition of CSR=0.5 were 21.75 mrad, 20.75 mrad, 18.75 mrad, 19.5 mrad and 21.5 mrad respectively. It can be found that the maximum δ_{eff} among the four discussed σ_{sp} was 21.75 mrad produced by $\sigma_{sp}=1$ mrad, demonstrating that higher optical quality reflector (i.e. small specularity error) does not always have better performance, which depends on the weather condition (i.e. the CSR).



(a)



(b)

Fig. 5.8 Variation of energy ratio bounded by radial angle of line light source under different specularity errors

Fig. 5.9 shows the variation of bounded energy ratio (P_{EN}) with radial angle (θ_l) of line light source for different CSRs in the case of $\sigma_{sp} = 5$ mrad. It is clearly seen from the figure that P_{EN} increased rapidly firstly and then grew slowly to 100% for all cases. The growth rate of P_{EN} for smaller CSR was greater than that for larger CSR. For example, the required radial angles for obtaining the energy proportion of 95% for CSR=0.1, CSR=0.3, CSR=0.5 and CSR=0.7 were 11.75mrad, 13.75mrad, 19.75mrad and 25.75mrad respectively. This indicates that larger effective radial sizes are required in the sites with more cloudy weather (i.e. larger CSR).

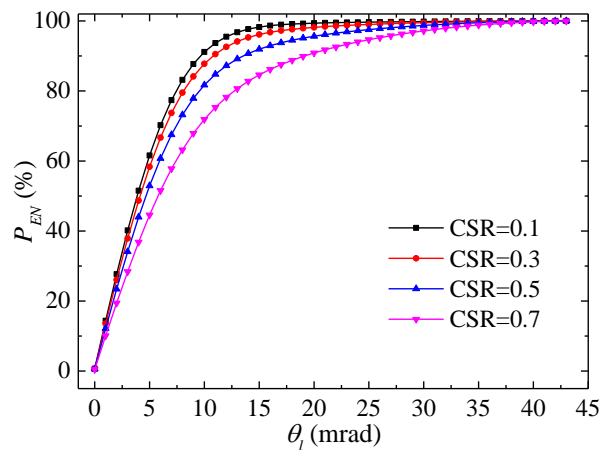


Fig. 5.9 Variation of energy ratio bounded by radial angle of line light source under different CSRs

In engineering practice, the solar disk with a radial angle of 4.65 mrad is used to represent the whole solar profile, which usually causes overestimation of the optical efficiency. Thus, this part discusses the energy ratio contained in the solar disk. Fig. 5.10 shows the variation of energy ratio (P_{EN}) contained in the solar disk ($\delta = 4.65$ mrad)

with specular error (σ_{sp}) under different CSRs. It shows clearly that P_{EN} decreased consistently with the increase of σ_{sp} , and the larger CSR resulted in smaller P_{EN} . The great difference of P_{EN} between different CSRs and σ_{sp} indicates that it is not feasible to use the solar disk as the representative solar size for all cases in practice. For example, the P_{EN} in the case of CSR=0.1 and $\sigma_{sp}=1$ mrad was 89.99%, whereas that in the case of CSR=0.4 and $\sigma_{sp}=1$ mrad was 73.73%, and that in the case of CSR=0.1 and $\sigma_{sp}=5$ mrad was just 58.20%. Obviously, if the solar disk is used to represent the whole solar profile, the optical performance of the PTC will be overestimated. For the situations that both the CSR and σ_{sp} are very small (i.e. little atmospheric scattering and high optical quality), it is acceptable to use the solar disk to represent the whole reflected sunshape, since the energy proportion (P_{EN}) is large enough in these cases. For example, the P_{EN} in the case of CSR=0.02 and $\sigma_{sp}=1$ mrad was 95.5% which is acceptable to be used to represent the whole solar profile.

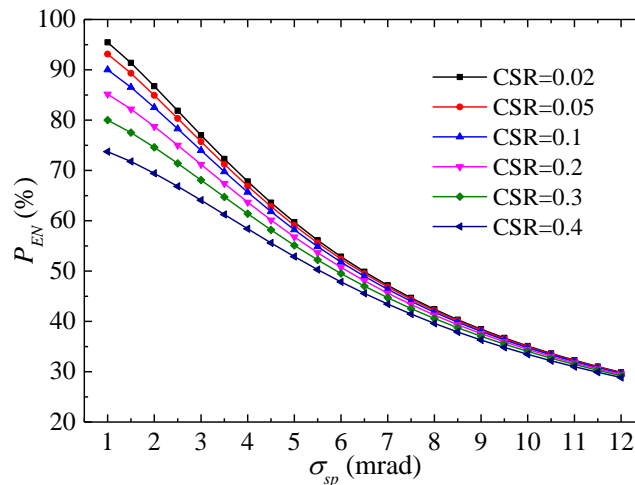


Fig. 5.10 Variation of energy ratio contained in the solar disk with specular error under different CSRs

5.4.3 Theoretical analysis of optical efficiency

As displayed in Fig. 4.15, the optical efficiency curves for two different specularity errors intersected at a certain CSR. When the CSR varied within a range less than the certain value, the η_o for smaller σ_{sp} was larger than the η_o for larger σ_{sp} . Whereas, if the CSR increased beyond the certain value, the η_o for smaller σ_{sp} would be smaller than that for larger σ_{sp} . For convenient analysis, Fig. 4.15 was copied here as the Fig. 5.11. For example, when the CSR was less than 0.47, the η_o for $\sigma_{sp}=1\text{mrad}$ were larger than the η_o for $\sigma_{sp}=7\text{mrad}$, whereas the η_o for $\sigma_{sp}=1\text{mrad}$ were smaller than the η_o for $\sigma_{sp}=7\text{mrad}$ in the case of CSR larger than 0.47.

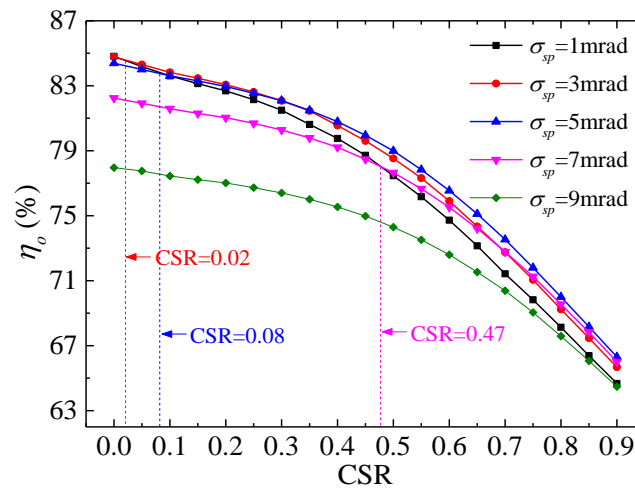


Fig. 5.11 Variation of optical efficiency with CSR under different specularity errors

The above phenomenon was just explained qualitatively in Section 4.4.1, and this part provides theoretical explanations as follows:

The radial acceptance angle (δ_a) of a PTC is defined as the radial angle in the reflected

cone that is intercepted by the absorber tube. The energy contained in the radial acceptance angle can be received by the absorber tube, while that outside the radial acceptance angle escape from the PTC. According to Eq. (5.1), the radial acceptance angle (δ_a) for any point A on the reflector can be calculated by Eq. (5.50).

$$\delta_a = \arcsin \left[\frac{d_a}{2 \cdot (x_A^2 / 4f_c + f_c)} \right] \quad (5.50)$$

The variation of the radial acceptance angle (δ_a) with the abscissa of point A (x_A) is depicted in Fig. 5.12. Given that the aperture width of LS-2 PTC module is 5 m, the maximum of x_A is 2.5. It can be found from the figure that δ_a decreased constantly with the increase of x_A . The maximum and minimum radial acceptance angles were 19.02 mrad (i.e. $\delta_{a,\max} = 19.02$ mrad) and 13.02 mrad (i.e. $\delta_{a,\min} = 13.02$ mrad) respectively.

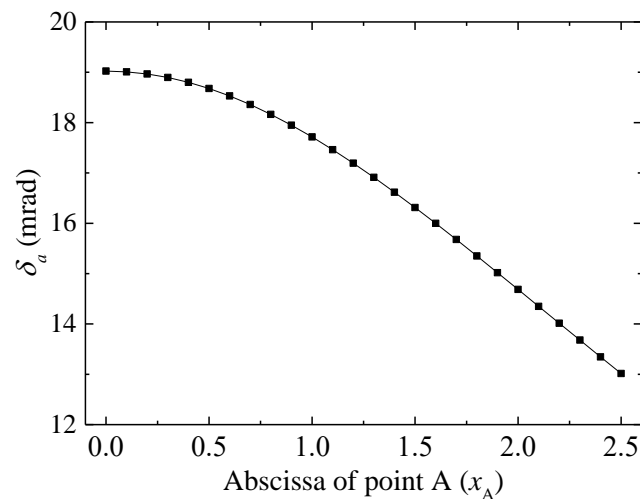


Fig. 5.12 Variation of the acceptance angle with the abscissa of point A

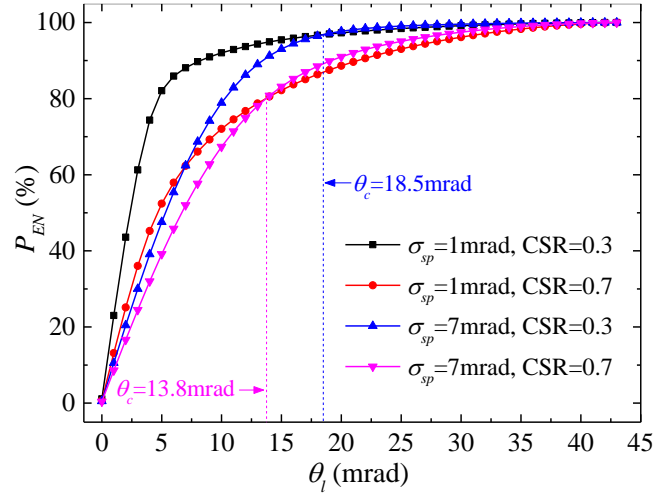


Fig. 5.13 Variation of energy ratio bounded by radial angle for $\sigma_{sp}=1$ mrad and $\sigma_{sp}=7$ mrad in the cases of CSR=0.3 and CSR=0.7

Taking two cases which are CSR=0.3 and CSR=0.7 as example, we compared the energy ratio (P_{EN}) bounded by different radial angles (θ_l) for two specularity errors which are $\sigma_{sp}=1$ mrad and $\sigma_{sp}=7$ mrad, as shown in Fig. 5.13. It can be seen from Fig. 5.13 that the critical radial angle (θ_c) for the two discussed specularity errors in the case of CSR=0.7 was 13.8 mrad, which means that when θ_l is larger than 13.8 mrad, the P_e for $\sigma_{sp}=7$ mrad will be larger than that for $\sigma_{sp}=1$ mrad. Since 13.8 mrad was just slightly larger than $\delta_{a,\min}$ ($\delta_{a,\min}=13.03$ mrad), the accepted energy for almost all the points on the reflector in the case of $\sigma_{sp}=7$ mrad was larger than the accepted energy in the case of $\sigma_{sp}=1$ mrad. Therefore, the optical efficiency (η_o) for $\sigma_{sp}=7$ mrad under the condition of CSR=0.7 was larger than that for $\sigma_{sp}=1$ mrad under the same CSR, as shown in Fig. 5.11. Similarly, the θ_c for the two discussed specularity errors in the case of CSR=0.3 was 18.5mrad, slightly smaller than $\delta_{a,\max}$ ($\delta_{a,\max}=19.02$ mrad), which means that the accepted energy for most of the points on

the reflector in the case of $\sigma_{sp}=1$ mrad was larger than the accepted energy in the case of $\sigma_{sp}=7$ mrad. Thus the η_o for $\sigma_{sp}=1$ mrad under the condition of CSR=0.3 was larger than that for $\sigma_{sp}=7$ mrad, as shown in Fig. 5.11.

Fig. 4.16 was copied as Fig. 5.14. The figure shows that η_o increased slowly firstly when σ_{sp} was small and then dropped quickly with further increasing σ_{sp} . The small growth of η_o for σ_{sp} varying in a small range can also be explained by the energy ratio (P_{EN}) bounded by different radial angles (θ_l). Taking CSR=0.5 as an example, the variation curves of P_{EN} for several specular errors (σ_{sp}) were plotted in Fig. 5.8. It can be found from Fig. 5.8 that the critical radial angles (θ_c) for $\sigma_{sp}=3$ mrad and $\sigma_{sp}=1$ mrad, and $\sigma_{sp}=5$ mrad were 8.5 mrad and 13.45 mrad respectively. Obviously, the former (8.5 mrad) is smaller than the minimum radial acceptance angle ($\delta_{a,\min}=13.02$ mrad) and the later (13.45 mrad) is just little bit larger than $\delta_{a,\min}$. This indicates that the total energy accepted by the absorber in the cases of $\sigma_{sp}=5$ mrad is more than that in the case of $\sigma_{sp}=3$ mrad which is larger than that in the case of $\sigma_{sp}=1$ mrad. Therefore, the growing optical efficiency is obtained when the specular error increases from 0 mrad to 5 mrad, as shown in Fig. 5.14. Similarly, the drop of optical efficiency in the case that the specular error is larger than 5 mrad can also be justified. In particular, we take $\sigma_{sp}=1$ mrad and $\sigma_{sp}=7$ mrad as example for detailed analysis. Fig. 5.8 shows that the θ_c for $\sigma_{sp}=1$ mrad and $\sigma_{sp}=7$ mrad was 15.75 mrad which is between $\delta_{a,\min}$ (13.02 mrad) and $\delta_{a,\max}$ (19.02 mrad). From Fig. 5.14, it can be found that the abscissa of point A corresponding to the radial acceptance angle of 15.75 mrad

was 1.65, which means that the accepted energy for $\sigma_{sp}=1$ mrad will be less for $x_A < 1.65$ and larger for $x_A > 1.65$ than the accepted energy for $\sigma_{sp}=7$ mrad. This indicates that the energy loss for $\sigma_{sp}=1$ mrad in the case of $x_A < 1.65$ will be compensated partially (or fully) by the energy increment in the case of $x_A > 1.65$, compared with the accepted energy for $\sigma_{sp}=7$ mrad. If fully compensated, the optical efficiency for $\sigma_{sp}=1$ mrad will be larger, otherwise it will be smaller. Fig. 16 shows that the η_o for $\sigma_{sp}=1$ mrad in the case of CSR=0.5 was 77.71%, slightly larger than the η_o , which was 77.65%, for $\sigma_{sp}=7$ mrad, demonstrating that the energy loss caused by $x_A < 1.65$ for $\sigma_{sp}=1$ mrad is completely compensated by the energy increment produced by $x_A > 1.65$. From above analyses, it can be found that the results obtained by MCRT are explained very well by the theoretical results, proving that the proposed algorithm and the MCRT are mutually validated by each other.

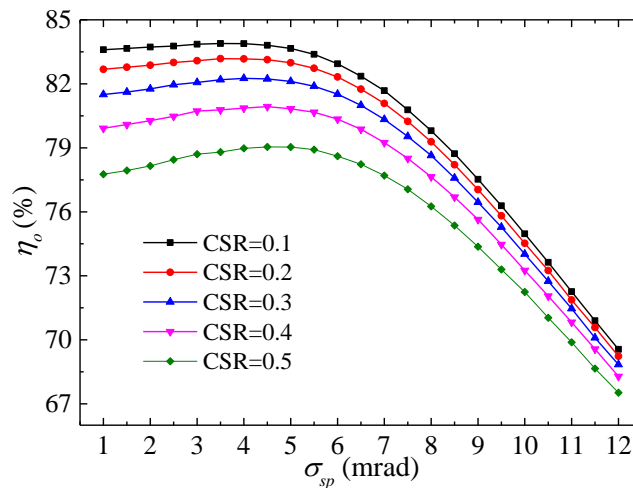
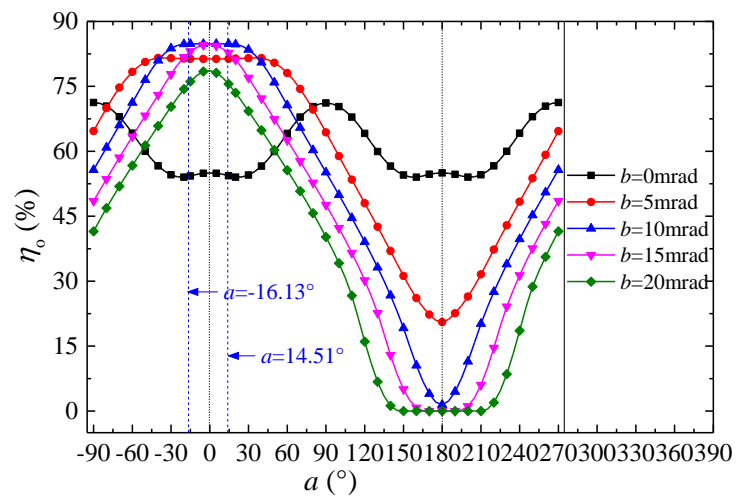


Fig. 5.14 Variation of optical efficiency with specularity error under different CSRs

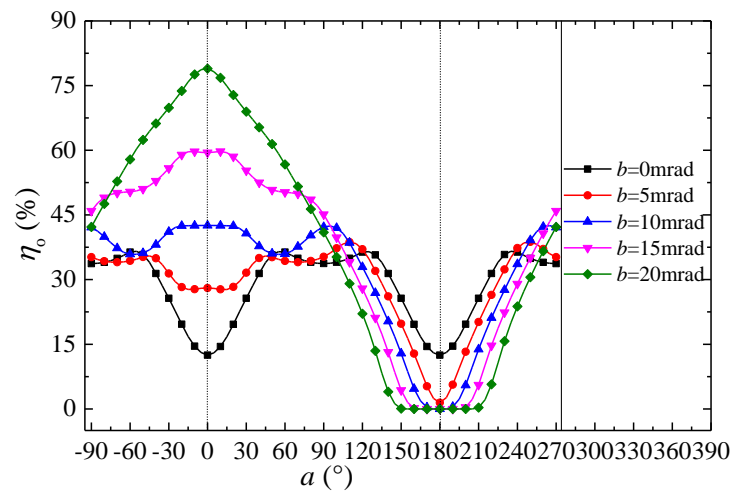
5.4.4 Coupling effects of optical errors

The results of coupling effects of absorber alignment error (a and l_a) and equivalent deflecting error (b) on the optical efficiency (η_o) are presented in Fig. 5.15. Note that the offset distances discussed in this part were 0.04 m (Fig. 5.15(a)) and 0.07 m (Fig. 5.15(b)), and the effective sunshape was CSR=0 and $\sigma_{sp}=0$. It can be seen from Fig. 5.15(b) that when there was no equivalent tracking error (i.e. $b=0$ mrad), the curve of η_o was symmetric about $a=90^\circ$ (i.e. Y-axis). As discussed in Section 4.4.3, because of the coupling effects (compensation effect or weakening effect) of absorber alignment error and equivalent deflecting error, η_o at $a=0^\circ$ in the case of $b \neq 0$ mrad were all larger than that obtained in the case of $b=0$ mrad. Meanwhile, η_o at $a=180^\circ$ in the case of $b \neq 0$ mrad were all smaller than that obtained in the case of $b=0$ mrad. Fig. 5.15 also shows clearly that when the absorber alignment error was in the same direction (from 90° to 270°) as the equivalent deflecting error (b), larger optical errors weakened more seriously the optical efficiency. It can be found from Fig. 5.15(a) that η_o at $a=0^\circ$ for $b=10$ mrad was the maximum ($\eta_{o,\max}=84.816\%$), whereas η_o for other deflecting errors at the same offset direction were all smaller. This demonstrates that the optical loss caused by the offset distance of 0.04 m in the direction of $a=0^\circ$ is completely compensated by the equivalent deflecting error of 10 mrad, and cannot be fully compensated by other equivalent deflecting errors. From Fig. 5.15(b), it can be found that the largest η_o at $a=0^\circ$ was obtained under the condition of $b=20$ mrad, which was just about 78.93%, smaller than the maximum ($\eta_{o,\max}=84.816\%$). This

indicates that the optical loss at $a=0^\circ$ caused by the offset distance of 0.07 m is only partially compensated by equivalent deflecting errors of less than 20 mrad. Therefore, it can be concluded from above analyses that there is an optimal range for absorber alignment error and equivalent deflecting error to completely compensate the optical loss caused by themselves.



(a)



(b)

Fig. 5.15 Variation of optical efficiency under different combinations of absorber alignment error and equivalent deflecting error: (a) $l_a=0.04$ m, (b) $l_a=0.07$ m

It can also be found from Fig. 5.15(a) that there was an offset angle range from -16.13° to 14.51° in which the optical efficiency (η_o) was kept at the maximum ($\eta_{o,max}=84.816\%$) under the condition of equivalent deflecting error of 10 mrad, whereas the optical efficiencies under other equivalent deflecting error conditions were all less than 84.816%. The reason is presented in Fig. 5.16 which shows the variation of the critical diameter ($d_{a,c}$) with offset angle (a) for different equivalent deflecting errors (b) under the condition of $l_a=0.04\text{m}$. It can be seen from Fig. 5.16 that when a was in the range between -16.13° and 14.51° , $d_{a,c}$ for $b=10\text{mrad}$ was less than the actual absorber outer diameter ($d_{a,o}=0.07\text{ m}$), perfectly avoiding rays-spillage, hence ensuring the maximum efficiency. The $d_{a,c}$ under other equivalent deflecting error conditions were all less than 0.07 m, leading to rays-spillage, thereby causing optical efficiencies less than the maximum. It can also be found from Fig. 5.16 that $d_{a,c}$ at $a=111.62^\circ$ and $a=248.38^\circ$ were the maximum under any equivalent deflecting error conditions. This indicates that $a=111.62^\circ$ and $a=248.38^\circ$ are the directions that will be most likely to cause rays-spillage. Considering that the rim angle of the adopted LS-2 PTC module is 68.38° ($\psi_{rim}=68.38^\circ$), when a is 111.62° or 248.38° , the offset direction (O'O") is perpendicular to the focus-edge connection line (i.e. O'M or O'N shown in Fig. 5.1) of the PTC. Therefore, it can be concluded that the offset direction which is in the same direction as the equivalent deflecting error and perpendicular to the focus-edge connection line of the PTC is the direction that will be most likely to cause rays-spillage. It can also be found from Fig. 5.16 that the critical diameter ($d_{a,c}$) for $a=0^\circ$ (positive X-axis direction) was the minimum under any equivalent deflecting error conditions,

which demonstrates that the offset direction that is along the X-axis and in the opposite direction of the equivalent deflecting error is the direction that will be least likely to cause rays-spillage.

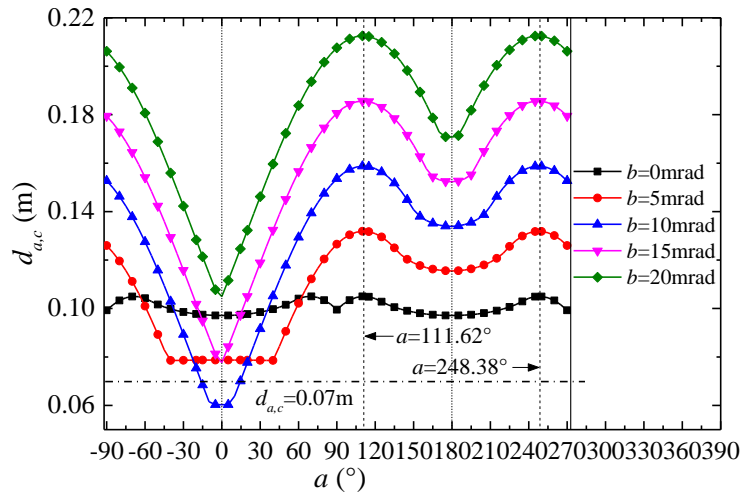


Fig. 5.16 Variation of critical diameter with offset angle under different equivalent deflecting errors ($l_a=0.04$ m)

5.5 Summary

This chapter conducted detailed theoretical analyses on the rays-concentrating process of the PTC under non-ideal optical conditions. The major work can be summarized as follows:

- (1) Based on the theory of spatial analytic geometry, the formulas of critical absorber diameter under any optical error conditions are derived. A new theoretical algorithm based on the idea of viewing the sun as consisting of countless line light sources is

developed for quick calculation of optical efficiency. It is proved that the proposed algorithm, compared with the MCRT, has great advantages of high accuracy and time saving, which is suitable for engineering application.

(2) The effective solar radial size is discussed based on the derived formulas and the proposed algorithm. It is revealed that the effective solar radial size depends on both the optical quality of the reflector and the weather condition. For the situations that both the circumsolar ratio and the specular error are very small (i.e. little atmospheric scattering and high optical quality), it is acceptable to use the solar disk to represent the whole reflected sunshape.

(3) The changing properties of optical efficiency achieved by the MCRT method are expounded using the theoretical results. For any couple of specular errors, there is usually a critical radial angle, of which the bounded energy ratios for the two specular errors are the same. In practice, if the radial acceptance angle of the PTC is smaller than the critical radial angle, the optical efficiency of the smaller specular error will be larger than that of the larger specular error. Otherwise, the optical efficiency of the smaller specular error will instead be smaller. The good agreement of the results between the MCRT and the proposed algorithm proves that the two methods are mutually validated by each other.

(4) The drop of optical efficiency caused by rays-spillage is well explained by the

critical absorber diameter calculated by the theoretically deduced formulas. For any point on the reflector, the offset direction which is in the same direction as the equivalent deflecting error and perpendicular to the focus-edge connection line is the direction that is most likely to cause rays-spillage. Whereas, the offset direction along the X-axis which is in the opposite direction of the equivalent deflecting error is the direction that is least likely to cause rays-spillage.

CHAPTER 6

THERMAL PERFORMANCE IMPROVEMENT USING UNILATERAL SPIRAL RIBBED ABSORBER TUBE FOR PARABOLIC TROUGH SOLAR COLLECTOR

6.1 Introduction

The thermal performance of the receiver tube is another important aspect of the overall performance of the PTC. As discussed in the preceding chapter, enhancing the heat transfer in the absorber tube can not only improve the thermal efficiency but also reduce the circumferential temperature difference effectively. Considering that the high heat flux is distributed on the part of the absorber tube facing to the reflector (i.e. the bottom part), enhancing the heat transfer between the bottom inner surface of the absorber tube and the fluid will improve significantly the thermal performance of the receiver tube. Therefore, this chapter proposes a novel receiver tube with spiral ribs laid on the bottom half inner surface of the absorber, named as unilateral spiral ribbed parabolic trough receiver (USR-PTR), to improve the thermal performance of the PTC.

The thermal performance of the conventional straight-smooth parabolic trough receiver (CSS-PTR) is first discussed, and then a comprehensive comparison between the USR-PTR and the CSS-PTR is conducted in terms of both thermal and hydraulic performances. The heat flux distribution obtained by the MCRT method is added as the

boundary condition on the absorber outer surface by User Defined Functions (UDF) to realize the simulation of heat transfer under actual conditions. According to the field synergy theory, the mechanism of thermal improvement of the USR-PTR is further analyzed. Moreover, based on the performance evaluation criteria (PEC), the influences of the rib's structural parameters, including pitch interval, rib height, corner radius, crest radius and spiral angle, on the overall performance of the USR-PTR are investigated comprehensively.

6.2 Introduction to the USR-PTR

6.2.1 Description of the USR-PTR

As shown in Fig. 6.1(a), the unilateral spiral ribbed parabolic trough receiver (USR-PTR) is designed by placing spiral ribs on the bottom half inner surface of the absorber tube. This new absorber can be made by rolling the sheet metal with inclined rib stripes embossed on the surface into a tube. The major parameters of the USR-PTR, including the inner and outer diameters of the absorber tube and glass envelope ($d_{a,i}$, $d_{g,i}$, $d_{a,o}$, $d_{g,o}$), the rib pitch interval (p), the rib height (Δh), the rib crest radius (R_{cr}), the rib corner radius (R_{co}) and the spiral angle (α_s), are displayed in Fig. 6.1(b). Note that the conventional straight and smooth parabolic trough receiver (CSS-PTR) used for comparison in this study is the SEGS LS-2 PTR, the diameters of the absorber tube and the glass envelope of the proposed USR-PTR are the same as that of the SEGS LS-2

PTR, as given in Table 3.1.

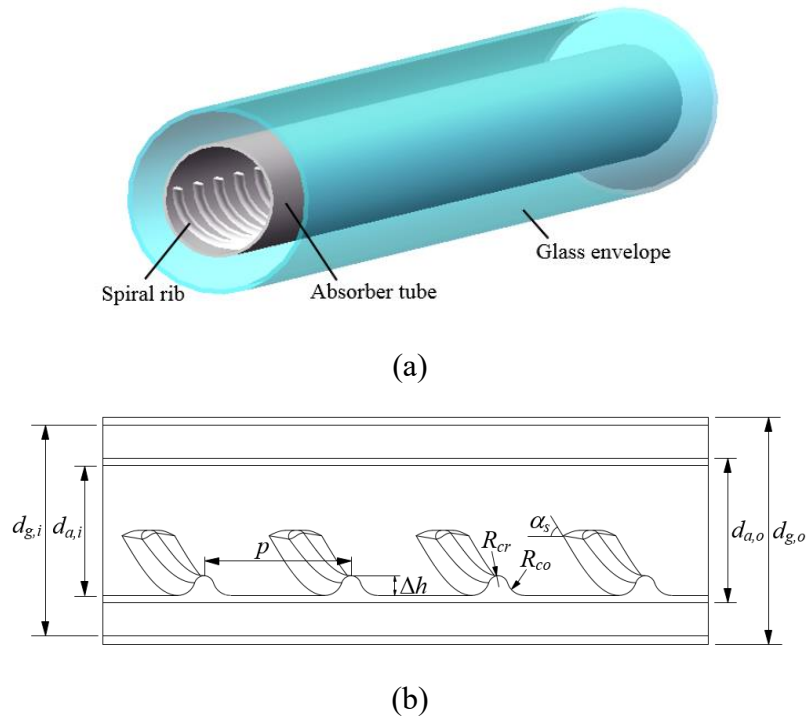


Fig. 6.1 Schematic of the USSR-PTR: (a) 3D model, (b) longitudinal section

6.2.2 Material properties

The heat transfer process in the receiver tube involves various materials, including metal, glass, heat transfer fluid (HTF) and air, the thermal property parameters of which have great effects on the results. The materials for the absorber tube and glass envelope used in this study are 321H stainless steel and high-borosilicate glass respectively, and their property parameters are listed in Table 6.1 [93]. The property parameters of air are also given in the table.

Table 6.1 Property parameters of materials [93]

Components	Density (kg/m ³)	Specific heat (J/kg·K)	Heat conductivity (W/m·K)	Dynamic viscosity (Pa·s)
Absorber tube	7900	470	0.0153T+10.6	---
Glass envelope	2230	900	1.2	---
Air	1.225	1006.43	0.0242	1.79×10 ⁻⁵

The emittance of the glass envelope is 0.86. The selective coating is the Luz Cermet, and its emittance in the temperature range between 300 K and 700 K is given by Eq. (6.1) [93].

$$\varepsilon_{coa} = 0.000327 \times T - 0.065971 \quad (6.1)$$

where T is the temperature of the material.

The HTF used in this study is the thermal oil Syltherm 800 and its thermal property parameters given in Table 6.2 [159].

Table 6.2 Thermophysical parameters of the HTF (Syltherm 800) [159]

Parameters	Formulas
Density (kg/m ³)	$\rho = -6.061657 \times 10^{-4} T^2 - 0.4153495 T + 1105.702$
Specific heat (J/kg·K)	$c_p = 1.708 T + 1.107798$
Heat conductivity (W/m·K)	$\lambda = -5.753496 \times 10^{-10} T^2 - 1.875266 \times 10^{-4} T + 0.190021$
Dynamic viscosity (Pa·s)	$\mu = 6.672331 \times 10^{-13} T^4 - 1.56003 \times 10^{-9} T^3 + 1.388285 \times 10^{-6} T^2 - 5.541277 \times 10^{-4} T + 0.08486612$

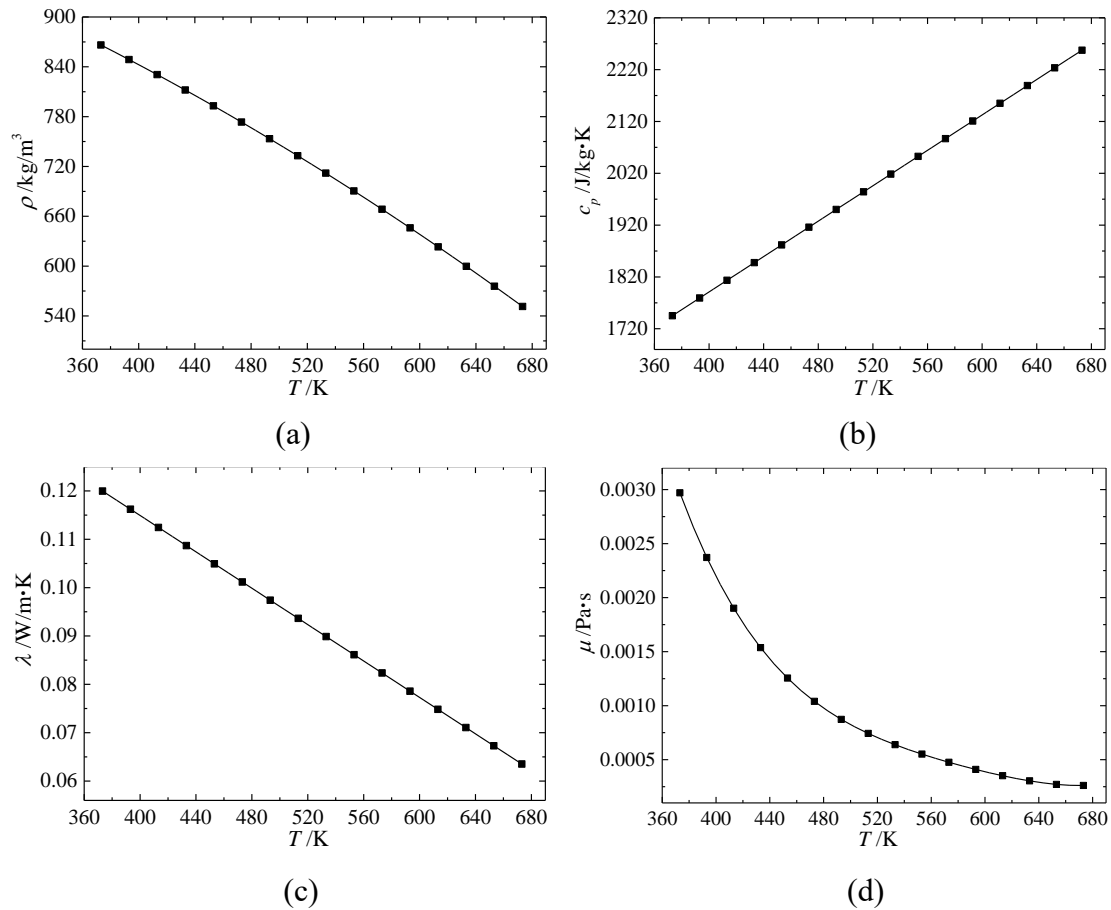


Fig. 6.2 Variation of thermophysical parameters of the HTF with temperature: (a) density, (b) specific heat, (c) conductivity, (d) dynamic viscosity

The variation of the thermophysical parameters of the HTF (Syltherm 800) with temperature is shown in Fig. 6.2. It can be seen from the figure that the specific heat increased constantly with the increase of temperature, and the other three parameters including density, heat conductivity and dynamic viscosity all decreased with increasing the temperature. The characteristics of thermophysical property changing with temperature of the HTF affect heat transfer in the receiver tube, which will be discussed in later sections.

6.3 Parameters for assessing the thermal performance of the PTR

6.3.1 Performance evaluation criteria (PEC)

Generally, irregular tubes enhance the heat transfer capacity at the expense of increasing obviously the pressure loss, due to the generation and extinction of more vortices and the constraints of special components such as fins and grooves. Therefore, both the heat transfer enhancement and the pressure loss should be considered for evaluating the overall performance of a new structured tube. The Nusselt number (Nu), representing the heat transfer capacity, and the friction factor (f), denoting the pressure loss, are given by Eq. (6.2) and Eq. (6.3) respectively.

$$Nu = \frac{q_u}{A_{a,i} (T_{a,i} - T_f)} \times \frac{d_{a,i}}{\lambda} \quad (6.2)$$

$$f = \frac{2(P_{in} - P_{out})d_{a,i}}{\rho V^2 L_a} \quad (6.3)$$

where T_f is the fluid average temperature, $A_{a,i}$ is the area of the absorber inner surface, $T_{a,i}$ is the average temperature of the absorber inner surface, V is the fluid average velocity, L_a is the length of the receiver tube, P_{in} and P_{out} are the inlet and outlet pressure respectively.

In this study, the CSS-PTR is used as the basis for assessing the performance of the proposed USR-PTR. Nu/Nu_0 and f/f_0 are used for assessing the heat transfer enhancement and pressure loss increase respectively. A performance evaluation

criterion (PEC) taking into account simultaneously the heat transfer enhancement and the pressure drop penalty is given by Eq. (6.4) [160, 161]. The PEC compares the heat transfer capacity between the USR-PTR and the CSS-PTR with the same pumping work, which can be used as the overall performance factor of the USR-PTR. When the PEC is more than 1, the overall performance of the USR-PTR is better than that of the CSS-PTR, otherwise poorer.

$$\text{PEC} = \frac{(Nu / Nu_0)}{(f / f_0)^{1/3}} \quad (6.4)$$

where Nu and Nu_0 are the Nusselt number for the USR-PTR and the CSS-PTR respectively, f and f_0 are the friction factor for the USR-PTR and the CSS-PTR respectively.

6.3.2 Field synergy theory

At the end of the 20th century, the field synergy theory was established for revealing the internal mechanism of convective heat transfer from the perspective of velocity field and heat flow field (i.e. temperature gradient field) [162, 163]. According to the field synergy theory, when the physical property, velocity, temperature difference of the fluid is kept constant, the better the synergy between the velocity field and the heat flow field, the better the heat transfer performance. The field synergy theory reveals theoretically the essential law of convective heat transfer, which unifies the existing single heat transfer enhancement theories and has universality. The concept of field synergy was first derived from the two-dimensional thermal boundary layer issues, which is given

as follows:

Energy equation:

$$\int_0^{\delta_t} \rho c_p (\mathbf{U} \cdot \nabla T) dy = -\lambda \left. \frac{\partial T}{\partial y} \right|_w \quad (6.5)$$

where δ_t is the thickness of the thermal boundary layer, \mathbf{U} is the fluid velocity vector.

Dimensionless processing:

$$\bar{\mathbf{U}} = \frac{\mathbf{U}}{U_\infty}, \quad \bar{\nabla T} = \frac{\nabla T}{(T_\infty - T_w) / \delta_t}, \quad \bar{y} = \frac{y}{\delta_t} \quad (6.6)$$

where T_w is the wall temperature, Therefore, the dimensionless relation can be obtained:

$$Nu = Re \cdot Pr \int_0^1 (\bar{\mathbf{U}} \cdot \bar{\nabla T}) d\bar{y} \quad (6.7)$$

where the integrating factor can be written by:

$$\bar{\mathbf{U}} \cdot \bar{\nabla T} = |\bar{\mathbf{U}}| \cdot |\bar{\nabla T}| \cdot \cos \beta_s \quad (6.8)$$

where β_s is the angle between the velocity vector and the temperature gradient, defined as the synergy angle.

It can be clearly seen from Eq. (6.7) that in addition to Re and Pr , the intensity of convective heat transfer also depends on the $\bar{\mathbf{U}} \cdot \bar{\nabla T}$, which is the degree of synergy between velocity field and heat flow field. According to Eq. (6.8), when the velocity and temperature difference are constant, the synergy angle (β_s) is the key factor determining the heat transfer performance. Obviously, the smaller the synergy angle is,

the better the heat transfer will be. This chapter will further reveal the mechanism of the heat transfer enhancement of the USR-PTR based on the field synergy theory.

In this study, the volumetric weighted average synergy angle was used for analysis, and calculated by the following equation.

$$\beta_s = \sum \frac{dV_i}{\sum dV_i} \cdot \beta_{s,i} \quad (6.9)$$

where the local synergy angle ($\beta_{s,i}$) is calculated by Eq. (6.10)

$$\beta_{s,i} = \arccos \left[\left(u_i \frac{dT_i}{dx} + u_j \frac{dT_i}{dy} + u_k \frac{dT_i}{dz} \right) / \left(\sqrt{u_i^2 + u_j^2 + u_k^2} \cdot \sqrt{\left(\frac{dT_i}{dx} \right)^2 + \left(\frac{dT_i}{dy} \right)^2 + \left(\frac{dT_i}{dz} \right)^2} \right) \right] \quad (6.10)$$

where u_i , u_j , u_k are the velocity components, dV_i is the volume of the i th control cell.

6.4 Numerical model and validation

6.4.1 Analysis of the heat transfer in the receiver tube

The heat transfer process in the receiver tube involves the coupling of conduction, convection and radiation, as shown in Fig. 6.3(a). The incoming solar energy (q_{solar}) that passes through the glass envelope is absorbed by the selective coating on the absorber outer surface, and then transmits in two directions: On one hand, some energy goes into the absorber inner surface by conduction ($q_{ao-ai,cond}$) and then is transferred to the HTF by convection ($q_{ai-f,conv}$). On the other hand, the remaining energy is

transferred to the glass envelope inner surface by conduction ($q_{ao-gi,cond}$), convection ($q_{ao-gi,conv}$) and radiation ($q_{ao-gi,rad}$), and then conducted through the glass envelope to the outer surface ($q_{gi-go,cond}$). Finally, the energy at the glass outer surface is lost to the ambient environment by convection ($q_{go-amb,conv}$) and radiation ($q_{go-sky,rad}$). Due to the vacuum state, both the conduction and the convection in the annulus are very small. Thus, the heat radiation dominates the heat transfer in the annulus space. For more clarity, the thermal resistance network is displayed in Fig. 6.3(b).

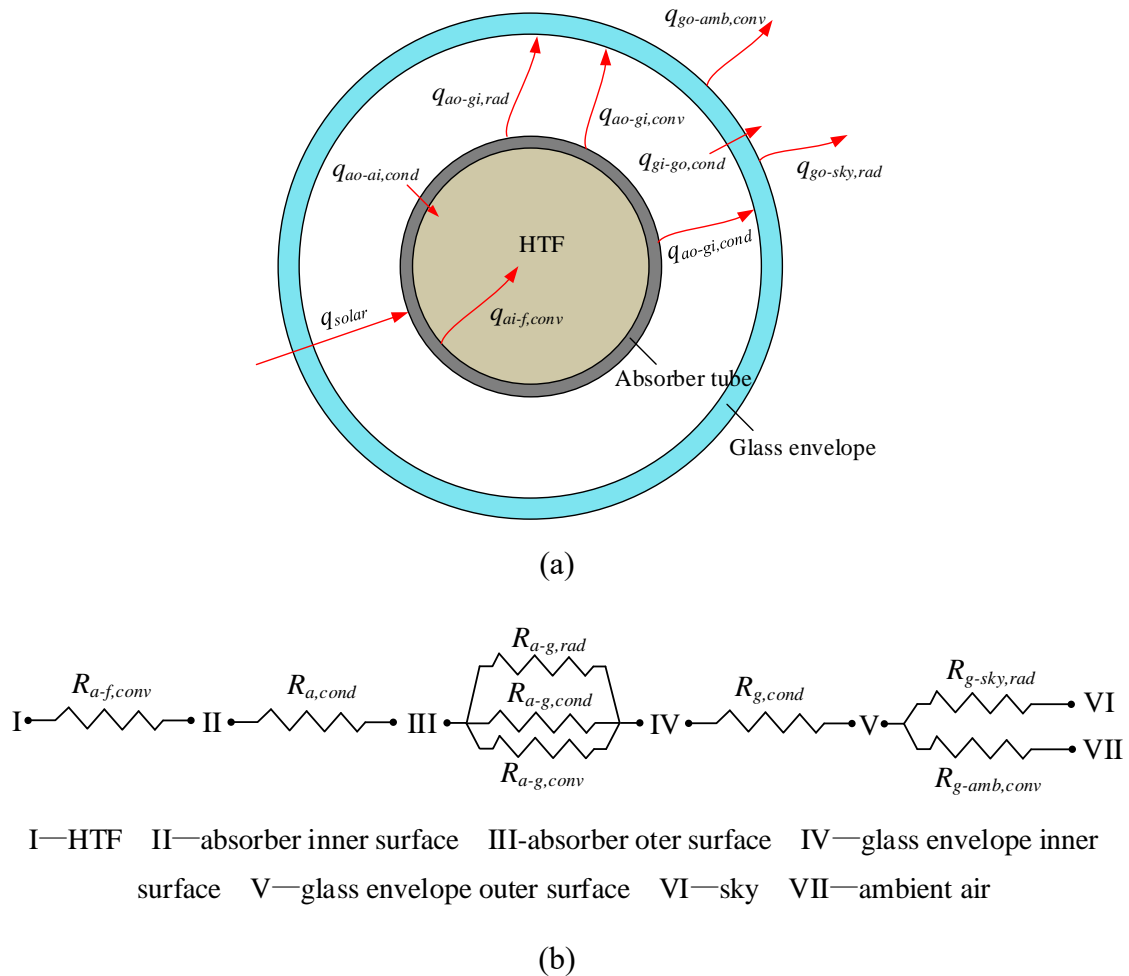


Fig. 6.3 Heat transfer in the cross section of the receiver tube: (a) heat transfer process, (b) thermal resistance network

Several important parameters were used to evaluate the performance of the PTC, as given as follows:

As Table 6.2 shows, the specific heat (c_p) is linearly dependent on temperature (T).

Thus, the useful energy (q_u) obtained by the HTF can be calculated by Eq. (6.11):

$$q_u = m \cdot \frac{c_{p,in} + c_{p,out}}{2} \cdot (T_{out} - T_{in}) \quad (6.11)$$

where m is the mass flow rate of the fluid, $c_{p,in}$ and $c_{p,out}$ are the average heat specific of the inlet and outlet fluid respectively, T_{in} and T_{out} are the average temperature of the inlet and outlet fluid respectively.

The optical efficiency is calculated by Eq. (6.12)

$$\eta_o = \frac{q_u + q_{loss}}{I_D \cdot W_c \cdot L_c} \quad (6.12)$$

where q_{loss} is the total heat loss of the receiver tube.

The thermal efficiency of the receiver tube is given by Eq. (6.13)

$$\eta_t = \frac{q_u}{q_u + q_{loss}} \quad (6.13)$$

Therefore, the collector efficiency is expressed by Eq. (6.14)

$$\eta_c = \eta_o \cdot \eta_t \quad (6.14)$$

6.4.2 Numerical model

The governing equations of continuity, momentum and energy can be given by Eq. (6.15) ~ Eq. (6.17).

Continuity equation:

$$\frac{\partial(\rho u_i)}{\partial x_i} = 0 \quad (6.15)$$

Energy equation:

$$\frac{\partial(\rho c_p T u_i)}{\partial x_i} = \frac{\partial}{\partial x_i} \left[\left(\lambda + \frac{\mu_t}{\sigma_t} \right) \frac{\partial T}{\partial x_i} \right] + S_r \quad (6.16)$$

Momentum equation:

$$\frac{\partial(\rho u_i u_j)}{\partial x_j} = -\frac{\partial p}{\partial x_i} + \frac{\partial}{\partial x_j} \left[(\mu + \mu_t) \left(\frac{\partial u_i}{\partial x_j} + \frac{\partial u_j}{\partial x_i} \right) - \frac{2}{3} (\mu + \mu_t) \frac{\partial u_i}{\partial x_i} \delta_{ij} - \frac{2}{3} \rho k \delta_{ij} \right] + \rho F_i \quad (6.17)$$

where p is the pressure, u_i and u_j are velocity components, S_r is the radiation source.

Due to the disturbance and deflection of the discontinuous spiral ribs, rotational flow and vortices will be generated, causing much more complicated turbulent flow than the straight smooth tube. Therefore, this study adopts the RNG $k - \varepsilon$ model, which has greater adaptability in simulating the spiral flow and secondary flow, to perform turbulence calculation. The k equation and the ε equation are given as follows:

The k equation:

$$\frac{\partial(\rho k u_i)}{\partial x_i} = \frac{\partial}{\partial x_i} \left[\left(\mu + \frac{\mu_t}{\sigma_k} \right) \frac{\partial k}{\partial x_i} \right] + G_k - \rho \varepsilon \quad (6.18)$$

The ε equation:

$$\frac{\partial(\rho \varepsilon u_i)}{\partial x_i} = \frac{\partial}{\partial x_i} \left[\left(\mu + \frac{\mu_t}{\sigma_\varepsilon} \right) \frac{\partial \varepsilon}{\partial x_i} \right] + c_1 \frac{\varepsilon}{k} G_k - c_2 \rho \frac{\varepsilon^2}{k} - R_\varepsilon \quad (6.19)$$

The last term (R_ε) in ε equation is the modification of the standard k - ε model, which makes the model more accurate in simulating rotational flow, secondary flow and separation flow, and it is calculated by Eq. (6.20).

$$R_\varepsilon = \frac{c_\mu \rho \zeta^3 (1 - \eta/4.38) \varepsilon^2}{1 + 0.012 \zeta^3} \frac{\varepsilon^2}{k} \quad (6.20)$$

where the time-average strain rate (ζ) is given by Eq. (6.21).

$$\zeta = \frac{k}{\varepsilon} \sqrt{\frac{1}{2} \left(\frac{\partial u_i}{\partial x_j} + \frac{\partial u_j}{\partial x_i} \right)} \quad (6.21)$$

The constants in the turbulence model are listed in Table 6.3 [164].

Table 6.3 Constants in the turbulence models [164]

c_1	c_2	c_μ	σ_k	σ_ε
1.42	1.68	0.0845	0.719	0.719

6.4.3 Boundary conditions and solution method

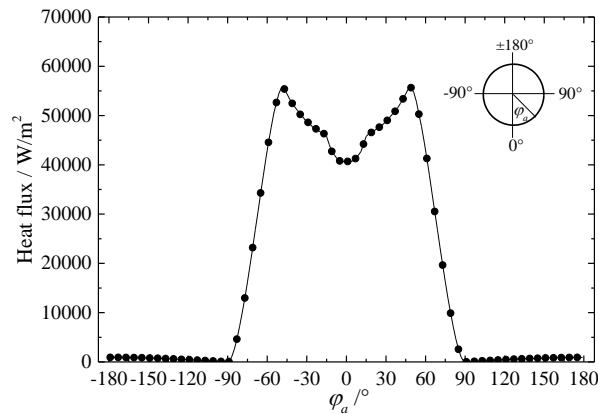
6.4.3.1 Boundary conditions

The boundary conditions were set as follows:

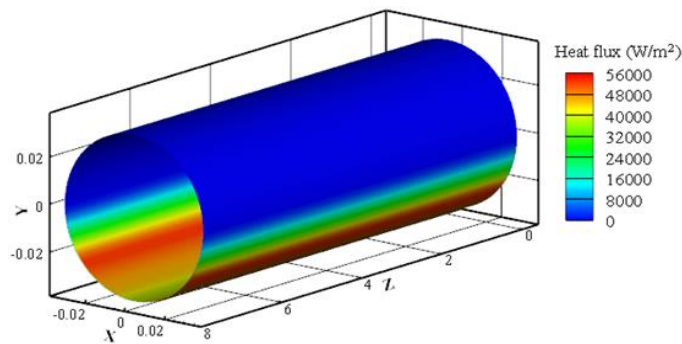
(1) Inlet: mass flow inlet, $m_{in} = m_z$, $m_x = m_y = 0$, $T_{in} = T$, $k_{in} = 1\% \cdot 0.5 \cdot \rho u_z^2$,
 $\varepsilon_{in} = c_{\mu} \rho k_{in}^2 / \mu_t$ [164].

Outlet: outflow and fully developed condition [164].

All the solid walls: No-slip boundary condition.



(a)



(b)

Fig. 6.4 Heat flux distribution on the absorber outer surface: (a) produced by MCRT,

(b) loaded by UDF

(2) The circumferential heat flux is calculated by the MCRT and loaded to the absorber

outer surface using UDF; Note that the thermal simulation conducted in this chapter is performed under ideal optical conditions (i.e. without any optical factors). The direct normal solar irradiance (I_D) used in this chapter is 1000 W/m². Fig. 6.4(a) and Fig. 6.4(b) shows respectively the heat flux distribution calculated by MCRT and that loaded by UDF. By comparing Fig. 6.4(a) and Fig. 6.4(b), it is clearly seen that the circumferential heat flux distribution depicted in the two figures were the same, which demonstrates that the developed UDF program is accurate.

(3) The radiation between the absorber outer surface and the glass inner surface is calculated by the Surface to Surface (S2S) model.

(4) The outer surface of the glass envelope is set as mixed boundary condition including convection between the surface and the ambient, and radiation between the surface and the sky. The convective heat transfer coefficient between the glass envelope outer surface and the ambient air is calculated by Eq. (6.22) [165], and the sky temperature is viewed as 8 K lower than the ambient temperature [93].

$$h_{g-amb} = 4V_{amb}^{0.58} d_{g,o}^{-0.42} \quad (6.22)$$

where h_{g-amb} is the convective heat transfer coefficient between the glass envelope outer surface and the ambient air, V_{amb} is the ambient wind velocity.

6.4.3.2 Solution method

The flow and heat transfer simulation is conducted using the FLUENT codes which are developed based on the Finite Volume Method (FVM). A UDF program is developed to describe the heat flux distribution calculated by the MCRT, and is then read by the FLUENT as the boundary condition. The SIMPLE algorithm is adopted to couple the pressure and velocity. The governing equations are discretized by second order upwind scheme. Given that the $k - \varepsilon$ turbulence model is not applicable in the vicinity of the pipe wall, the enhanced wall treatment is used to solve the flow and heat transfer close to the solid walls. Two criteria are used to guarantee the convergence of the solution: the maximum residual for all the equations are less than 10^{-6} , and the outlet temperature of the fluid remains constant for the last 1000 iterations.

6.4.4 Grid independence checking

The number of grid cells should be determined by considering both the results' precision and the computing time. Given the complex internal structure of the USR-PTR, unstructured grids are utilized in this study, and the total number of the cells in the grid is determined by setting respectively the size of the cells in each computational domain. The structural parameters of the USR-PTR used for grid independence checking is listed in Table 6.4. The mass flow rate is 2 kg/s and the inlet fluid temperature is 573.15 K. For simplification, this study adopts the receiver tube with the length of one meter as the research object.

Table 6.4 Parameters of the USR-PTR used for grid independence checking

p (mm)	Δh (mm)	R_{co} (K)	R_{cr} (mm)	α_s (°)
100	5	5	3	60

The results for grid independence checking is shown in Table 6.5. It can be seen from the table that when the number of grids was more than 1130000, the results of T_{out} , Nu and f all changed little. Therefore, the grid system with 1130000 cells was used in this study. The schematic of domain discretization (meshing) of the receiver tube is shown in Fig. 6.5.

Table 6.5 Results for grid independence checking

Grid system	T_{out} (K)	Nu	f
420000	576.44	997.97	0.07991
710000	575.56	995.84	0.08454
900000	574.75	992.28	0.08719
1130000	574.33	991.38	0.08838
1210000	574.37	991.45	0.08841
1570000	574.32	991.21	0.08837

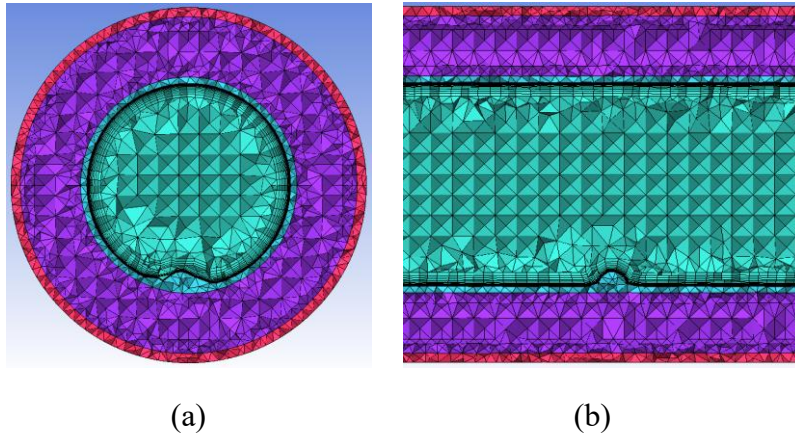


Fig. 6.5 Schematic of domain discretization (meshing): (a) transverse section, (b) longitudinal section

6.4.5 Model validation

As mentioned in previous chapters, the SEGS LS-2 PTC, which has been tested in the AZTRAK rotating platform by Sandia National Laboratories [77], is adopted as the prototype in this study. Six typical cases are selected from Ref. [77] for validation of the established models, as given in Table 6.6.

Table 6.6 Typical test data selected from Ref. [77] for model validation

Case	I_D (W/m ²)	m (kg/s)	V_{amb} (m/s)	T_{amb} (K)	T_{in} (K)	$T_{out,t}$ (K)
1	933.7	0.6782	2.6	294.35	375.35	397.15
2	937.9	0.6206	1.0	301.95	570.95	590.05
3	968.2	0.6536	3.7	295.22	424.15	446.45
4	813.1	0.7254	3.6	298.95	374.35	392.15
5	858.4	0.7207	3.1	300.75	427.45	444.85
6	896.4	0.664	0.9	303.15	523.85	540.95

The established models are validated by comparing the outlet temperature of the HTF between the simulation ($T_{out,s}$) and the test ($T_{out,t}$) under the conditions presented in Table 6.6. The relative deviation (e_T) is defined by Eq. (6.23).

$$e_T = \frac{|T_{out,s} - T_{out,t}|}{|T_{out,t} - T_{in}|} \times 100\% \quad (6.23)$$

The comparison results are given in Table 6.7. It can be found from the table that the simulation results agreed well with the test results. The maximum relative deviation of the outlet temperature was 11.01% and the average relative deviation was about 9.41%, demonstrating that the established models are reliable for simulating the flow and heat transfer in the receiver tube.

Table 6.7 Comparison of results between simulation and test

Case	T_{in} (K)	$T_{out,t}$ (K)	$T_{out,s}$ (K)	$ T_{out,t} - T_{in} $ (K)	$ T_{out,s} - T_{out,t} $ (K)	e_T (%)
1	375.35	397.15	399.55	21.8	2.4	11.01
2	570.95	590.05	591.89	19.1	1.84	9.64
3	424.15	446.45	448.27	22.3	1.82	8.16
4	374.35	392.15	393.95	17.8	1.8	10.11
5	427.45	444.85	446.18	17.4	1.33	7.64
6	523.85	540.95	542.66	17.1	1.69	9.89

In Sandia test, a solid plug was inserted concentrically in the absorber tube to ensure large velocity. In this study, the solid plug was removed, which is more practical. In order to further validate the applicability of the established models for simulation in the

hollow tube, the obtained results of Nu and f were compared with that calculated by the classical empirical equations proposed respectively by Gnielinski [166] and Petukhov [167], as shown in Fig. 6.6. The two formulas were given by Eq. (6.24) and Eq. (6.25) respectively.

$$Nu_G = \frac{(f/8)(Re-1000)Pr_f}{1+12.7(f/8)^{1/2}(Pr_f^{2/3}-1)} \left[1 + \left(\frac{d_{a,i}}{L_a} \right)^{2/3} \right] \left(\frac{Pr_f}{Pr_{a,i}} \right)^{0.11} \quad (6.24)$$

$$f_P = [1.82 \log_{10}(Re) - 1.64]^{-2} \quad (6.25)$$

It is clearly seen from the Fig. 6.6 that the simulation results were in good accordance with the results calculated by the empirical formulas. As the mass flow rate increased from 0.5 kg/s to 3.5 kg/s, the maximum relative deviation of Nu and f was 5.13% and 10.31% respectively, and the average relative deviation was only about 4.25% and 2.91%, respectively, validating again the reliability of the established models.

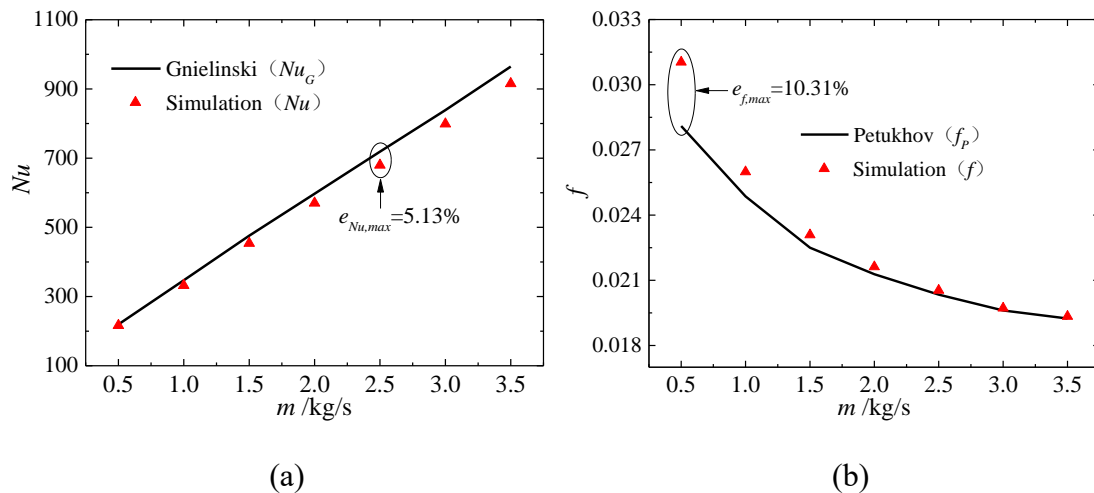


Fig. 6.6 Comparison of the results between simulation and empirical formulas: (a) results of Nu , (b) results of f

6.5 Thermal performance of the CSS-PTR

This section explores the basic thermal performance of the CSS-PTR, revealing the internal heat transfer mechanism of the PTR and providing foundations for later studies on its thermal performance improvement. In this section, the used case is as follows: the direct normal solar irradiance used is 1000 W/m^2 , the mass flow rate is 1 kg/s , the inlet fluid temperature is 573.15 K , the ambient temperature is 293.15 K , the wind velocity is 2 m/s .

6.5.1 Distribution of fluid temperature and velocity

Fig. 6.7 shows the fluid temperature distribution at each section along the longitudinal direction (Z -axis). It can be seen from the figure that the fluid temperature increased along the longitudinal direction as the heat from the absorber tube wall is absorbed along the path. It also shows that the fluid temperature distribution at each section was not uniform, showing stratification. For detailed analysis, the section at $z=7.5\text{m}$ was taken as an example. Fig. 6.8 displays the fluid temperature distribution at $z=7.5\text{m}$, which shows clearly that the maximum temperature difference of the fluid reached more than 10 K , and the highest temperature appeared near the bottom of the absorber tube. This is because the bottom of the absorber tube receives most of the concentrated solar radiation, so that the fluid in this part get the maximum heat. It can also be seen from Fig. 6.8 that, in general, the closer the fluid to the absorber wall, the higher the

temperature was, and the fluid temperature presented a circular annular stratification with high external temperature and low internal temperature. This is due to the high thermal conductivity of metal, which heats the absorber wall before the internal fluid is heated. Therefore, it can be reasonably speculated that when the fluid velocity is large enough, causing stronger disturbance, heat will be transferred to the fluid more quickly due to the improvement of the heat transfer inside the absorber, which will produce vertical stratification of the fluid temperature, rather than the annular stratification.

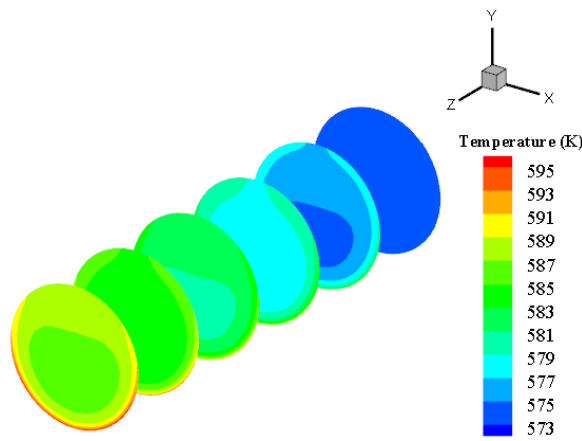


Fig. 6.7 Fluid temperature distribution at each section

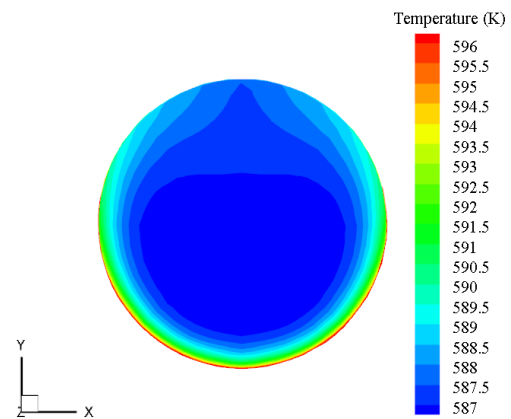


Fig. 6.8 Fluid temperature distribution at $z=7.5$ m

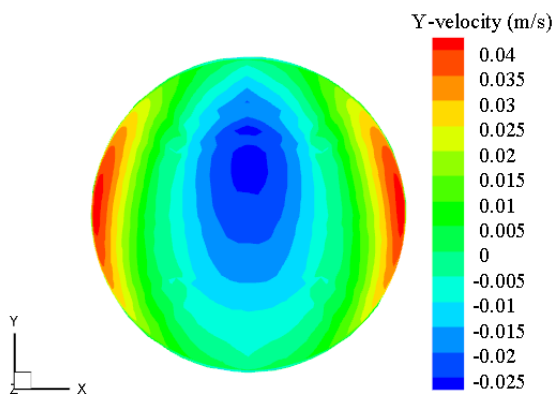


Fig. 6.9 Distribution of fluid velocity along Y-axis at $z=7.5$ m

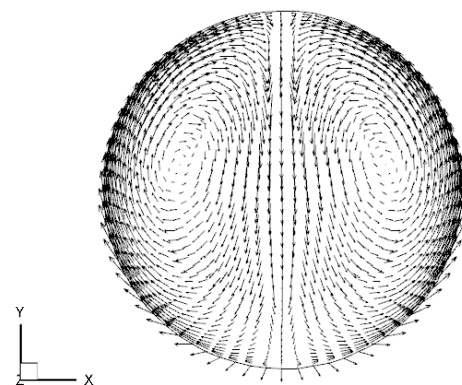


Fig. 6.10 Vector diagram of fluid velocity at $z=7.5$ m

It can also be found from Fig. 6.8 that the fluid temperature in the lower center region of the absorber tube was lower than that on both sides and upper region, which is mainly caused by the secondary flow in the tube. As Fig. 6.2(a) depicts, the fluid density decreased constantly with increasing temperature. Therefore, the fluid at the bottom and on both sides of the absorber tube is heated, reducing the density, and hence flowing upward under the density difference, while the fluid with lower temperature in the middle and upper region flows downward, forming a secondary flow of hot fluid flowing upward on both sides and cold fluid flowing downward in the middle. The color map and the vector diagram of the secondary flow are displayed in Fig. 6.9 and Fig. 6.10, respectively. Both the two figures showed the same phenomenon. It is precisely because of the secondary flow that the hot fluid on both sides rises and the cold fluid in the middle falls, resulting in the lowest fluid temperature at the lower center region of the absorber tube, as shown in Fig. 6.8.

Fig. 6.11 shows the effects of the mass flow rate on the distribution of the fluid temperature at the section of $z=7.5$. As discussed in the above part, when the mass flow rate was 1 kg/s, the fluid temperature had the distribution of annular stratification with higher external temperature and lower internal temperature, as presented in Fig. 6.11(a). However, when the mass flow rate was more than 3 kg/s, the annular stratification was changed to vertical stratification with higher bottom temperature and lower upper temperature, as given in Fig. 6.11(b) ~ (d). One of the reasons is that larger flow rates

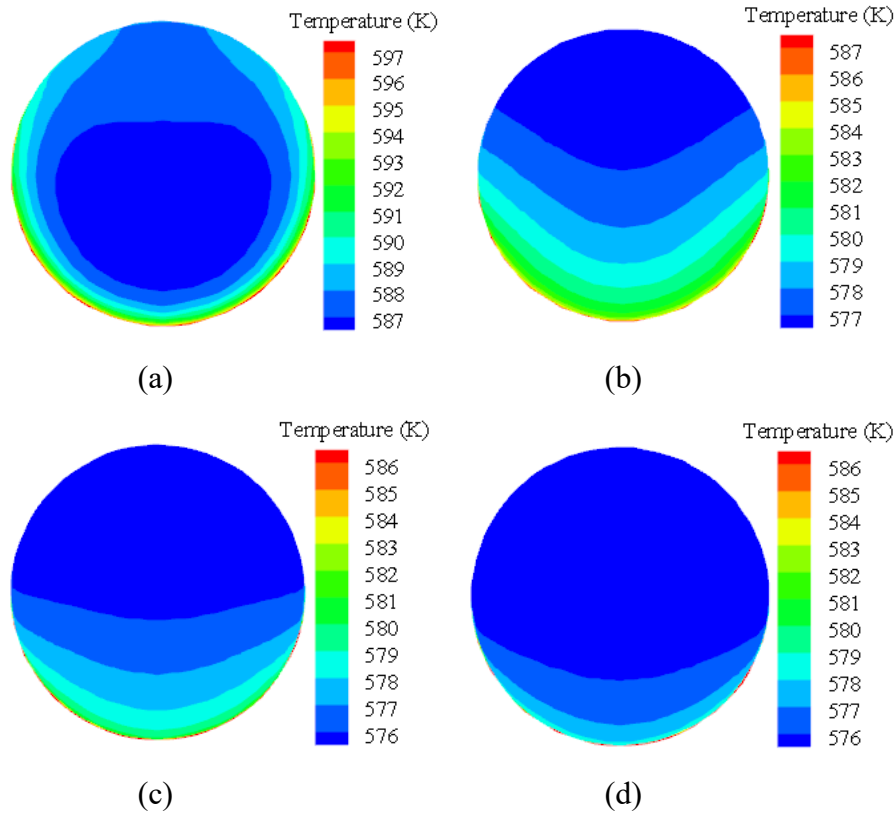


Fig. 6.11 The distribution of fluid temperature at $z=7.5$ m under different mass flow rates: (a) $m=1$ kg/s, (b) $m=3$ kg/s, (c) $m=5$ kg/s, (d) $m=7$ kg/s

increase the turbulence intensity, accelerating the upward heat transfer and hence facilitating the vertical stratification. The other reason is that the large flow rates weaken the annular secondary flow, as shown in Fig. 6.12 which displays the distribution of fluid velocity along Y axis at the section of $z=7.5$ m under mass flow rates of 1 kg/s and 7 kg/s. It can be clearly found from Fig. 6.12 that the intensity of the annular secondary flow in the case of $m=1$ kg/s was much larger than that in the case of $m=7$ kg/s. This indicates that the center of the absorber tube will not be affected by the upper cold fluid flowing downward, which promotes the heat flow from the bottom up, consequently causing vertical stratification. Obviously, it can also be found from Fig.

6.11 that due to the fluid turbulence enhanced by the increased flow rate, the uniformity of the fluid temperature distribution at the cross section was better in the case of larger flow rates.

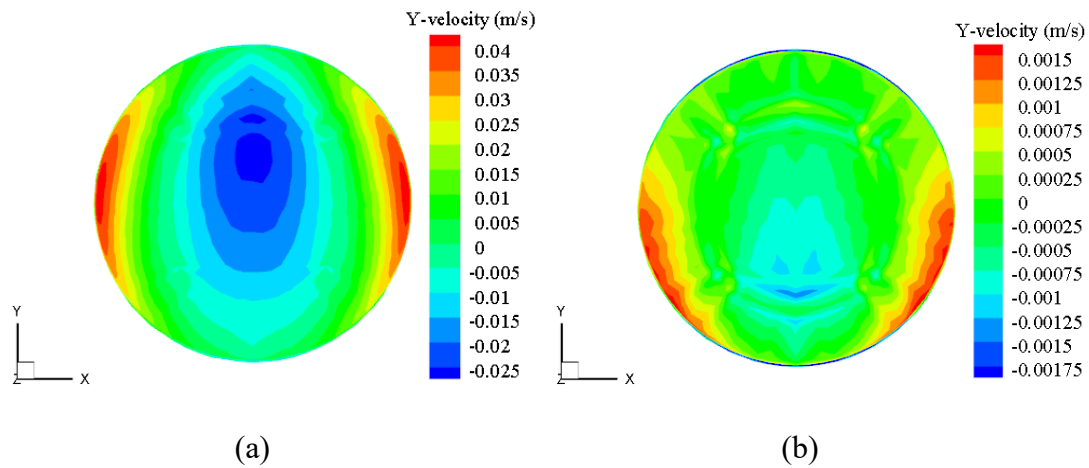


Fig. 6.12 The distribution of fluid velocity along Y axis at $z=7.5$ m under different mass flow rates: (a) $m=1$ kg/s, (b) $m=7$ kg/s

6.5.2 Distribution of absorber tube temperature

Fig. 6.13 shows the absorber tube temperature distribution at each section along the longitudinal direction (Z-axis). It is clearly seen from the figure that the absorber temperature increased along the longitudinal direction, which is attributed to the longitudinal increase of the fluid temperature. Moreover, because of the concentrated heat flux distributed on the bottom part of the absorber tube, the bottom part of the absorber wall temperature was obviously higher than the upper part.

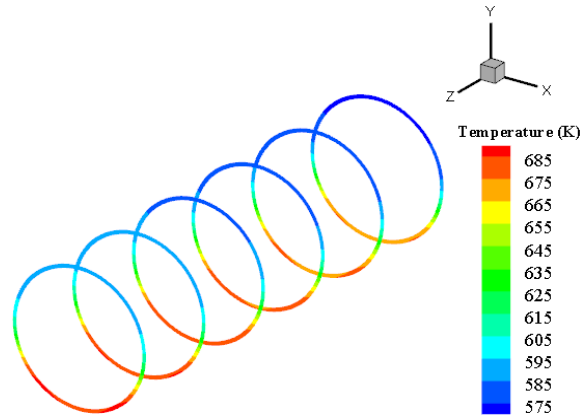


Fig. 6.13 Distribution of the absorber temperature at each section

For clearer presentation of the absorber temperature distribution, Fig. 6.14 and Fig. 6.15 show respectively the circumferential distribution of the absorber outer surface temperature at different sections and the longitudinal distribution of the absorber outer surface temperature at different circumferential angles. From both the two figures, it can be seen that the absorber temperature increased along the longitudinal direction, which is the same as what is shown in Fig. 6.13. From Fig. 6.14, it can be found that the maximum circumferential temperature difference at each section is more than 100 K. This great uneven temperature distribution causes thermal deformation of the absorber tube, producing thermal stress, which not only endangers the safety of the receiver structure, but also deviates the absorber tube from the focal line, leading to rays-spillage. Thus, reducing the circumferential temperature difference of the absorber tube is of great significance to ensuring high performance of the receiver tube. It is easily found from Fig. 6.15 that the growth rates of the absorber temperatures along the longitudinal direction at different circumferential angles were almost the same, indicating that the circumferential temperature difference along the longitudinal

direction remains constant. Therefore, when analyzing the circumferential temperature difference, only one section is needed for discussion. In this study, the section of $z=7.5$ m is adopted as the representative for discussion.

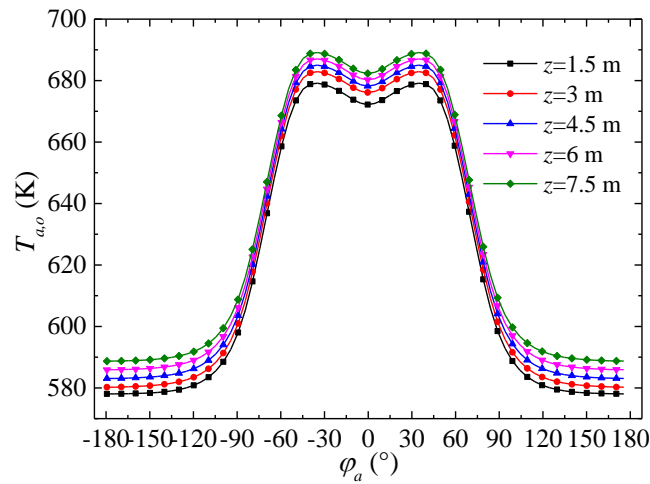


Fig. 6.14 Circumferential distribution of the absorber outer surface temperature at different sections

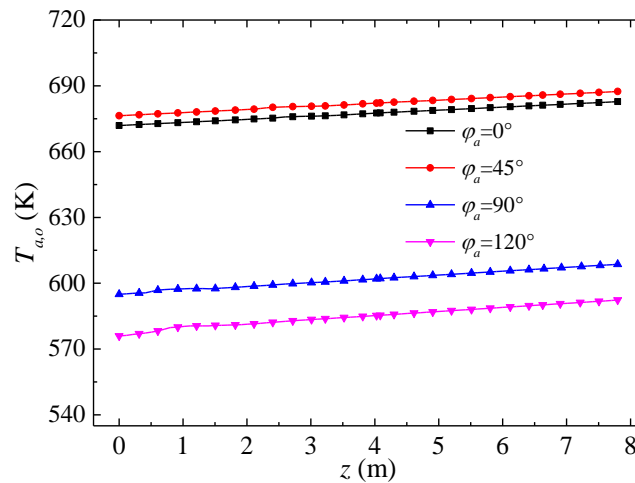


Fig. 6.15 Longitudinal distribution of the absorber outer surface temperature at different circumferential angles

Fig. 6.16 shows the temperature distribution of the inner and outer surfaces of the

absorber tube at $z=7.5\text{m}$. The results show that the temperature distributions of the inner and outer surfaces were consistent. There was a temperature difference of about 4.5 K between the inner and outer surfaces in the high heat flux area (bottom part of the absorber), while the temperature difference in the low heat flux area (upper part of the absorber) was basically zero. This is because the high heat flux in the bottom part of the absorber heats the outer surface first and then is transferred to the inner surface and the upper part of the absorber. It can be easily found from the above analyses that the circumferential temperature difference is much larger than the inner and outer surface temperature difference, having the dominant effects on the thermal performance of the receiver tube. Therefore, in later sections, only the variation of circumferential temperature difference will be discussed.

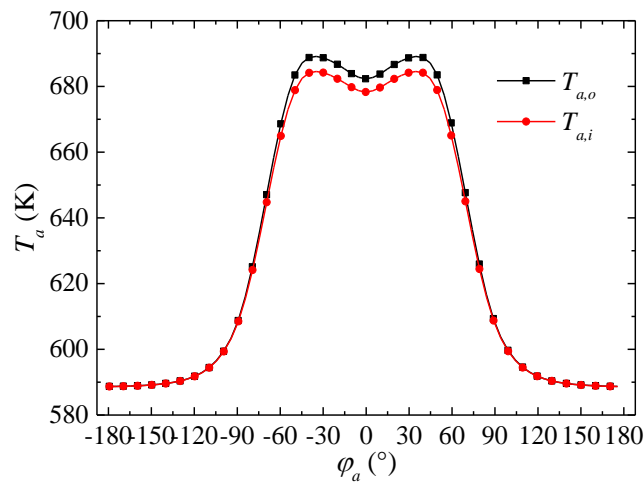


Fig. 6.16 Distribution of the temperature of inner and outer surfaces of the absorber at $z=7.5\text{ m}$

6.5.3 Distribution of glass envelope temperature

Fig. 6.17 shows the distribution of the glass envelope temperature at each section along the longitudinal direction. It can be seen from the figure that the temperature distribution of the glass envelope was similar to that of the absorber tube, increasing along the longitudinal direction and showing uneven distribution with higher bottom part and lower upper part. This is because the heat source of the glass envelope is the absorber tube, thereby having the similar temperature distribution with the absorber tube. Comparing Fig. 6.13 and Fig. 6.17, it is easily found that the temperature of the glass envelope was much smaller than that of the absorber tube. This is because the vacuum annulus weakens greatly the heat transfer between the absorber tube and the glass envelope.

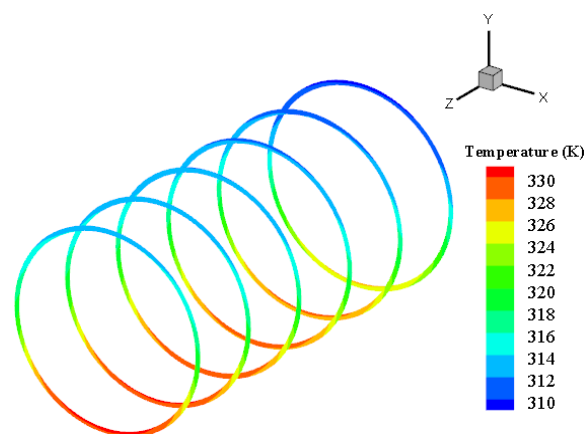


Fig. 6.17 Distribution of the glass envelope temperature at each section

Fig. 6.18 shows the circumferential distribution of the glass envelope inner surface temperature at different sections. From the figure, it can be seen that the glass envelope

inner surface temperature increased along the longitudinal direction, which is the same as what is presented in Fig. 6.17. It also shows that the maximum circumferential temperature difference of the glass envelope at each section is about 17.5 K, which, given the fact that the allowable stress of glass is small, is the main cause of thermal deformation of the glass envelope. As mentioned above, the glass envelope temperature is dependent on the absorber tube temperature. Thus, reducing the circumferential temperature difference of the absorber tube will also reduce the circumferential temperature difference of the glass envelope.

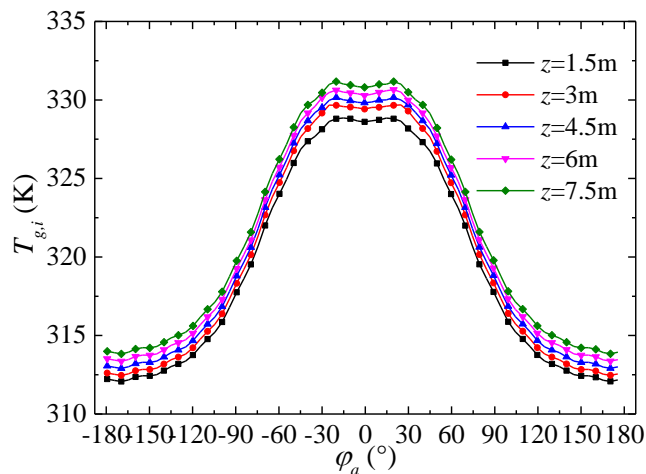


Fig. 6.18 Circumferential distribution of the glass envelope inner surface temperature at different sections

Fig. 6.19 shows the temperature distribution of the inner and outer surfaces of the glass envelope at $z=7.5\text{m}$. It can be seen from the figure that the temperature distributions of the inner and outer surfaces of the glass envelope were similar. There existed temperature difference between the inner and outer surfaces of the glass envelope on

the whole circumference, which is different from that of the absorber tube which only has temperature difference in the high heat flux area. This should be attributed to the heat transfer process between the absorber tube and the glass envelope: The inner surface of the glass envelope is first heated up by the absorber outer surface by radiation, and then the absorbed energy is transferred to the outer surface by conduction. Since the temperature at the bottom part of the absorber tube is obviously higher than that at the upper part, the temperature at the bottom part of the glass envelope rises faster than the upper part. Meanwhile, due to the small thermal conductivity (1.2 W/m^2) of the glass, leading to poor heat transfer capacity, the temperature difference between the inner and outer surfaces of the glass envelope at the bottom part will be larger than that at the upper part. As Fig. 6.19 shows, the maximum temperature difference at the bottom part of the glass envelope was about 2.5 K, while that at the upper part was only about 1.5 K, which completely accords with the above analysis.

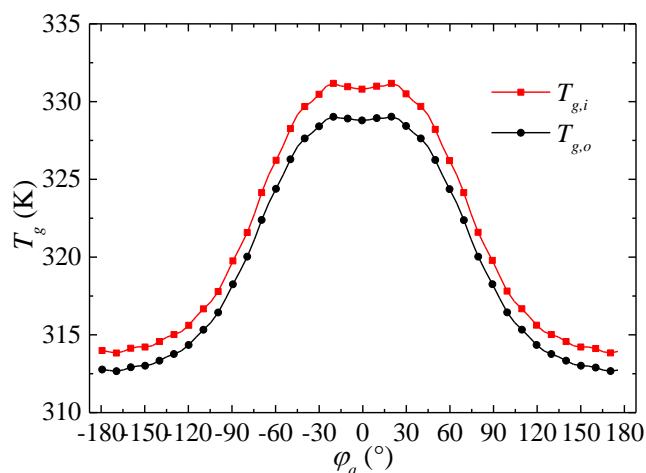


Fig. 6.19 Distribution of the temperature of the inner and outer surfaces of the glass envelope at $z=7.5 \text{ m}$

6.5.4 Analysis of heat loss and collector efficiency

In practical engineering, due to long time of use, the vacuum seal of the receiver tube may be destroyed under various external loads and repeated heating and cooling effects, causing the outside air entering the annular space, thereby increasing the heat loss of the collector tube. Extremely, the glass envelope may be broken by the large loads, such as wind load, thermal load and pressure load, exposing the absorber tube completely to the ambient environment, consequently causing huge the heat loss.

Fig. 6.20 shows the variations of the heat loss and the collector efficiency in three cases: vacuum annular space, air filled in the annular space, and glass envelope broken. It is clearly seen from the figure that when the annulus was kept vacuum, the radiation loss accounted for almost all the heat loss (both conduction loss and convection loss were slight). The heat loss in the other two cases, i.e. air filled and glass broken, were much larger than that in the case of vacuum annulus. It is easily obtained from the figure that the heat loss in those three cases were 1685 W, 2978 W and 13604 W respectively. It can also be found from the figure that the increase of heat loss was mainly caused by the significant increase of conduction loss and convection loss. This is because the heat conduction and convection, especially the convection, are increased remarkably as the annulus is filled with air or the glass breaks. The figure shows that the collector efficiency in those three cases was 80.53%, 76.22% and 54.43% respectively. The

collector efficiency in the case of air filled and glass broken was reduced respectively by 4.31% and 26.1%, compared with the case of vacuum annulus. Additionally, when working in the air-filled environment, the selective coating is easily oxidized under high temperature conditions, which weakens significantly its absorptivity. Therefore, maintaining the vacuum degree of the annular space is of great significance to achieving efficient operation of the PTR.

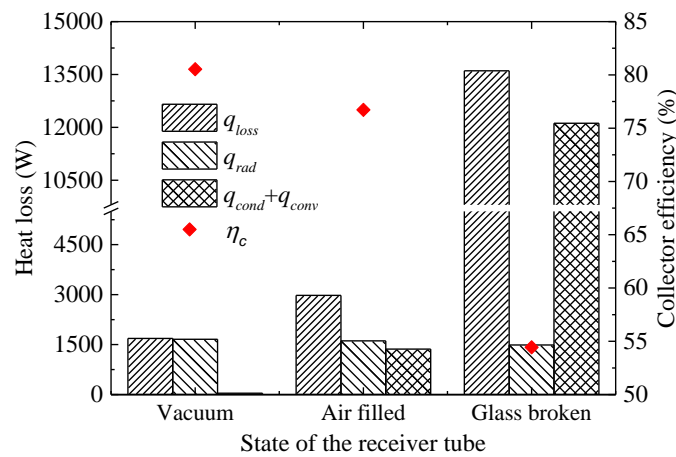


Fig. 6.20 Heat loss and collector efficiency under different receiver tube conditions

6.6 Comparison of USR-PTR and CSS-PTR

In this section, the USR-PTR and the CSS-PTR are compared in terms of both thermal and hydraulic performance, aiming at revealing the mechanism of the heat transfer enhancement in the USR-PTR. The CSS-PTR used as the reference was the SEGS LS-2 PTR. The rib parameters of the USR-PTR used for comparison in this section is given in Table 6.4. The mass flow rate of 2 kg/s and a periodic length of the PTR from $z=0.6$ m to $z=0.7$ m are selected as representative for detailed analysis.

The study is performed under the following conditions: the length of the PTR is 1 m; the incident solar radiation intensity is 1000 W/m²; the ambient temperature is 293.15 K; the wind velocity is 2 m/s; the inlet temperature of the fluid is 573.15 K; the mass flow rate ranges from 0.5 kg/s to 3.5 kg/s. The inlet Reynolds number corresponding to each mass flow rate is listed in Table 6.8.

Table 6.8 Mass flow rate and the corresponding inlet Reynolds number

m (kg/s)	0.5	1	1.5	2	2.5	3	3.5
Re	20254	40508	60763	81017	101272	121526	141781

6.6.1 Comparison of thermal performance

Fig. 6.21 shows the variation of the Nusselt number (Nu) with the mass flow rate (m) for both USR-PTR and CSS-PTR. It is clearly seen from the figure that Nu increased almost linearly with the increase of m for both the two PTRs. The Nu and its growth rate of the USR-PTR were both obviously larger than those of the CSS-PTR. When the m increased from 0.5 kg/s to 3.5 kg/s, the Nu of the CSS-PTR grew from 217 to 916, rising by 3.22 times, whereas the Nu of the USR-PTR increased greatly from 312 to 1598, growing by 4.12 times. It can be calculated from Fig. 6.21 that the heat transfer enhancement of the USR-PTR, compared with the CSS-PTR, ranged from 44% to 76%. This indicates that the USR-PTR has great capacity of improving the heat transfer of

the PTR.

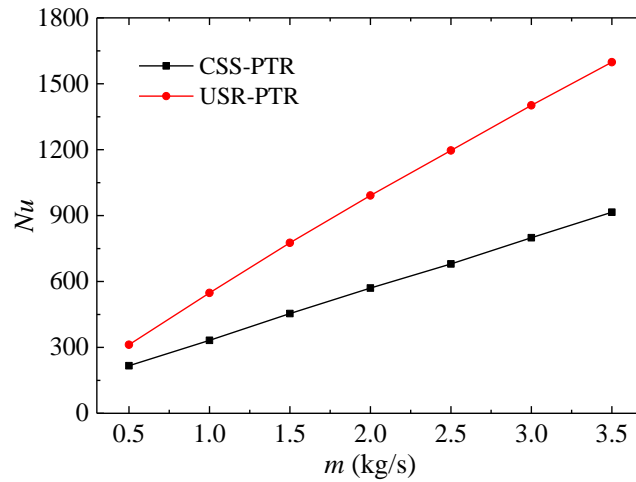


Fig. 6.21 Variation of the Nusselt number (Nu) with mass flow rate (m)

Fig. 6.22 shows the fluid temperature distribution in the longitudinal section from $z=0.6$ m to $z=0.7$ m under condition of $m=2$ kg/s for both USR-PTR and CSS-PTR. Overall, the fluid temperature in the USR-PTR was higher and more uniform than that in the CSS-PTR. This is because the larger turbulence caused in the USR-PTR enhances the mixing and heat transfer of the fluid. There existed a thermal boundary layer in the vicinity of the bottom inner surface of the absorber, which produces the main thermal resistance of the heat transfer between the absorber and the fluid. It can be clearly seen from Fig. 6.22 that the thermal boundary layer of the USR-PTR was much thinner than that of the CSS-PTR, leading to smaller thermal resistance and hence producing larger heat transfer ability. For more clarity, a local enlarged view was presented in Fig. 6.22(b). It can be seen from the enlarged view that the thermal boundary layer was thickened along the flow direction and peaked at the upstream of the rib, and then was

reduced obviously after the rib. The possible reason is that the disturbance (even vortices) caused by the rib destroys the boundary layer. This periodic disturbance inhibits the development of the boundary layer, reducing effectively the thermal resistance and thereby improving the heat transfer.

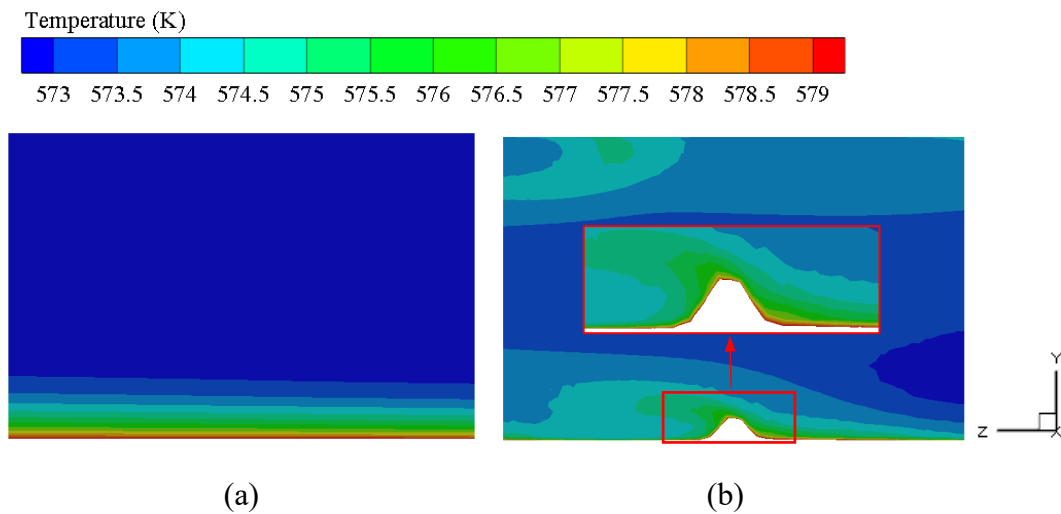


Fig. 6.22 Distribution of the fluid temperature in the longitudinal section under condition of $m=2$ kg/s ($z=0.6\sim 0.7$ m): (a) CSS-PTR, (b) USR-PTR

Fig. 6.23 presents the absorber temperature distribution from $z=0.6$ m to $z=0.7$ m under condition of $m=2$ kg/s for both USR-PTR and CSS-PTR. It is obviously observed from the figure that the temperature of the bottom part of the absorber of the USR-PTR was smaller than that of the CSS-PTR. This means the circumferential temperature difference of the USR-PTR will be smaller than that of the CSS-PTR, reducing the thermal strain and hence improving the safety of the PTR. Fig. 6.23 also shows that the temperature of the absorber outer surface was higher than that of the inner surface. This is because the incident solar radiation is concentrated on the outer surface of the

absorber.

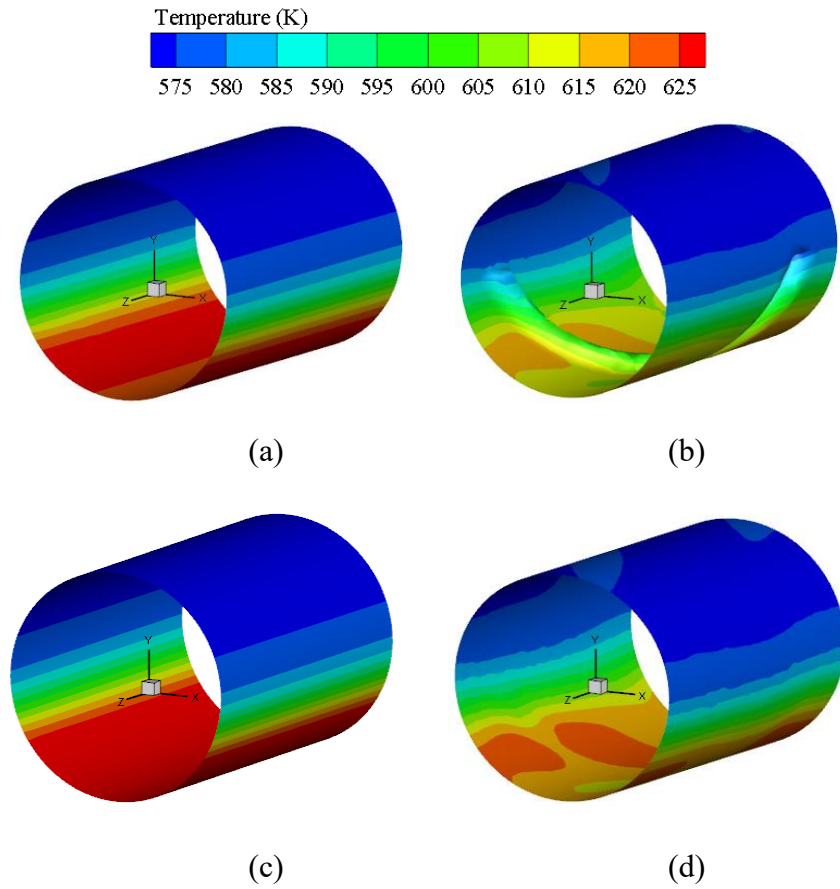


Fig. 6.23 Distribution of the absorber temperature under condition of $m=2$ kg/s ($z=0.6\sim 0.7$ m): (a) inner surface of the CSS-PTR, (b) inner surface of the USR-PTR, (c) outer surface of the CSS-PTR, (d) outer surface of the USR-PTR

Taking the cross-section of $z=0.6$ m as an example, the variation of the maximum ($T_{a,max}$) and minimum ($T_{a,min}$) temperature of the absorber wall with mass flow rate (m) is shown in Fig. 6.24. It can be found from the figure that the $T_{a,min}$ for both the two PTRs were almost the same, while the $T_{a,max}$ of the USR-PTR was consistently smaller than that of the CSS-PTR for all the discussed mass flow rates. Accordingly, the maximum

circumferential temperature difference of the absorber of the USR-PTR was smaller than that of the CSS-PTR. For example, when $m=2$ kg/s, the maximum circumferential temperature difference of the CSS-PTR was about 59.5 K, while that of the USR-PTR was only about 46.6 K, 21.7% smaller than the former. As a matter of fact, compared with the CSS-PTR, the maximum decrease of the circumferential temperature difference of the USR-PTR was up to 27.4%. It can be concluded from the above analysis that the security and stability of the PTR will be improved by using the USR-PTR, especially in the cases of larger flow rates.

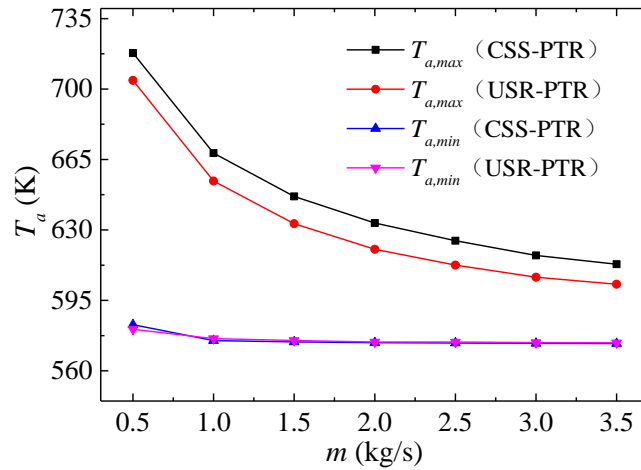


Fig. 6.24 Variation of the maximum ($T_{a,max}$) and minimum ($T_{a,min}$) temperature of the absorber at $z=0.6$ m with mass flow rate (m)

6.6.2 Comparison of hydraulic performance

Fig. 6.25 depicts the variation of the pressure drop (ΔP) with mass flow rate (m) for both USR-PTR and CSS-PTR. It is clearly seen from the figure that the ΔP increased

constantly with the increase of m for both the two PTRs. The ΔP and its growth rate for the USR-PTR were much larger than those for the CSS-PTR. As the m increased from 0.5 kg/s to 3.5 kg/s, the ΔP for the CSS-PTR increased from 8.7 Pa to 236.1 Pa, rising by 26.1 times, whereas the ΔP for the USR-PTR grew greatly from 26.5 Pa to 1098.9 Pa, increasing by 40.5 times. This indicates that the USR-PTR enhances the heat transfer at the obvious expense of increasing the pressure drop penalty.

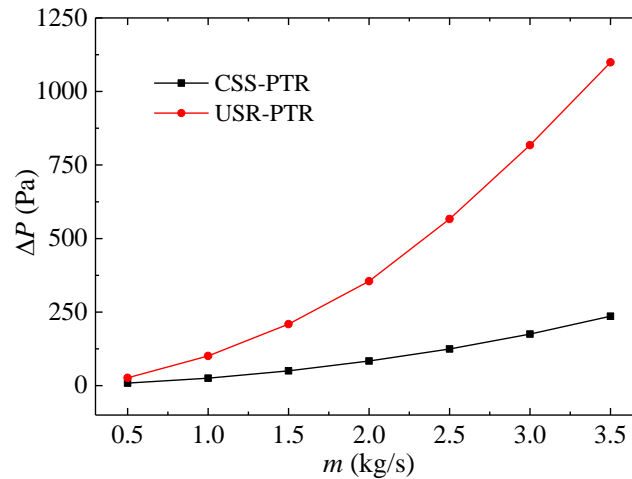


Fig. 6.25 Variation of the pressure drop (ΔP) with mass flow rate (m)

The comparison of the friction factor (f) between the two PTRs are presented in Fig. 6.26. It shows clearly that the value of f of the USR-PTR was much larger than that of the CSS-PTR. For example, the value of f of the USR-PTR in the case of $m=2$ kg/s was about 0.0884, 4.09 times larger than that of the CSS-PTR, which was only 0.0216. It can also be found from Fig. 7.9 that the f decreased with the increase of m , indicating that, according to Eq. (6.3), the growth rate of the ΔP is smaller than that of the kinetic energy with the increase of mass flow rate.

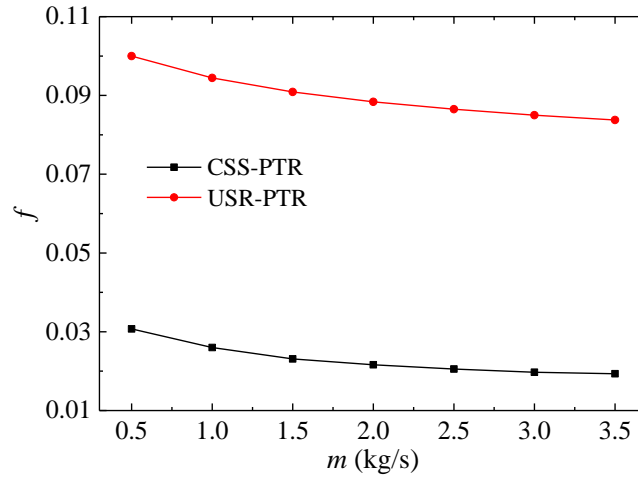


Fig. 6.26 Variation of the friction factor (f) with mass flow rate (m)

Fig. 6.27 shows the fluid velocity vector distribution in the longitudinal section from $z=0.6$ m to $z=0.7$ m under condition of $m=2$ kg/s for both USR-PTR and CSS-PTR. Obviously, the velocity vectors in the CSS-PTR were parallel, whereas those in the USR-PTR interblent with each other, especially in the near-wall region. It can be seen from the local enlarged view in the figure that, compared with the CSS-PTR, counter-flow was induced at the back of the rib in the USR-PTR, forming a recirculation zone. The velocity vectors were separated in the recirculation zone and then adhered again to the wall in the downstream region, which is very beneficial for breaking the boundary layer and therefore reducing the thermal resistance. It can also be found from Fig. 6.27(b) that, although the spiral ribs were only placed on the bottom surface of the absorber, the turbulence caused also affected remarkably the fluid flowing in the upper region of the absorber, which demonstrates that the heat transfer around the whole tube is enhanced.

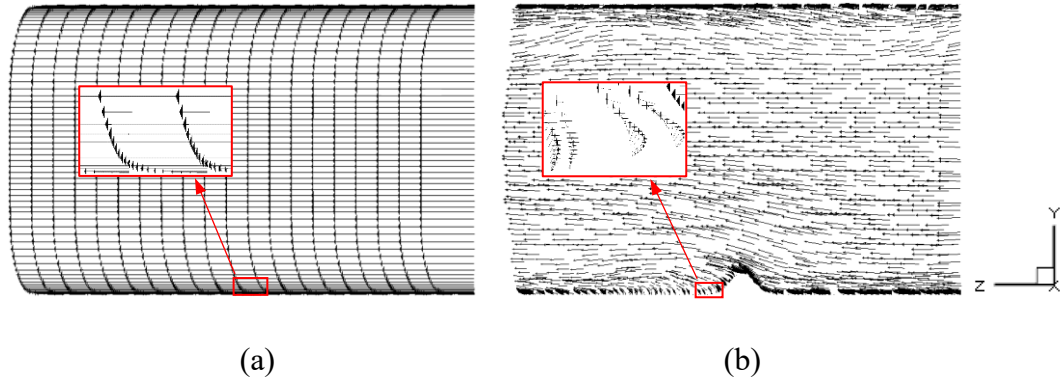


Fig. 6.27 Diagram of the fluid velocity vector in the longitudinal section under condition of $m=2$ kg/s ($z=0.6\sim 0.7$ m): (a) CSS-PTR, (b) USR-PTR

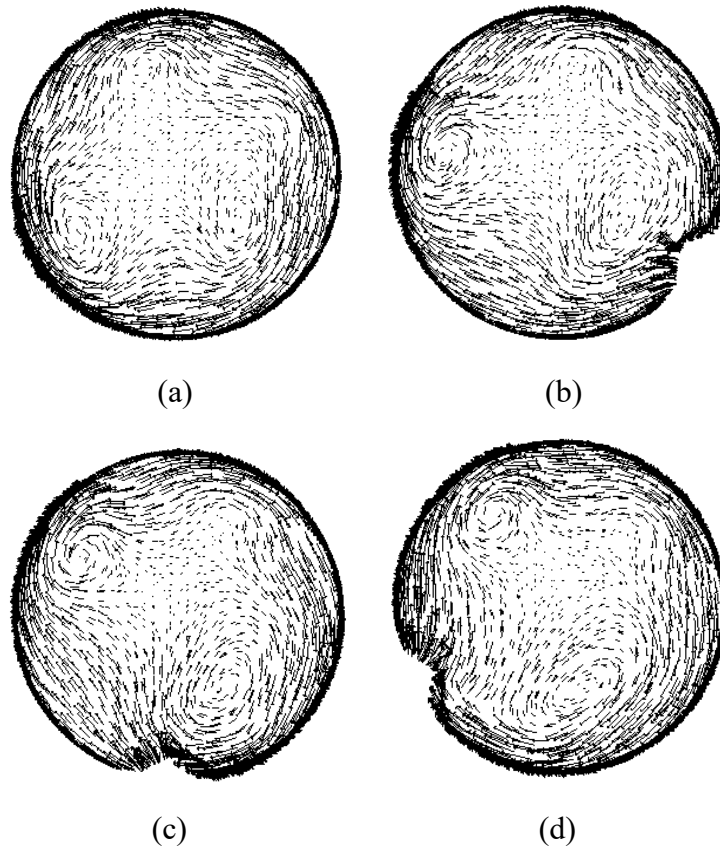


Fig. 6.28 Diagram of fluid velocity vector in different cross sections of the USR-PTR under condition of $m=2$ kg/s: (a) $z=0.6$ m, (b) $z=0.63$ m, (c) $z=0.65$ m, (d) $z=0.67$ m

In order to further explore the flow properties in the USR-PTR, the velocity vectors in

four typical cross sections in one periodic tube length are depicted in Fig. 6.28. It is obviously seen from the figure that the rotational flow was induced in the cross section of the USR-PTR, which will enhance fluid mixing and disturbance, consequently improving the heat transfer capacity. From the Fig. 6.28, it can also be found that three longitudinal vortices were generated in each cross section, which will further increase the disturbance of the fluid and enhance the heat transfer in the tube. What is noted is that the greater turbulence in the USR-PTR is also the main cause of the larger pressure drop than the CSS-PTR (as shown in Fig. 6.25).

Fig. 6.29 depicts the distribution of the turbulent kinetic energy (TKE) in the longitudinal section from $z=0.6$ m to $z=0.7$ m under condition of $m=2$ kg/s for both USR-PTR and CSS-PTR. It can be easily seen from the figure that the TKE in the USR-PTR was much larger than that in the CSS-PTR. The TKE in most regions of the CSS-PTR was less than $0.002 \text{ m}^2/\text{s}^2$, while that in the whole USR-PTR was more than $0.004 \text{ m}^2/\text{s}^2$. The maximum TKE in the CSS-PTR was less than $0.01 \text{ m}^2/\text{s}^2$, while that in the USR-PTR was more than $0.02 \text{ m}^2/\text{s}^2$. This demonstrates that the fluid in the USR-PTR is mixed more drastically than in the CSS-PTR, consequently enhancing the heat transfer and increasing the pressure loss as well. Fig. 6.29 also shows that, in the USR-PTR, the maximum TKE occurred after fluid flowing over the rib because of the great disturbance and vortices caused by the rib. The maximum TKE was close to the absorber inner surface, which can reduce the boundary layer and decrease the thermal resistance. It can be seen from the two local enlarged views that there existed a thin

layer of fluid with extremely small TKE (≈ 0) near the absorber inner surface. This is because the viscosity of the fluid dominates in the near-wall region, reducing the TKE remarkably. From the figure, it can also be found that the flow layer with small TKE in the USR-PTR was thinner than that in the CSS-PTR, indicating that the thermal resistance in the USR-PTR is reduced effectively. Fig. 6.29(b) also shows that the TKE of the fluid in the upper region of the absorber of the USR-PTR was larger than that in the central region. This is caused by the rotational flow induced by the spiral ribs, which increases the heat transfer between the fluid and the upper absorber wall.

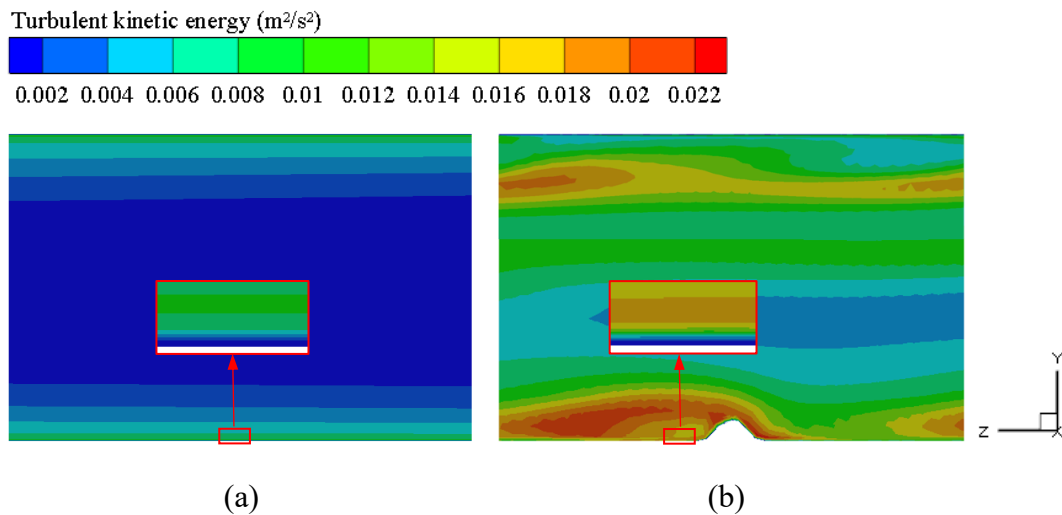


Fig. 6.29 Distribution of the turbulent kinetic energy (TKE) in the longitudinal section under condition of $m=2$ kg/s ($z=0.6\sim 0.7$ m): (a) CSS-PTR, (b) USR-PTR

6.6.3 Comparison of field synergy

Fig. 6.30 shows the distribution of the synergy angle in the longitudinal section from $z=0.6$ m to $z=0.7$ m under condition of $m=2$ kg/s for both USR-PTR and CSS-PTR. As

shown in the figure, the synergy angle in most areas of the two PTRs are almost equal to 90° , suggesting that there is a lot of room to improve the synergy of the velocity field and heat flow field (i.e. temperature gradient field), which is also the theoretical basis for the continuous development of heat transfer enhancement technologies. It can also be found from Fig. 6.30 that the distribution of the synergy angle in the two PTRs are different. In the CSS-PTR, as shown in Fig. 6.30(a), there was a narrow band area near the tube center where the synergy angle was about 75° , while the other areas had synergy angles of near 90° . In the USR-PTR, as shown in Fig. 6.30(b), the synergy angle ($\approx 85^\circ$) in the band area was larger than that ($\approx 75^\circ$) in the CSS-PTR. However, the biggest difference is that the synergy angle near the inner surface of the USR-PTR is much smaller than that in the same area of the CSS-PTR. As clearly shown in Fig. 6.30(b), the synergy angle in large part of areas near the upper surface and the bottom surface, especially the area behind the rib, of the USR-PTR, was less than 75° , and the minimum was about 60° , which indicates that the field synergy degree of the fluid near the wall of the USR-PTR is much better than that of the CSS-PTR. As discussed in previous sections, the near-wall region is exactly the main area of thermal resistance. Therefore, the higher degree of field synergy in the near-wall region of the USR-PTR reduces effectively the thermal resistance, consequently producing larger heat transfer capacity than the CSS-PTR.

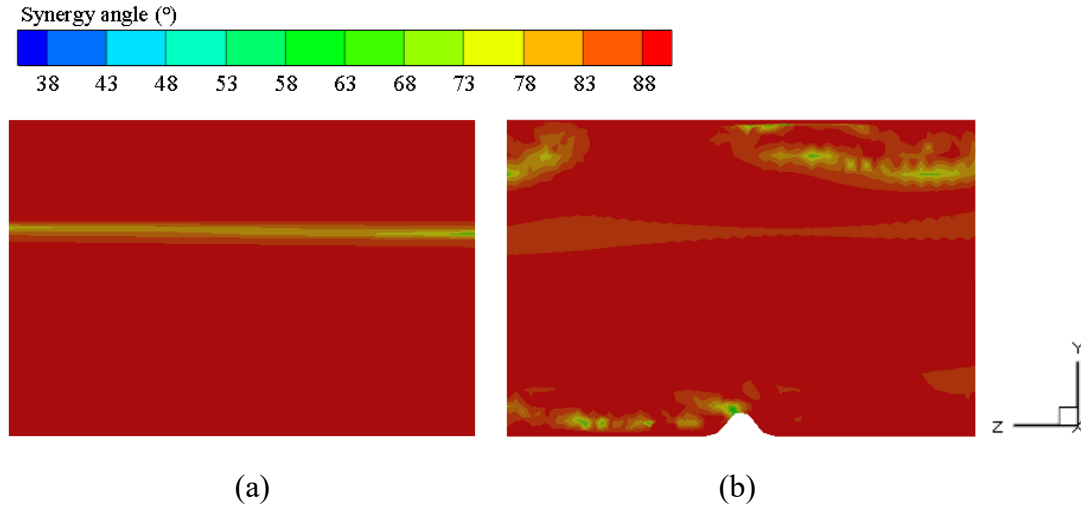


Fig. 6.30 Distribution of synergy angle in the longitudinal section under condition of $m=2$ kg/s ($z=0.6\sim 0.7$ m): (a) CSS-PTR, (b) USR-PTR

Fig. 6.31 and Fig. 6.32 shows respectively variation of the average synergy, and the dot product of the velocity vector and the temperature gradient with the mass flow rate. It is clearly seen from Fig. 6.31 that the average synergy angle in the USR-PTR was consistently larger than that in the CSS-PTR as the mass flow rate changed, indicating that the field synergy degree in the USR-PTR is better than that in the CSS-PTR. It can be obtained in Fig. 6.31 that the average angle in the USR-PTR was about 83.5° , about 4.5° smaller than that ($\approx 88^\circ$) in the CSS-PTR. Combining with Fig. 6.21, it can be concluded that small reduction of synergy angle can significantly increase heat transfer capacity. It can be obviously seen from Fig. 6.32 that the average of the dot product of the velocity vector and the temperature gradient in the USR-PTR was about 6.5, while that in the CSS-PTR was only about 2.5. This further demonstrates directly that the synergy degree of the velocity field and the heat flow field in the USR-PTR is much higher than that in the CSS-PTR, thereby producing better heat transfer performance.

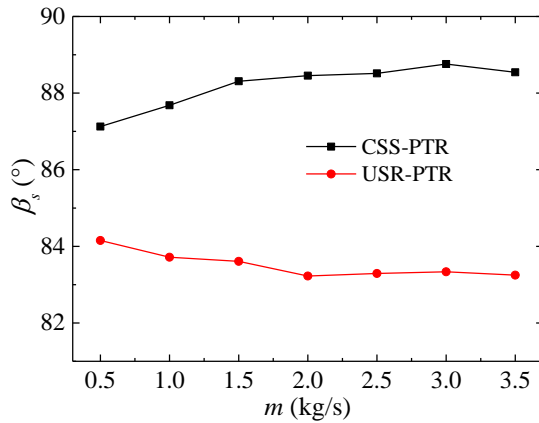


Fig. 6.31 Variation of the average synergy angle

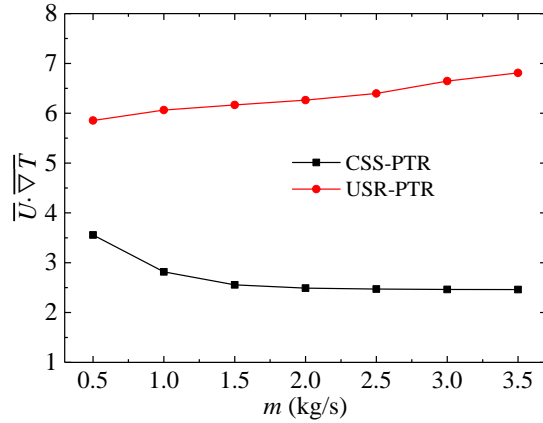


Fig. 6.32 Variation of the dot product of the velocity vector and the temperature gradient

6.7 Influences of structural parameters of the rib

In this section, the influences of the structural parameters of the rib, including the pitch interval, the rib height, the corner radius, crest radius and the spiral angle, on the performance of the USR-PTR are discussed in detail. Four or five different values will be set for each structural parameter, while other parameters remain the same as those given in Table 6.4. The parameters of the CSS-PTR with a subscript of “0” are used as the reference, and the performance of the USR-PTR is represented by the ratio to the CSS-PTR (i.e. Nu/Nu_0 and f/f_0). The PEC is used to evaluate the overall performance of the USR-PTR.

6.7.1 Influences of the pitch interval of the rib

Fig. 6.33 shows the variation of Nu/Nu_0 with mass flow rate (m) under different pitch intervals (p). It is clearly seen from the figure that Nu/Nu_0 for all p first increased quickly, and then declined slowly with the increase of m . That is to say, there is an optimal flow rate range within which the USR-PTR can achieve the maximum heat transfer enhancement. As p increased, Nu/Nu_0 was reduced. For example, when the m was 2 kg/s, the Nu/Nu_0 for $p=50$ mm, $p=100$ mm, $p=150$ mm and $p=200$ mm was 1.792, 1.738, 1.642 and 1.599 respectively. This is because larger p cuts down the number of the ribs in a certain length of tube, reducing the disturbance frequency and hence weakening the heat transfer. The maximum Nu/Nu_0 was obtained for $p=50$ mm in the case of $m=2.5$ kg/s, which was about 1.805. This means that, compared with the CSS-PTR, the enhancement of the heat transfer of the USR-PTR can be up to 80.5% by changing the pitch interval of the rib (p).

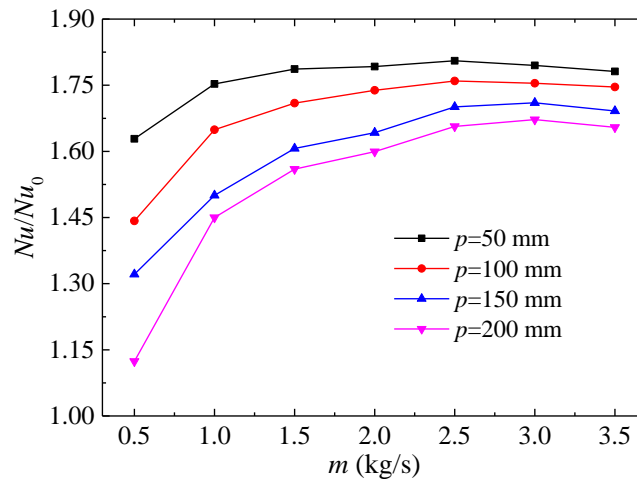


Fig. 6.33 Variation of Nu/Nu_0 with mass flow rate under different pitch intervals

Fig. 6.34 shows the variation of f/f_0 with mass flow rate (m) under different pitch intervals (p). Obviously, f/f_0 for all p first increased, and then declined slightly with the

increase of m . Since both the disturbance frequency and constraint effect are weakened by increasing p , f/f_0 decreased constantly with the increase of p . For example, when the m was 2 kg/s, the f/f_0 for $p=50$ mm, $p=100$ mm, $p=150$ mm and $p=200$ mm was 4.7, 4.09, 3.67 and 3.14 respectively. The maximum f/f_0 was about 4.97 obtained for $p=50$ mm in the case of $m=3$ kg/s, indicating that the pressure drop will be increased by up to 3.97 times by decreasing the pitch interval of the rib (p).

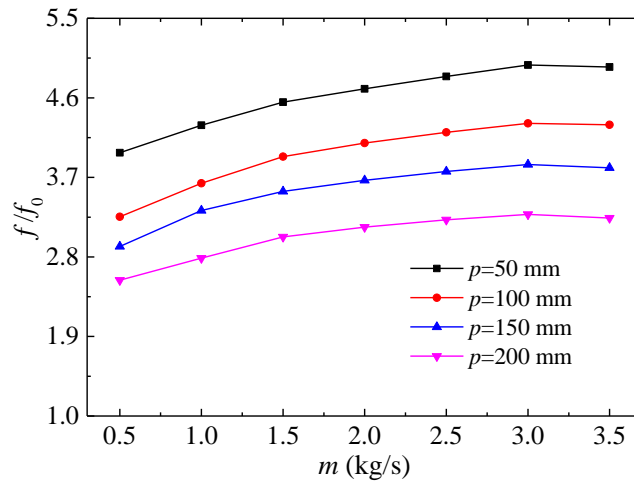


Fig. 6.34 Variation of f/f_0 with mass flow rate under different pitch intervals

Fig. 6.35 depicts the variation of PEC with mass flow rate (m) under different pitch intervals (p). It is clearly seen that PEC first increased, and then decreased slowly with the increase of m . Take $p=150$ mm as an example, the PEC increased from 0.924 at $m=0.5$ kg/s to the peak value of 1.093 at $m=2.5$ kg/s, and then dropped to 1.083 at $m=3.5$ kg/s. It can also be found from the figure that the m that achieves the maximum PEC varied with p , which means that the optimum flow rate for the best overall performance is closely associated with the pitch interval. When m was less than 0.75 kg/s, the overall

performance of the USR-PTR with p larger than 100 mm is not so good as the CSS-PTR ($PEC < 1$), demonstrating that the USR-PTR is not very suitable for application in the case of small flow rate. The figure also shows that when m was less than 1 kg/s, the PEC decreased with increasing p , while increased with increasing p as m was more than 2.5 kg/s. Therefore, the USR-PTRs with larger pitch interval have greater advantages when applied under condition of large flow rates. The maximum PEC was 1.125 obtained for $p=200$ mm at $m=3$ kg/s, indicating that the overall performance of the USR-PTR can be improved by 12.5% compared with the CSS-PTR by changing the pitch interval of the rib (p).

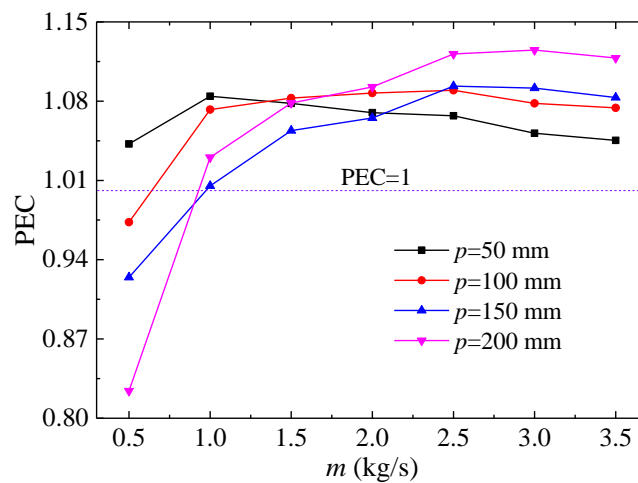


Fig. 6.35 Variation of PEC with mass flow rate under different pitch intervals

6.7.2 Influences of the height of the rib

Fig. 6.36 shows the variation of Nu/Nu_0 with mass flow rate (m) under different rib heights (Δh). It is easily observed from the figure that Nu/Nu_0 for all Δh first increased

quickly, and then dropped slowly with the increase of m . The heat transfer enhancement was more obvious as the flow rate was more than 1.5 kg/s. For example, when Δh was 5 mm, the Nu/Nu_0 increased from 1.442 at $m=0.5$ kg/s to the peak value of 1.76 at $m=2.5$ kg/s, and then dropped to 1.746 at $m=3.5$ kg/s. The figure also shows that Nu/Nu_0 increased constantly with the increase of Δh . Taking $m=2$ kg/s as the representative, the Nu/Nu_0 for $\Delta h=3$ mm, $\Delta h=5$ mm, $\Delta h=7$ mm and $\Delta h=9$ mm was 1.489, 1.738, 1.845 and 1.936, respectively. This is because larger Δh increased the disturbance intensity of the fluid, which enhances fluid mixing and weakens the boundary layer, hence improving the heat transfer. The increase of Nu/Nu_0 with increasing Δh was diminished, indicating that the heat transfer enhancement by increasing continuously rib height is limited. The maximum Nu/Nu_0 was achieved for $\Delta h=9$ mm in the case of $m=2.5$ kg/s, which was about 1.963. This means that, compared with the CSS-PTR, the heat transfer of the USR-PTR can be augmented by up to 96.3% by increasing the rib height (Δh).

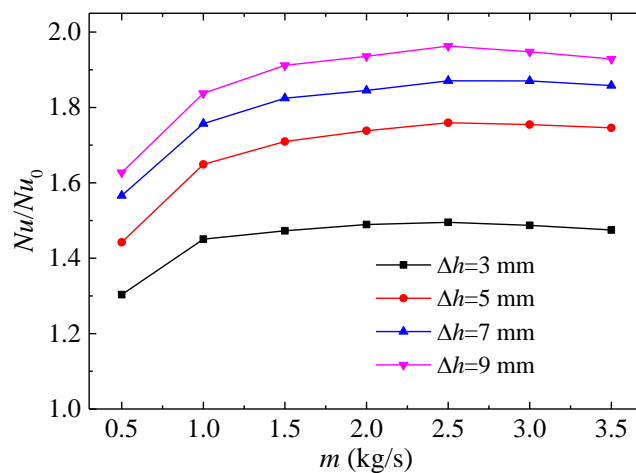


Fig. 6.36 Variation of Nu/Nu_0 with mass flow rate under different rib heights

Fig. 6.37 shows the variation of f/f_0 with mass flow rate (m) under different rib heights (Δh). Clearly, f/f_0 for all Δh increased slightly with the increase of m , indicating that the increase of pressure loss of the USR-PTR is almost the same as that of the CSS-PTR under conditions of different flow rates. For any mass flow rate, f/f_0 increased obviously with the increase of Δh . For example, when the m was 2 kg/s, the f/f_0 for $\Delta h=3$ mm, $\Delta h=5$ mm, $\Delta h=7$ mm and $\Delta h=9$ mm was 2.5, 4.09, 4.95 and 5.9, respectively. This is because the disturbance and constraint enhanced by increasing rib height increase the energy dissipation and flow resistance. It can also be found from the figure that the maximum f/f_0 was about 6.1 obtained for $\Delta h=9$ mm in the case of $m=3.5$ kg/s, indicating that the increase of pressure loss of the USR-PTR will be up to 5.1 times that of the CSS-PTR by increasing the rib height (Δh).

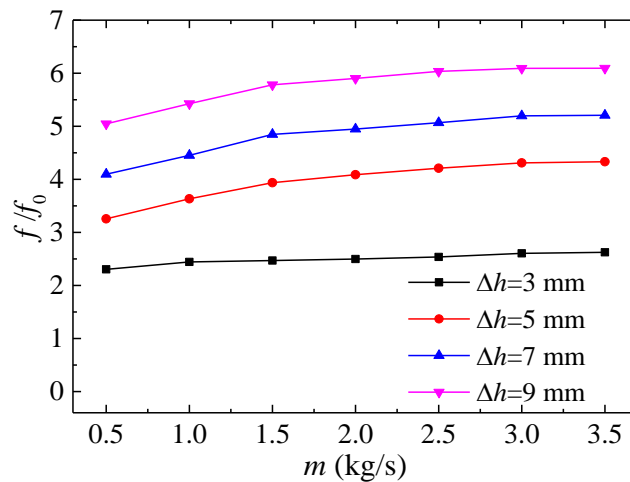


Fig. 6.37 Variation of f/f_0 with mass flow rate under different rib heights

Fig. 6.38 presents the variation of PEC with mass flow rate (m) under different rib heights (Δh). It is clearly seen that PEC first increased quickly, and then decreased

slowly with the increase of m . This indicates the overall performance of the USR-PTR is more susceptible to flow regime under conditions of small flow rates. The figure also shows that when m was 0.5 kg/s, PEC for all the discussed Δh were less than 1, indicating that the overall performance of the USR-PTR is inferior to the CSS-PTR under conditions of small flow rates. When applied in cases of larger flow rates, the advantage of the USR-PTR in improving the overall performance is more obvious. It can also be found from the figure that PEC decreased with the increase of Δh . For example, as the m was 2 kg/s, the PEC for $\Delta h=3$ mm, $\Delta h=5$ mm, $\Delta h=7$ mm and $\Delta h=9$ mm was 1.098, 1.087, 1.083 and 1.071, respectively. This demonstrates that the growth rate of the heat transfer enhancement with increasing rib height is smaller than that of the increase of pressure loss. Therefore, in view of the overall performance, the USR-PTR with small rib height is more applicable in practice. The maximum PEC was 1.098 obtained for $\Delta h=3$ mm at $m=2$ kg/s, indicating that the overall performance of the USR-PTR can be improved by 9.8% to the CSS-PTR by changing the rib height (Δh).

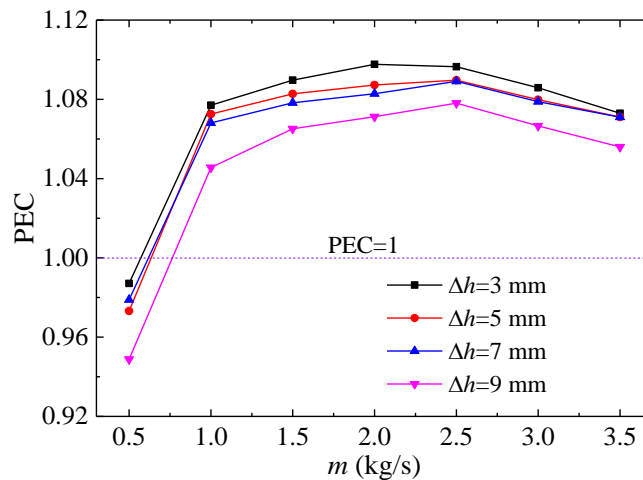


Fig. 6.38 Variation of PEC with mass flow rate under different rib heights

6.7.3 Influences of the corner radius of the rib

Fig. 6.39 shows the variation of Nu/Nu_0 with mass flow rate (m) under different corner radiuses (R_{co}). It is clearly seen from the figure that for all R_{co} , Nu/Nu_0 first increased quickly, and then declined slowly with the increase of m . For instance, when R_{co} was 10 mm, the Nu/Nu_0 increased from 1.414 at $m=0.5$ kg/s to the peak value of 1.723 at $m=3$ kg/s, and then dropped to 1.704 at $m=3.5$ kg/s. Furthermore, the Nu/Nu_0 under condition of large flow rate was larger and more stable than that under condition of small flow rate, indicating that the USR-PTR is more suitable for situations with larger flow rate. It can also be found that Nu/Nu_0 decreased consistently with the increase of R_{co} . Take $m=2$ kg/s as an example, the Nu/Nu_0 for $R_{co}=5$ mm, $R_{co}=10$ mm, $R_{co}=15$ mm and $R_{co}=20$ mm was 1.738, 1.699, 1.662 and 1.634, respectively. The reason is that when R_{co} is increased, the bottom edges of the rib become more flat and smooth, allowing the fluid flowing more gently over the rib, consequently reducing the disturbance intensity and weakening the heat transfer. The maximum Nu/Nu_0 was 1.76 achieved for $R_{co}=5$ mm in the case of $m=2.5$ kg/s, which means that, compared with the CSS-PTR, the heat transfer of the USR-PTR can be enhanced by up to 76% by reducing the corner radius (R_{co}).

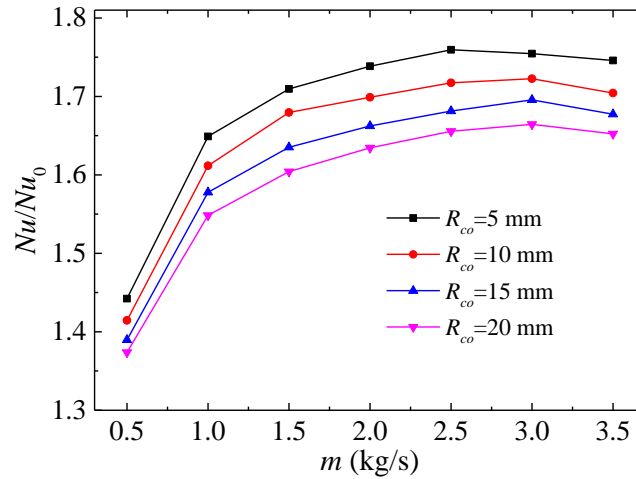


Fig. 6.39 Variation of Nu/Nu_0 with mass flow rate under different corner radiuses

Fig. 6.40 shows the variation of f/f_0 with mass flow rate (m) under different corner radiuses (R_{co}). Obviously, the variation curves of f/f_0 for all R_{co} first increased with the increase of m , and then became flat. This demonstrates that the increase of pressure loss of the USR-PTR is getting closer to that of the CSS-PTR with the increase of flow rate. For any m , f/f_0 decreased constantly with the increase of R_{co} . For instance, when the m was 2 kg/s, the f/f_0 for $R_{co}=5$ mm, $R_{co}=10$ mm, $R_{co}=15$ mm and $R_{co}=20$ mm was 4.07, 3.75, 3.46 and 3.24, respectively. This is because increasing the corner radius makes the rib bottom edges more flat and smooth, hence reducing the flow resistance. The maximum f/f_0 was about 4.33 obtained for $R_{co}=5$ mm in the case of $m=3.5$ kg/s, indicating that the pressure drop of the USR-PTR can be up to 4.33 times that of the CSS-PTR by decreasing the corner radius (R_{co}).

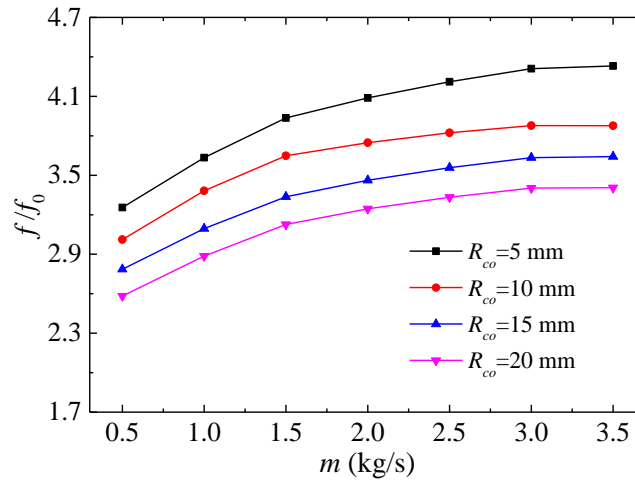


Fig. 6.40 Variation of f/f_0 with mass flow rate under different corner radiuses

Fig. 6.41 presents the variation of PEC with mass flow rate (m) under different corner radiuses (R_{co}). It is clearly seen from the figure that PEC first increased quickly and then maintained slow growth, and finally decreased with the increase of m . When m was 0.5 kg/s, the PEC for $R_{co}=5$ mm, $R_{co}=10$ mm and $R_{co}=15$ mm were all less than 1, which means that the overall performance of the USR-PTR is poorer than the CSS-PTR in those cases. The overall performance of the USR-PTR was much better under conditions of larger flow rate ($m > 1$ kg/s). It can also be found from the figure that PEC increased continuously with the increase of R_{co} . For example, when the m was 2 kg/s, the PEC for $R_{co}=5$ mm, $R_{co}=10$ mm, $R_{co}=15$ mm and $R_{co}=20$ mm was 1.087, 1.094, 1.099 and 1.104, respectively. This demonstrates that the drop rate of the increase of pressure loss with increasing corner radius is larger than that of the heat transfer enhancement. Therefore, increasing the corner radius is an effective way to improve the overall performance of the USR-PTR. The maximum PEC was 1.108 obtained for $R_{co}=20$ mm at $m=2.5$ kg/s, indicating that the overall performance of the USR-PTR can

be improved by up to 10.8% compared with the CSS-PTR by increasing the corner radius of the rib (R_{co}).

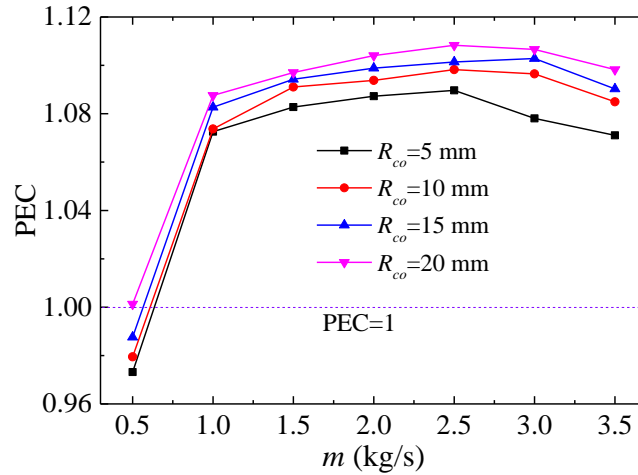


Fig. 6.41 Variation of PEC with mass flow rate under different corner radiuses

6.7.4 Influences of the crest radius of the rib

Fig. 6.42 shows the variation of Nu/Nu_0 with mass flow rate (m) under different crest radiuses (R_{cr}). It is clearly seen from the figure that for all R_{cr} , Nu/Nu_0 first increased quickly, and then declined slightly with the increase of m . For instance, when R_{cr} was 3 mm, the Nu/Nu_0 increased from 1.442 at $m=0.5$ kg/s to the peak value of 1.759 at $m=2.5$ kg/s, and then dropped to 1.746 at $m=3.5$ kg/s. The figure also shows that Nu/Nu_0 decreased consistently with the increase of R_{co} . Take $m=2$ kg/s as an example, the Nu/Nu_0 for $R_{cr}=5$ mm, $R_{cr}=10$ mm, $R_{cr}=15$ mm and $R_{cr}=20$ mm was 1.775, 1.738, 1.698 and 1.661, respectively. The reason is that when R_{cr} is increased, the crest edges of the rib become more flat and smooth, allowing the fluid flowing more gently over the rib,

consequently reducing the disturbance intensity and weakening the heat transfer. The maximum Nu/Nu_0 was 1.8 achieved for $R_{cr}=2$ mm in the case of $m=2.5$ kg/s, which means that, compared with the CSS-PTR, the heat transfer of the USR-PTR can be enhanced by up to 80% by reducing the crest radius (R_{cr}).

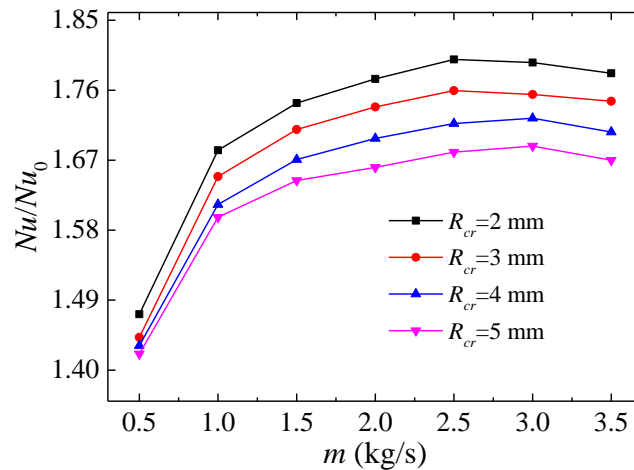


Fig. 6.42 Variation of Nu/Nu_0 with mass flow rate under different crest radiuses

Fig. 6.43 shows the variation of f/f_0 with mass flow rate (m) under different crest radiuses (R_{cr}). It is clearly seen from the figure that the f/f_0 for all R_{cr} increased with the increase of m , while the growth rate decreased consistently. This demonstrates that the increase of pressure loss of the USR-PTR is getting closer to that of the CSS-PTR with the increase of flow rate. For any m , f/f_0 decreased constantly with the increase of R_{cr} . For example, when the m was 2 kg/s, the f/f_0 for $R_{cr}=2$ mm, $R_{cr}=3$ mm, $R_{cr}=4$ mm and $R_{cr}=5$ mm was 4.34, 4.09, 3.77 and 3.48, respectively. This is because increasing the crest radius makes the rib upper edges more flat and smooth, hence reducing the flow resistance. The maximum f/f_0 was about 4.61 obtained for $R_{cr}=2$ mm in the case of $m=3.5$ kg/s, indicating that the pressure drop of the USR-PTR can be up to 4.33 times

that of the CSS-PTR by decreasing the crest radius (R_{cr}).

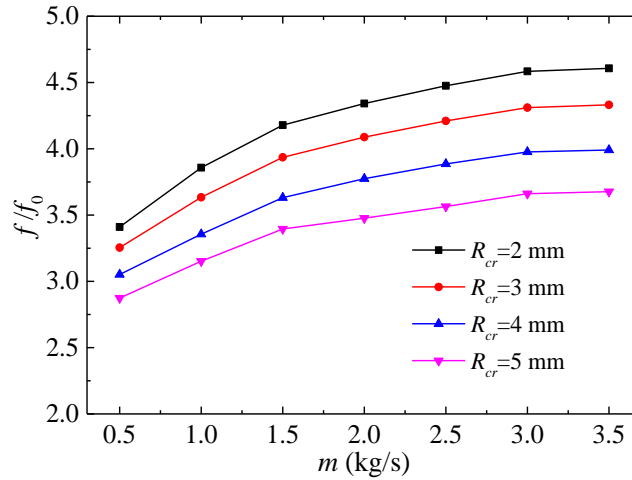


Fig. 6.43 Variation of f/f_0 with mass flow rate under different crest radiuses

Fig. 6.44 depicts the variation of PEC with mass flow rate (m) under different crest radiuses (R_{cr}). It is clearly seen from the figure that PEC first increased quickly and then maintained slow growth, and finally decreased with the increase of m . Except the case that m was 0.5 kg/s, the PEC for other mass flow rates were all larger than 1, indicating that the overall performance of the USR-PTR is better than the CSS-PTR in most cases. It can also be found from the figure that the PEC curves for $R_{cr}=2$ mm and $R_{cr}=3$ mm almost coincided, and afterwards the PEC increased with further increasing R_{cr} . Therefore, increasing the crest radius is an effective way to improve the overall performance of the USR-PTR. The maximum PEC was 1.096 obtained for $R_{cr}=5$ mm at $m=2.5$ kg/s, indicating that the overall performance of the USR-PTR can be improved by 9.6% compared with the CSS-PTR by increasing the crest radius of the rib (R_{cr}).

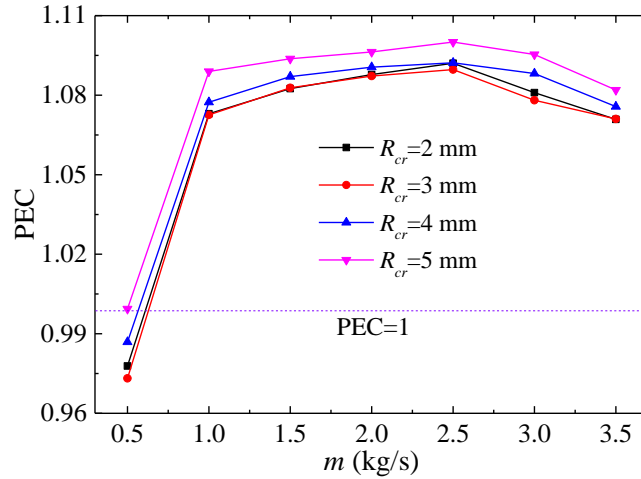


Fig. 6.44 Variation of PEC with mass flow rate under different crest radiuses

6.7.5 Influences of the spiral angle of the rib

Fig. 6.45 shows the variation of Nu/Nu_0 with mass flow rate (m) under different spiral angles (α_s). It can be clearly seen from the figure that Nu/Nu_0 for all α_s first increased, and then decreased slowly with the increase of m . Overall, the heat transfer enhancement of USR-PTR is more obvious under conditions of large flow rates. It can also be found from the figure that Nu/Nu_0 first increased and then declined slightly with the increase of α_s . Take $m=2$ kg/s as an example, the Nu/Nu_0 for $\alpha_s=15^\circ$, $\alpha_s=30^\circ$, $\alpha_s=45^\circ$, $\alpha_s=60^\circ$ and $\alpha_s=75^\circ$ was 1.272, 1.648, 1.699, 1.738 and 1.522 respectively. Obviously, $\alpha_s=60^\circ$ is the spiral angle that produces the maximum heat transfer enhancement among the five discussed spiral angles. The maximum Nu/Nu_0 was 1.76 achieved for $\alpha_s=60^\circ$ in the case of $m=2.5$ kg/s, which indicates that, compared with the CSS-PTR, the heat transfer of the USR-PTR can be augmented by 76% by changing the spiral angle (α_s).

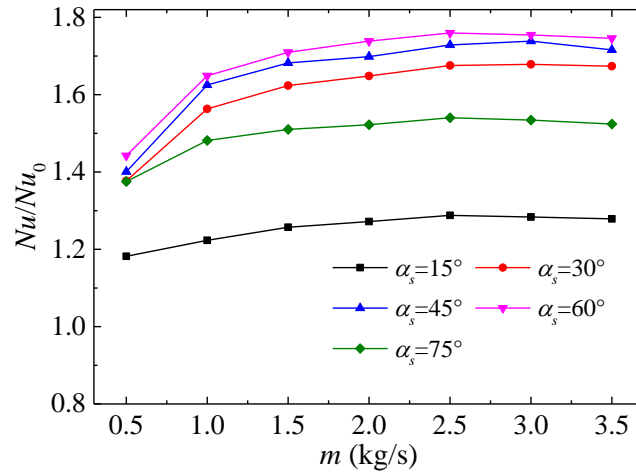


Fig. 6.45 Variation of Nu/Nu_0 with mass flow rate under different spiral angles

Fig. 6.46 shows the variation of ff_0 with mass flow rate (m) under different spiral angles (α_s). It can be seen from the figure that ff_0 for most R_{co} increased with the increase of m , and the growth rate increased with the increase of R_{co} . This means that the pressure loss is more easily affected by the flow rate in the cases of larger spiral angles. For any m , ff_0 increased constantly with the increase of R_{co} . For instance, when the m was 2 kg/s, the ff_0 for $\alpha_s=15^\circ$, $\alpha_s=30^\circ$, $\alpha_s=45^\circ$, $\alpha_s=60^\circ$ and $\alpha_s=75^\circ$ was 1.47, 2.09, 2.86, 4.09 and 5.13 respectively. The main reason is that the constraint effect of the ribs is enhanced by increasing the spiral angle, consequently increasing the flow resistance. The maximum ff_0 was about 5.51 obtained for $\alpha_s=75^\circ$ in the case of $m=3.5$ kg/s, indicating that the pressure drop of the USR-PTR can be increased by up to 4.51 times that of the CSS-PTR by increasing the spiral angle (α_s).

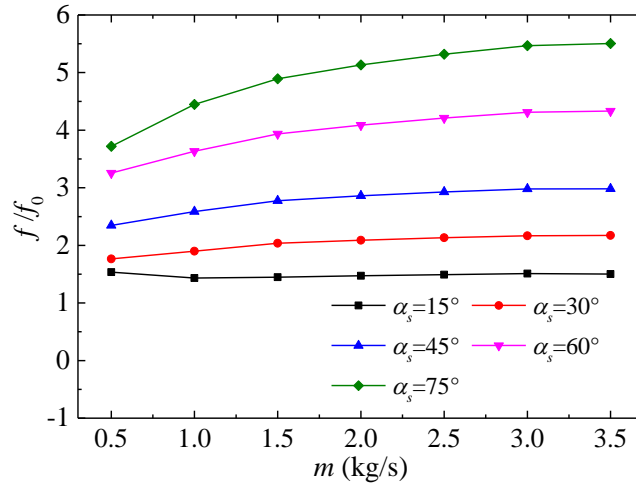


Fig. 6.46 Variation of f/f_0 with mass flow rate under different spiral angles

Fig. 6.47 presents the variation of PEC with mass flow rate (m) under different spiral angles (α_s). It is easily seen from the figure that the PEC for $\alpha_s=75^\circ$ was smaller than 1 in the discussed flow rate range, revealing that the overall performance of the USR-PTR is always poorer than that of the CSS-PTR in this case. Thus, the spiral angle of the rib should not be too large in practical application. PEC for other four spiral angles first increased quickly and then varied slightly with the increase of m . This demonstrates that the overall performance enhancement of the USR-PTR is more obvious and stable under condition of large flow rates. The figure also shows that the PEC first increased and then decreased with the increase of α_s . Take $m=2$ kg/s as an example, the PEC for $\alpha_s=15^\circ$, $\alpha_s=30^\circ$, $\alpha_s=45^\circ$, $\alpha_s=60^\circ$ and $\alpha_s=75^\circ$ was 1.118, 1.289, 1.196, 1.087 and 0.882 respectively. It is easily found from the figure that $\alpha_s=30^\circ$ is the optimum among the five discussed spiral angles that produces the maximum overall performance for the USR-PTR. Therefore, in view of overall performance, the spiral angle of 30° is the most advisable for structural design. The maximum PEC was 1.301 obtained for $\alpha_s=30^\circ$ at

$m=2.5$ kg/s, which demonstrates that, compared with the CSS-PTR, the overall performance of the USR-PTR can be improved by up to 30.1% by changing the spiral angle of the rib (α_s).

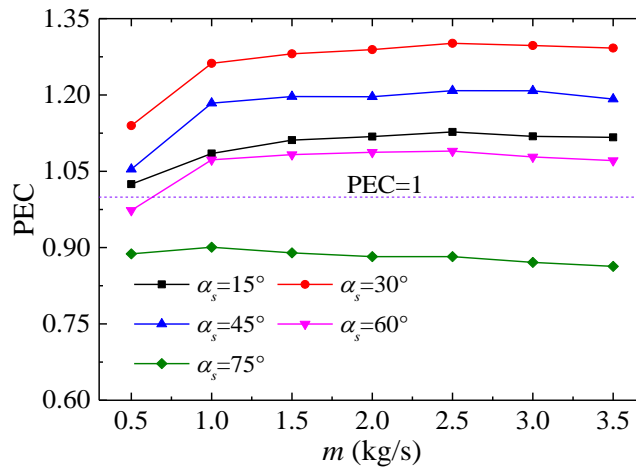


Fig. 6.47 Variation of PEC with mass flow rate under different spiral angles

6.8 Summary

Based on the idea of enhancing the heat transfer between the bottom inner surface of the absorber tube and the fluid, this chapter proposed a novel unilateral spiral ribbed parabolic trough receiver (USR-PTR) for improving the thermal performance of PTC. The thermal performance of the conventional straight-smooth parabolic trough receiver (CSS-PTR) is first discussed, and then a comprehensive comparison between the USR-PTR and the CSS-PTR is conducted, revealing the advantage and potential of the USR-PTR in thermal enhancement. Based on the performance evaluation criteria (PEC), the influences of the structural parameters of the spiral rib on the overall performance of

the USR-PTR were also investigated comprehensively. Some important conclusions can be drawn as follows:

(1) The temperature distribution of the absorber wall depends completely on the heat flux distribution. The circumferential temperature difference is much larger than the inner and outer surface temperature difference and remains constant along the longitudinal direction, which is the main cause of receiver deformation. As the mass flow rate grows, the distribution of fluid temperature on the cross-section changes from annular stratification to vertical stratification. When the annular space is filled with air or the glass envelope is broken, the collector efficiency is reduced respectively by 4.31% and 26.1% to the case of vacuum annulus, indicating that ensuring the vacuum state in the annulus is critical to achieving high performance of the PTR.

(2) Fluid disturbance, secondary rotational flow and local longitudinal vortices induced by the discontinuous spiral ribs are the three main causes of heat transfer enhancement in the USR-PTR. The USR-PTR enhances the heat transfer capacity at the expense of increasing obviously the pressure loss. The temperature on the absorber wall is more uniform and the circumferential temperature difference is reduced effectively by using the USR-PTR. For the structure discussed in the study, the circumferential temperature difference of the USR-PTR is reduced at most by 25% to the CSS-PTR. The degree of synergy between velocity field and

temperature gradient field of the fluid in the USR-PTR is much better than that in the CSS-PTR, revealing clearly the heat transfer enhancement mechanism. The advantage of the USR-PTR in improving the overall performance of the PTR is more obvious in the cases of large flow rates. In practice, the USR-PTR should be applied in cases of relatively large flow rates ($m > 1.25$ kg/s).

- (3) Both heat transfer and pressure loss increase with reducing the rib pitch interval or increasing the rib height or reducing the corner radius or reducing the crest radius. When the mass flow rates is larger than 2.5 kg/s, the overall performance of the USR-PTR is enhanced by increasing the rib pitch interval, while weakened as the mass flow rate is less than 1 kg/s. Within the discussed flow rate range (0.5 ~ 3.5 kg/s), the overall performance of the USR-PTR is improved constantly by decreasing the rib height or increasing the corner radius or increasing the crest radius. The maximum improvement of the overall performance of the USR-PTR, compared with the CSS-PTR, by setting individually the pitch interval, the rib height, the corner radius and the crest radius is 12.5%, 9.8%, 10.8% and 9.6% respectively.
- (4) With the increase of the rib spiral angle, the heat transfer increases first and then decreases, while the pressure loss increases continuously. The pressure loss is more sensitive to the flow rate under the condition of larger spiral angles. Among the five discussed spiral angles (15°, 30°, 45°, 60° and 75°), the optimal one to achieve the

maximum overall performance for the USR-PTR is 30° . Compared with the CSS-PTR, the overall performance of the USR-PTR can be improved by up to 30.1% by using the optimal spiral angle ($\alpha_s=30^\circ$).

CHAPTER 7

CONCLUSIONS AND RECOMMENDATIONS FOR FUTURE WORK

7.1 Conclusions

This thesis investigates comprehensively the optical and thermal performance of the parabolic trough solar collector (PTC), revealing its mechanism of photo-thermal conversion. The Monte Carlo Rays Tracing (MCRT) method coupled with theoretical analyses are used for investigating the rays-concentrating process, and a computational fluid dynamics (CFD) tool is adopted for simulation of the thermal and hydraulic performance of the parabolic trough receiver (PTR). Based on the idea of enhancing the heat transfer between the fluid and the high heat flux area (i.e. the bottom part) of the absorber tube, a novel unilateral spiral ribbed parabolic trough receiver (USR-PTR) is proposed for improving the thermal performance of the PTC and evaluated accordingly. The main conclusions are summarized as follows:

The optical performance of the PTC under ideal optical conditions is first investigated using the MCRT method coupled with geometrical analyses. Some important parameters including the critical absorber diameter, the rim angle, the effective angle span receiving concentrated rays, the angle span at the bottom of the absorber that cannot receive concentrated rays and the width at the apex area of the reflector that

cannot receive incident solar rays, are derived theoretically. The effects of structural parameters, including aperture width, focal length and absorber diameter, on the optical performance of the PTC are investigated comprehensively. It is found that there is a critical absorber diameter, smaller than which the absorber can only receive partially reflected rays, resulting in rays-spillage and consequently causing huge optical loss. Both the aperture width and the focal length should be kept in a certain range ($W_c \leq 12.93$ m and $0.21 \text{ m} \leq f_c \leq 7.31$ m) to avoid rays-spillage. The distribution range of high local concentration ratio (LCR) on the absorber outer surface increases with increasing aperture width, while decreases with increasing focal length. The peak LCR increases constantly with increasing aperture width, while drops firstly and then increases with increasing focal length. As the aperture width is smaller or the focal length is larger than a certain value ($W_c \leq 0.92$ m or $f_c \geq 4$ m), the only peak LCR occurs at the bottom of the absorber (i.e. $\varphi_a = 0^\circ$), Larger absorber diameter reduces both the peak LCR and the high LCR distribution range, and increases the optical efficiency. As the focal length is small or the absorber diameter is large enough, the apex area of parabolic reflector and the bottom area of the absorber cannot receive any solar rays due to the shadowing effect of the absorber itself.

Then, the effects of various non-ideal optical factors on the PTC's optical performance are also explored. All the non-ideal optical factors, such as uneven sunshape and various optical errors including specular error, tracking error, slope error and absorber alignment error, and incident angle are characterized individually according to their

generation principles. Coordinate transformation is performed and an effective sunshape model is established for building non-ideal optical models. Results show that both larger CSRs and larger specular errors produce more uniform heat flux distribution. Small specular errors (< 5 mrad) play the role of cutting peaks and filling valleys in the high heat flux area. The advantage of the high optical quality reflector in increasing the optical efficiency is outstanding only in clear days. Both the tracking error and the slope error should be less than a threshold (4 mrad and 2 mrad respectively) to achieve high optical efficiency. The optical efficiency is more sensitive to the slope error than to the tracking error, indicating that improving the local topography of the reflector surface is an effective way to improve the PTC's performance. The offset direction along X-axis causes the greatest optical loss, and that along the positive Y-axis (i.e. $\alpha=90^\circ$) poses threat of overheat on the absorber surface. When the absorber alignment error and the tracking error are in the opposite direction, the optical loss can to some extent be compensated by themselves, defined as compensation effect, whereas that in the same direction will aggravate the optical loss, defined as weakening effect. The slope error weakens the compensation effect and aggravates the weakening effect. Moreover, the extent to which the slope error reduces the compensation effect is greater than the extent to which the slope error aggravates the weakening effect. The non-zero incident angle results in cosine loss and end loss, which, respectively, weakens the effective incident solar irradiance and causes rays-spillage at one end of the collector, reducing significantly the optical efficiency. Due to the end loss, a near-zero heat flux section is formed at one end of the absorber, the length of which increases with

increasing incident angle. The weakening effects of optical factors (CSR, tracking error, slope error and absorber alignment error) on the optical efficiency become less obvious as incident angle increases. The optical efficiency is more sensitive to the offset angle under larger offset distances, and this sensitivity decreases with the increase of incident angle.

Succeeding to the above MCRT simulation, detailed theoretical analyses on the rays-concentrating process of the PTC under non-ideal optical conditions are performed. Based on the theory of spatial analytic geometry, the formulas of critical absorber diameter under any optical error conditions are derived. A new theoretical algorithm based on the idea of viewing the sun as consisting of countless line light sources is developed for quick calculation of optical efficiency. It is proved that the proposed algorithm, compared with the MCRT method, has great advantage of time saving, which is suitable for engineering application. The effective solar radial size is further discussed based on the derived formulas and the proposed algorithm. It is revealed that the effective solar radial size depends on both the optical quality of the reflector and the weather condition. For the situations that both the circumsolar ratio and the specular error are very small (i.e. little atmospheric scattering and high optical quality), it is acceptable to use the solar disk to represent the whole reflected sunshape. The changing properties of optical efficiency achieved by the MCRT method in the preceding chapter are well explained using the theoretical results. For any couple of specular errors, there is usually a critical radial angle, of which the bounded energy ratios for the two

specularity errors are the same. In practice, if the radial acceptance angle of the PTC is smaller than the critical radial angle, the optical efficiency of the smaller specularity error will be larger than that of the larger specularity error. Otherwise, the optical efficiency of the smaller specularity error will instead be smaller. The drop of optical efficiency caused by rays-spillage is well explained by the critical absorber diameter calculated by the theoretically deduced formulas. It is found that the offset direction which is in the same direction as the equivalent deflecting error and perpendicular to the focus-edge connection line is the direction that is most likely to cause rays-spillage. Whereas, the offset direction along the X-axis which is in the opposite direction of the equivalent deflecting error is the direction that is least likely to cause rays-spillage.

Based on the idea of enhancing the heat transfer between the fluid and the high heat flux area of the absorber tube, a novel unilateral spiral ribbed parabolic trough receiver (USR-PTR) is proposed for improving the thermal performance of PTC. The thermal performance of the conventional straight-smooth parabolic trough receiver (CSS-PTR) is first discussed, and a comprehensive comparison between the USR-PTR and the CSS-PTR is then conducted. The heat flux distribution obtained by the MCRT method is added as the boundary condition on the absorber outer surface by User Defined Functions (UDF) to realize the simulation of heat transfer under actual conditions. The thermal enhancement mechanism of the USR-PTR is analyzed based on the synergy theory. Based on the performance evaluation criteria (PEC), the influences of the structural parameters of the spiral rib on the overall performance of the USR-PTR

are also investigated comprehensively. Results show that the temperature distribution of the absorber wall depends completely on the heat flux distribution. The circumferential temperature difference remains constant along the longitudinal direction, which is the main cause of receiver deformation. When the annular space is filled with air or the glass envelope is broken, the collector efficiency is reduced respectively by 4.31% and 26.1% to the case of vacuum annulus. As the mass flow rate grows, the distribution of fluid temperature on the cross-section changes from annular stratification to vertical stratification. In most cases of the discussed flow rates (0.5~3.5 kg/s), the overall performance of the USR-PTR was better than that of the CSS-PTR. For the structure discussed in the study, the circumferential temperature difference of the USR-PTR is reduced at most by 27.4% to the CSS-PTR. The synergy between velocity field and temperature gradient field (i.e. heat flow field) of the fluid in the USR-PTR is much better than that in the CSS-PTR, revealing clearly the heat transfer enhancement mechanism. The advantage of the USR-PTR in improving the overall performance of the PTR is more obvious in the cases that the flow rates are larger than 1.25 kg/s. Both the heat transfer capacity and the pressure loss increased with reducing the rib pitch interval or increasing the rib height or reducing the corner radius or reducing the crest radius. When the mass flow rate is larger than 2.5 kg/s, the overall performance of the USR-PTR is enhanced by increasing the rib pitch interval, while weakened as the mass flow rate is less than 1 kg/s. Within the discussed flow rate range, the overall performance of the USR-PTR is improved constantly by decreasing the rib height or increasing the corner radius or increasing the crest radius. The maximum PEC

of the USR-PTR, compared with the CSS-PTR, by setting individually the pitch interval, the rib height, the corner radius and the crest radius is 1.125, 1.098, 1.108 and 1.096 respectively. With the increase of the rib spiral angle, the heat transfer increases first and then decreases, while the pressure loss increases continuously. The pressure loss is more sensitive to the flow rate under the condition of larger spiral angle. Among the five discussed spiral angles (15° , 30° , 45° , 60° and 75°), the optimal one to achieve the maximum PEC for the USR-PTR is 30° , which produces the PEC of 1.301.

This thesis conducts detailed study on the optical and thermal performance of the PTR, aiming to reveal its rays-concentrating mechanism and seek thermal improvement methods. The findings in this study enrich the basic research theory in the field of PTR, and provide important theoretical guidance for the application and promotion of PTRs. The developed algorithm for quick calculation of optical efficiency is very suitable for engineering application, and the proposed thermal improvement method provides a new idea for engineers and designers to optimize the structure of the PTR.

7.2 Recommendations for future work

Due to time limitation, there is still insufficiency in this study, which deserves further research in the future.

As mentioned in literatures, the uneven temperature distribution leads to thermal stress

which is the direct cause of receiver tube destruction. Therefore, it is necessary to investigate the distribution of the thermal stress and its impacts on the receiver tube deformation in the future.

As for the proposed USR-PTR, this study conducted a detailed numerical simulation to reveal its heat transfer enhancement mechanism and the individual influences of each structural parameter. An experimental study is needed in the future to test the actual performance of the proposed USR-PTR. Furthermore, a parametrical optimization should be conducted for the USR-PTR, taking into account the coupling effects of all the structural parameters.

The Optical efficiencies of different sizes of PTCs under various non-ideal conditions and the allowable optical error ranges can be summarized in the future to be made into charts for quick engineering query.

REFERENCES

- [1] Global Energy Review. Enerdata Publication, 2012.
- [2] BP Statistical Review of World Energy, 2018.
- [3] He ZN. Solar Thermal Utilization. Hefei: University of Science and Technology of China Press, 2009. (In Chinese)
- [4] Smil V. General energetics: energy in the biosphere and civilization. New York: John Wiley & Sons; 1991.
- [5] Vijay D, Mansoor A, Soma SS, Robert-C G, Douglas N, Craig N. Solar energy: Trends and enabling technologies. Renewable and Sustainable Energy Reviews 2013; 19: 555-564.
- [6] Kalogirou SA. Solar thermal collectors and applications. Progress in Energy and Combustion Science 2004; 30: 231-295.
- [7] Solangi KH, Islam MR, Saidur R, Rahim NA, Fayaz H. A review on global solar energy policy. Renewable and Sustainable Energy Reviews 2011; 15: 2149-2163.
- [8] Wang FQ, Cheng ZM, Tan JY, Yuan Y, Shuai Y, Liu LH. Progress in concentrated solar power technology with parabolic trough collector system: A comprehensive review. Renewable and Sustainable Energy Reviews 2017; 79: 1314-1328.
- [9] Li J. Scaling up concentrating solar thermal technology in China. Renewable and Sustainable Energy Reviews 2009; 13: 2051-2060.
- [10] Xu XH, Vignarooban K, Xu B, Hsu K, Kannan AM. Prospects and problems of concentrating solar power technologies for power generation in the desert regions.

Renewable and Sustainable Energy Reviews 2016; 53:1106-1131.

[11] International Energy Agency. IEA Technology Roadmap: Concentrating Solar Power: Complete Edition. SourceOECD 2015.

[12] <http://www.cspplaza.com/article-14058-1.html>

[13] Price H, Lufert E, Kearney D, Zarza E, et al. Advances in parabolic trough solar power technology. Journal of Solar Energy Engineering 2002; 124: 109-125.

[14] Schiel W. Collector development for solar parabolic trough power plants. Bautechnik 2012; 89: 182-191.

[15] Jebasingh VK, Joselin Herbert GM. A review of solar parabolic trough collector. Renewable and Sustainable Energy Reviews 2016; 54: 1085-1091.

[16] Fernandez GA, Zarza E, Valenzuela L. Perez M. Parabolic-trough solar collectors and their applications. Renewable and Sustainable Energy Reviews 2010; 14: 1695-1721.

[17] Kalogirou SA. Parabolic trough collectors for industrial process heat in Cyprus. Energy 2002; 27: 813-830.

[18] Collins T, Parker SA. Parabolic-trough solar water heating, renewable technology for reducing water-heating costs. Federal Technology Alert. Tech. Rep. No. DOE/GO-102000-0973. Washington: DOE; 2000.

[19] Kalogirou SA. Use of parabolic trough solar energy collectors for sea-water desalination. Applied Energy 1998; 60: 65-88.

[20] Cabrera FJ, Fernandez-Garcia A, Silva RMP, Perez-Garcia M. Use of parabolic trough solar collectors for solar refrigeration and air-conditioning applications.

Renewable and Sustainable Energy Reviews 2013; 20: 103-118.

[21] Abedini-Sanigy MH, Ahmadi F, Goshtasbirad E, Yaghoubi M. Thermal stress analysis of absorber tube for a parabolic collector under quasi-steady state condition. Energy Procedia 2015; 69: 3-13.

[22] Burkhard DG, Shealy DL, SEXTL RU. Specular reflection of heat radiation from an arbitrary reflection of heat radiation from an arbitrary receiver surface. International Journal of Heat and Mass Transfer 1973; 16: 271-280.

[23] Evans DL. On the performance of cylindrical parabolic solar concentrators with flat absorbers. Solar Energy 1977; 19: 379-385.

[24] Nicolas RO, Duran JC. Generalization of the two-dimensional optical analysis of cylindrical concentrators. Solar Energy 1980; 25: 21-31.

[25] Duran JC, Nicolas RO. Development and application of a two-dimensional optical analysis of non-perfect cylindrical concentrators. Solar Energy 1984; 34: 257-269.

[26] Jeter SM. The distribution of concentrated solar radiation in paraboloid collectors. Journal of Solar Energy Engineering 1986; 108: 219-225.

[27] Jeter SM. Calculation of the concentrated flux density distribution in parabolic trough collectors by a semifinite formulation. Solar Energy 1986; 37: 335-345.

[28] Jeter SM. Analytical determination of the optical performance of practical parabolic trough collectors from design data. Solar Energy 1987; 39: 11-21.

[29] Cheng ZD, He YL, Cui FQ. A new modelling method and unified code with MCRT for concentrating solar collectors and its applications. Applied Energy 2013; 101: 686-698.

- [30] Cheng ZD, He YL, Wang K, Du BC, Cui FQ. A detailed parameter study on the comprehensive characteristics and performance of a parabolic trough solar collector system. *Applied Thermal Engineering* 2014; 63: 278-289.
- [31] Cheng ZD, He YL, Cui FQ, Du BC, Zheng ZJ, Xu Y. Comparative and sensitive analysis for parabolic trough solar collectors with a detailed Monte Carlo ray-tracing optical model. *Applied Energy* 2014; 115: 559-572.
- [32] Cheng ZD, He YL, Du BC, Wang K, Liang Q. Geometric optimization on optical performance of parabolic trough solar collector systems using particle swarm optimization algorithm. *Applied Energy* 2015; 148: 282-293.
- [33] Cheng ZD, Zhao XR, He YL. Novel optical efficiency formulas for parabolic trough solar collectors: computing method and applications. *Applied Energy* 2018; 224: 682-697.
- [34] Zhao D, Xu E, Yu Q, Lei D. The simulation model of flux density distribution on an absorber tube. *Energy Procedia* 2015; 69: 250-258.
- [35] Liang HB, You SJ, Zhang H. Comparison of three optical models and analysis of geometric parameters for parabolic trough solar collectors. *Energy* 2016; 96: 37-47.
- [36] Liang HB, Fan M, You SJ, Zheng WD, Zhang H, Ye TZ, Zheng XJ. A Monte Carlo method and finite volume method coupled optical simulation method for parabolic trough solar collectors. *Applied Energy* 2017; 201: 60-68.
- [37] Fan M, You SJ, Xia JB, Zheng WD, Zhang H, Liang HB, Li XL, Li BJ. An optimized Monte Carlo ray tracing optical simulation model and its applications to line-focus concentrating solar collectors. *Applied Energy* 2018; 225: 769-781.

- [38] Song JF, Zhou ZL, Tong K. An algorithm for the flux distribution over the flat absorber of a parabolic trough concentrator. *Solar Energy* 2016; 125: 32-42.
- [39] Song JF, Tong K, Li L, Luo G, Yang LJ, Zhao J. A tool for fast flux distribution calculation of parabolic trough solar concentrators. *Solar Energy* 2018; 173: 291-303.
- [40] Serrano-Aguilera JJ, Valenzuela L, Fernandez-Reche J. Inverse Monte Carlo Ray-Tracing method (IMCRT) applied to line-focus reflectors. *Solar Energy* 2016; 124: 184-197.
- [41] Serrano-Aguilera JJ, Valenzuela L, Fernandez-Reche J. Modified geometry of line-focus collectors with round absorbers by means of the inverse MCRT method. *Solar Energy* 2016; 139: 608-621.
- [42] Atkinson Carol, Sansom Chris L, Almond Heather J, Shaw Chris P. Coatings for concentrating solar systems – A review. *Renewable and Sustainable Energy Review* 2015; 45: 113-122.
- [43] Manikandan GK, Iniyan S, Goic R. Enhancing the optical and thermal efficiency of a parabolic trough collector - A review. *Applied Energy* 2018; 235: 1524-1540.
- [44] Jamali H. Investigation and review of mirrors reflectance in parabolic trough solar collectors (PTSCs). *Energy Reports* 2019; 5: 145-158.
- [45] Tsai C-Y. Optimized solar thermal concentrator system based on free-form trough reflector. *Solar Energy* 2016; 125: 146-160.
- [46] Zhu Y, Shi J, Li Y, Wang L, Huang Q, Xu G. Design and experimental investigation of a stretched parabolic linear Fresnel reflector collecting system. *Energy Conversion and Management* 2016; 126: 89-98.

- [47] Ma XL, Zheng HF, Chen ZL. An investigation on a compound cylindrical solar concentrator (CCSC). *Applied Thermal Engineering* 2017; 120: 719-727.
- [48] Wang YJ, Liu QB, Sun J, Lei J, Ju Y, Jin HG. A new solar receiver/reactor structure for hydrogen production. *Energy Conversion and Management* 2017; 133: 118-126.
- [49] Canavarro D, Chaves J, Collares-Pereira M. New second-stage concentrators (XX SMS) for parabolic primaries; comparison with conventional parabolic trough concentrators. *Solar Energy* 2013; 92: 98-105.
- [50] Wang K, He YL, Cheng ZD. A design method and numerical study for a new type parabolic trough solar collector with uniform solar flux distribution. *Science China Technological Sciences* 2014; 57: 531-540.
- [51] Rodriguez-Sanchez D, Rosengarten G. Improving the concentration ratio of parabolic troughs using a second-stage flat mirror. *Applied Energy* 2015; 159: 620-632.
- [52] Wirz M, Petit J, Haselbacher A, Steinfeld A. Potential improvements in the optical and thermal efficiencies of parabolic trough concentrators. *Solar Energy* 2014; 107: 398-414.
- [53] Wang FQ, Tan JY, Ma LX, Wang CC. Effects of glass cover on heat flux distribution for tube receiver with parabolic trough collector system. *Energy Conversion and Management* 2015; 90: 47-52.
- [54] Xu CM, Chen ZP, Li M, Zhang P, Ji X, Luo X, Liu JT. Research on the compensation of the end loss effect for parabolic trough solar collectors. *Applied Energy* 2014; 115: 128-139.
- [55] Li M, Xu CM, Ji X, Zhang P, Yu QF. A new study on the end loss effect for

- parabolic trough solar collectors, *Energy* 2015; 82: 382-394.
- [56] Bellos E, Tzivanidis C. Investigation of a booster secondary reflector for a parabolic trough solar collector. *Solar Energy* 2019; 179: 174-185.
- [57] Gaul HH, Rabl AA. Incidence-angle modifier and average optical efficiency of parabolic trough collectors. *ASME. Journal of Solar Energy Engineering* 1980; 102 (1): 16-21.
- [58] Neumann A, Schubnell M. Irradiance and sunshape measurements for the Cologne site. *Proceedings of the 8th International Solar Forum, 1992*, pp. 1173-1183.
- [59] Neumann A, Witzke A, Jones SA, Schmitt G. Representative terrestrial solar brightness profiles. *Journal of Solar Energy Engineering* 2002; 124: 198-204.
- [60] Buie D, Monger AG, Dey CJ. Sunshape distributions for terrestrial solar simulations. *Solar Energy* 2003, 74: 113-122.
- [61] Bendt P, Rabl A, Gaul HW, Reed KA. Optical analysis and optimization of line focus solar collector. *SERI, Golden, CO 1979, Paper No. SERI / TR-34-092*.
- [62] Buie D, Monger AG. The effect of circumsolar radiation on a solar concentrating system. *Solar Energy* 2004; 76: 181-185.
- [63] Thomas A, Guven HM, Effect of optical errors on flux distribution around the absorber tube of a parabolic trough concentrator. *Energy Conversion and Management* 1994; 35(7): 575-582.
- [64] Treadwell G, Grandjean N. Systematic rotation and receiver location error effects on parabolic trough annual performance. *Journal of Solar Energy Engineering* 1982; 104: 345-348

- [65] Guven HM, Bannerot RB. Derivation of universal error parameters for comprehensive optical analysis of parabolic troughs. *Journal of Solar Energy Engineering* 1986; 108: 275-281.
- [66] Guven HM, Bannerot RB. Determination of error tolerances for the optical design of parabolic troughs for developing countries. *Solar Energy* 1986; 36: 535-550.
- [67] Grena R. Optical simulation of a parabolic solar trough collector. *International Journal of Sustainable Energy* 2010; 29: 19-36.
- [68] Grena R. Efficiency Gain of a solar trough collector due to an ir-reflective film on the non-irradiated part of the receiver. *International Journal of Green Energy* 2011; 8: 715-733.
- [69] Huang WD, Hu P, Chen ZS. Performance simulation of a parabolic trough solar collector. *Solar energy* 2012; 86: 746-755.
- [70] Zhu GD, Lewandowski A. A new optical evaluation approach for parabolic trough collectors: First-Principle optical intercept calculation. *Journal of Solar Energy Engineering*. 2012; 134: 041005-1-8.
- [71] Binotti M, Zhu GD, Gray A, Manzolini G, Silva P. Geometric analysis of three-dimensional effects of parabolic trough collectors. *Solar Energy* 2013; 88: 88-96.
- [72] Zhao DM, Xu ES, Wang ZF, Yu Q, Li X, Zhu LZ. Influences of installation and tracking errors on the optical performance of a solar parabolic trough collector. *Renewable Energy* 2016; 94: 197-212.
- [73] Mwesigye A, Huan ZJ, Bello-Ochende T, Meyer JP. Influence of optical errors on the thermal and thermodynamic performance of a solar parabolic trough receiver. *Solar*

Energy 2016; 135: 703-718.

[74] Zhang CZ, Xu GQ, Quan YK, Li HW. Optical sensitivity analysis of geometrical deformation on the parabolic trough solar collector with Monte Carlo Ray-Trace method, Applied Thermal Engineering 2016; 109: 130-137.

[75] Song JF, Tong K, Luo G, Li Lei. Influence of non-ideal optical factors in actual engineering on the safety and stability of a parabolic trough collector. Renewable Energy 2017; 113: 1293-1301.

[76] Aichouba A, Merzouk M, Valenzuela L, Zarza E, Kasbadji-Merzouk N. Influence of the displacement of solar receiver tubes on the performance of a parabolic-trough collector. Energy 2018; 159: 472-481.

[77] Dudley VE, Kolb GJ, Mahoney AR, Mancini TR, Matthews CW, Sloan M, Kearney D. Test Results: SEGS LS2 Solar Collector. Report of Sandia National Laboratories, Albuquerque, NM, USA, 1994; SANDIA 94-1884.

[78] Dudley VE, Evans LR, Matthews CW. Test Results Industrial Solar Technology Parabolic Trough Solar Collector Report of Sandia National Laboratories, Albuquerque, NM, USA, 1995, SANDIA 94-1117.

[79] Moss TA, Brosseau DA. Final Test Results for the Schott HCE on a LS-2 Collector. Report of Sandia National Laboratories, Albuquerque, NM, USA, 2005, SANDIA 2005-4034.

[80] Burkholder F, Kutscher C. Heat-Loss Testing of Solel's UVAC3 Parabolic Trough Receiver. 2008, Technical Report NREL/TP-550-42394.

[81] Burkholder F, Kutscher C. Heat-Loss Testing of of Schott's 2008 PTR70 Parabolic

Trough Receiver. 2009, Technical Report NREL/TP-550-45633.

[82] Gong GJ, Huang XY, Wang J, Hao ML. An optimized model and test of the China's first high temperature parabolic trough solar receiver. *Solar Energy* 2010; 84: 2230-2245.

[83] Kumaresan G, Sridhar R, Velraj R. Performance studies of a solar parabolic trough collector with a thermal energy storage system. *Energy* 2012; 47: 395-402.

[84] Chafie M, Aissa MFB, Bouadila S, Balghouthi M, Farhat A, Guizani A. Experimental investigation of parabolic trough collector system under Tunisian climate: Design, manufacturing and performance assessment. *Applied Thermal Engineering* 2016; 101: 273-283.

[85] Zhang L, Yu ZT, Fan LW, Wang WJ, et al. An experimental investigation of the heat losses of a U-type solar heat pipe receiver of a parabolic trough collector-based natural circulation steam generation system. *Renewable Energy* 2013; 57: 262-268.

[86] Lei DQ, Li Q, Wang ZF, Li J, Li JB. An experimental study of thermal characterization of parabolic trough receivers. *Energy Conversion and Management* 2013; 69: 107-115.

[87] Xu L, Wang ZF, Li X, Yuan GF, Sun FH, Lei DQ. Dynamic test model for the transient thermal performance of parabolic trough solar collectors. *Solar Energy* 2013; 95: 65-78.

[88] Xu L, Wang ZF, Li X, Yuan GF, Sun FH, Lei DQ, Li SD. A comparison of three test methods for determining the thermal performance of parabolic trough solar collectors. *Solar Energy* 2014; 99: 11-27.

- [89] Coccia G, Nicola GD, Sotte M. Design, manufacture, and test of a prototype for a parabolic trough collector for industrial process heat. *Renewable Energy* 2015; 74: 727-736.
- [90] Lu JF, Yuan QY, Ding J, Wang WL, Liang JM. Experimental studies on nonuniform heat transfer and deformation performances for trough solar receiver. *Applied Thermal Engineering* 2016; 109: 497-506.
- [91] Wu YT, Liu SW, Xiong YX, Ma CF, Ding YL. Experimental study on the heat transfer characteristics of a low melting point salt in a parabolic trough solar collector system. *Applied Thermal Engineering* 2015; 89: 748-754.
- [92] Salgado CL, Rodriguez-Pulido A, Calderon G. Thermal performance of parabolic trough solar collectors. *Renewable and Sustainable Energy Reviews* 2017; 67: 1345-1359.
- [93] Forristall R. Heat transfer analysis and modelling of a parabolic trough solar receiver implemented in engineering equation solver. 2003, Technical Report NREL/TP-550-34169.
- [94] Padilla RV, Demirkaya G, Goswami DY, Stefanakos E, Rahman MM. Heat transfer analysis of parabolic trough solar receiver. *Applied Energy* 2011; 88: 5097-5110.
- [95] Daniel P, Joshi Y, Das AK. Numerical investigation of parabolic trough receiver performance with outer vacuum shell. *Solar Energy* 2011; 85: 1910-1914.
- [96] Kalogirou SA. A detailed thermal model of a parabolic trough collector receiver. *Energy* 2012; 48: 298-306.
- [97] Patil RG, Panse SV, Joshi JB. Optimization of non-evacuated receiver of solar

collector having non-uniform temperature distribution for minimum heat loss. *Energy Conversion and Management* 2014; 85: 70-84.

[98] Yilmaz IH, Sylemez MS. Thermo-mathematical modeling of parabolic trough collector. *Energy Conversion and Management* 2014; 88: 768-784.

[99] Behar O, Khellaf A, Mohammedi K. A novel parabolic trough solar collector model – Validation with experimental data and comparison to Engineering Equation Solver (EES). *Energy Conversion and Management* 2015; 106: 268-281.

[100] Liang HB, You SJ, Zhang H. Comparison of different heat transfer models for parabolic trough solar collectors. *Applied Energy* 2015; 148: 105-114.

[101] Huang WD, Xu Q, Hu P. Coupling 2D thermal and 3D optical model for performance prediction of a parabolic trough solar collector. *Solar Energy* 2016; 139: 365-380.

[102] Guo JF, Huai XL, Liu ZG. Performance investigation of parabolic trough solar receiver. *Applied Thermal Engineering* 2016; 95: 357-364.

[103] Guo JF, Huai XL. Multi-parameter optimization design of parabolic trough solar receiver. *Applied Thermal Engineering* 2016; 98: 73-79.

[104] He YL, Xiao J, Cheng ZD, Tao YB. A MCRT and FVM coupled simulation method for energy conversion process in parabolic trough solar collector. *Renewable Energy* 2011; 36: 976-985.

[105] Cheng ZD, He YL, Cui FQ, Xu RJ, et al. Numerical simulation of a parabolic trough solar collector with non-uniform solar flux conditions by coupling FVM and MCRT method. *Solar Energy* 2012; 86:1770-1784.

- [106] Cheng ZD, He YL, Cui FQ. Numerical investigations on coupled heat transfer and synthetical performance of a pressurized volumetric receiver with MCRT-FVM. *Applied Thermal Engineering* 2013; 50: 1044-1054.
- [107] Lu JF, Ding J, Yang JP, Yang XX. Nonuniform heat transfer model and performance of parabolic trough solar receiver. *Energy* 2013; 59: 666-675.
- [108] Cheng ZD, He YL, Yu Q. A detailed nonuniform thermal model of a parabolic trough solar receiver with two halves and two inactive ends. *Renewable Energy* 2015; 74: 139-147.
- [109] Wang YJ, Liu QB, Lei J, Jin HG. Performance analysis of a parabolic trough solar collector with non-uniform solar flux conditions. *International Journal of Heat and Mass Transfer* 2015; 82: 236-249.
- [110] Hachicha AA, Rodriguez L, Capdevila R, Oliva A. Heat transfer analysis and numerical simulation of a parabolic trough solar collector. *Applied Energy* 2013; 111: 581-592.
- [111] Zaversky Fritz, Medina R, Garcia-Barberena J, Sanchez M, Astrain D. Object-oriented modeling for the transient performance simulation of parabolic trough collectors using molten salt as heat transfer fluid. *Solar Energy* 2013; 95: 192-215.
- [112] Silva R, Perez M, Fernandez-Garcia A. Modeling and co-simulation of a parabolic trough solar plant for industrial process heat. *Applied Energy* 2013; 106: 287-300.
- [113] Wu Z, Lei DQ, Yuan GF, Shao JJ, Zhang YT, Wang ZF. Structural reliability analysis of parabolic trough receivers. *Applied Energy* 2014; 123: 232-241.
- [114] Wu Z, Li SD, Yuan GF, Lei DQ, Wang ZF. Three-dimensional numerical study of

heat transfer characteristics of parabolic trough receiver. *Applied Energy* 2014; 113: 902-911.

[115] Okafor IF, Dirker J, Meyer JP. Influence of non-uniform heat flux distributions on the secondary flow, convective heat transfer and friction factors for a parabolic trough solar collector type absorber tube. *Renewable Energy* 2017; 108: 287-302.

[116] Yang S, Sensoy TS, Ordonez JC. Dynamic 3D volume element model of a parabolic trough solar collector for simulation and optimization. *Applied Energy* 2018; 217: 509-526.

[117] Al-Ansary H, Zeitoun O. Numerical study of conduction and convection heat losses from a half-insulated air-filled annulus of the receiver of a parabolic trough collector. *Solar Energy* 2011; 85(11): 3036-3045.

[118] Chandra YP, Singh A, Mohapatra SK, Kesari JP, Rana L. Numerical optimization and convective thermal loss analysis of improved solar parabolic trough collector receiver system with one sided thermal insulation. *Solar Energy* 2017; 148: 36-48.

[119] Osorio JD, Rivera-Alvarez A, Girurugwiro P, Yang S, Hovsopian R, Ordonez JC. Integration of transparent insulation materials into solar collector devices. *Solar Energy* 2017; 147: 8-21.

[120] Yang HL, Wang QL, Huang XN, Li J, Pei G. Performance study and comparative analysis of traditional and double-selective-coated parabolic trough receivers. *Energy* 2018; 145: 206-216.

[121] Wang QL, Yang HL, Huang XN, Li J, Pei G. Numerical investigation and experimental validation of the impacts of an inner radiation shield on parabolic trough

- solar receivers. *Applied Thermal Engineering* 2018; 132: 381-392.
- [122] Wang QL, Hu MK, Yang HL, Cao JY, Li J, Su YH, Pei Gang. Energetic and exergetic analyses on structural optimized parabolic trough solar receivers in a concentrated solar-thermal collector system. *Energy* 2019; 171: 611-623.
- [123] Sandeep HM, Arunachala UC. Solar parabolic trough collectors: A review on heat transfer augmentation techniques. *Renewable and Sustainable Energy Reviews* 2017; 69: 1218-1231.
- [124] Bellos E, Tzivanidis C. Alternative designs of parabolic trough solar collectors. *Progress in Energy and Combustion Science* 2019; 71: 81-117.
- [125] Kumar KR, Reddy KS. Thermal analysis of solar parabolic trough with porous disc receiver. *Applied Energy* 2009; 86: 1804-1812.
- [126] Kumar KR, Reddy KS. Effect of porous disc receiver configurations on performance of solar parabolic trough concentrator. *Heat and Mass Transfer* 2012; 48: 555-571.
- [127] Reddy KS, Kumar KR, Ajay CS. Experimental investigation of porous disc enhanced receiver for solar parabolic trough collector. *Renewable Energy* 2015; 77: 308-319.
- [128] Munoz J, Abanades A. Analysis of internal helically finned tubes for parabolic trough design by CFD tool. *Applied Energy* 2011; 88: 4139-4149.
- [129] Cheng ZD, He YL, Cui FQ. Numerical study of heat transfer enhancement by unilateral longitudinal vortex generators inside parabolic trough solar receivers. *International Journal of Heat and Mass Transfer* 2012; 55: 5631-5641.

- [130] Wang P, Liu DY, Xu C. Numerical study of heat transfer enhancement in the receiver tube of direct steam generation with parabolic trough by inserting metal foams. *Applied Energy* 2013; 102: 449-460.
- [131] Song XW, Dong GB, Gao FY, Diao XG, Zheng LQ, Zhou FY. A numerical study of parabolic trough receiver with nonuniform heat flux and helical screw-tape inserts. *Energy* 2014; 77: 771-782.
- [132] Ghadirijafarbeigloo S, Zamzamian AH, Yaghoubi M. 3-D numerical simulation of heat transfer and turbulent flow in a receiver tube of solar parabolic trough concentrator with louvered twisted-tape inserts. *Energy Procedia* 2014; 49: 373-380.
- [133] Mwesigye A, Bello-Ochende T, Meyer JP. Heat transfer and thermodynamic performance of a parabolic trough receiver with centrally placed perforated plate inserts. *Applied Energy* 2014; 136: 989-1003.
- [134] Mwesigye A, Bello-Ochende T Meyer JP. Multi-objective and thermodynamic optimization of a parabolic trough receiver with perforated plate inserts. *Applied Thermal Engineering* 2015; 77: 42-56.
- [135] Chang C, Xu C, Wu ZY, Li X, Zhang QQ, Wang ZF. Heat transfer enhancement and performance of solar thermal absorber tubes with circumferentially non-uniform heat flux. *Energy Procedia* 2015; 69: 320-327.
- [136] Wang FQ, Lai QZ, Han HZ, Tan JY. Parabolic trough receiver with corrugated tube for improving heat transfer and thermal deformation characteristics. *Applied Energy* 2016; 164: 411-424.
- [137] Wang FQ, Tang ZX, Gong XT, Tan JY, Han HZ, Li BX. Heat transfer performance

enhancement and thermal strain restraint of tube receiver for parabolic trough solar collector by using asymmetric outward convex corrugated tube. *Energy* 2016; 114: 275-292.

[138] Mwesigye A, Bello-Ochende T, Meyer JP. Heat transfer and entropy generation in a parabolic trough receiver with wall-detached twisted tape inserts. *International Journal of Thermal Sciences* 2016; 99: 238-257.

[139] Kalidasan B, Shankar R, Srinivas T. Absorber tube with internal hinged blades for solar parabolic trough collector. *Energy Procedia* 2016; 90: 463-469.

[140] Jaramillo OA, Borunda Monica, Velazquez-Lucho KM, Robles M. Parabolic trough solar collector for low enthalpy processes: An analysis of the efficiency enhancement by using twisted tape inserts. *Renewable Energy* 2016; 93: 125-141.

[141] Bellos E, Tzivanidis C, Antonopoulos KA, Gkinis G. Thermal enhancement of solar parabolic trough collectors by using nanofluids and converging-diverging absorber tube. *Renewable Energy* 2016; 94: 213-222.

[142] Zhu XW, Fu YH, Zhao JQ. A novel wavy-tape insert configuration for pipe heat transfer augmentation. *Energy Conversion and Management* 2016; 127: 140-148.

[143] Zhu XW, Zhu L, Zhao JQ. Wavy-tape insert designed for managing highly concentrated solar energy on absorber tube of parabolic trough receiver. *Energy* 2017; 141: 1146-1155.

[144] Gong XT, Wang FQ, Wang HY, Tan JY, Lai QZ, Han HZ. Heat transfer enhancement analysis of tube receiver for parabolic trough solar collector with pin fin arrays inserting. *Solar Energy* 2017; 144: 185-202.

- [145] Huang Z, Li ZY, Yu GL, Tao WQ. Numerical investigations on fully-developed mixed turbulent convection in dimpled parabolic trough receiver tubes. *Applied Thermal Engineering* 2017; 114: 1287-1299.
- [146] Bellos E, Tzivanidis C, Tsimpoukis D. Thermal enhancement of parabolic trough collector with internally finned absorbers. *Solar Energy* 2017; 157: 514-531.
- [147] Bellos E, Tzivanidis C, Daniil I, Antonopoulos KA. The impact of internal longitudinal fins in parabolic trough collectors operating with gases. *Energy Conversion and Management* 2017; 135: 35-54.
- [148] Bellos E, Tzivanidis C, Tsimpoukis D. Multi-criteria evaluation of parabolic trough collector with internally finned absorbers. *Applied Energy* 2017; 205: 540-561.
- [149] Bellos E, Tzivanidis C, Tsimpoukis D. Optimum number of internal fins in parabolic trough collectors. *Applied Thermal Engineering* 2018; 137: 669-677.
- [150] Bellos E, Tzivanidis C. Investigation of a star flow insert in a parabolic trough solar collector. *Applied Energy* 2018; 224: 86-102.
- [151] Bellos E, Daniil I, Tzivanidis C. Multiple cylindrical inserts for parabolic trough solar collector. *Applied Thermal Engineering* 2018; 143: 80-89.
- [152] Ghasemi SE, Ranjbar AA. Numerical thermal study on effect of porous rings on performance of solar parabolic trough collector. *Applied Thermal Engineering* 2017; 118: 807-816.
- [153] Chang C, Sciacovelli A, Wu ZY, Li X, Li YL, Zhao MZ, Deng J, Wang ZF, Ding YL. Enhanced heat transfer in a parabolic trough solar receiver by inserting rods and using molten salt as heat transfer fluid. *Applied Energy* 2018; 220: 337-350.

- [154] Bitam EW, Demagh Y, Hachicha AA, Benmoussa H, Kabar Y. Numerical investigation of a novel sinusoidal tube receiver for parabolic trough technology. *Applied Energy* 2018; 218: 494-510.
- [155] Pettit RB. Characterization of the reflected beam profile of solar mirror materials. *Solar Energy* 1977; 19: 733-741.
- [156] Taneja P, Kandpal TC, Mathur SS. Concentration characteristics of a two stage solar concentrator: effect of primary mirror surface errors. *International Journal of Energy Research* 1992; 16: 203-211.
- [157] Pottler K, Lupfert E, Johnston GHG, Shortis MR. Photogrammetry: a powerful tool for geometric analysis of solar concentrators and their components. *Journal of Solar Energy Engineering* 2005, 127: 94-101.
- [158] Ulmer S, Heinz B, Pottler K, Lupfert E. Slope error measurements of parabolic troughs using the reflected image of the absorber tube. *Journal of Solar Energy Engineering* 2009, 131: 011-014.
- [159] Agustin MD-T, Lourdes GR. Comparison of solar technologies for driving a desalination system by means of an Organic Rankine Cycle. *Desalination* 2007; 216: 276-291.
- [160] Webb RL. Performance evaluation criteria for use of enhanced heat transfer surfaces in heat exchanger design. *International Journal of Heat and Mass Transfer* 1981; 24(4) 715-726.
- [161] Hasanpour A, Farhadi M, Sedighi K. A review study on twisted tape inserts on turbulent flow heat exchangers: the overall enhancement ratio criteria. *International*

Communications in Heat and Mass Transfer 2014; 55: 53-62.

[162] Guo ZY. Mechanism and control of convective heat transfer - Coordination of velocity and heat flow fields. Chinese Science Bulletin 2001; 46(7): 596-599.

[163] Li ZX, Guo ZY. Field synergy theory for heat convection optimization. Science Press, Beijing; 2010. (In Chinese)

[164] Tao WQ. Numerical Heat Transfer (2nd Edition). Xi'an Jiaotong University Press, Xi'an; 2001. (In Chinese)

[165] Mullick SC, Nanda SK. An improved technique for computing the heat loss factor of a tubular absorber. Solar Energy 1989; 42: 1-7.

[166] Gnielinski V. New equations for heat and mass transfer in turbulent pipe and channel flow. International Chemical Engineering 1976; 16(2): 359-368.

[167] Petukhov BS. Heat Transfer and Friction in Turbulent Pipe Flow with Variable Physical Properties. Advances in Heat Transfer 1970; 6: 503-564.